UNIVERSITY OF BELGRADE

Faculty of Technology and Metallurgy

Mr Khaled Taleb

Application of macroporous resin and cellulose based materials modified with iron oxides for arsenic removal

Doctoral Dissertation

Belgrade, 2016.

UNIVERZITET U BEOGRADU

Tehnološko-metalurški fakultet

Mr Khaled Taleb

Primena makroporoznih smola i materijala na bazi celuloze modifikovanih oksidima gvožđa za uklanjanje arsena

Doktorska disertacija

Beograd, 2016.

Faculty of Technology and Metallurgy
University of Belgrade

INFORMATION ABOUT THE THESIS ADVISOR AND EXAMINATION COMMITTEE

Thesis Advisor: dr Aleksandar Marinković, assistant professor

Faculty of Technology and Metallurgy, University of Belgrade

Final examining committee:

dr Aleksandar Marinković, assistant professor, University of Belgrade, Faculty of Technology and Metallurgy,

dr Mirjana Ristić, full professor, University of Belgrade, Faculty of Technology and Metallurgy,

dr Aleksandra Perić-Grujić, full professor, University of Belgrade, Faculty of Technology and Metallurgy,

dr Vladimir Pavlović, full professor, University of Belgrade, Faculty of Agriculture.

Date:

ACKNOWLEDGEMENT

Faculty of Technology and Metallurgy
University of Belgrade

Information regarding Ph.D Thesis

Title: Application of macroporous resin and cellulose based materials modified with iron oxides for arsenic removal

Abstract: Arsenic is classified as a Class A human carcinogen, toxic and mutagen and prevention of drinking water contamination has been a challenge of global magnitude. To limit the exposure to arsenic, the World Health Organization defined new water standards and decreased the maximum contaminant level (MCL) of arsenic to10 μg L^{-1}. Due to this strict regulation extensive development of technologies applicable for effective arsenic removal was necessary to be developed. Among the possible arsenic removal techniques, adsorption is considered as simple, efficient and economic method which offers flexibility in design and generating high-quality treated effluent. In that sense the research topic of the doctoral thesis was focused on synthesis of new high performance adsorbents applicable for effective arsenic removal. First part of the work was related to preparation of porous materials, *i.e.* amino modified macroporous resin obtained in first step was followed by precipitation of iron(III)-oxyhydroxide in goethite form, and by application of freeze/drying technique high performance **ER/DETA/FO** adsorbent was obtained. Synthesis performed within second part was related to nanocellulose isolation (**NC**) followed by modification with PEG-6-arm amino polyethylene glycol (PEG-NH$_2$) *via* maleic anhydride (**MA**) linker producing **NC-PEG** intermediary material. Also, introduction of organic branched structure on **NC** *via* four consecutive steps: maleic acid anhydride (**MA**), ethylenediamine (**EDA**), ethyl acrylate (**EA**), and finally with **EDA** produce amino modified **NC-L** material. Subsequent precipitation of goethite (**FO**) on both **NC-PEG** and **NC-L** produced **NC-PEG/FO** and **NC-L/FO** adsorbents. Extension of the study on the cellulosic based materials was related to modification of **NC** and microfibrillar cellulose (**MC**) for the preparation of magnetite (**MG**) based high performance adsorbent. Precipitation of **MG** on amino terminal branched organic structure, **L'**, linked either by maleic acid residue on **NC** surface (**NC-MA/L'**)

or by oxalyl bridge on **MC** surface (**MC-O/L'**) was used as support for **MG** precipitation. Design and synthesis of structure **L'**, obtained by successive reactions of **NC-MA** and **MC-O** with ethylenediamine (**EDA**), ethylenediamine-tetraacetic acid (**EDTA**) ethyl ester and **EDA** in a final step, produced significant number of amino terminal groups. Nanosized **MG** was deposited/precipitated in an optimized/controlled manner on both **NC-MA/L** and **MC-O/L** surfaces producing **NC-MA/L'-MG** and **MC-O/L'-**MG adsorbents, respectively. Obtained materials were characterized by XRD, SEM/TEM electron microscopy, FTIR, Raman, TGA, and BTE/BJH analysis. Efficiency of adsorption was studied with respect to functionalization methods, solution pH, contact time, temperature, initial arsenate concentration and interfering ions influence. The high maximum adsorbent capacity of the tested adsorbents, obtained according to Langmuir model, indicated successful arsenic removal at both low and high adsorbate concentrations. A pseudo-second order equation fitted well the kinetic data for all materials, while intra-particle diffusion proved to be a limiting step of the adsorptions. Thermodynamic parameters indicated exothermic and spontaneous nature of adsorption processes. Results of the modelling of the influences of competitive ions, pH and ionic strength of the solution, obtained by Visual MINTEQ equilibrium speciation modeling program, was in good agreement with experimental results. Arsenic removal capabilities of the hybrid goethite impregnated macroporous resin were evaluated from batch adsorption tests and simulating the breakthrough curve was performed with a pore surface diffusion model (PSDM). The PSDM was able to provide a good prediction of the media's capacity and intraparticle mass transport properties under high hydraulic loading rates at pilot scale testing, after being verified by a short bed column (SBC) test. The interpretation of the synthesis and modification method influences on the properties of adsorbents and possibility of their practical application was discussed.

Tehnološko-metalurški fakultet
Univerzitet u Beogradu

Informacije o doktorskoj disertciji

Naslov: Primena makroporoznih smola i materijala na bazi celuloze modifikovanih oksidima gvožđa za uklanjanje arsena

Rezime: Arsen spada u kategoriju karcinogena klase A, toksičan je i mutagen i prevencija kontaminacije vode za piće izazvana arsenom je izazov koji je globalnog značaj. U cilju smanjenja izloženosti arsenu, Svetska zdravstvena organizacija definisala je standard za vodu kojim se smanjuje maksimalni nivo (MCL) arsena na 10 $\mu g\ L^{-1}$. Usled strogih propisa sprovode se obimna istraživanja na razvoju novih tehnologija primenjivih za efikasno uklanjanje arsena. Među mogućim primenjivim tehnikama za uklanjanje arsena, adsorpcija je jednostavna, efikasna i ekonomična tehnika koja nudi fleksibilnost pri dizajnu, a daje visok kvalitet tretirane vode. U skladu sa navedenim istraživanja u okviru ove doktorske disertacije izvršene su sinteze novih adsorbenata koji imaju optimalna adsorpciona svojstva za efikasno uklanjanje arsena iz vode.

Prvi deo rada se odnosio na pripremu visokoporozne osnove, tj. amino modifikovane makroporozne smole koja je dalje, u drugom stupnju, modifikovana gvožđe(III)-oksihidroksidom u obliku goetita i primenom metode liofilizacije dala **ER/DETA/FO**/**FD** adsorbent. Sinteze izvedene u drugom delu doktorske disertacije su se odnosile na izolovanje nanoceluloze, modifikaciju sa PEG-6-arm amino polietilen glikol (PEG-NH$_2$) preko ostatka malein anhidrida, čime je sintetisan **NC-PEG** materijal. Takođe, uvođenjem organske razgranate strukture na **NC** preko četiri sukcesivna koraka: anhidrida maleinske kiseline (**MA**), etilendiamina (**EDA**), etil akrilata (**EA**), i **EDA** dobijen je amino modifikovani **NC-L** materijal. Naredni korak je uključivao taloženje getita (**FO**) na **NC-PEG i NC-L,** a dobijeni su **NC-PEG/FO** i **NC-L/FO** adsorbenti. Nastavak rada u drugom delu se odnosio na modifikovanje nanoceluloze (**NC**) i mikrofibrilarne celuloze (**MC**) kako bi se izvršilo taloženje magnetita (**MG**) i dobili hibridni adsorbenti visokih performansi. Taloženje **MG** na amino funkcionalizovanu razgranatu organsku strukturu, **L**', povezane ili preko ostatka maleinske kiseline na **NC** površinu (**NC-MA/L'**) ili oksalil mosta na **MC** površini (**MC-O/L'**) je korišćena kao osnova za taloženje magnetita.

Dizajn i sinteza strukture **L'**, dobijena uzastopnim reakcijama **NC-MA** i **MC-O** sa **EDA**, etil estrom etilendiamin-tetrasirćetne kiseline (**EDTA**) i **EDA** u završnom koraku, daje značajan broj amino terminalnih grupa. Nano **MG** je deponovan pri optimalnim/kontrolisanim uslovima na površinama **NC-MA/L'** i **MC-O/L'** pri čemu se dobijaju **NC-MA/L'-MG** i **MC-O/L'-MG** adsorbenti. Dobijeni materijali su karakterisani primenom XRD, SEM/TEM elektronske mikroskopije, FTIR, Raman, TGA i BET/BJH analize. Efikasnost adsorpcije je ispitivana u zavisnosti od metoda funkcionalizacije, pH rastvora, vremena trajanja procesa, temperature, koncentracije adsorbata i uticaja konkurentnih jona u rastvoru. Visoki adsorpcioni kapaciteti ispitivanih materijala, određeni prema modelu Lengmirove adsorpcione izoterme, ukazuju da mogu biti uspešno korišćeni za uklanjanje arsena, kako pri niskoj, tako i pri visokoj koncentraciji. Jednačinom pseudo-drugog reda opisana je kinetika procesa adsorpcije, a unutarčestična difuzija je definisana kao limitirajući korak reakcije. Rezultati termodinamičkih ispitivanja su ukazali na spontanost i egzotermnu prirodu procesa adsorpcije kod svih ispitivanih materijala. Upotrebom računarskog programa Visual MINTEQ dobijena su dobra slaganja između eksperimentalnih rezultata i izračunatih pri ispitivanju uticaja konkurentnih jona, pH i jonske jačine rastvora. Uklanjanje arsena primenom makroporozne smole impregnisane getitom je procenjeno izvođenjem adsorpcionih eksperimenata u šaržnom sistemu i simuliranjem krive proboja pomoću *pore surface diffusion* modela (PSDM). PSDM obezbeđuje dobro predviđanje kapaciteta adsorbenta i opis unutarčestičnog transporta mase u uslovima visoke brzine protoka efluenta u protočnom pilot postrojenju, nakon što su verifikovani na osnovu eksperimenata na kratkoj koloni (*short bed column* - SBC). U okviru rada razmatran je uticaj sinteze i metoda modifikacije na svojstva krajnjeg proizvoda, tj. adsorbenta, u zavisnosti od njegovih adsorptivnih svojstava i primene.

LIST OF TABLES

LIST OF FIGURES

ABBREVIATIONS

a_K – Khan isotherm model exponent

a_R – Redlich–Peterson isotherm constant ($1mg^{-1}$)

a_{RP} – Radke–Prausnitz isotherm model constant

a_S – Sips isotherm model constant (L mg^{-1})

a_T – Toth isotherm constant (L mg^{-1})

A – Koble–Corrigan isotherm constant ($L^n mg^{1-n} g^{-1}$)

A_T – Tempkin isotherm equilibrium binding constant (L g^{-1})

b_K –Khan isotherm model constant

b_T – Tempkin isotherm constant

B – Koble–Corrigan isotherm constant (L mg^{-1})n

B_{DR} – Dubinin–Radushkevich isotherm constant

C_e – equilibrium concentration (mgL^{-1})

C_o – adsorbate initial concentration (mg L^{-1})

C_s – adsorbate monolayer saturation concentration (mg L^{-1})

C_{BET} – BET adsorption isotherm relating to the energy of surface interaction (L mg^{-1})

d – Interlayer spacing (m)

ε – Dubinin–Radushkevich isotherm constant

E – mean free energy ($kJmol^{-1}$)

g – Redlich–Peterson isotherm exponent

ΔG° – Gibbs energy change (kJ mol^{-1})

k – MacMillan–Teller (MET) isotherm constant

K_{ad} – Dubinin–Radushkevich isotherm constant ($mol^2 kJ^{-2}$)

K_D –Hill constant

K_F – Freundlich isotherm constant (mg g^{-1}) (L $g^{-1})^n$ related to adsorption capacity

K_{FH} - Flory–Huggins isotherm equilibrium constant (L g^{-1})

K_L – Langmuir isotherm constant (L g^{-1})

K_R – Redlich–Peterson isotherm constant (L g^{-1})

K_s – Sips isotherm model constant (L g^{-1})

K_T –Toth isotherm constant (mg g^{-1})

n – adsorption intensity

n_{FH} – Flory–Huggins isotherm model exponent

n_H – Hill cooperativity coefficient of the binding interaction

p – number of parameter

q_e – amount of adsorbate in the adsorbent at equilibrium (mg g^{-1})

$q_{e,calc}$ – calculated adsorbate concentration at equilibrium (mg g^{-1})

$q_{e,meas}$ – measured adsorbate concentration at equilibrium (mg g^{-1})

q_s – theoretical isotherm saturation capacity (mg g^{-1})

q_{sH} – Hill isotherm maximum uptake saturation (mg L^{-1})

Q_o – maximum monolayer coverage capacities (mg g^{-1})

r – inverse power of distance from the surface

r_R – Radke–Prausnitz isotherm model constant

β_R – Radke–Prausnitz isotherm model exponent

R – universal gas constant ($8.314 \text{ J mol}^{-1} \text{ K}^{-1}$)

R^2 – correlation coefficient

R_L – separation factor

t – Toth isotherm constant

T – temperature (K)

MF – Microfiltration

UF – Ultrafiltration

RO – Reverse osmosis

NF – Nanofiltration

CMC – Critical micelle concentration

MCL – Maximum contaminant level

CNT – Carbon nanotubes

α-Fe_2O_3 – Alpha phase of iron(III) oxide (maghemite)

β-Fe_2O_3 – Beta phase of iron(III) oxide (hematite)

γ-Fe_2O_3 – Gama phase of iron(III) oxide

PEG-MWCNT – Multiwall carbon nanotubes functionalized with polyethylene glycol

Ti-BYC – Titanium-loaded basic yttrium carbonate

CeO_2 – CNT – Cerium(III) oxide-loaded carbon nanotubes

Fe_3O_4 – Magnetite

Fe_2O_3 – Iron(III) oxide

nZVI – Zero-valent iron nanoparticles

TiO_2 – Titanium-dioxide

MNPs – Magnetite nanoparticles

KNO_3 – Potassium nitrate

$FeCl_3$ – Ferric chloride

$Al_2(SO_4)_3$ x $18H_2O$ – Aluminium sulphate octadecahydrate

$ZrCl_4$ – Zirconium(IV) chloride

$TiCl_3$ – Titanium(III)chloride

$TiCl_4$ – Titanium(IV)chloride

$TiOCl_2$ – Titanium(IV)oxychloride

$ZrOCl_2$ – Zirconium(IV)oxychloride

$Fe_2(SO_4)_3$ – Ferric sulphate

$Ti(SO_4)_2$ – Titanium(IV) sulfate

ODR – Orthogonal distance regression

DLM – Diffuse-layer model

HFO – Hydrous ferric oxide

HWIR – Hazardous Waste identification Rule

CCM – Constant Capacitance Model

TLM – Triple Layer Model

BSM – Basic Stern Model

TPM – Three Plane Model

NEM – Non-Electrostatic Model

HMO – Hydrated oxide of manganese

HSDM – Homogeneous solid diffusion model

α-FeOOH – Goethite
β – FeOOH – Akaganeite
γ – FeOOH – Lepidocrocite
δ' – FeOOH – Feroxyhyte
$Fe_5H0_8 \times 4H_20$ – Ferrihydrite
EXAF – Extended X-ray absorption fine structure spectroscopy
PVA – Polyvinyl acetate
DH – Degree of hydrolysis
PVC – Poly(vinil chloride)
VCM – Vinyl chloride monomer vinyl chloride monomer
MAR – Macroporous adsorption resin
AIBN – α,α'-azo-bis-isobutyronitrile (2,2′-Azobis(2-methylpropionitrile)
IUPAC – International Union of Pure and Applied Chemistry
SEM – Scanning electron microscopy
TEM – Transmission electron microscopy
AFM – Atomic force microscopy
SP – Suspension polymerization
HSP – The Hildebrand solubility parameter
PCR – Porous copolymer resin
NFC – Nanofibrillated cellulose
CNC – Cellulose nanocrystals
BC – Bacterial cellulose
AC – Algae cellulose
MFC – Microfibrillated cellulose
CNF – Cellulose nanofibrils
E_A – Elastic modulus in axial direction
E_T – Elastic modulus in transverse direction
σ_f – Tensile strength (tensile testing)
ε_f – Strain to failure (tensile testing)
CBM – Cellulose binding modules
CBD – Cellulose binding domains
DIW – Deionized water
GMA – Glycidyl methacrylate
EGDMA – Ethylene glycol dimethacrylate
PVP – Poly(N-vinylpyrrolidone)
DETA – Diethylene triamine
THF – Tetrahydrofurane
EtOH – Ethanol
$PEG-NH_2$ – PEG-6-arm amino polyethylene glycol
MA – Maleic anhydride
DMF – N,N-dimethylformamide
$NaHCO_3$ – Sodium hydrogencarbonate
$FeSO_4 \cdot 7H_20$ – Iron(II) sulfate heptahydrate
EDA – Ethylenediamine
EDTA – Ethylenediaminetetraacetic acid

DMF – *N,N*-dimethylformamide
KOH – Potassium hydroxide
TEA – Triethylamine
EOC – Ethyl oxalyl chloride
DMAc – *N,N*-dimethylacetamide
DCC – Dicyclohexylcarbodiimide
NMP – *N*-methylpyrrolidone
$Na_2HAsO_4 \cdot 7H_2O$ – Sodium arsenate dibasic heptahydrate
$NaAsO_2$ – Sodium arsenite
$NaOH$ – Sodium hydroxide
NaH_2PO_4 – Dihydrogen phosphate
Na_2SO_4 – Sodium sulfate
$Ca(NO_3)_2 \cdot 4H_2O$ – Calcium nitrate
$MgNO_3 \cdot 6H_2O$ – Magnesium nitrate
Na_2SiO_3 – Sodium metasilicate solution
$NaCl$ – Sodium chloride
BET – **B**runauer-**E**mmett-**T**eller
BJH – **B**arrett-**J**oyner-**H**alenda
FTIR – Fourier-transform infrared spectra
RSD – Relativestandard deviation
ICP-MS – Inductively coupled plasma mass spectrometry
pH_{PZC} – Point of zero charge
LoD – Limit of detection
SEM – Scanning electron microscopy
TEM – Transmission electron microscopy
LM – Levenberg-Marquardt
EBV – Empty bed volume
EBCT – Empty bed contact time
H – Bed depth
SBC – Short bed column
γ – Linear flow rate
ΔG^o – The standard Gibb's free energy change
ΔH^o – The enthalpy change
ΔS^o – Theentropy change
θ – degree of surface coverage
α – Frenkel–Halsey–Hill isotherm constant (J m^r/mole) with r is the sign of inverse power of distance from the surface
β_S – Sips isotherm model exponent
ER – Epoxy functionalized cross-linked macroporous resin
ER/DETA – Diethylenetriamine modified **ER** resin
ER/DETA/FO – Iron(III) oxide modified **ER/DETA** support
ER/DETA/FO/VD – **ER/DETA/FO** vacum dried
ER/DETA/FO/FD – **ER/DETA/FO** freeze dried
NC – Nanocellulose
NC-MA – **NC** modified with malic anhydride

PEG – PEG-6-arm amino polyethylene glycol

NC-PEG – **NC-MA** modified **PEG**

NC-PEG/FO – **NC-PEG** modifid with iron(III) oxide

NC-MA-EDA – **NC-MA** modified with **EDA**

NC-MA-EDA-EA – **NC-MA-EDA** mosified with ethyl acrylate

NC-MA-EDA-EA-EDA (NC-L) – **NC-MA-EDA-EA** modified with **EDA**

NC-L/FO – **NC-L** modified with iron(III) oxide

NC-MA/EDA-EDTA – **NC-MA-EDA** modified with *N*, *N*'-1,2-ethanediylbis[*N*-(2-ethoxy-2-oxoethyl)]-1,1'-glycine diethyl ester (tetraethyl ester of EDTA)

NC-MA/EDA-EDTA-EDA (**NC-MA/L'**) – **NC-MA/EDA-EDTA** modified with **EDA**

NC-MA/L'-MG – **NC-MA/L** modified with **MG**

MC-O – **MC** modified with **EOC**

MC-O/L' – **MC-O** modifies with **L'**

MC-O/L-MG – **MC-O/L'** modified with **MG**

Contents

xiv

1. INTRODUCTION

Increased awareness of the harmful effects of arsenic in drinking water has influenced the increase in the volume of new research methods and materials for the removal of arsenic but so far none of them have fully met all necessary requirements, both technological and economic. Since the discovery of macroporous resins and cellulosic materials with significant number of functionalization/modification contribute to appropriate mechanical and chemical properties which provide possibility for their application in various fields of science and technology, with of the interesting areas of application in water treatment/purification. Due to this, four new adsorbents were synthesized based on macroporous resin and cellulose based materials modified with iron oxides and studied in a processes of arsenic removal. Modern scientific trends in the field of separation technology emphasis on the economic viability of the plant used in a water purification, and therefore the price of the used technology and materials is a important decisive criteria for estimation of its applicability.

The content of the thesis. This doctoral thesis is written on 228 pages, contains 50 pictures, 45 tables and 330 references. The dissertation consists of the following parts: Introduction, Theoretical part, Experimental part, Results and Discussion and Conclusions. In the Introduction (Chapter 1) the objectives of the doctoral dissertation was explained. Theoretical part (Chapter 2) consists of five parts. Chapter 2 addresses the problem of arsenic contamination of water and related water purification technologies. Theoretical aspects of the adsorption process and the mathematical modeling of adsorption process were given in detail. Synthesis, properties and uses of iron(III) oxides in a processes of arsenic removal was also presented. Possibilities of the use of new macroporous and cellulosic based materials in the field of water treatment polluted with arsenic are also discussed in this chapter. Further, the macroporus resins and cellulose based materials, their properties and methods of synthesis, the most common methods of functionalization, characterization methods, the safety of their use and application in the field of water treatment is presented. In the Experimental part, Chapter 3, materials, methods of synthesis of adsorbents, characterization techniques, experimental procedures and conditions in adsorption experiments and mathematical modeling was presented. The Results and Discussion section, given as Chapter 4, comprised experimental results on the optimization of syntheses and

characterization of adsorbents, results of the data modeling from adsorption and kinetic study in non-competitive and competitive condition, calculation of thermodynamic and activation parameters by different methodologies, and short techno-economic analysis of selected adsorbents. In conclusion, it is emphasized the contribution of this thesis (Chapter 5).

The subject of the work. In this dissertation, optimization of the synthesis of cross-linked macroporous polymer *in-situ* impregnated with hydrous iron oxide *via* an oxidative deposition, and post-process of obtained material by application of freeze/drying technique, produces high performance adsorbent **ER/DETA/FO/FD** applicable for efficient arsenic removal. In second part of the work two novel goethite modified nanocellulosic support were prepared. **NC-PEG** was obtained by modification of nanocellulose (**NC**) with PEG-6-arm amino polyethylene glycol (PEG-NH$_2$) *via* maleic anhydride (**MA**) linker, and subsequent precipitation of goethite (**FO**) on **NC-PEG** produced **NC-PEG/FO** adsorbent. Introduction of organic branched structure on **NC***via* four consecutive steps: maleic acid anhydride (**MA**), ethylenediamine (**EDA**), ethyl acrylate (**EA**), and finally with **EDA** produce amino modified **NC-L** product. Subsequent modification of **NC-L** with goethite gave **NC-L/FO**. Both **NC-PEG/FO** and **NC-L/FO** were effective adsorbents in a arsenic removal processes. In the last part comparative adsorption study related to benefits of parent media size, *i.e.* microfibrillated cellulose (**MC**) *versus* nanocellulose (**NC**) support, for the preparation of magnetite (**MG**) based high performance adsorbent for arsenic removal was conducted. Precipitation of **MG** on amino terminal branched organic structure, **L'**, linked either by maleic acid residue on **NC** surface (**NC-MA/L'**) or linked by oxalyl bridge on **MC** surface (**MC-O/L'**) produced **NC-MA/L'-MG** and **MC-O/L'-MG** adsorbents, respectively. Precipitation of nanosized **MG** on amino functionalized **NC-MA/L'** and **MC-O/L'**, performed according to optimized procedure, contributed to improved textural properties and adsorptive/kinetic performances of novel adsorbents. Synthesized adsorbents was characterized by using scanning electron microscopy (SEM), transmission electron microscopy (TEM), energy dispersive spectroscopy (EDS), X-ray diffraction analysis (XRD), infrared spectroscopy with Fourier transform (FTIR), Raman spectroscopy, and determination of the specific surface gas adsorption method (BET/BJH).

Analysis of adsorbent performances comprised material characterization, equilibrium and kinetic study, influences of interfering ions and modeling of adsorption data in ion free and

competitive conditions. Kinetic study, *i.e.* fitting by using different kinetic models, Weber-Morris model and single resistance mass transfer model was useful information on adsorption mechanism and rate-controlling step. Adsorption and kinetic experiments, performed at different temperature, was used for determination of thermodynamic and activation parameters. Activation parameters, determined by using model free kinetics confirmed beneficial uses of **MC-O/L'-MG** *versus* **NC-MA/L'-MG**, due to low activation energy dependence on the extent of adsorption.

Competitive kinetic study in the presence of interfering ions shows low detrimental effect on both capacity and kinetic of arsenic removal. Visual MINTEQ modeling software was used for the prediction of adsorbent performances and interfering ion influences. It was also valuable to obtain useful information on the adsorbent and discussion on possibilities of simulation and prediction of potential impacts of significant parameters on adsorption.

Preliminary fixed-bed column study was accomplished by the use of Bohart-Adams, Yoon-Nelson, Thomas and Modified dose-response model with **ER/DETA/FO/FD**. Also, arsenic removal capabilities of the hybrid goethite impregnated media were evaluated by conducting batch sorption tests, developing isotherms and simulating the breakthrough curve with a pore surface diffusion model (PSDM), after being verified by a short bed column (SBC) test.

Due to complexicity of the methodology presented experimental work of this thesis were carried out in the laboratories of the Department of Organic Chemistry and the Department of Environmental Engineering, Faculty of Technology and Metallurgy, University of Belgrade, Institute for Nuclear Sciences Vinča and Agriculture faculty, University of Belgrade.

Scientific research goals. The aim of this PhD thesis was related to syntheses of efficient adsorbents for arsenic removal. According to described processes four new adsorbents were synthesized by precipitation of iron(III) oxides in goethite and magnetite forms on amino-functionalized macroporous resin and amino terminal organic structure bonded to surface of nanocellulose/microcellulose. In order to increase number of amino terminal groups

Amino terminal groups at functionalized **ER/DETA, NC-PEG**, **NC-L**, **NC-MA/L'** and **MC-O/L'** are good support for further modification with iron(III) oxides in the form of goethite and magnetite by performing optimized procedures produced high performance adsorbent for arsenic removal. Optimization procedure was design by using RSM methodology, performed to ensure uniform precipitation and achievement of the optimal quantity of the iron(III) oxides on

amino functionalized support, by varying the concentration, temperature, time and pH value of the solution. Detailed characterization was performed in order to establish relationship between synthesis process parameters and material/adsorptive properties in the course of optimization procedure with the aim of obtaining of improved adsorption properties to meet/satisfy new, more stringent water quality criteria. Special care was devoted to successfulness of amino functionalization, *i.e*. number of terminal amino groups, introduced by change of the structure/functionality of organic linker bonded to support. The influence of the homogeneity of distribution and amount of deposited iron(III) oxide on the **ER/DETA, NC-PEG**, **NC-L**, **NC-MA/L'** and **MC-O/L'** *versus* adsorption of As(V) and As(III) ions was established. Except of this, synthesis of macroporous copolymer enable controllable production of spherical nanoparticle support media with different geometries, porosity while maintaining high mechanical strength and uniformity of the obtained hybrid media.

Actuality of the problem in the world. The presence of arsenic in drinking water and its harmful effects to the health of humans and animals is a real problem faced by many countries in the world, and also some area in the Republic Serbia have been affected by arsenic contamination. Conventional materials and methods, and currently technology in use can not satisfy stringent requirements and established criteria for water quality. Due to this, a large numbers of study related to application of iron(III) oxides modified macroporous cross-linked resins and cellulose based materials in a processes of protection and preservation of the environment are promising course which needs further improvement. Significance of this topics and related materials developed is evidenced by the large number of scientific papers published in recent years. In this context, research in this doctoral thesis contribute to a better understanding of the processes of adsorption by using modified macroporous resin and cellulose based materials for separation of arsenic from water.

2. THEORETICAL PART

2.1. As environmental and health problem

The toxicity of arsenic has been known for decades, but in recent times has been proven and its carcinogenicity. Repeated studies linking increased concentrations of arsenic in drinking water and cancer of the skin, lung and other cancers. For these reasons in the US, as well as in the world, is increasingly focusing on methods of removing or reducing the concentration of arsenic in water, resulting in the improvement of existing and introduction of new technologies in water treatment.

Arsenic (As) is a chemical element in the atmosphere, soil, rocks, natural waters and organisms. Most environmental problems, as well as the mere appearance of arsenic in water, is the result of natural processes such as melting, biological and volcanic activity. Aresnic influence on human occurs as a results of activities in mining industry, emissions caused by burning fossil fuels, and the use of products of arsenic in the form of pesticides and herbicides whose application was widespread in recent decades. Arsenic based products are still frequently used in the timber industry to protect wooden objects.

In many regions of the world, including the northern part of Serbia [1,2], arsenic occurs as a natural component of underground water in high concentrations. As groundwater is one of the most important resources for the preparation of drinking water, it is important to ensure that the concentration of arsenic is reduced to the permissible level and thus it is minimized the negative impact on human health [3].

The concentrations of arsenic found in groundwater in some areas greatly exceed the maximum permissible concentration. The highest levels of arsenic in water have been reported in Southeast Asia (India, China, Bangladesh, Philippines, Taiwan) with 400 to 3400 g L^{-1}, then in Southeast America (Chile, Mexico, Argentina) 140-300 g L^{-1} and in some parts of the United States and Japan. More than 50 million people in the territory of Bangladesh was poisoned by consuming water with arsenic mass concentration of 1 g L^{-1}. High concentrations of arsenic in water have been reported in the areas with high thermal activity. Thus, the hight concentration of 8.5 g L^{-1} was recorded in thermal water of New Zealand [4].

The origin of arsenic in water may be natural or anthropogenic and occurs mainly due to leaching arsenic compounds from soils. In natural waters As exist in various forms, which greatly affects the methods of analysis, separation methods, as well as the toxicity of these compounds. Arsenic compounds in the trivalent form are 25-60 times more toxic than pentavalent arsenic compounds. The As(III) compounds are typically present in the water in the form of weak acid arsenical H_3AsO_3 (pKa = 9.22), while As(V) is a much stronger H_3AsO_4 arsenic acid (pKa = 2.20), and it exists in its deprotonated anionic form $H_2AsO_4^-$ and $HAsO_4^{2-}$.

In the first half of the 20th century it was found that arsenic-contaminated water has negative effects on the health of people. The scientists found that adverse effects can be caused by very small doses of arsenic, when introduced into the body, food or water, for a long time.

2.1.1 Arsenic and its compounds

Arsenic is 1250, discovered by Albertus Magnus (Germany). The name comes from the Greek word arsenikon gold auripigment (As_2S_3). The root of the word can also be found in the Arabic name for auripigment - *az-zernikh*. Arsenic occurs in two allotropes, yellow and unstable to stable silver-gray alotropskoj modification. The gray arsenic is in the nature, is brittle and metallic luster. Elementary gray arsenic can be obtained by thermal decomposition arsenopyrite absence of air being sublimated by the equation (2.1):

4FeAsS(s) → 4FeS(s) + 4 As (g)   (2.1)

It is resistant to water, acids and alkalis. Arsenic is toxic and carcinogenic and is especially dangerous because of the cumulative effect. The compounds have a highly toxic if ingested. In nature comes mostly in the form of sulphides, arsenopyrite (FeAsS) auripigment (As_2S_3) and arsenopyrite oxide (As_4O_6). It is also used for controlling insects, mice and rats.

Sublimes at atmospheric pressure at a temperature of 613 °C (not melted) and at a pressure of 36.4 kPa as the pressure of its own vapor, melted at 817 °C. Arsenic vapor to 800 °C corresponds to Formula As_4, above 1700 °C. As_2 the formula. With moist air reacts even at room temperature, and the heated air creating a flame burning bluish sooth As_2O_3 of garlic odor.

At room temperature directly connects with fluorine and chlorine being heated, with bromine, iodine and sulfur. Not combines with nitrogen, boron, silicon and carbon. Strong

oxidizing acids, such as concentrated nitric oxidize it into arsenic acid while diluted nitric acid oxidized to arsenic acid.

Yellow arsenic (beta-arsenic) is hexagonal structure formed by rapid quenching arsenic vapor. Itis soft, waxy and do not conduct electric current. It is unstable at room temperature and the action of light, quickly and easily converted into gray arsenic.

Amorphous black arsenic obtained by sublimation of arsenic in the absence of air. Decomposition of AsH_3 by heating As in the form of steam create a mirror coating (so-called. "arsenical mirror"). This reaction is used for the detection of small amounts of arsenic in the case of suspected poisoning (Marsh test). Heating to 360 °C passes into stable lives with the development of heat. Elemental arsenic has no special applications. In small amounts is used as a dietary copper and lead and some alloys that they increase the resistance, hardness or shine (eg. it is added to lead that is used for the production of pellets to a concentration of 0.3%). It is also used in semiconductor technology as doping agent in admixture of crystals containing germanium and silicon. Gallium arsenide is used in lasers as the laser medium. More important is the use of compounds of arsenic that is used in the leather, in the glass and the pharmaceutical industry, mostly in agriculture to protect plants from pests.

The toxicity of arsenic depends on the form in which arsenic appear. Extremely toxic arsenic(V) which is soluble in water and arsenic(III) which is difficult to isolate, or easily accomplished using MnO_2. When arsenic poisoning the human body goes through several stages; The first phase is manifested in increased concentration of arsenic in blood, urine, hair and nails, and the second phase of the appearance of skin lesions. In the body, the arsenic can enter by inhalation (phenomena observed in the mines in France, USA, Sweden) and absorption through the skin and further by spreading to other internal organs (liver, kidneys, lungs, *etc*.). The complete mechanism of action of arsenic in the body is not yet known. Chronic arsenic poisoning can be a result of accumulation of arsenic compounds in the body, as a result of the consumption of water with in creased concentration of arsenic, although poisoning was observed at lower concentrations (2 g L^{-1})[5].

The most common changes in the body caused by the intake of arsenic in the body are:

➢ Inactivation of the enzyme; arsenite is prone to -SH groups of proteins, which leads to the inactivation of the enzyme,

➢ Chromosomal changes; if arsenic occurs during DNA replication, interferes with DNA repair enzymes, binding to SH group,

➢ Protein binding, as demonstrated by affinity column Protein isolation with p-aminofenilarsin-oxide,

➢ Damage to liver function, which is observed by measuring liver function tests, and alanine transaminase (ALT) and aspatrat transaminase (AST), glutamate transaminase (GGT) and alkaline phosphatase activity, which is related to the increase of total arsenic in urine,

➢ Occurrence of arsenic in blood, hair and urine at a concentration of arsenic in drinking water is higher than 100 g L^{-1}.

➢ Diabetes mellitus, metabolic disease with characteristic persistent hyperglycemia and a number of other disorders (problems with the eyes, kidneys, nerves and blood vessels)

➢ Cardiac ischemia at a concentration of arsenic in drinking water is higher than 100 g L^{-1},

➢ Hypertension, with systolic pressure higher than 140 mmHg and diastolic higher than 90 mmHg,

➢ Peripheral vascular disease ("black foot disease") that result in gangrene of the affected limb,

➢ Melanosis by reducing the concentration of arsenic in water may disappear,

➢ Disease "fever black leather" characterized keratoses and nodules on the palms and soles,

➢ Carcinoma, lung and internal organs (bladder, kidney, liver). Entering arsenic food and water can result in bladder cancer. Carcinogenicity of arsenic are frequently examined as well as the incidence of mortality from cancer as a result of consumption of water with arsenic. Water use of 2 L/day with arsenic concentrations of 0.5 g L^{-1} is the risk of cancer in a ratio of 1: 10000, and with increase the concentration to 5 g L^{-1} it rise to 1: 1000, or the concentration of 50 g L^{-1} it become more probable at 1: 100 [5].

United States Public Health Service - U.S. PHS in 1942 limited the maximum permissible concentration (MPC) of arsenic in drinking water at 50 μg L^{-1}. A similar standard is adopted by the World Health Organization in 1963. However, epidemiological studies have

shown that even at such low concentrations significantly increased risk to human health, so that the World Helth Organization - WHO in 2001 recommended that the maximum allowable concentration of arsenic in drinking water decreases form 50 to 10 μg L^{-1}, because it has been found that arsenic damaging to human health [3,6–8], even at the lower level of exposure. Strict adopted criteria related to the quality of drinking water has been implemented in the legislation of many countries, including the Republic of Serbia, created the need for the development of new technologies, in order to fulfill the requirements [7,9].

2.1.2 Geochemistry of arsenic

Important compounds

Arsenic(III) oxide (As_2O_3, arsenic) known as rat poison, is a white odorless powder, sweet taste, slightly soluble in water, is very toxic and is applied to means for the rodent control, weed killers, for treatment of leather and wood, and animal preparation. In medicine it is used as a chemotherapeutic agent. Obtained by roasting arsenic ores or arsenonosnog materials and condensation sublimated vapor. Lethal dose for humans is from 0.1 to 0.15 grams.

Arsenic trihydride (AsH_3, arsine) is extremely poisonous gas and one of the strongest inorganic poisons. No practical (useful) applications, but is important in the industrial toxicology because the processing of alloy (containing arsenic) acids may arise arsenovodik and cause poisoning organisms. By replacing hydrogen atoms in the alkyl group yardstick occurring organic derivatives of arsine, which are toxic and some of them may serve as a chemical warfare. Maximum concentration arsenic trihydride in the air should not exceed 50 ppm.

Arsenic(V) sulfide (As_4S_4, realgar, sandarac, arsenic ruby, red arsenic glass) in the nature of such mineral realgar in the form of red crystals in which four arsenic atoms occupy tetrahedral position or as a red glassy mass. It is used for hair removal in the leather industry and in pyrotechnics to obtain white Bengal fire.

Arsenic disulfide (As_2S_2) is used to pull the hair in the leather industry and as the white fire in fireworks prodution. Arsenic(III) sulfide (As_2S_3, yellow arsenic glass) appear in nature as a mineral pigment in the form of golden leaves. It is a yellow amorphous mass of pearly shine.

Melts at 300 °C gives CI a red melt that cooling hardens as the red mass. It is used for removing hair in the leather industry, as an insecticide, the blue fire in pyrotechnics and as a yellow color.

Arsenic(III) chloride ($AsCl_3$) is a colorless, oily, highly toxic liquid which fumes in the air due to the dissolution of the HCl and As_2O_3. It is used as: halogenating in organic synthesis and for the production of poison gas, for example Lewisite.

Arsenic acid (H_3AsO_4) is obtained by heating arsenic with nitric acid, in the manufacture of paints and to make organic arsenic preparations. Its salts, arsenates, serve as preservate for wood and capture of pests.

2.1.3 Arsenic in soil and natural water: chemical and microbiological processes

Transformation of arsenic between different valence states and chemical species in the soil and natural waters depends on abiotic and biotic processes. Of course, like all biogeochemical processes, better understanding of the factors that are responsible for the transformation As required deserved recognition of chemical and microbiological achievements, but in most cases contributions of all factors are very mutually dependent. Chemists and microbiologists often work within paradigms that it is simple to understand and predict electron transfer reactions in natural systems.

For example, geochemists have mostly relied on the fact that the thermodynamic stability of the oxidized and reduced species is determined by the activity of the electron $pE = \log(e^-)$ and that it is an important indicator of the concentration of oxidized and reduced species. Although this led to the erroneous conclusion, conceptual electron interaction is often referred to as a "master" variable, with pH values in the definition of the ratio of oxidized or reduced species. But it is known that one measures the redox potential of a systematic (pE) useful for defining the ratio of the oxidized and reduced species of the redox couples all simultaneously exist.

Several studies have shown non-equilibrium behavior of As(V)/As(III) relative to the other indicators redox status (e.g., O_2 melted, the measure electrode Pt), wherein As(III) is most frequently observed in the region of the oxidised, while As (V) does not exist in the middle of the oxidised. In such cases, slow kinetics and/or other biological phenomena are usually call them to explain the shortcomings of thermodynamic equilibrium. Better precision type and fate

As in natural waters will require more information about the proportions of individual reactions, which contribute either directly or indirectly to oxidation and reduction of arsenic, regardless of which reactions can be biological or abiotic. In reality, processes such as surface complexation, dissolution of minerals, dissimilatory reduction or detoxification are connected in real systems which define As tansformation pathways. As for the biological pathways of oxidation and reduction, microbiologists can often rely on the cultivation and simple characterization of pure isolated culture as the primary tool for understanding microbial reactions transfer electrons in natural systems. Such a simple approach effectively ignores the physical-chemical context that defines the actual microbial habitat in the soil and water, and ignored the issues related to how the cultured organisms associated with the measured oxidation-reduction processes that were observed in the environments of studies.

It is believed that progress towards better understanding and prediction of redox transformations important for the cycling of As, and it will be understood with great emphasis on complex approaches that will define the ratios of specific abiotic and biotic pathways to appropriate and realistic environmental conditions, to explore patterns in microbial ecology connecting the microbial communities with their chemical-physical environments, and to shed light on the functional pathways of microbial redox transformations. Thus we are limited in part ratios events oxidation-reduction process and the heterogeneity and complexity of microenvironment that are typical for systems soil and natural waters. No matter, wherever possible, future studies will focus on clarifying the mechanisms As the transformation should apply a set of measuring tools that provide accurate insight into the chemical and microbiological processes that are essential for the natural environment. This chapter discusses the chemical and microbiological processes that mediate transformations between As(III) and As(V).

2.1.4 Chemistry of arsenic(III) and arsenic(V) in soil and natural water

Chemical equilibrium

Diagrams pE-pHdependent are commonly used to predict the stability of oxidized and reduced species. Of arsenic, such diagrams are published using different assumptions, and that the general conclusion of As(V) provides that the thermodynamically stable at a valence of Eh

values that are larger than about 100 mV at pH 8 and 300 mV higher than the pH of the fourth below these redox potentials, As(III) has a thermodynamically stable valence, present in the form H_3AsO_3 types As-S compound (eg. $H_2As_3S_6$ compound) or As(III) such as solid phase. As_2S_3. They are not shown for the stability of a region of reduced forms of As (e.g., As(0) or A(III)) due to limited knowledge of their occurrence in natural water and soil, and the uncertainty associated with the appropriate thermodynamic data.

The values of pE, wherein the activity of As(III) and As(V) may be the same type, defined using equilibrium expressions given in Table 2.1 (the value of E_h may be used as an alternative furnace, wherein at 25 °C, E_h (mV) = 59 pE (1)). Eg. pE-pH links that define the main equivalence of As(III) and As(V) species are the following:

$H_3AsO_3{}^0$ - $H_2AsO_4{}^-$: pE = 10.9 - 1.5 pH

$H_3AsO_3{}^0$- $HAsO_4{}^{2-}$: pE = 14.3 – 2 pH
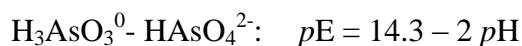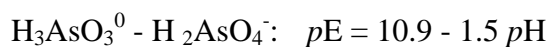
where $H_2AsO_4{}^-$ the main form of As(V) between pH 2.5 and 7, $HAsO_4{}^{2-}$ has a predominant form of As(V) between pH 7 and 12, and $H_3AsO_3{}^0$ is the main form of As(III) below pH 9.3. From the thermodynamic stability of the connection, the standard electrode potential conditions (pE_0) of the pH 7 to As(V) and As(III) redox couple can be displayed about a $NO_3{}^-$ / N_2 (g) and $Fe(OH)_3$ S / Fe^{2+} redox pairs.

Of course, these calculations rely on assumptions concerning the activities of oxidized and reduced species, and it is well to recall that the relative position of these redox couples depends on what assumptions are used to define the activity of oxidized and reduced species, and the concentration of compounds. Stumm and Morgan excellent in the above example using Fe(III) / Fe(II) redox couple wherein, depending on kompleksnosnti links that are present in the types of solid phases that control the activity of Fe type, pe calculated for Fe(III) / Fe(II) redox couple can be between 1 000 mV to less than 400 mV.

Regardless, the electrode potential of As(V) / As(III) of a pair is set up in such a way that the oxidation-reduction reactions involving the As(III) or As(V) species can be mediated by various abiotic species and potential oxidants which reduktanata bit in the soil and natural waters, or biotic through biochemical pathways of prokaryotic and eukaryotic organisms.

Specifically, the electrode potential of As(V) / As(III) vapor intrusion within a dynamic ratio of redox potential values that are commonly observed in the sediments, aquifers, lakes, rivers, oceans and soils with fluctuating water content and / or river beds. It is expected during the circulation of As(V) / As(III) to be equal to the Earth-aqueous systems such as the circulation of Fe(III) / Fe(II), N(V) / N(0) / N(III), Mn(IV) / Mn(II) or S(VI) / S(IV) / S(0) / S(II).
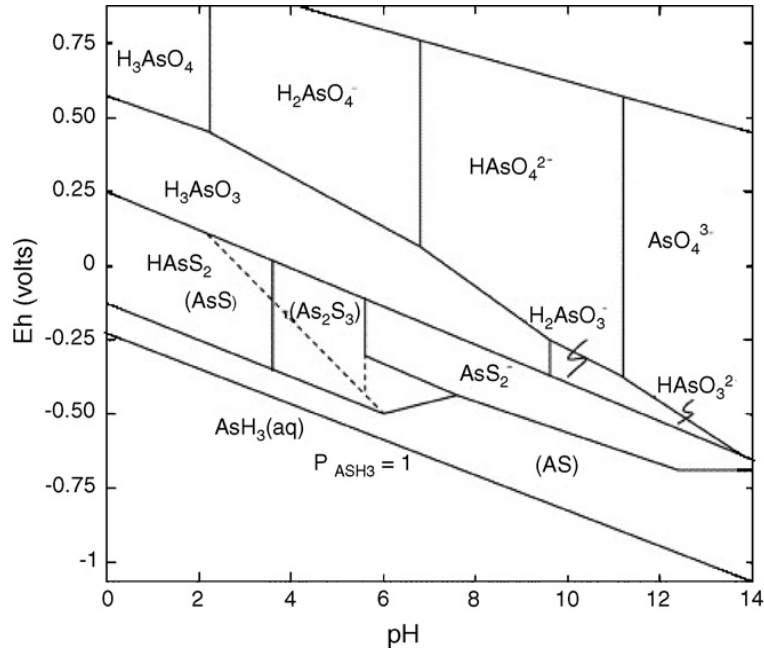
Figure 2. 1. E_h - pH diagram for arsenic at 25 °C and 101.3 kPa [7].

Table 2. 1. The most important chemical and thermodynamic equilibrium constants relevant to the classification and circulation of As (V) and As (III) in soil and natural waters [10]

Description	Reaction	Log K
As(V)/As(III) couple	$H_3AsO_3°+H_2O\rightarrow HAsO_4^{2-}+4H^++2e^-$	-28.63
As(III) dissociation	$H_3AsO_3°\rightarrow H_2AsO_3^-+H^+$	-9.29
As(V) dissociation	$H_3AsO_4°\rightarrow H_2AsO_4^-+H^+$ $H_2AsO_4^-\rightarrow HAsO_4^{2-}+H^+$ $HAsO_4^{2-}\rightarrow AsO_4^{3-}+H^+$	-2.24 -6.94 -12.19
As(III)-S solubility – amorphous As₂S₃	$0.5As_2S_3(s)+3H_2O\rightarrow H_3AsO_3°+1.5H_2S\ (aq)$ $0.5As_2S_3(s)+H_2O+0.5\ H_2S\rightarrow AsO(SH)_2^-+H^+$ $1.5As_2S_3(s)+1.5\ H_2S\rightarrow H_2As_3S_6^-+H^+$	-11.9 -7.9 -5.5
orpiment	$0.5As_2S_3(s)+3H_2O\rightarrow H_3AsO_3°+1.5H_2S\ (aq)$	-12.6
As(III)-S complexation	$H_3AsO_3°+2H_2S(aq)\rightarrow0.33\ H_2As_3S_6^-+0.33H^++3H_2O$ $H_3AsO_3°+2H_2S(aq)\rightarrow AsO(SH)_2^-+H^++2H_2O$	10.3 ~4

Of the several forms of arsenic, As(III) and As(V), undergo acid–base equilibria, thus different major and minor species will be present depending on the pH.
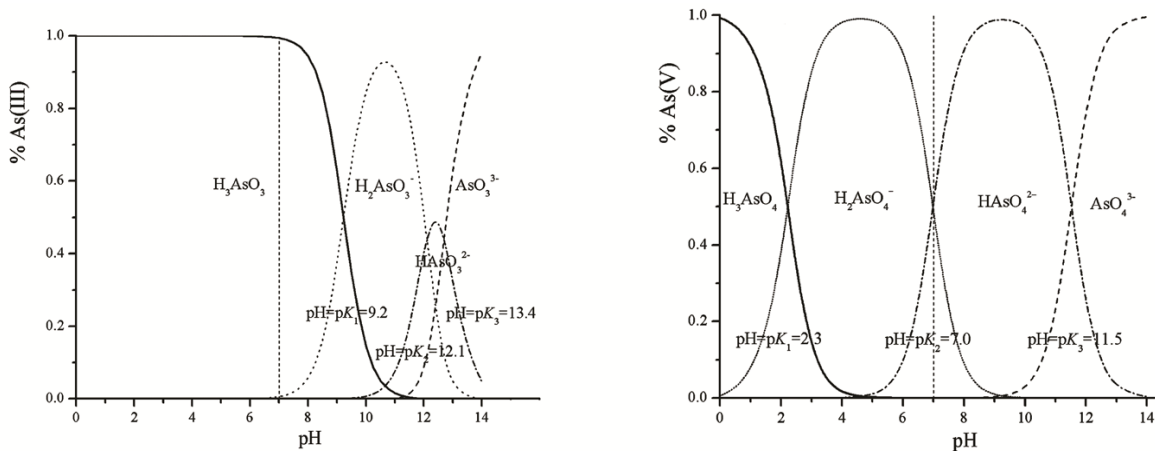
Figure 2. 2. pH dependent speciation of As(III) and As(V)

Figure 2.2 shows that at neutral pH, As(OH)₃ is the dominant species while $As(OH)_2O^-$ represents a small fraction (1.0%) and the contribution of $As(OH)O_2^-$ and AsO_3^- is insignificant.

Solid phase surface complexation and reaction

The solid phase As(V) or As(III) that may be important in the natural system, including Fe, Mn, Ca and arsenate and arsenic(III) sulfide as auripigmenta (As_2S_3), and may be amorphous As_2S_3 realgar (AsS). Arsenopyrite (FeAsS) is an important primary source of minerals As. Arsenatske salts of Fe, Ca, Mn, Mg and Al generally control activity As (V) in soils and natural waters, although skorodit ($FeAsO_4$ x $2H_2O$) can be formed during the early stages of oxidation of arsenic rich or FeAsS pyrite. Often the activity of arsenate controlled surface complexation reactions and the oxyhydroxides of Al, Mn and Fe.

Arsenate shows a strong attraction to most metal oxides and hydroxides and clay minerals, which are common in soil and water, which form surface complexes analogue phosphates. Arsenite is selective, and shows an affinity for iron oxides and hydroxides. Both types of oxyanions have increased sorption with decreasing pH or sorption maximum centered around the pKa. Although the arsenite usually set to a low sorption capacity of the soil particles and water that are associated with arsenate, arsenite actually has a higher sorption capacity to ferrihydrite and goethite of arsenate except in very low concentrations of the solution. For iron oxides, the sorption capacity compared arsenite or arsenate exceeds that, with the said first shows little pH dependence of the adsorption centered at pH 8 while the other of said continuously increases with decreasing pH. While inverse trend was recorded for the sorption of amorphous $Al(OH)_3$. Sorption arsenite is highly dependent on pH, the time to move around pH 9, and disappears completely when phase dissolution of arsenic even at low coverage areas. Conversely, arsenate sorption on $Al(OH)_3$ has a limited pH dependence, and completely removed from the mixture at a pH of 4-10. Despite their different trends in sorption at a given pH, arsenate and arsenite form similar complexes on the surface of goethite[11].

In short, the sorption of arsenate and arsenite on solid Fe(III) oxide is one of the most important things for arsenic in water and soil. It has been shown to Fe(III) phase-oxide can act to release high concentrations of arsenic from the hot water and mineral water accumulating substantial amounts of As. Analysis of fate and transport As the individual soil, aquifers, lakes or river beds must take into account the reaction of As(III) and As(V) species with Fe(III) oxide phases. Eg., the pH dependence of sorption of arsenate with Fe(III) oxide has important

implications for the management of toxic Mine materials that remain after mining. Although it is widely known and accepted that calcification (and a significant increase in the pH of the soil), preferably to increase the re-vegetation and to minimize the mobility of metals such as Cu, Zn, Cd and Pb, can have exactly the opposite effect on the mobility of arsenic where an increase in the pH of the soil of 8 can increased mobilization of arsenate out of the soil profile. Furthermore, the reductive dissolution of Fe(III) oxide containing sorbed arsenic can be an important source of arsenic in natural waters.

Taking into account the tendency of arsenate and arsenite to sorption on Fe(III) oxides, it is important to recognize that the microorganisms that are able to use the As(V) and As(III) for metabolic purposes often operate under convince where Fe(III) oxide phases control the activity of arsenic and its availability.
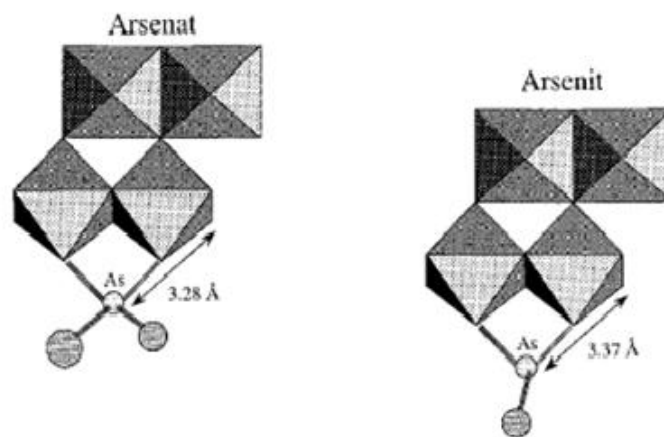
Figure 2. 3. The dominant surface structure arsenate and arsenite on goethite, indicating Fe(III) - As a connection established by using EXAF technique [11].

The reduction of As(V) to As(III) in soils and natural water - As Dissolution times of Fe(III) - oxide phase

The reduction of As(V) to As(III) is most commonly observed in aerobic or anoxic conditions such as those found in sediments, flooded soils and tank ships. Under these conditions, Pt electrodes Octave redox potentials ranging usually from 100 to 200 mV. Since

arsenite is more mobile and more toxic to microorganisms and plants of arsenate, As(III) in such systems may become a significant environmental concern.

One mechanism which can explain the increase in total dissolved arsenic and arsenic mobilization in reducing conditions and the increasing concentration of the reducing mobility of dissolved Fe(III) oxide which allow the release of As(V) to the aqueous phase, with a strong reduction of As (V) either by abiotic or biotic pathways. Alternatively, As(V) can be reduced to As(III) to the surface and then released by reductive dissolution Fe(III) oxide. Established increased rate of dissolution of minerals Fe(III) by microorganisms using Fe(III) as an electron acceptor (for respiration to lactate or acetate).

In the case of Fe(III) oxide, reductive dissolution ratios may depend on the crystal structure and the surface of the solid. The ratios are much higher for areas with high surface area and amorphous ferrihydrite are compared with the well-crystallized goethite.Certainly stirred microbiological culture can cause reductive dissolution of an amorphous phase resulting ferihidritne increased solubility sorbed As(V) (the extent of 38 μM As h^{-1}). It has shown that Fe(III) *Shewanella* algareduction (Bry strain) can be omitted As(V) in which measures are approaching 35 μM h^{-1} during the reductive dissolution skorodita (FeAsO$_4$ x 2 H$_2$O) in the presence of 10 mM of lactate as a carbon source. Although this specific microorganism is not capable of reducing As(V) to As(III), by a reduction of Fe(III) phase, reduction of As(V) to As(III) can occur very quickly in the soil and using other microorganisms.

Has recently been shown that anaerobic organism (*Sulfurospirillum Barnesia*) which is capable of dissolving the reducing Fe(III) oxide and the reduction of As(V) to As(III). These mechanisms may be important for the release of As(III) from anaerobic sediments containing As sorbed to Fe(III) oxides. For example. As the solubility of water-bearing sediments in groundwater in Bangladesh was thought to be caused by reductive melting of Fe(III) -oxide phase containing sorbed arsenic. The highest concentrations in groundwater As found in the aquifer depths corresponding to zones with high organic material where the high activity of the microbe causing reductive dissolution rate of Fe(III) -oxide phase.

Microbial reduction of As (V)

Microbial reduction of arsenate to arsenite can occur using two main mechanisms: disimilatornom reduction where the As(V) is used as a final electron acceptor during anaerobic respiration and detoxification activities involving the reduction of arsenate. It is worth noting that the detoxification reduction of As(V) occur under anaerobic or aerobic conditions in soils or natural waters. The concentration of As(V) in many arsenic contaminated soils in general is not high enough to be supported by significant growth of aerobic organisms that use arsenic as the dominant electron acceptor. Secondly, disimilatorna reduction of As(V) may require strictly anaerobic conditions where organic acids such as lactate electron donor.

Abiotic pathways responsible for the reduction of As (V) to As (III)

In this work will be shown the potential role of chemical reducing agents that (an electron donor) to As(V) ie. The processes that are most often observed in soils and natural waters. One of the chemical species that may contribute to the reduction of As(V) is dissolved sulfide (H_2S, HS^-), especially at low pH. Reduction of arsenate by the dissolved sulfide is very slow at neutral pH values. At pH values of less than 5, the reduction of arsenate wanting sulphide can be significant in natural systems, a short half-life (21 hours for all of abiotic processes) [12]. He also demonstrated the potential importance of intermediaries As-O-S species in electron transfer reactions between sulphides and arsenate, like $H_2As^VO_3S$, $H_2As^{III}O_2S^-$ and $H_2As^{III}OS_2^-$. It is not known whether these chemical species may serve as an important redox active species of microbial metabolism. These authors also compared the rate of As(V) reduction in the presence of sulfide versus those rates that are expected at disimilatorne reduction by organisms that breathe arsenate (strain SES-3) and for those that are measured in lake sediments. When the pH value of less than 5, reducing the rate for dissolved sulfide may become more important than reducing the rate occurring anaerobic respiration where the As (V) is used as the final electron acceptor.

2.1.5 Oxidation pathways arsenic (III) to arsenic (V) in soils and natural waters

Chemical processes

There are many potential oxidants that can contribute to the oxidation of As(III) in soils and natural waters such and are here briefly discussed together with the paths whose brokers microorganisms. Arsenitnih salt solutions are generally stable under ambient conditions and does not show as rapid oxidation of As(V). Specifically, the apparent half-life that appears to As(III) oxidation with oxygen is approximately one year. Recent publications have shown that the homogeneous oxidation of As(III) may exist, but only at pH values greater than 9. It is necessary to say that, although thermodynamically suitable, but that is not an important mechanism of the oxidation of As(III) in most soil and water. Fe(III) in the water can contribute to the oxidation of As(III) at low pH (pH <3) and high concentrations of Fe(III), or does not play a significant role in most natural waters.

Although oxidation of sorbed As(III) to As(V) to Fe(III) N-oxide surfaces can occur in a limited amount (~ 20%), recent studies do not suggest significant oxidation of As(III) by Fe(III) - oxide surface. $Mn^{IV}O_1$ birnesita like solid phase are efficient oxidizers of As(III). Under controlled laboratory conditions at high levels of MnO_2, half-oxidation of As(III) is less than one hour. Judging from such a rapid oxidation states (III), suggesting that oxidation of As(III) in marine sediments was controlled by presence of MnO_2 phase. At minimal levels, seems to be that the surface of Mn(IV) oxide represent an important way of oxidation of As(III) in natural systems. Recent studies have also evaluated the oxidation of As(III) in the presence of H_2O_2 and irradiated solutions of Fe(III) - oxalate. Under appropriate conditions, H_2O_2 may be suitable oxidant for As(III). It was shown that at a pH of 10 (where H_2AsO_3 dominant species dissolved As(III)) and the high ratio of H_2O_2:As(III), the half-life of oxidation of As(III) is short, only 00:02 hours . Oxidation time is pH dependent and rates decrease significantly with decreasing pH. At a pH below 8, and the actual concentration of H_2O_2, this time will not significantly contribute to the oxidation of As (III) observed in most natural systems.

In natural waters exposed to ultraviolet light oxidation of As(III) reactions that generate free radicals such as ferioksalatnih system can be significant factor. For example, at pH values ranging from 3-7, the oxidation speed of 18 uM (III) can be achieved in the presence of

irradiated 18 μM Fe(III) and 1 mM oxalate solution, with an apparent half-life of ~ 1 hour. The oxidation of As(III) is shown in correlation with the production of OH- species produced during the decomposition of H_2O_2 in the presence of Fe(II). This cause, though production requires the generation of OH- H_2O_2, H_2O_2 is not a significant oxidizer of As(III) in these conditions. This specific As(III) oxidation time can play only a limited role in the soils and sediments in order to its logical limit UV light that penetrates them. This can be a very important process in surface waters where it is not a rarity complexation of dissolved Fe(III) with UV-absorbing organic chromophores. This specific oxidation time is a reminder of the role of free radical species in the transmission of the oxidation-reduction reactions that may be hidden in many different environments.

2.1.6 Arsenic in drinking water

Millions of people today consume drinking water in which the arsenic found in elevated concentrations. By using this kind of drinking water comes to the entry of arsenic in the body that is manifested by increasing the arsenic concentration in the blood, hair, nails, inactivation of various enzymes of this phenomenon keratosis and lung cancer. In addition to the toxicity of arsenic in his thesis describes the most common methods of determining arsenic: spectrometric with silver dietiltiokarbonatom and hydride technique of atomic absorption spectrometer.

To remove arsenic from drinking water is applied several methods: coagulation arsenic with iron and aluminum salts, membrane processes (nanofiltration and reverse osmosis), adsorption on activated carbon, ion exchange, and others. The paper presents the possibility of removing arsenic using a household system water treatment.

2.1.7 Conventional techniques for removal of As from water

The chemistry and composition of arsenic-contaminated water are the major factors determining the removal of arsenic [13]. Most of the available removal technologies are more efficient for arsenate given that arsenite is predominantly non-charged at pH below 9.2 [14]. This

makes the trivalent form of arsenic less available for precipitation, adsorption, or ion exchange. Accordingly, treatment technologies are believed to be more effective by using a two-step approach consisting of an initial oxidation from arsenite to arsenate followed by a technique for the removal of arsenate [15]. The presently available technologies that can be used for the removal of arsenic from water are summarized as follow[16]:

➢ Oxidation (Oxidation and filtration, photochemical oxidation, photocatalithic oxidation, biological oxidation, *In situ* oxidation)

➢ Membrane technologies (Microfiltration, Ultrafiltration, Nanofiltration, Reverse osmosic)

➢ Coaugulation/Flocculation

➢ Ion exchange

➢ Adsorption (Activated alumina, Iron based sorbents, Zero valent iron, *etc.*)

2.1.8 Arsenic removal by oxidation techniques

Oxidation involves the conversion of soluble arsenite to arsenate. This alone does not remove arsenic from the solution, thus, a removal technique, such as adsorption, coagulation, or ion exchange, must follow [14]. For anoxic groundwater, oxidation is an important step since arsenite is the prevalent form of arsenic at near neutral pH [13]. Aside from atmospheric oxygen, many chemicals, as well as bacteria, have already been used to directly oxidize arsenite in water and these are enumerated in Table 2.2.

Table 2. 2. Different oxidants used to oxidize arsenite to arsenate, their operating conditions, properties, and efficiencies [16]

Coagulant	pH	Initial As concentration	Type of water	Remarks
Ferric chloride	7.0	2 mg L^{-1}	Distilled water	At an optimum FeCl$_3$ dosage of 30 mg L^{-1}, As(III) and As(V) removal efficiencies were approximately 45% and 75%, respectively. Arsenic removal was enhanced at higher FeCl$_3$ concentrations, however, residual iron after coagulation exceeded MCL of iron in drinking water.
Aluminium sulphate octadeca hydrate	7.0	20 μg L^{-1}	River water	About 90% of initial As(V) concentration was removed from the solution using 40 mg L^{-1} Al$_2$(SO$_4$)$_3$ x 18 H$_2$O. As(III) removal with alum was negligible even at higher alum doses.
Zirconium(IV) chloride	7.5	50 μg L^{-1}	Distilled water	The percentage removal of As(V) with 2 mg L^{-1} ZrCl$_4$ dosage was approximately 55%. This value increased at pH 6.5 and decreased at pH 8.5. In contrast to that of As(V), the removal efficiency of As(III) was approximately 8% regardless of pH.
Titanium(III) chloride	7.5	50 μg L^{-1}	Distilled water	With 2 mg L^{-1} TiCl$_3$, As(III) and As(V) removal efficiencies of 32% and 75% were achieved, respectively. Both As(III) and As(V) removal were highly pH dependent.

Table 2. 2. Continuous [16]

Coagulant	pH	Initial As concentration	Type of water	Remarks
Titanium(IV) chloride	7.5	50 μg L^{-1}	Distilled water	As(V) removal was highly pH dependent, whereas As(III) removal was independent of pH. With 2 mg L^{-1} TiCl$_4$ dosage, approximately 55% of As(V) was removed, while As(III) removal was 26%.
Titanium(IV) oxychloride	7.5	50 μg L^{-1}	Distilled water	Both As(V) and As(III) removal were pH dependent. The percent removal of As(V) with 2 mg L^{-1} TiOCl$_2$ dosage was 37%. Given the same conditions, As(III) removal was about 20%.
Zirconium(IV) oxychloride	7.5	50 μg L^{-1}	Distilled water	With 2 mg L^{-1} ZrOCl$_2$ dosage, approximately 8% and 59% of As(III) and As(V) were removed, respectively. As(V) removal was highly pH dependent, whereas As(III) removal was independent of pH.
Ferric Sulphate	7.0	1 mg L^{-1}	Double distilled water	As(III) removal efficiency of 80% was achieved with 25 mg L^{-1} Fe$_2$(SO$_4$)$_3$ dosage.
Titanium(IV) Sulfate	7.0	1 mg L^{-1}	Double distilled water	Ti(SO$_4$)$_2$ was employed for enhanced As(III) removal. The removal efficiency of As(III) was 90% at a coagulant dose of 25 mg L^{-1}.

Atmospheric oxygen, hypochlorite, and permanganate are the most commonly used oxidants. On the other hand, chemicals, such as chlorine, ozone, and permanganate, can rapidly oxidize As(III) to As(V) as presented in Table 2.2 However, despite this enhanced oxidation, interfering substances present in water need to be considered in selecting the proper oxidant as these substances can greatly affect and dictate the kinetics of As(III) oxidation [13]. Competing anions and organic matter in groundwater greatly affect the use of UV/titanium dioxide (TiO$_2$) in arsenic oxidation [17]. To efficiently remove arsenic from a solution by oxidation, oxidants should be selected carefully.

Coagulation-flocculation

Coagulation and flocculation are among the most employed and documented techniques for arsenic removal from water [14,18]. In coagulation, positively charged coagulants (e.g., aluminumsulphate ($Al_2(SO_4)_3$), ferric chloride ($FeCl_3$)) reduce the negative charge of colloids, thereby making the particles collide and get larger. Flocculation, on the other hand, involves the addition of an anionicflocculant that causes bridging or charge neutralization between the formed larger particles leadingto the formation of flocs. During these processes, dissolved arsenic is transformed by the chemicals into an insoluble solid, which undergoes precipitation later [19]. Alternatively, soluble arsenic species can be incorporated into a metal hydroxide phase and be co-precipitated [14]. Obtained solids can be removed afterwards through sedimentation and/or filtration. Arsenic removal efficiency of different coagulants varies as a function of pH. Below pH 7.6, $Al_2(SO_4)_3$, and $FeCl_3$ are equally effective in removing arsenic from water [20]. Between the two inorganic arsenic species, most researchers suggested that arsenate is more efficiently removed, compared to arsenite, and that $FeCl_3$ is a better coagulant than $Al_2(SO_4)_3$ at pH higher than 7.6 [20,21].T he major drawback of coagulation-flocculation is the production of high amounts of arsenic-concentrated sludge [13].

Membrane technologies

In view of drinking water production, membrane filtration is a technique that can be used for the removal of arsenic and other contaminants from water. Typically, membranes are synthetic materials with billions of pores acting as selective barriers, which do not allow some constituents of the water to pass through [22]. A driving force, such as pressure difference between the feed and the permeate sides, is needed to transport the water through the membrane [23]. Generally, there aretwo categories of pressure-driven membrane filtrations:

➢ low-pressure membrane processes, such as microfiltration (MF) and ultrafiltration (UF); and

➢ high-pressure membrane processes, such asreverse osmosis (RO) and nanofiltration (NF) [19,22].

Using membranes with pore sizes between 0.1 and 10 μm, MF alone cannot be used to remove dissolved arsenic species from arsenic-contaminated water. Thus, the particle size of

arsenic-bearing species must be increased prior to MF; the most popular processes for this being coagulation and flocculation [13]. However, the pH of the water and the presence of other ions are major factors affecting the efficiency of this arsenic immobilization. Since arsenate is negatively charged in this pH range, it can bind by surface complexation resulting in efficient arsenate removal. Thus, for this technique to be effective, complete oxidation of arsenite to arsenate is needed. Adding cationic surfactant to contaminated drinking water at a concentration above the critical micelle concentration (CMC) of the water will lead to formation of micelles, which can bind to negatively charged arsenic species. In fact, arsenic removal in the permeate as the surfactant aggregates are large enough to pass through the membrane pores.

Adsorption and ion exchange

Adsorption is a process that uses solids as medium for the removal of substances from gaseous or liquid solutions [13]. Basically, substances are separated from one phase followed by their accumulation at the surface of another. This process is driven mainly by van der Waals forces and electrostatic forces between the adsorbate molecules and the adsorbent surface. From this point of view it is important to characterize the adsorbent surface properties (e.g., surface area, polarity) before being used for adsorption [18]. A variety of sorbents has already been studied in several research areas. These include activated carbon, coal, red mud, fly ash, chicken feathers, kaolinite, montmorillonite, goethite, zeolites, activated alumina, titanium dioxide, iron hydroxide, zero-valent iron, chitosan, and cation-exchange resins. Iron-based adsorption is an emerging technique for the treatment of arsenic-contaminated water. This can be explained by the fact that there exists a high affinity between inorganic arsenic species and iron. Iron can remove arsenic from water either by acting as a sorbent, co-precipitant or contaminant-immobilizing agent, or by behaving as areductant [19]. Adsorption has been reported as the most widely used technique for arsenic removal due toits several advantages including relatively high arsenic removal efficiencies [24,25], easy operation, and handling [25], cost-effectiveness [26], and no sludge production [13]. However, adsorption ofarsenic strongly depends on the system's concentration and pH. At low pH, arsenate adsorptionis favored, whereas for arsenite, maximum adsorption can be obtained between pH 4 and 9 [27]. Moreover, contaminated water does not

only contain arsenic; it is always accompanied by other ions,such as phosphate and silicate, competing for the adsorption sites [28]. Aside from the system'sconditions, the effectiveness of adsorption in arsenic removal can also be hindered by the type ofadsorbent itself. However, most conventional adsorbents have irregular pore structuresand low specific surface areas, leading to low adsorption capacities. Lack of selectivity, relativelyweak interactions with metallic ions, and regeneration difficulties can also confine the ability of thesesorbents in lowering arsenic concentrations to levels below maximum contaminant level (MCL) [29,30].

2.1.9Application of nanoparticles for removal of arsenic from water

Recently, advances in nanoscience and nanotechnology have paved the way to the development of various nanomaterials for the remediation of contaminated water [31]. Due to their high specific surface area, high reactivity, and high specificity, nanoparticles have been given considerable environmental attention as novel adsorbents of contaminants, such as heavy metals and arsenic, from aqueous solutions [32]. Carbon nanotubes and nanocomposites, titanium-based nanoparticles,iron-based nanoparticles, and other metal-based nanoparticles are among the most widely used and investigated nanoparticles for the treatment of arsenic-contaminated water. Table 2.3 presents a summary of the comparative evaluation of some nano-adsorbents used for arsenic removal.

Table 2. 3. Comparative evaluation of various nano-adsorbents for arsenic removal [16]

| Nano-adsorbent | Properties | | pH | Adsorbent dosage (mgL^{-1}) | T (°C) | Sorption capacity (mg g^{-1}) | |
	Average Particle Size (nm)	Surface Area (m2g^{-1})				As(III)	As(V)
PEG-MWCNT[*]	17.4	22.5	4	0.1	25	-	13
Hydrous titanium dioxide	4.8	312	7	500	25	83	-
Iron-doped TiO$_2$	108	-	7	4000	-	-	20.4
Ti-BYC[**]	10-30	82	7	1000	25	-	348.5
α-Fe$_2$O$_3$	5	162	7	100	25	95	47
γ-Fe$_2$O$_3$	7-12	168.73	-	-	-	67.02	-
Fe$_2$O$_3$	12.3	-	6	100	-	20	4.9
Magnetite	20	69.4	6.5	400	25	8	8.8
Fe$_3$O$_4$	5	178.48	7	60	-	46.04	16.56
Ceria	6.6	86.85	-	5000	30	18.02[*]	
CeO$_2$–CNT	-	189	7	25	-	-	81.9
Zirconium oxide	10.8	98	7	100	-	5.2	6
Zirconium oxide	-	327.1	7	100	25	83	32.4

[*]Multiwall carbon nanotubes functionalized with polyethylene glycol; [**]Ti-loaded basic yttrium carbonate

Carbon nanotubes (CNTs)

CNTs have been reported to be effective in the adsorption of various organic chemicals and metal-ions after treatment with oxidants [33,34]. As(III) adsorption efficiency of Multiwall CNTs was approximately 34.22% after 30 min, given an initial As(III) concentration of 542 μg L^{-1} and a sorbent concentration of 1 g L^{-1}. Furthermore, the results revealed that Multiwall CNTs are able to remove arsenic to safe limits, but only for a low initial arsenic concentration. CNTs can also be functionalized in order to increase removal efficiency for metal ions[16].

Titanium-based nanoparticles

Adsorption of arsenite and arsenate by nanocrystalline TiO$_2$ reached equilibrium within four hours, whereas with commercial nonporous TiO$_2$ particles, it was already reached in an hour. Furthermore, higher adsorption capacity wasobtained using nanocrystalline TiO$_2$, which

can be due to its higher specific surface area than thenonporous TiO_2 particles. At an equilibrium arsenic concentration of 45 g L^{-1}, more than 80% of both arsenic species was adsorbed by this nano-adsorbent. In terms of oxidation, nanocrystalline TiO_2 was also shown as an efficient photocatalyst considering that arsenite was completely converted to arsenate within 25 min in the presence of sunlight and dissolved oxygen.

Iron-Based Nanoparticles

Among the most important nanomaterials studied for the treatment of arsenic-contaminatedwater are iron-based nanoparticles, which include zero-valent iron nanoparticles (nZVI) and ironoxide nanoparticles (i.e., Fe_3O_4, and γ-Fe_2O_3). The oxidation state of iron in these particles has amajor influence on their capability to remove contaminants [35]. Several mechanisms are involvedin these removal processes (Figure 2.4).
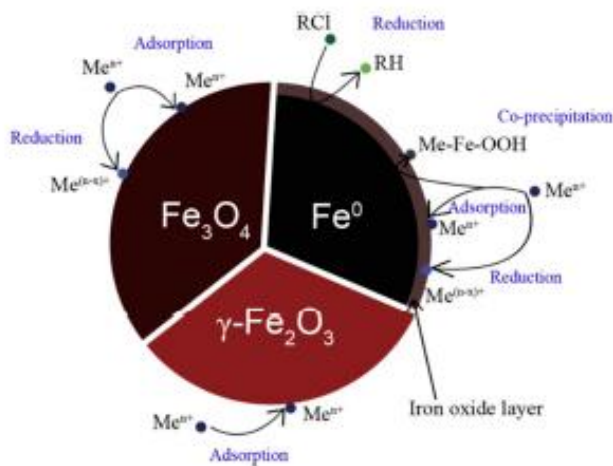
Figure 2. 4. Schematic model of the removal mechanisms of nZVI, Fe_3O_4, and γ-Fe_2O_3 [16]

For instance, dyeing reagents can be adsorbed effectively to functionalized nZVI, which exhibited a maximum adsorption capacityof 191.5 mg g^{-1} for one type of dye studied [36]. In this case, adsorption was the result of donor-acceptor bonds formed in the reaction between the functional group –NH_2 on the surface and the –OH group on the target compound. As for heavy metals, adsorption and co-precipitationare generally accepted mechanisms involved in removal

by nZVI [30]. As schematically shown inFigure 2.4, these mechanisms occur because an iron oxide shell is formed once nZVI is brought incontact with air or water. Removal of arsenic is a widely studied example [31,37]. Ramos et al. [38] studied the arsenic immobilization mechanism using nZVI. Primarily due to the core-shell structure of nZVI, it was shown that both reductive and oxidative mechanisms take place upon application of nZVI. This structure is characterized by a highly reducing metal core and a thin layer of amorphous iron(oxy)hydroxide that helps in the coordination and oxidation of As(III). Other metal-based nanoparticles which can be used for adsorption of arsenic are ceria and zirconium oxide nanoparticles as well as metal organic frameworks as novel porous adsorbents [16].

2.2 Adsorption theory

2.2.1 Adsorption isotherms models

In general, an adsorption isotherm is an invaluable curve describing the phenomenon governing the retention (or release) or mobility of a substance from the aqueous porous media or aquatic environments to a solid-phase at a constant temperature and pH [39,40]. Adsorption equilibrium (the ratio between the adsorbed amount with the remaining in the solution) is established when an adsorbate containing phase has been contacted with the adsorbent for sufficient time, with its adsorbate concentration in the bulk solution is in a dynamic balance with the interface concentration [41]. Typically, the mathematical correlation, which constitutes an important role towards the modeling analysis, operational design and applicable practice of the adsorption systems, is usually depicted by graphically expressing the solid-phase against its residual concentration [42]. Its physico-chemical parameters together with the underlying thermodynamic assumptions provide an insight into the adsorption mechanism, surface properties as well as the degree of affinity of the adsorbents [43].

Over the years, a wide variety of equilibrium isotherm models (Langmuir, Freundlich, Brunauer–Emmett–Teller, Redlich– Peterson, Dubinin–Radushkevich, Temkin, Toth, Koble– Corrigan, Sips, Khan, Hill, Flory–Huggins and Radke–Prausnitz isotherm), have been formulated in terms of three fundamental approaches [44]. Kinetic consideration is the first

approach to be referred. Hereby, adsorption equilibrium is defined being a state of dynamic equilibrium, with both adsorption and desorption rates are equal [45]. Whereas, thermodynamics, being a base of the second approach, can provide a framework of deriving numerous forms of adsorption isotherm models [46], and potential theory, as the third approach, usually conveys the main idea in the generation of characteristic curve [47]. However, an interesting trend in the isotherm modeling is the derivation in more than one approach, thus directing to the difference in the physical interpretation of the model parameters [48].

2.2.2 Two parameter isotherms

Langmuir isotherm model[45]

Langmuir adsorption isotherm, originally developed to describe gas–solid-phase adsorption onto activated carbon, has traditionally been used to quantify and contrast the performance of different bio-sorbents [45]. In its formulation, this empirical model assumes monolayer adsorption (the adsorbed layer is one molecule in thickness), with adsorption can only occur at a finite (fixed) number of definite localized sites, that are identical and equivalent, with no lateral interaction and steric hindrance between the adsorbed molecules, even on adjacent sites [49]. In its derivation, Langmuir isotherm refers to homogeneous adsorption, which each molecule possess constant enthalpies and sorption activation energy (all sites possess equal affinity for the adsorbate) [50], with no transmigration of the adsorbate in the plane of the surface [51].

Graphically, it is characterized by a plateau, an equilibrium saturation point where once a molecule occupies a site, no further adsorption can take place [40]. Moreover, Langmuir theory has related rapid decrease of the intermolecular attractive forces to the rise of distance. The mathematical expression of Langmuir isotherm models are illustrated in Table 2.5. Hereby, a dimensionless constant, commonly known as separation factor (R_L) defined by Webber and Chakkravorti [52] can be represented as:

$$R_L = \frac{1}{1+K_L C_0} \tag{2.1}$$

where K_L (Lmg^{-1}) refers to the Langmuir constant and C_0 is denoted to the adsorbate initial concentration (mgL^{-1}). In this context, lower R_L value reflects that adsorption is more favourable. In a deeper explanation, R_L value indicates the adsorption nature to be either unfavourable ($R_L > 1$), linear ($R_L = 1$), favourable ($0 < R_L < 1$) or irreversible ($R_L = 0$).

Freundlich isotherm model[53]

Freundlich isotherm [53] is the earliest known relationship describing the non-ideal and reversible adsorption, not restricted to the formation of monolayer. This empirical model can be applied to multilayer adsorption, with non-uniform distribution of adsorption heat and affinities over the heterogeneous surface [54]. Historically, it is developed for the adsorption of animal charcoal, demonstrating that the ratio of the adsorbate onto a given mass of adsorbent to the solute was not a constant at different solution concentrations. In this perspective, the amount adsorbed is the summation of adsorption on all sites (each having bond energy), with the stronger binding sites are occupied first, until adsorption energy are exponentially decreased upon the completion of adsorption process [55].

At present, Freundlich isotherm is widely applied in heterogeneous systems especially for organic compounds or highly interactive species on activated carbon and molecular sieves. The slope ranges between 0 and 1 is a measure of adsorption intensity or surface heterogeneity, becoming more heterogeneous as its value gets closer to zero. Whereas, a value below unity implies chemisorptions process where 1/n above one is an indicative of cooperative adsorption [56]. Its linearized and nonlinearized equations are listed in Table 2.4. Recently, Freundlich isotherm is criticized for its limitation of lacking a fundamental thermodynamic basis, not approaching the Henry's law at vanishing concentrations.

Dubinin–Radushkevich isotherm model[57]

Dubinin–Radushkevich isotherm [57], is an empirical model initially conceived for the adsorption of subcritical vapors onto micropore solids following a pore filling mechanism. It is generally applied to express the adsorption mechanism with a Gaussian energy distribution onto

a heterogeneous surface. The model has often successfully fitted high solute activities and the intermediate range of concentrations data well, but has unsatisfactory asymptotic properties and does not predict the Henry's law at low pressure. The approach was usually applied to distinguish the physical and chemical adsorption of metal ions, withits mean free energy, E per molecule of adsorbate (for removing a molecule from its location in the sorption space to the infinity) can be computed by the relationship [58]:

$$E = \left[\frac{1}{\sqrt{2B_{DR}}} \right] \tag{2.2}$$

where B_{DR} is denoted as the isotherm constant. Meanwhile, the parameter ε can be correlated as:

$$\varepsilon = RT ln \left[1 + \frac{1}{C_e} \right] \tag{2.3}$$

where R, T and Ce represent the gas constant (8.314 Jmol^{-1} K^{-1}), absolute temperature (K) and adsorbate equilibrium concentration (mg L^{-1}), respectively. One of the unique features of the Dubinin–Radushkevich isotherm model lies on the fact that it is temperature-dependent, which when adsorption data at different temperatures are plotted as a function of logarithm of amount adsorbed vs the square of potential energy, all suitable data will lie on the same curve, named as the characteristic curve.

Temkin isotherm model [59]

Temkin isotherm is the early model describing the adsorption of hydrogen onto platinum electrodes within the acidic solutions. The isotherm contains a factor that explicitly taking into the account of adsorbent–adsorbate interactions. By ignoring the extremely low and large value of concentrations, the model assumes that heat of adsorption (function of temperature) of all molecules in the layer would decrease linearly rather than logarithmic with coverage [59]. As implied in the equation, its derivation is characterized by a uniform distribution of binding energies (up to some maximum binding energy). Temkin equation is excellent for predicting the gas phase equilibrium (when organization in a tightly packed structure with identical orientation is not necessary), conversely complex adsorption systems including the liquid-phase adsorption isotherms are usually not appropriate to be represented.

Flory–Huggins isotherm model [60]

Flory–Huggins isotherm model [60], which occasionally deriving the degree of surface coverage characteristics of adsorbate onto adsorbent, can express the feasibility and spontaneous nature of an adsorption process. In this respect, θ is the degree of surface coverage, where K_{FH} and n_{FH} are the indication of its equilibrium constant and model exponent. Its equilibrium constant, K_{FH} that used for the calculation of spontaneity free Gibbs energy, is related to the equation [49]:

$$\Delta G^o = -RT \ln(K_{FH}) \tag{2.4}$$

Hill isotherm model [61]

Hill equation [61] was postulated to describe the binding of different species onto homogeneous substrates. The model assumes that adsorption is a cooperative phenomenon, with the ligand binding ability at one site on the macromolecule, may influence different binding sites on the same macromolecule.

2.2.3 Three parameter isotherms

Redlich–Peterson isotherm model [62]

Redlich–Peterson isotherm [62] is a hybrid isotherm featuring both Langmuir and Freundlich isotherms, which incorporate three parameters into an empirical equation. The model has a linear dependence on concentration in the numerator and an exponential function in the denominator to represent adsorption equilibiria over a wide concentration range, that can be applied either in homogeneous or heterogeneous systems due to its versatility. Typically, a minimization procedure is adopted in solving the equations by maximizing the correlation coefficient between the experimental data points and theoretical model predictions with solver add-in function of the Microsoft excel. In the limit, it approaches Freundlich isotherm model at

high concentration (as the exponent β tends to zero) and is in accordance with the low concentration limit of the ideal Langmuir condition (as the β values are all close to one).

Sips isotherm model[63]

Sips isotherm [63] is a combined form of Langmuir and Freundlich expressions deduced for predicting the heterogeneous adsorption systems [64] and refelct the limitation of the rising adsorbate concentration associated with Freundlich isotherm model. At low adsorbate concentrations, it reduces to Freundlich isotherm; while at high concentrations, it predicts a monolayer adsorption capacity characteristic of the Langmuir isotherm. As a general rule, the equation parameters are governed mainly by the operating conditions such as the alteration of pH, temperature and concentration [51].

Toth isotherm model[65]

Toth isotherm model [65], is another empirical equation developed to improve Langmuir isotherm fittings (experimental data), and useful in describing heterogeneous adsorption systems, which satisfying both low and high-end boundary of the concentration [49]. Its correlation presupposes an asymmetrical quasi-Gaussian energy distribution, with most of its sites has an adsorption energy lower than the peak (maximum) or mean value.

Koble–Corrigan isotherm model[66]

Similar to the Sips isotherm model, Koble–Corrigan isotherm [66] is a three-parameter equation, which incorporated both Langmuir and Freundlich isotherm models for representing the equilibrium adsorption data. The isotherm constants, A, B and n are evaluated from the linear plot using a trial and error optimization.

Khan isotherm model [67]

Khan isotherm [67] is a generalized model suggested for the pure solutions, with b_K and a_K are devoted to the model constant and model exponent. At relatively high correlation coefficients and minimum ERRSQ or chi-square values, its maximum uptake values can be well determined.

Radke–Prausnitz isotherm model [49]

The correlation of Radke–Prausnitz isotherm is usually predicted well by the high RMSE and chi-square values. Its model exponent is represented by β_R, where a_R and r_R are referred to the model constants [49].

Multilayer physisorption isotherms [68]

Brunauer–Emmett–Teller (BET) [68] isotherm is a theoretical equation, most widely applied in the gas–solid equilibrium systems. It was developed to derive multilayer adsorption systems with relative pressure ranges from 0.05 to 0.30 corresponding to a monolayer coverage lying between 0.50 and 1.50. As a note, the empirical isotherm is reasonable fit to Frenkel–Halsey–Hill (F_{HH}) or MacMillan–Teller (MET) isotherms for relative pressures higher than 0.8 and approximately Brunauer–Emmett–Teller (BET) isotherm for relative pressures lower than 0.35.

Table 2. 4.Adsorption isotherms models[69]

Isotherm	Linear form[a]	Nonlinear form[a]
Langmuir [45]	$\dfrac{C_e}{q_e} = \dfrac{1}{K_L Q_0} + \dfrac{C_e}{Q_0}$	$q_e = \dfrac{Q_o K_L C_e}{1 + K_L C_e}$
Freundlich [70]	$\log q_e = \log K_F + \dfrac{1}{n}\log C_e$	$q_e = K_F C_e^{1/n}$
Dubinin–Radushkevich [57]	$\ln(q_e) = \ln(q_s) - k_{ad}\varepsilon^2$	$q_e = (q_s)exp(-k_{ad}\varepsilon^2)$
Tempkin [71]	$q_e = \dfrac{RT}{b_T}\ln A_T + \left(\dfrac{RT}{b_T}\right)\ln C_e$	$q_e = \dfrac{RT}{b_T}\ln A_T\, C_e$
Flory–Huggins [60]	$\log\dfrac{\theta}{C_o} = \log(K_{FH}) + n_{FH}\log(1-\theta)$	$\dfrac{\theta}{C_o} = K_{FH}(1-\theta)^{nFH}$
Hill [61]	$\log(\dfrac{q_e}{q_{sh} - q_e}) = n_h\log(C_e) - \log(K_D)$	$q_e = \dfrac{q_{SH}C_e{}^{n_H}}{K_D + C_e{}^{n_H}}$
Redlich–Peterson [62]	$\ln(K_R\dfrac{C_e}{q_e} - 1) = g\ln(C_e) + \ln(a_R)$	$q_e = \dfrac{K_R C_e}{1 + a_R C_e{}^g}$
Sips [63]	$\beta_S\ln(C_e) = -\ln\left(\dfrac{K_S}{q_e}\right) + \ln(a_S)$	$q_e = \dfrac{K_S C_e{}^{\beta_S}}{1 + a_S C_e{}^{\beta_S}}$
Toth [65]	$\ln\left(\dfrac{q_e}{K_T}\right) = \ln(C_e) - \dfrac{1}{t}\ln(a_T + C_e)$	$q_e = \dfrac{K_T C_e}{(a_T + C_e)^{1/t}}$
Koble–Corrigan [66]	$\dfrac{1}{q_e} = \dfrac{1}{AC_e^n} + \dfrac{B}{A}$	$q_e = \dfrac{AC_e^n}{1 + BC_e^n}$
Khan [67]	-	$q_e = \dfrac{q_s b_K C_e}{(1 + b_K C_e)^{a_K}}$
Radke–Prausnitz [49]	-	$q_e = \dfrac{a_{RP} r_R C_e{}^{\beta R}}{a_{RP} + r_R C_e{}^{\beta R - 1}}$
BET [68]	$\dfrac{C_e}{q_e(C_s - C_e)} = \dfrac{1}{q_S C_{BET}} + \dfrac{[C_{BET} - 1]}{q_s C_{BET}}\dfrac{C_e}{C_s}$	$q_e = \dfrac{q_S C_{BET} C_{Ce}}{(C_s - C_e)[1 + (C_{BET} - 1)(C_e/C_s)]}$
F$_{HH}$[72]	-	$\ln\left(\dfrac{C_e}{C_s}\right) = -\dfrac{\alpha}{RT}\left(\dfrac{q_s}{q_e^d}\right)^r$
MET [73]	-	$q_e = q_s\left(\dfrac{k}{\ln(C_s/C_e)}\right)^{1/3}$

2.2.4 Orthogonal distance regression (ODR) algorithm

Orthogonal distance regression (ODR) algorithm minimizes the residual sum of squares by adjusting both fitting parameters and values of the independent variable in the iterative process. The residual in ODR is not the difference between the observed value and the predicted value for the dependent variable, but the orthogonal distance from the data to the fitted curve [74]. Considering that values of both axes are affected by measurement error in the process of

experimental data by adsorption isotherm models fitting, the use of ODR modeling procedure is statistically correct [75] and can be presented by following eq. (2.5):

$$\text{ODR} = \sum_{i=1}^{n} \left[\left(\frac{q_i - \hat{q}_i}{q_i} \right)^2 + \left(\frac{C_{fi} - \hat{C}_{fi}}{C_{fi}} \right)^2 \right]$$

(2.5)

where n, q_i, q_i, C_{fi} and $\hat{C}_{fi}$ denote the number of data points, the experimental and the estimated values of adsorption capacity and equilibrium adsorbate concentration.

2.2.5 Adsorption kinetic

It is essential to describe precisely the kinetics of adsorption, to compare the predicted adsorption parameters calculated by models to the experimental adsorbent behavior, in different adsorbent adsorbate systems and in varied experimental conditions [76]. From the kinetic analysis, the solute uptake rate, which determines the residence time required for completion of adsorption reaction, may be established. Also, one can know the scale of an adsorption apparatus based on the kinetic information. Generally speaking, adsorption kinetics is the base to determine the performance of fixed-bed or any other flow-through systems [77].

In the past decades, several mathematical models have been proposed to describe adsorption data, which can generally be classified as adsorption reaction models and adsorption diffusion models. Both models are applied to describe the kinetic process of adsorption; however, they are quite different in nature. Adsorption diffusion models are always constructed on the basis of three consecutive steps: (1) diffusion across the liquid film surrounding the adsorbent particles, *i.e.,* external diffusion or film diffusion; (2) diffusion in the liquid contained in the pores and/or along the pore walls, which is so-called internal diffusion or intra-particle diffusion; and (3) adsorption and desorption between the adsorbate and active sites, *i.e*., mass action. However, adsorption reaction models originating from chemical reaction kinetics are based on the whole process of adsorption without considering these steps mentioned above. [77].

Adsorption reaction models

Lagergren (1898) [78] presented a first-order rate equation to describe the kinetic process of liquid-solid phase adsorption of oxalic acid and malonic acid onto charcoal. In recent years, it has been widely used to describe the adsorption of pollutants from wastewater. It can be presented as equation **a** in Table 2.5. Integrating eq. (**a**) with the boundary conditions of $q_t=0$ at $t=0$ and $q_t=q_t$ at $t=t$, yields, equation **a** obtains form **b** (Table 2.5).

In 1995, Ho described a kinetic process of the adsorption of divalent metal ions onto peat [79], in which the chemical bonding among divalent metal ions and polar functional groups on peat, such as aldehydes, ketones, acids, and phenolics are responsible for the cation-exchange capacity of the peat.The rate of adsorption may be given as equation **c** (Table 2.5.). The driving force, (q_e-q_t), is proportional to the available fraction of active sites [80]. Then, it yields on equation **d** (Table 2.5.). Integrating eq.(**d**) with the boundary conditions of $q_t=0$ at $t=0$ and $q_t=q_t$at $t=t$, yields **e** (Table 2.5.). This equation has been successfully applied to the adsorption of metal ions, dyes, herbicides, oils, and organic substances from aqueous solutions [9].

A kinetic equation of chemisorption was established by Zeldowitsch (1934) [55] and was used to describe the rate of adsorption of carbon monoxide on manganese dioxide that decreases exponentially with an increase in the amount of gas adsorbed [80], which is the so-called Elovich equation (equation **f** (Table 2.5.)). Elovich equation can be rearranged to a linear form as equation **g** (Table 2.5.). Elovich's equation has been widely used to describe the adsorption of gas onto solid systems [81]. Recently it has also been applied to describe the adsorption process of pollutants from aqueous solutions. With the assumption of $a\alpha t>>1$, eq.(**g**) was integrated by using the boundary conditions of $q=0$ at $t=0$ and $q=q$ at $t=t$ and obtains form eq.(**h**) (Table 2.5.).

The second-order rate equations were reasonably applied to describe adsorption reactions occurring in soil and soil minerals.The typical second-order rate equation in solution systems is presented as equation **i** (Table 2.5.). Eq. (**i**) was integrated with the boundary conditions of $C_t=0$ at $t=0$ and $C_t=C_t$at $t=t$ to yield eq.(**j**) (Table 2.5).

Adsorption diffusion models

It is generally known that a typical liquid/solid adsorption involves film diffusion, intraparticle diffusion, and mass action. For physical adsorption, mass action is a very rapid process and can be negligible for kinetic study. Thus, the kinetic process of adsorption is always controlled by liquid film diffusion or intrapartical diffusion.

Liquid film diffusion model
Linear driving force rate law

In liquid/solid adsorption systems the rate of solute accumulation in the solid phase is equal to that of solute transfer across the liquid film according to the mass balance law. The rate of solute accumulation in a solid particle clearly equals to $V_p \left(\frac{\partial \bar{q}}{\partial t} \right)$, where q represents the average solute concentration in the solid, and V_p the volume of the particle. Meanwhile the rate of solute transfer across the liquid film is proportional to the surface area of the particle A_s and the concentration driving force $(C - C_i)$. Therefore, it equals to $k_f A_s (C - C_i)$, where k_f represents the film mass transfer coefficient. With the discussion above we can obtain equation **k** (Table 2.5.), where C_i and C denote the concentration of solute at the particle/liquid interface and in the bulk of the liquid far from the surface, respectively. The ratio A_s/V_p that is the particle surface area per unit particle volume can be defined as S_0. Then, eq. (**k**) can be written as eq.(**l**) (Table 2.5.). Eq.(**l**) is called as "linear driving force" rate law, which is usually applied to describe the mass transfer through the liquid film.

Film diffusion mass transfer rate equation

The film diffusion mass transfer rate equation presented by Boyd *et al.*(1947) [82] are eq. (**m**) and eq. (**n**) (Table 2.5.). A plot of $\ln(1 - q_t/q_e) \sim t$ should be a straight line with a slope $-R_1$ if the film diffusion is the ratelimiting step. The film diffusion mass transfer rate equation has been successfully applied to model several liquid/solid adsorption cases.

Intraparticle diffusion model

Homogeneous solid diffusion model (HSDM)

A typical intraparticle diffusion model is the so-called homogeneous solid diffusion model (HSDM), which can describe mass transfer in an amorphous and homogeneous sphere. The HSDM equation can be presented asequation **o** (Table 2). Crank (1956) [83] gave an exact solution to eq. (**o**) for the "infinite bath" case where the sphere is initially free of solute and the concentration of the solute at the surface remains constant. External film resistance can be neglected according to the constant surface concentration. Then, Crank's solution is written as equation **p** (Table 2). For a long time, eq. (**p**) may be written as equation **q** (Table 2.5.).The linearization of eq. (**q**) gives equation **r** (Table 2.5.). In recent years, HSDM has been applied to different kinds of adsorption systems, such as the adsorption of salicylic acid and 5-sulfosalicylic acid from aqueous solutions.

Weber-Morris model

Weber-Morris [77] found that in many adsorption cases, solute uptake varies almost proportionally with $t^{1/2}$ rather than with the contact time *t* (equation **s** (Table 2.5.)). According to Weber-Morris equation, a plot of $q_t \sim t^{1/2}$ should be a straight line with a slope kint when the intraparticle diffusion is a rate-limiting step. However, it is not always the case and adsorption kinetics may be controlled by film diffusion and intraparticle diffusion simultaneously.

Dumwald-Wagner model

Dumwald-Wagner proposed another intraparticle diffusion model as [84] eq. (**u**) (Table 2.5.). A plot of $\log(1-F^2) \sim t$ should be linear and the rate constant *K* can be obtained from the slope. Dumwald-Wagner model proved to be reasonable to model different kinds of adsorption systems, e.g., *p*-toluidine adsorption from aqueous solutions onto hypercrosslinked polymeric adsorbents.

Double-exponential model (DEM)

A double-exponential function proposed by Wilczak and Keinath (1993) [85] was used to describe lead and copper adsorption onto activated carbon. In this case, the uptake process of both metals could be divided into two steps, namely a rapid phase involving external and internal diffusions, followed by a slow phase controlled by the intraparticle diffusion. It was demonstrated that the two-step mechanism can be described fairly well with the double-exponential model [86], which is presented as equation **x** (Table 2.5.). If $K_1 \gg K_2$, it means that the rapid process can be assumed to be negligible on the overall kinetics. Nevertheless, values of K_1 and K_2 are not sufficient to describe and interpret the influence of external and internal diffusions. DEM can also describe a process where the adsorbent offers two different types of adsorption sites. On the first-type site rapid adsorption equilibration occurs within a few minutes, whereas on the second site type, adsorption is more slowly. DEM isparticularly suitable for modeling heavy metals adsorption, e.g., adsorption of Cu(II) and Pb(II) from aqueous solutions by activated carbon and grafted silica.

Table 2. 5. Adsorption diffusion models equations[77]

Eq.	Mathematical equations [a]	Eq.	Mathematical equations [a]
a	$\dfrac{dq_t}{dt} = k_{p1}(q_e - q_t)$	l	$\dfrac{\partial \bar{q}}{\partial t} = k_f S_0 (C - C_i)$
b	$\ln\left(\dfrac{q_e}{q_e - q_t}\right) = k_{p1} t$	m	$\ln\left(1 - \dfrac{q_t}{q_e}\right) = R^1 t$
c	$\dfrac{d(P)_t}{dt} = k_{p2}[(P)_0 - (P)_t]^2$	n	$R^1 = \dfrac{3 D_e^1}{r_0 \Delta r_0 k'}$
d	$\dfrac{dq_t}{(q_e - q_t)^2} = k_{p2} dt$	o	$\dfrac{\partial q}{\partial t} = \dfrac{D_s}{r^2}\dfrac{\partial}{\partial r}\left(r^2 \dfrac{\partial q}{\partial r}\right)$
e	$\dfrac{1}{(q_e - q_t)} = \dfrac{1}{q_e} + k_{p2} t$	p	$\dfrac{q}{q_s} = 1 + \dfrac{2R}{\pi r}\displaystyle\sum_{n=1}^{\infty}\dfrac{(-1)^n}{n}\sin\dfrac{n\pi r}{R}exp\left(\dfrac{-D_s n^2 \pi^2 t}{R^2}\right)$
f	$\dfrac{dq}{qt} = ae^{-\alpha q}$	q	$\dfrac{\bar{q}}{q_\infty} = 1 - \dfrac{6}{\pi^2}exp\left(\dfrac{-D_s \pi^2 t}{R^2}\right)$
g	$q = \dfrac{(2.3)}{\alpha}\log(t + t_0) - \left(\dfrac{2.3}{\alpha}\right)\log t_0$	r	$\ln\left(1 - \dfrac{\bar{q}}{q_\infty}\right) = \dfrac{-D_s \pi^2}{R^2} t + \ln\dfrac{6}{\pi^2}$
h	$q = \alpha \ln(a\alpha) + \alpha \ln t$	s	$q_t = k_{int} t^{1/2}$
i	$\dfrac{dC_t}{dt} = -k_2 C_t^2$	t	$F = \dfrac{q_t}{q_e} = 1 - \dfrac{6}{\pi^2}\displaystyle\sum_{n=1}^{\infty}\dfrac{1}{n^2}exp(-n^2 Kt)$
j	$\dfrac{1}{C_t} = k_2 t + \dfrac{1}{C_0}$	u	$\log(1 - F^2) = -\dfrac{K}{2.303} t$
k	$V_p\left(\dfrac{\partial \bar{q}}{\partial t}\right) = k_f A_s (C - C_i)$	x	$q_t = q_e - \dfrac{D_1}{m_a}exp(-K_1 t) - \dfrac{D_2}{m_a}exp(-K_2 t)$

2.2.6 Error functions

Within recent decades, linear regression has been one of the most viable tool defining the best-fitting relationship [87] quantifying the distribution of adsorbates, mathematically analyzing the adsorption systems [88] and verifying the consistency and theoretical assumptions of an isotherm model [89]. Due to the inherent bias resulting from the transformation which riding towards a diverse form of parameters estimation errors and fits distortion, several mathematically rigorous error functions (sum square error, Hybrid fractional error function, sum of absolute errors, average relative error, Marquardt's percent standard deviation, coefficient of determination, Spearman's correlation coefficient, standard deviation of relative errors, nonlinear chi-square test, coefficient of nondetermination and sum of normalized errors) (Table 2.6.) have lately drastically been addressed and confronted [87]. Concomitant with the development of computer technology in the 1980s, the progression of the nonlinear isotherm modeling has extensively been facilitated and motivated [89]. Contrary to the linearization models, nonlinear regression usually involves the minimization or maximization of error distribution (between the experimental data and the predicted isotherm) based on its convergence criteria [87].

Sum square error (ERRSQ)[88]

Despite ERRSQ is the most widely used error function [88], at higher end of the liquid-phase concentration ranges, the magnitude and squares of the errors tend to increase, illustrating a better fit for the isotherm parameters derivation.

Hybrid fractional error function (HYBRID)[90]

The error function was developed to improve ERRSQ fit at low concentrations. Hereby, each ERRSQ value is divided by the experimental solid-phase concentration with a divisor included in the system as a term for the number of degrees of freedom (the number of data points minus the number of parameters within the isotherm equation).

Average relative error (ARE)[91]

ARE model [91] which indicates a tendency to under or overestimate the experimental data, attempts to minimize the fractional error distribution across the entire studied concentration range.

Sum of absolute errors (EABS)[92]

The approach is similar to the ERRSQ function, with an increase in the errors will provide a better fit, leading to the bias towards the high concentration data [92].

Marquardt's percent standard deviation (MPSD)[93]

Marquardt's percent standard deviation (MPSD) error function has previously practiced by a number of researchers in the isotherm studies [93]. According to the number of degrees of freedom in the system, it is similar to some respects of a modified geometric mean error distribution [94].

Coefficient of determination (R^2), Spearman's correlation coefficient (r_s) and standard deviation of relative errors (s_{RE})[89]

Coefficient of determination, which represents the percentage of variability in the dependent variable (the variance about the mean) is employed to analyze the fitting degree of isotherm and kinetic models with the experimental data. Its value may vary from 0 to1 [87] where Spearman's correlation coefficient and standard deviation of relative errors are individually determined to evaluate the global correlation and the dispersion of its relative errors.

Nonlinear chi-square test (χ^2)[89]

Nonlinear chi-square test is a statistical tool necessary for the best fit of an adsorption system, obtained by judging the sum squares differences between the experimental and the

calculated data, with each squared difference is divided by its corresponding value (calculated from the models). Small value indicates its similarities while a larger number represents the variation of the experimental data.

Coefficient of non-determination (K₂)[95]

Another statistical term, coefficient of non-determination, is much useful in describing the extent relationship between the transformed experimental data and the predicted isotherms, and minimization of the error distribution [95].

Sum of normalized errors (SNE)[69]

Consequence of different error criteria is likely to produce different sets of isotherm parameters, a standard procedure normalizing and combining various errors for better and meaningful comparison between the parameter sets (for the single isotherm model) is adopted. The calculation orientation is revealed as follows:

➢ Selection of an isotherm model and error function, and determination of the adjustable parameters which minimize the error function.

➢ Determination of all other error functions by referring to the parameter set.

➢ Computation of other parameter sets associated with their error function values (initiation of the procedure by minimizing the error function).

➢ Normalization and selection of the maximum parameter sets with respect to the largest error measurement.

➢ Summation of each parameter set which generates the minimum normalization error.

Table 2. 6. Lists of error functions[69]

Error functions abbreviation	Definition/expression [a]
R^2[89]	$$\dfrac{\left(q_{e,meas} - \overline{q_{e,calc}}\right)^2}{\Sigma\left(q_{e,meas} - \overline{q_{e,calc}}\right)^2 + \left(q_{e,meas} - q_{e,calc}\right)^2}$$
χ^2[89]	$$\sum_{i=1}^{n} \dfrac{\left(q_{e,calc} - q_{e,meas}\right)^2}{q_{e,meas}}$$
MPSD [93]	$$100\sqrt{\dfrac{1}{n-p}\sum_{i=1}^{n}\left(\dfrac{q_{e,meas} - q_{e,calc}}{q_{e,meas}}\right)^2}$$
HYBRID [90]	$$\dfrac{100}{n-p}\sum_{i=1}^{n}\left[\dfrac{q_{e,mas} - q_{e,calc}}{q_{e,mas}}\right]$$
ARE[91]	$$\dfrac{100}{n}\sum_{i=1}^{n}\left|\dfrac{q_{e,meas} - q_{e,calc}}{q_{e,meas}}\right|$$
ARS[69]	$$\sqrt{\sum_{i=1}^{n}\dfrac{\left(\dfrac{qe_i^{exp} - qe_i^{cal}}{qe_i^{exp}}\right)^2}{n-1}}$$
ERRSQ/SSE [96]	$$\sum_{i=1}^{n}\left(q_{e,calc} - q_{e,meas}\right)_i^2$$
s_{RE} [89]	$$\sqrt{\dfrac{\sum_{i=1}^{n}\left[\left(q_{e,meas} - q_{e,calc}\right)_i - ARE\right]_i^2}{n-1}}$$
EABS [89]	$$\sum_{i=1}^{n}\left|q_{e,meas} - q_{e,calc}\right|$$
r_s [89]	$$1 - \dfrac{6\sum_{i=1}^{n}\left(q_{e,meas} - q_{e,calc}\right)_i^2}{n(n-1)^2}$$

2.2.7 Adsorption process modeling

Adsorption is the process through which ions are removed from solution and accumulate at a solid surface. The ion accumulation takes place at the interface between the surface and the solution forming a two-dimensional structure. Adsorption can occur either specifically or non-specifically. Specific adsorption occurs when ions have a high affinity for the surface and it

45

results in the formation of inner-sphere surface complexes. Inner-sphere surface complexes are complexes that contain no water molecules between the adsorbing ion and the surface functional group which are a source of solid surface charge since they undergo dissociation and/or protonation reactions as a result of changes in solution pH. Specific anion adsorption occurs via ligand exchange where the adsorbing ion replaces a reactive surface hydroxyl from the surface functional group. Nonspecific adsorption is dominated by electrostatic attraction and results in outer-sphere complex formation or in adsorption in the diffuse ion swarm. Adsorption in the diffuse ion swarm is the weakest type of adsorption since the ion does not attach to a specific surface functional group but remains free in the aqueous solution, neutralizing surface charge only by its proximity to the charged solid surface. Outer-sphere surface complexes are also formed through nonspecific adsorption and contain at least one water molecule between the adsorbing ion and the surface functional group [97].

Surface complexation models are chemical models that give a molecular description of adsorption phenomena using an equilibrium approach. Analogous to complex formation in solution, surface complexation models define surface species, chemical reactions, equilibrium constants, mass balances, and charge balances and their molecular features can be given thermodynamic significance. One of the major advancements of surface complexation models is consideration of the charge on both the adsorbing ion and the solid adsorbent surface. Surface complexation models constitute a family of models having many common characteristics and adjustable parameters. The models differ in their structural representation of the solid-solution interface, *i.e*., the location and surface configuration of the adsorbed ions [97].

Members of the surface complexation model family include the two-pK models: constant capacitance, diffuse-layer, triple-layer. Two-pK models are based on a reactive surface functional group, SOH, that undergoes both protonation and dissociation. In the constant capacitance model and the diffuse layer model all surface complexes are inner-sphere and are located in a single surface plane. The diffuse-layer model (DLM) includes a diffuse layer that commences at the d-plane and extends into solution. In the triple-layer model ions forming inner-sphere surface complexes adsorb in the surface o-plane and ions forming outer-sphere surface complexes adsorb in a-plane located between the o-plane and the d-plane [97].

The most commonly studied oxide surfaces by surface complexation models have been the iron oxides, goethite and ferrihydrite. Subsequently, the models were extended to include adsorption on day minerals, organic materials, and soil samples. In extending the models to natural samples certain approximations and modifications are necessary [98]:

➢ oxide surfaces are presented as idealized and stretched flush planes with the surface active hydroxyl centers. Equations are used for describing the reaction on each of these specific surface locations;

➢ Reactions on the surface are in local balance and they are described by thermodynamic laws;

➢ the variation of minerals surface electrical charge is a direct consequence of chemical reactions on a surface;

➢ the impact of surface charge on the measured equilibrium constant is calculated, while characteristic equilibrium constants are obtained from experimental measurements.

Diffuse-Layer Model

The diffuse-layer model has been used to describe adsorption on iron, aluminum, manganese, titanium, and silicon oxides, kaolinite, montmorillonite and biotite minerals, natural organic matter, bacterial cell walls, and sediments. Adsorbing ions that have been investigated include the cation and metal ions: calcium, strontium, barium, copper, nickel, zinc, cadmium, lead, cobalt, aluminum, chromium, silver, mercury, uranium and the anions: phosphate, sulfate, selenite, selenate, arsenate, arsenite, borate, chromate, fluoride, vanadate, thiosulfate, oxalate, phthalate, salicylate, benzoate, and fulvate [97].

The diffuse layer model of the oxide-solution interface was proposed by Stumm and coworkers and developed as the generalized two-layer model by Dzombak and Morel (1990). The assumptions in the diffuse layer model are [99]:

➢ all surface complexes are inner sphere complexes;

➢ no surface complexes are formed with ions in the background electrolyte;

➢ two planes of charge represent the surface;

➢ the relationships between surface charges and surface potentials are appropriate equations.

DLM model describe the reactions that take place during the adsorption in the diffuse layer of hydrated iron oxide (hydrous ferric oxide, HFO). The reactions will be used in

describing (modeling) of hazardous waste behavior and which are in accordance with the rules of identification of hazardous waste (Hazardous Waste identification Rule, HWIR). A database which includes a variety of reactions that take place during the adsorption of cations (H_3O^+, Ba^{2+}, Cd^{2+}, Cu^{2+}, Pb^{2+}, Ni^{2+}, Zn^{2+}) and anions As(III) and As(V) was used in early HWIR models procedure presented in Dzombak dissertation [100]. Dzombak and Morel have developed a thermodynamic database on HFO for the sorption of inorganic ions in natural systems using surface complexation model with a simple model of solid-water phase boundary. Although a simple two-layer model (a surface layer and the diffuse layer of competing ions in solution) has limitations, its benefits are reflected in the data by fitting the equilibrium sorption of ions in the oxide surfaces under different conditions in the solution as do more complex models.

The main objective of developing HFO database was to enable the formation of a larger database, which includes important oxide sorbents that are of interest in science and engineering, environmental protection. After publishing of HFO database in 1990, two-layer model and the methodology were used to develop a goethite base. The primary sources for updating the diffuse-Layer adsorption database are the reactions represented by Dzombak in 1990 [101]. This database contains numerous reactions that have already been given in the first database presented by Dzombak in 1986 [100], with some revised constants.

Visual MINTEQ

Equilibrium models which include surface complexation models are MINTEQ, SOILCHEM and HYDRAQL, while TRANQL, HYDROGEOCHEM and Jennings models are transporting models [99]. Simulation of ions distribution between adsorbed and dissolved phases in colloidal suspension can be done by surface complexation models contained in the Visual MINTEQ software package. Ions accumulation (pure electrostatic interactions) on the electrified surface is considered using ion exchange by Gaines-Thomas. MINTEQ package includes two models: the mathematical structure of MINEQL program [102] and thermodynamic database. Visual MINTEQ includes six different models of surface complexation [102]:

➢ *Constant Capacitance Model* (CCM);
➢ *Diffuse Layer Model* (DLM);
➢ *Triple Layer Model* (TLM);

➢ *Basic Stern Model* (BSM);

➢ *Three Plane Model* (TPM);

➢ *Non-Electrostatic Model* (NEM).

These six models have been linked in several ways. Each of these model views sorption as a reaction surface complexation and account surface electrostatic potential. The difference is in present of influence of electrostatic adsorption primarily. The database are define by Software package Visual MINTEQ [102]:

➢ HFO (ferrihydrite surface complexation reactions by the model 2-pK DLM);

➢ HMO (hydrated oxide of manganese surface complexation reactions by the model 2-pK DLM);

➢ Goethite (goethite surface complexation reactions by the model 1-pK TPM (CD-MUSIC));

➢ Gibbs-DLM (gibbsite surface complexation reactions by the model 2-pK DLM);

➢ FH-2 center (ferrihydrite surface complexation reactions by the model 1-pK TPM (CD-MUSIC));

➢ FH-3 center (ferrihydrite surface complexation reactions by the model 1-pK TPM (CD-MUSIC)). This database is different than the previous one because it defines one more location with different affinity.

2.3 Adsorption on iron oxide nanoparticles

Conventional adsorbents used in arsenic removal are activated carbons and alumina, soils, and resins, which can be coated with different materials like iron or alumina [103–106]. The major detriments of these techniques are difficult separation, waste formation and in many cases poor adsorption capacity [107]. However, because of the selectivity and affinity of Fe(III) toward inorganic arsenic species, Fe(III)-bearing materials are widely used in arsenic adsorption [108–111]. Nonetheless, significant challenges remain regarding post-treatment separation of adsorbent nanoparticles from treated water [112]. In particular, engineered nanomaterials such as titanium oxide nanoparticles, zerovalent iron nanoparticles, carbon nanotube, and iron oxide

nanoparticles are novel adsorbents because of greatly enhanced As removal efficiency at nanometer scale [112]. The popularity of these nanosized particles arises from their unique characteristics such as high surface area, interfacial reactivity, and magnetic properties. Within recent decade iron-based nanoparticles have been widely applied for arsenic removal from soils and aqueous surroundings [37,103,113]. The major iron oxides and oxide hydroxides are shown in Table 2.7.

Table 2. 7. The major iron oxides and oxide hydroxides [114]

Oxyhydroxides		Oxides	
Formula	Mineral	Formula	Mineral
α-FeOOH	Goethite	Fe_5HO_8 x $4H_2O$	Ferrihydrite
β-FeOOH	Akaganeite	α-Fe_2O_3	Hematite
γ-FeOOH	Lepidocrocite	β-Fe_2O_3	Maghemite
δ'-FeOOH	Feroxyhyte	Fe_3O_4	Magnetite

However, applicability of the iron nanoparticles is shown to suffer from their poor chemical stability and mechanical strength and tendency to aggregate. Furthermore, these nanoparticles as such are not suitable for fixed-bed column or flow-through systems due to for instance mass transport problems and significant pressure drops. To overcome the above drawbacks different solid supports have been used in order to prepare composite materials without losing the beneficial properties of the nanoparticles. Table 2.8. shows literature review of maximum adsorption capacity for As(V) removal of iron oxyhydroxide adsorbents.

Table 2. 8. Maximum adsorption capacity of some reported iron oxyhydroxide adsorbents used for As(V) removal

Adsorbents	q_m (mg g^{-1})	References
Goethite	7.24	[28]
Magnetite-doped activated carbon fiber	4.18	[115]
Magnetite decorated MWCNT	53.15	[116]
Hematite	0.20	[7]
Akaganeite	141.3	[7]
Sand, sulfate modified, iron oxide coated	0.13	[117]
Graphene oxide/ferric hydroxide composite	23.78	[7]
Iron(III) loaded chelatin resin	60	[7]
Iron oxide coated cement	6.43	[7]
FeCl-SW	12.85	[118]
FeNit-SW	6	[118]
Fe exchanged zeolite	0.1	[119]
Iron oxide coated multiwall carbon nanotubes	0.189	[120]
e-MWCNT/Fe^{2+}	23.47	[121]
e-MWCNT/Fe^{3+}	13.74	[121]
Quartz sand iron	0.8131	[122]
GAC iron	2.7524	[122]

2.3.1 Goethite

Goethite (α-FeOOH) is a widespread soil mineral and a major component of many ores, sediments and soils and it is one of the most thermodynamically stable iron oxide [123]. The orthorhombic structure of goethite has been confirmed as hexagonally close-packed array of O^{2-} and OH^- anions with Fe^{3+} in the center of the octahedral [123]. The two octahedrons compose double chains of octahedral formed by edge sharing, running parallel to the [001] direction. Figure 2.5. shows these chains are linked to adjacent double chains by corner-sharing with one chain and the OH groups are linked to another O atom in a chain diagonally opposite.
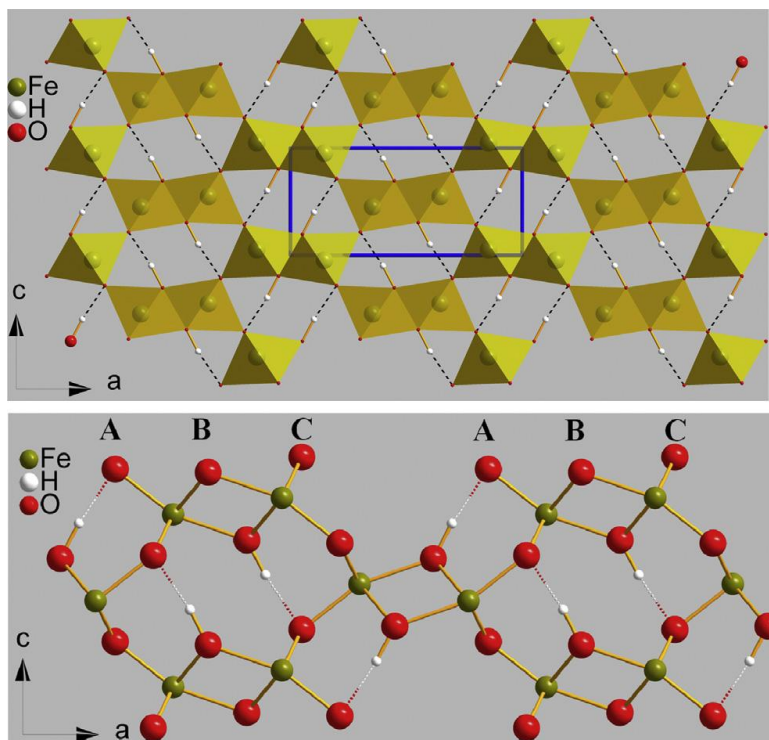
Figure 2.5. (010) plane of goethite (top) polyhedral framework and (bottom) ball and stick model (Blue line represents unit cell and the dash line denotes the hydrogen bonding) [124]

As is written in the book [125], the general formation process can be described as followed chemical equations:

$$2Fe_2SiO_4 + O_2 + 6H_2O = 4\alpha\text{-FeOOH} + 2H_4SiO_4 \tag{2.6}$$

$$4FeS_2 + 15O_2 + 10H_2O = 4\alpha\text{-FeOOH} + 8H_2SO_4 \tag{2.7}$$

Goethite formed from weathering is often poorly crystalline and rich in defects and impurities, which makes goethite has much good surface activity. Moreover, goethite displays nanometer sized particles in width and several microns in length for both naturally formed and the laboratory synthesized analog. Such sizes make goethite with a high specific surface area, varying from 10 to 132 $m^2\ g^{-1}$[126,127]. The wide spread in nature and special physicochemical properties attracted many attentions on the study of the structure, surface physiochemical properties and adsorption capacity of goethite, especially for anions, organic compounds, organic acids, cations and gases. List for inorganic anion adsorption on goethite is shown in Table 2.9.

Table 2. 9. List for inorganic anion adsorption on goethite [124]

Inorganic anions	References
Silicate	[128]
Selenite/Selenate	[129–132]
Phosphate	[133–149]
Fluoride	[150–152]
Chloride	[151]
Sulfate	[153]
Silicate	[152,154]
Arsenate/Arsenite/ Arsenic	[155]
Chromate	[156,157]
Carbonate	[148,158]

The adsorption of chromate and arsenate/arsenite is also widely investigated due to their toxicity to humans. Guo et al. [159] investigated mechanism of arsenic adsorption during mineral transformation from siderite to goethite. They synthesized siderite to remove As(III) and As(V) from water solutions under anoxic conditions and oxic conditions. Results showed that As adsorption on synthetic siderite under anoxic conditions was around 10 mg/g calculated with Langmuir isotherm. However, the calculated As adsorption on synthetic siderite under oxic conditions ranged between 115 and 121 mg g^{-1}, which was around 11 times higher than that under anoxic conditions. They found that 75% siderite was transformed into goethite during oxic adsorption. However, synthetic goethite had lower As adsorption capacity than siderite under oxic conditions, although its adsorption capacity was a little higher than siderite under anoxic conditions. It suggested that the coexistence of goethite and siderite bimineral during mineral transformation probably contributed to the robust adsorption capacity of siderite under oxic conditions. Results of extended X-ray absorption fine structure (EXAF) spectroscopy indicated both As(III) and As(V) formed inner-sphere complexes on the surface of As-treated solid regardless of substrates, including the bidentate binuclear corner-sharing (2C) complexes and the monodentate mononuclear corner-sharing (1V) complexes. Monodenate (1V) and bidentate (2C) complexes would be related to high As adsorption capacity of siderite under oxic conditions. It showed that more Fe atoms were coordinated with As atom in the monodentate complexes and the bidentate complexes of As(V)/As(III)-treated siderite under oxic conditions, in comparison with As(V)/As(III)-treated siderite under anoxic conditions and As(V)/As(III)-treated goethite. Calcinations of natural siderite resulting in the coexistence of goethite and siderite greatly

53

increased As adsorption on the solid, which confirmed that the coexistence of bimineral during mineral transformation from siderite to goethite greatly enhanced As adsorption capacity of siderite adsorbent. The observation can be applied for modification of natural siderite for As removal from high As waters.
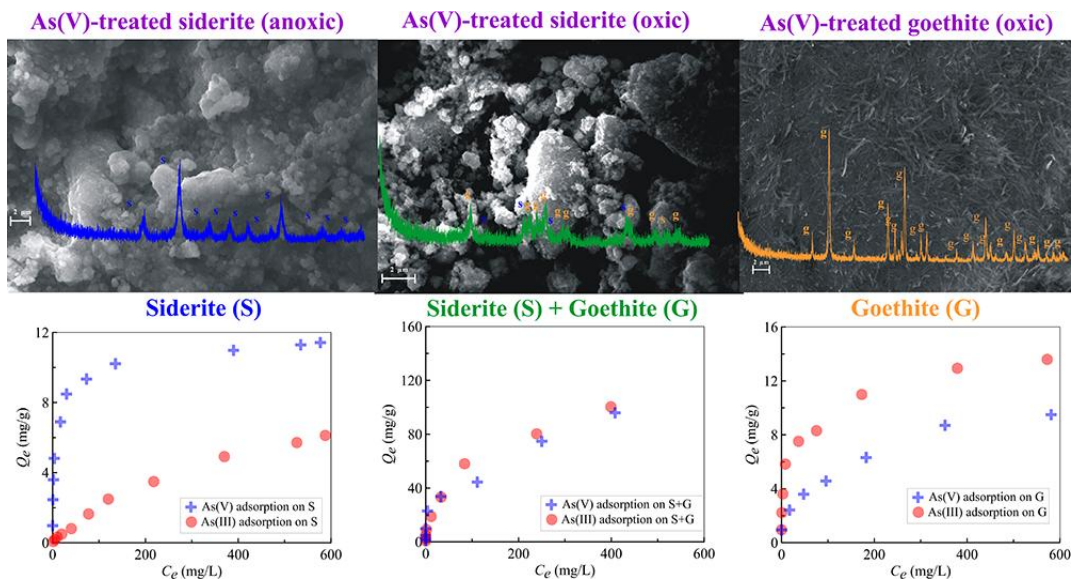
Figure 2. 6. SEM images, XRD spectra and Langmuir adsorption isotherm of As(V)-treated siderite under anoxic condition and oxic conditions, and As(V)-treated goethite under oxic conditions [159]

2.3.2 Magnetite

Magnetite, Fe_3O_4, contains Fe(II) as well as Fe(III) in its structure. It is, therefore, not thermodynamically stable at atmospheric O_2 pressure. Magnetite is an inverse spinel: the tetrahedral positions are completely occupied by Fe(III), the octahedral ones by equal amounts of Fe(III) and Fe(II). For sufficiently large crystals, such as those of magnetites in rocks, the rate of oxidation by the atmosphere is, however, slow enough so that no protection against oxidation is needed. Synthetic, low temperature magnetite crystals are, on the other hand, often very small (< 100 nm) and may, if not protected against atmospheric oxygen, oxidise either during synthesis or thereafter. There are two basic ways to produce magnetite only the first of which is described here in detail:

➢ by partial oxidation of a Fe(II) salt solution with KNO_3 under alkaline conditions at 90 °C, and

➢ by precipitation of a mixed Fe(II)/Fe(III) solution with a Fe(II)/Fe(III) ratio of 0.5 or of 10

Because superparamagnetic properties, magnetite nanoparticles (MNPs) can be easily separated from aqueous solution with a low external magnetic field, there has been growing interest in As removal by MNPs [160]. This is particularly well-suited for applications in water treatment facilities or in situ groundwater remediation. To better develop the magnetite-based As removal technique, more fundamental knowledge of both macroscopic and microscopic aspects of As adsorption by MNPs is needed. Over the last several years, macroscopic adsorption studies have provided valuable insight on the effects of adsorbent particle size, solution pH and ionic strength on As adsorption by MNPs. However, convincing and indisputable evidence on the molecular mechanism of As adsorption by magnetite has been sparse with conflicting reports in the literature [161,162].

Jönsson et al. [162] investigated sorption of As(III) and As(V) to siderite, green rust (fougerite) and magnetite. They have founded that As(V) sorbs to fougerite, magnetite, and siderite by forming inner-sphere surface complexes resulting from corner sharing between AsO_4 groups and FeO_6 octahedra. No evidence of As(V) reduction is found. As(III) also forms inner-sphere surface complexes on magnetite and fougerite but only a (presumably) weak outer-sphere complex on siderite. As(V) desorbs from magnetite, fougerite and siderite at pH>8; however, As(III) sorption to all three phases is enhanced with increasing pH. Hence, dissimilatory reduction of iron oxides, followed by precipitation of fougerite, magnetite or siderite will released dissolved As(V) at pH>8; however, if As(V) is also reduced to As (III), sorption of As will be enhanced. The equilibrium stability fields for arsenic species and iron phases when $pCO_2=10–3.5$ bar and total Fe $=1×10–5$ mol/L is shown on Figure 2.7. The dashed line is the boundary between goethite and metastable GR1 is evaluated based on the thermodynamic data. The stability field of symplesite is unknown. Thermodynamic data for scorodite ($FeAsO_4x$ $2H_2O$) place it outside the stability field of GR1, magnetite and siderite.
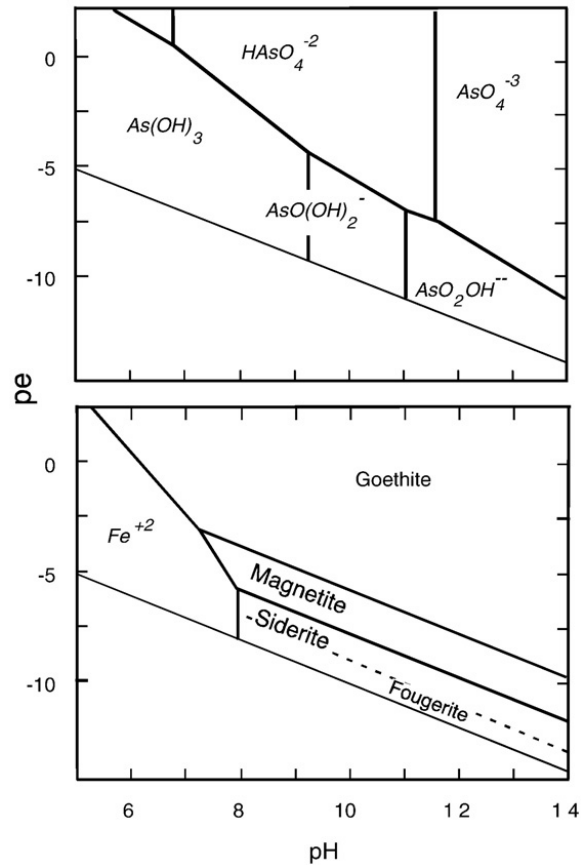
Figure 2.7. p_e-pH diagrams showing the equilibrium stability fields for arsenic species and iron phases [162]

2.4. Macroporous adsorbent

2.4.1. Suspension polymerization processes

Suspension polymerization (SP) is used for the commercial manufacture of many important polymers including poly(vinyl chloride), poly(methyl methacrylate), expandable polystyrene, styrene-acrylonitrile copolymers and a variety of ion exchange resins. In suspension polymerization, drops of a monomer containing phase are dispersed in a continuous liquid phase and polymer is produced inside the drops. In many cases, the monomer contains no diluent and the chemical reactions that occur inside the drops are very similar to those found in bulk polymerization.

In most suspensions, polymer is formed by a chain reaction mechanism that includes the following steps:

Initiation:

$$I \rightarrow 2A* \tag{2.8}$$

$$A* + M \rightarrow AM* \tag{2.9}$$

Propagation:

$$AMn* + M \rightarrow AMn+1* \tag{2.10}$$

Termination:

$$AMn* + AMm* \rightarrow AMn+mA \tag{2.11}$$

$$AMn* + AMm* \rightarrow AMn + AMm \tag{2.12}$$

Transfer:

$$AMn* + T \rightarrow AMn + T* \tag{2.13}$$
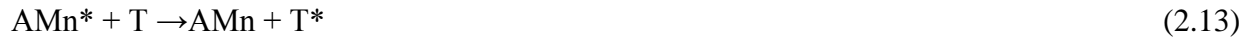
Here, M is the monomer and A* could be an anion, a cation or a free radical. In most industrial processes M is a vinyl compound and a free-radical chain mechanism is used. Then, the growing polymer chains, AMn*, are written as $AMn^{\bullet}$. That species has a short lifetime (usually << 1 sec) and completed polymer molecules are formed throughout the process. The generation of radicals, $A^{\bullet}$, is usually induced by thermal decomposition of an organic initiator, I, that is soluble in the monomer. Organic peroxides are often used as initiators. T represents any species that reacts as a chain transfer agent. T can be monomer, polymer, a solvent or a species that is added specifically to function as a chain transfer agent. If T* is sufficiently active, it can behave as A* and initiate a new polymer chain. In some cases, such as the polymerization of vinyl chloride, chain transfer to monomer is significant and it has a major effect on the average molecular weight of the polymer. Suspension polymerization has been reviewed previously by Yuan et al.[163], Vivaldo-Lima et al.[164], and Arshady[165].

In most industrial suspension polymerization agitated batch (or semibatch) reactors are used and the continuous phase is aqueous. That is advantageous because the process is often exothermic and good heat transfer from the reactor is required. The ratio of surface area to volume is relatively high for small drops, so that the rate of heat transfer to the aqueous phase is high. Although drop viscosity may increase substantially, the overall viscosity of the suspension is usually much lower than that encountered in the equivalent bulk polymerization.

57

Consequently, agitation of the reactor contents is possible and heat transfer through the aqueous phase to the reactor wall is good. Also, high conversions of monomer to polymer can be achieved inside the drops whereas in bulk polymerization increasing viscosity of the polymer-monomer solution often limits the extent of monomer conversion. In suspension polymerization, the final conversion can be increased by including a second initiator which is activated by a late temperature increase; also, a second initiator may be added (as a *finishing catalyst*) near the end of the polymerization. Residual monomer can sometimes be removed by spraying the polymer dispersion (at conditions chosen to promote monomer release) or by putting the dispersion in contact with an appropriate ion exchange resin [166].

Suspension polymerization is particularly useful when the final polymer is required to be in the form of small *beads* (which often have the same size distribution as the drops from which they are formed). However, product contamination can be a problem if the drop stabilizers cannot be removed. Suspension polymerization usually requires larger reactor volumes than bulk processes because the vessels are usually half full with water.

The attainment of high monomer conversion can affect the reaction kinetics. From the reaction scheme shown above, it can be seen [167] that the rate of homogeneous polymerization is given by the expression:

$$R_p = k_p C_M \left(\frac{2 f k_d C_I}{k_t} \right) \tag{2.14}$$

where, C_I is the concentration of the initiator and C_M is the monomer concentration. Here, k_p is the propagation rate coefficient, k_d is the initiator decomposition rate coefficient and f is an efficiency factor. In eq. (2.14), the overall chain termination rate coefficient, k_t, is derived from the rate coefficients of the two chain termination steps shown in the above reaction scheme. At high polymer concentrations, chain termination is often diffusion-controlled and the value of k_t diminishes substantially. Radical diffusion can depend on solution viscosity, polymer volume fraction and polymer molecular weight. The latter three entities are interrelated in complicated ways [168] but the effects of viscosity on the polymerization rate can be distinguished from the effects of polymer volume fraction [169]. The value of f may depend on the polymer content [170] and the value of k_p may also decrease [171]. From eq. (2.14), it can be seen that the

58

reduction in k_t leads to an increase in polymerization rate, a phenomenon often described as a *gel effect*.

2.4.2. Suspending agents

If an inadequate amount of a drop stabilizer was used, the suspension would be unstable and the monomer/polymer drops would coalesce and become large. Water-miscible polymers, both naturally occurring and synthetic, are often used as drop stabilizers. When partially hydrolyzed polyvinyl acetate (PVA) is used as a stabilizer, its behavior depends on the extent to which the acetate groups are hydrolyzed [172]. Good drop stabilization can be achieved in aqueous media when the degree of hydrolysis (DH) is between 70 and 80 %; then, drops can retain their integrity even when agitation levels are reduced. Although organic substances are commonly used as drop stabilizers, finely divided particulate inorganic solids can be used to stabilize the monomer drops in aqueous suspension by the Pickering effect [173].

2.4.3. Suspension copolymerization

Functional groups can be introduced through copolymerization with appropriate monomers [174] but control and prediction of copolymer compositions in suspension polymerization can be difficult if one, or more, of the monomers is partially soluble in the continuous phase. Then, the actual monomer concentrations in the drops may be unknown, so that idealized relationships for predicting copolymer compositions, which apply to homogeneous systems, are of little use unless appropriate partition coefficients for the two phases are available. Apparent reactivity ratios, obtained directly from suspension polymerization experiments will be different from those expected for the equivalent bulk processes if some monomer migrates to the continuous phase [175]. In some cases, when the continuous phase is aqueous, models that allow for water solubility of monomers have been developed [168].

2.4.4. Drop formation and stability [176]

Control of drop size distribution in suspension polymerization can be important. In many cases, the average drop diameters (and final average particles sizes) lie between 10 and 100 μm, but larger diameters might be produced if the polymer particles are to be used directly as beads [177]. The physical conditions in a suspension polymerization reactor affect the drop size distribution significantly. Drop breakage in agitated suspensions can be caused either by frictional forces (through viscous shear) or by inertial forces (through turbulence). In industrial suspension polymerization, the volume fraction of the dispersed phase is usually high and drop breakup is accompanied by drop coalescence. Thus, the average drop size and the drop size distribution are both influenced by drop breakage and drop coalescence[176].

2.4.5. Drop mixing [176]

To maintain product quality, it is sometimes important to ensure that all the polymer particles have the same chemical composition when suspension polymerization ends. Undesirable drift in copolymer composition may be avoided by adding one of the monomers to the reactor incrementally. That procedure will only be effective if the added monomer mixes quickly and uniformly with the existing drops. But, in some cases, rapid mixing of the dispersed phases does not occur and the added monomer can remain segregated from the existing drops for a significant period of time. Any new drops that are formed, will have a monomer composition that differs from that of the original drops. The new drops will also be unstable because the existing drops will have adsorbed most of the drop stabilizer. Adding extra drop stabilizer in order to stabilize new drops will reduce drop mixing rates further and hinder the transfer of radical generator from the "older" drops to the newer drops. Therefore, the polymerization rate is expected to be low in the new drops. A mixing problem can arise even when the concentration of radical generator is initially the same in all the monomer drops. Most of the vinyl monomers used in suspension polymerization have a high enthalpy of polymerization (often between 30 and 90 kJ mol^{-1}) and heat removal from large reactors can be difficult. Heat transfer through the reactor walls can be inadequate because large reactors have a relatively small surface/volume

ratio. Heat removal rates can be increased by allowing the monomer to vaporize and then condensing the vapor outside the reactor. If new drops from the returning monomer are to be stabilized, they must obtain sufficient drop stabilizer. Also, polymerization will only occur in new drops if they acquire some radical generator. In the suspension polymerization of vinyl chloride, monomer returning from a reflux condenser formed new drops that acquired initiator without coalescing with existing stabilized drops. In that case, the mechanism for initiator transfer through the continuous phase appeared to involve new small particles that were formed by simultaneous emulsion polymerization, so that the drop size distribution became bimodal [178]. Vinyl chloride is a very reactive monomer with a high enthalpy of polymerization.

Therefore, initiator is usually dispersed in the aqueous phase (and not predissolved in the monomer) to avoid premature polymerization. Subsequent mixing of monomer and initiator is found to be slow and many monomer drops can remain uninitiated even when monomer in other drops has polymerized to a considerable extent [178]. Transfer of initiator through the aqueous phase probably accounts for the simultaneous emulsion polymerization mentioned above. These phenomena lead to a non-uniformity in the drops (and particles) that can affect the final polymer properties. Some desirable properties of poly(vinil chloride) (PVC) are obtained by mixing the polymer with particulate additives. Effective incorporation of these additives might be achieved by premixing them with vinyl chloride before polymerization. Examining that possibility showed that the presence of the inorganic particles influences the properties of the monomer phase and affects the drop size distribution [178]. The extent of these changes dependson the particle size of the additive.

2.4.6. Particle structure

Polymers obtained from suspension polymerization are often recovered and processed in bulk form. But, in some cases, they are used directly as beads. Then, the internal bead structure can be important. If the beads are to be used for ion-exchange applications, the beads may need to be porous. Bead porosity can be introduced by using an inert *porogen* that is mixedwith the monomer before polymerization and then removed after polymerization [179]. Copolymerization of styrene (or functionalized styrene) with divinyl benzene can provide cross-linked beads and

their porosity can be controlled by using appropriate amounts of a porogen. However, the bead size distribution obtained from suspension polymerization isoften broad; that is a disadvantage if the beads are to be used in packed columns because it leads to high pressure drops. Narrower bead size distributions can sometimes be obtained by using template particles made of linear polymers. These particles, which can have a narrow size distribution, are swollen with the monomer mixture and the linear polymer is removedafter polymerization. In the manufacture of ion-exchange resins, porosity is enhanced by the phase separation that occurs during crosslinking. But, in vinyl chloride polymerization, phase separation is inherent because vinyl chloride monomer (VCM) and PVC are almost immiscible and the polymer structure is affected by coagulation of primary polymer particles inside the drops [180]. In that case, particle porosity facilitates the subsequent uptake of plasticizers by the PVC. If monomer reflux is used to aid heat transfer from the reactor, then, at low conversion, PVC porosity increases when the monomer reflux rate is high [181]. Suspension polymerization can also be used to make particles with a core-shell structure.

2.4.7. Aqueous monomer drops [176]

In some commercial suspension processes, water-miscible polymers are produced in aqueous monomer drops that are dispersed in a nonaqueous continuous phase (often a hydrocarbon). If the drops are very small, such a process is sometimes called *inverse emulsion polymerization*, but that is a misnomer because the initiator is usually located in the aqueous drops and the polymerization mechanism is different from that found in conventional emulsion polymerization. Although inorganic persulfates can be used as radical generators, redox initiators are sometimes preferred because they produce free radicals at relatively low temperatures. Then, at least one of the redox components is segregated from the monomer while the suspension is being formed. Otherwise, polymerization would begin prematurely. Aqueous reductant can be added to a dispersion of aqueous monomer drops that already contain an aqueous oxidant. Polymerization will begin when the two types of aqueous drops become mixed. Often, drops of an aqueous solution of monomer and oxidant are initially dispersed in the continuous phase which contains an oil-miscible suspending agent. Then, aqueous reductant is added to start the

reaction. The two types of aqueous drops, that are initially present, must become mixed before polymerization can begin. The drop mixing rate and viscosity changes inside the monomer dropscan be interdependent. In these *inverse* processes, the final particle size distributionscan be wide. That might be a disadvantage for some product applications but improved control of the size distributions can be achieved by using an oscillatory baffled reactor [182].

2.4.8. Macroporous adsorption resin (MAR)

Macroporous adsorption resins were first developed in the 1960s. These materials are porous polymeric spherical beads with a variety of surface polarities, surface areas and pore-size distributions. They are capable of effectively adsorbing organic molecules from aqueous solutions due to their highly porous polymeric structures with internal surfaces. The organic molecules are desorbed from the resin by solvent elution and may be recovered for use. The resin can be tailor made to selectively adsorb certain groups of organic molecules by varying surface polarity and pores structures such as surface areas and average pore-size distributions during manufacturing processes [183].

The synthesis of macroporous adsorption resins is based on manufacturing technology of ion-exchange resins. They are synthesized by suspension copolymerization of a monomer e.g. styrene, acrylate and a cross linking agent, *e.g.* divinylbenzene. Polymerization takes place in the presence of a pore-forming agent which is soluble in monomer mixture but itself is a poor solvent to the copolymer. The pore-forming agent is removed from the polymeric network after polymerization and a porous structure with mechanical stability is left. The resin structure is modified by varying polymerization conditions such as the amounts of monomers and pore-forming agents used in the polymerization reaction [184]. Such made macroporous resins are white, milky white or pale yellow spherical beads with 20-60 mesh in sizes. They are polymeric adsorbents with excellent physical,chemical and thermal stability. They can work under 150 °C and their stability are found in wide pH range. Their water content is around 40% to 70% [185].

The resins are mainly divided into three types − non-polar resins, medium polar resins and polar resins. For non-polar resins, they usually exhibit non-polar or hydrophobic behavior and so adsorb non-polar organic molecules from polar solvents such as water. For polar resins,

they usually exhibit polar or hydrophilic behavior and adsorb organic molecules with some degree of polarity from non-polar solvents such as hydrocarbons. For medium polar resins, they exhibit both hydrophobic and hydrophilic behaviors. In addition to polarity, the resins can be classified into different types according to their average pore sizes distribution and surface areas[185]. Most commercially available resins always contain non-reacted monomers, pore-forming agents and cross-linking agents remaining trapped within the pore structure after polymerization. These organic residues must be removed before use as they are toxic and affect the adsorption capacity of the resins. A common pretreatment method is to extract the resins by absolute ethanol for 8 hours in a Soxlet apparatus and then dry the resins under vacuum at 325K for 3 hours before use [185]. The resin will decrease its adsorption capacity or may be contaminated after a period of using. Thus, the resin needs regeneration. The method is to add 3%-5% hydrochloric acid to a level 10 cm above the resin layer in the column and immersed it for 2-4 hours. The resin is then rinsed by 3-4 bed volumes of hydrochloric acid and by distilled water until the pH of the effluent becomes neutral. Then 3%-5% sodium hydroxide is added to immerse the resin for 4 hours. After that, the resin is rinsed by 3-4 bed volumes of sodium hydroxide and finally by distilled water until pH of the effluent becomes neutral [185].

Adsorption mechanism[186]

Adsorption of organic molecules by macroporous resins is attributed to two types of molecular interactions including van der Waals forces and hydrogen bonding. Both of them are electrostatic attraction between dipoles, *i.e.* the attraction between the positive end of one molecule and the negative end of another molecule. There are three types of dipoles – permanent dipole, instantaneous dipole and induced dipole. Permanent dipole exists in all polar molecules as a result of the difference in the electronegativity of bonded atoms. Instantaneous dipole is a temporary dipole that exists as a result of fluctuation in the electron cloud. Induced dipole is a temporary dipole that is created due to the influence of a neighbouring dipole (which may be a permanent or an instantaneous dipole). Van der Waals force is a general term. It consists of two types of intermolecular attractions – dispersion forces (also known as London forces) and dipole-dipole attractions. The origin of van der Waals dispersion forces is temporary fluctuating dipoles.

64

This dispersion forces exist in all molecules. Attractions are electrical in nature. In a symmetrical molecule like hydrogen, it seems that no electrical distortion to produce positive or negative parts. But it is only true on average. The electron cloud distribution is generally symmetrical around the nucleus. However, theelectrons are mobile. As the instant mobility of the electron cloud, its position fluctuates all the time. At any particular instant, it is likely to be concentrated on oneend of the molecules, making that end slightly negative. The other end will be temporarily shortage of electron and so becomes slightly positive. Thus the molecule possesses an electric dipole (a polarity) at that particular instant. An instant later the electrons may move to the other end, reversing the polarity of the molecule a molecule with a temporary polaritya molecule without any polarity.When the right hand molecule which is entirely non-polar at that moment approaches, its electrons will tend to be attracted by the slightly positive end of the left hand one which has a temporary polarity (instantaneous dipole). This sets up an induced dipole in the approaching molecule,which is orientated in such a way that the δ + end of one is attracted to the δ– end of the other. Then, the two molecules interact with each other. Thus, the intermolecular attractions are created by these temporary dipoles.

Synthesis

As mentioned above, this review covers the topic of suspension polymerization as the main synthetic approach for preparing porous copolymer resin (PCR) materials. A schematic representation of this polymerization technique was described previously (Figure 2.8.) [187].
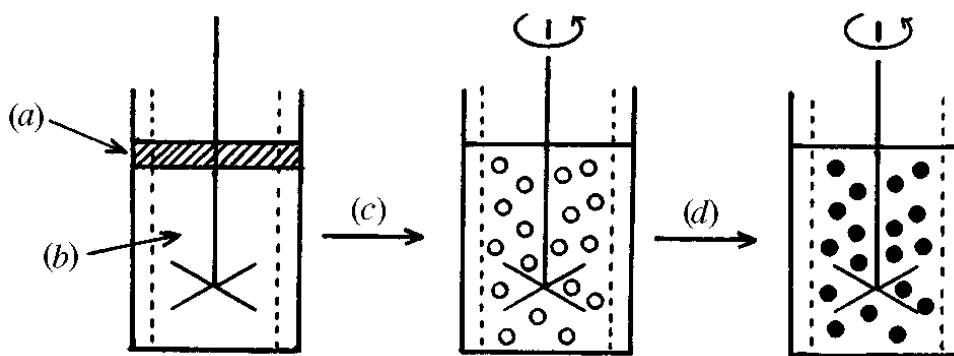
Figure 2. 8. Schematic representation of suspension polymerisation: (*a*) organic comonomer mixture (with porogen) containing dissolved initiator; (*b*) aqueous continuous phase containing dissolved polymeric suspension stabiliser; (*c*) shearing to form comonomer liquid droplets; (*d*) thermal polymerisation to form solid polymer resin beads[187].

In general, there is an organic phase (also referred to as the discontinuous phase) comprised of predetermined amounts of monomer(s), initiator, and solvent(s) which are added into an aqueous phase, and is also referred to as the continuous phase. The mixture is comprised of a suspension stabilizer in water in a reactor vessel at ~60–70 °C with mechanical stirring at a suitable speed for a desired particle size. The reaction is maintained ~80 °C for 3–24 hours and the resulting spherical particles are washed with water, ethanol, or methanol, and extracted with a suitable solvent such as acetone for 24–48 hours [187]. A commonly used polymerization initiator agent is α,α'-azo-*bis*-isobutyronitrile (AIBN).

Porosimetry

According to the International Union of Pure and Applied Chemistry (IUPAC), pores are classified into three categories according to their pore size: micropores (less than 2 nm), mesopores (2 to 50 nm), and macropores (larger than 50 nm). In the solid state, nitrogen porosimetry [188–190] is used to characterize micro- and mesopores in terms of specific surface area. The determination of the mesopore and macropore characteristics is evaluated on the basis of pore-volume and pore-volume distribution using mercury intrusion porosimetry [188,189].

Microscopy

Many studies have examined the use of scanning electron microscopy (SEM), transmission electron microscopy (TEM), and atomic force microscopy (AFM) to identify the morphology and texture of the polymers [190–192].

Solubility parameter

Research concerning PCR materials utilizes the SP as a relative measure of "good" or "bad" solvents, according to the solvating ability of a diluent. There are three types of SP values that are commonly used, *i.e.*, the one-component HSP (the Hildebrand solubility parameter), a two-component solubility (physical-chemical) parameter, and Hansen's three-component HSP value [193,194].

The HSP (δ) of the porogen and the polymer, respectively, are defined as shown in Equation (2.15) below:

$$\delta = \sqrt{C} = \sqrt{\frac{\Delta H - RT}{V_m}}$$ (2.15)

where C is the cohesive energy density, ΔH is the heat of vaporization, R is the gas constant, T is thetemperature, and V_m is the molar volume of the solvent. The SI unit for δ is MPa$^{1/2}$ while the conventional unit is (Jcm^{-3})$^{1/2}$. The closer the match between the porogen and the polymer implies a "good" solvent since solvents with similar HSP values are generally miscible. In other words, if ($|\Delta\delta|$) is near zero (where $|\Delta\delta| = |\delta$resin- δsolvent|), then miscibility is favored. In cases where $|\Delta\delta| > 3$ MPa$^{1/2}$, the solvent is considered "bad" for values between 1-3 MPa$^{1/2}$, the solvent possesses intermediate solubility and is considered "good" and "bad". However, this criterion has some exceptions when the resin and diluent are both polar or have specific polar-directional group interactions. Therefore, an extension to Hildebrand's theory was proposed by Hansen [194] where the SP was divided into three contributions, *i.e.*, dispersion forces (δ_d), dipolar interactions (δ_p) and H-bond capacity (δ_h), as shownin Equation (2.16).

$$\delta_T = \sqrt{\left(\delta_d^2 + \delta_p^2 + \delta_h^2\right)}$$ (2.16)

The above three-dimensional HSP (δ_T) is assumed to be a vector sum where the three components are treated as solubility coordinates. Hansen reported resin solubility values using a three-dimensional model and concluded that doubling of the dispersion forces (δ_d), a spherical volume of solubility would be formed for each resin.

Pore formation mechanism [187]

In order to have an improved understanding of the research describing the influence of solvents as porogens, the mechanism will be described in further detail. The general aspects of the mechanism are described in Figure 2.9. As the suspension polymerization process proceeds, the copolymer precipitates within emulsion droplets and forms spherical shapes, referred to as insoluble nuclei. The droplets form due to the relative difference in SP between the copolymer and the solvent ($|\Delta\delta|$). The nuclei transform into microspheres or microgel phases, and the microspheres agglomerate with each other to form a primary network. Upon further

polymerization, the primary network becomes a crosslinked porous network. The phase containing solvent strongly contracts in volume due to the loss of solvating co-monomers; thereafter, network formation and phase separation occurs. As the porogen is removed, the void spaces that remain are referred to as the pores in the polymer network. The pore sizes depend on the solvating ability of the porogen. If the porogen is a solvating diluent, *i.e.*, where $|\Delta\delta|$ is close to zero, the polymer chains remain dissolved in the mixture for a longer time prior to phase separation. As the microsphere particles undergo aggregation, they are likely to retain their microparticle nature; thereafter, resulting in smaller pores. As the value for $|\Delta\delta|$ becomes larger for a given porogen, the microsphere fails to retain its individuality and undergoes aggregation into larger clusters.
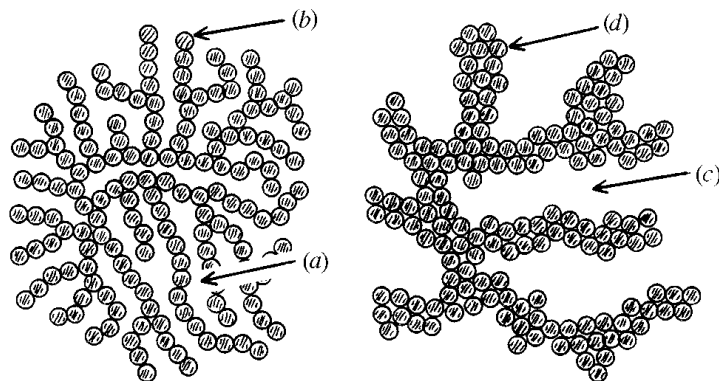
Figure 2.9. Connectivity of microgel particles showing formation of small pores (*a*) from a network of interconnecting individual microgel particles (*b*) and large pores (*c*) from a network of fused or aggregated microgel particles (*d*)[187]

Influence of the solvent (Porogen)

Pure Solvents

Research results on the influence of pure solvents as porogens for different resins are summarized in Table 2.10 [195]. Table 2.10 illustrates how the surface area varies in accordance with the use of different porogens. Additionally, the results show how a similar class of resins may be tuned to form micro-, meso- and macropores [196,197]. As mentioned above, solvents that act as solvating diluents may generate micropores; thereby, increasing the polymer surface area. For example, the results from reference [16] in Table2.10 show that toluene is a solvating diluent and cyclohexanone is a non-solvating diluent. 2-Ethylhexanol is an intermediate case

between solvating and non-solvating diluent. The results were explained by the trend for the HSP values; toluene (18.2 MPa$^{1/2}$), 2-ethylhexanoic acid (19.4 MPa$^{1/2}$), and cyclohexanone (20.3 MPa$^{1/2}$); whereas, the resin is ~17–18 MPa$^{1/2}$.

According to the HSP values, toluene has a closer match to the resin, and this is based on the one-component HSP using Hildebrand solubility parameters. However, this criterion has a fault which is illustrated in Table 2.10. [189,198–200]. The authors argue that 1-chlorodecane is a non-solvating diluent for the resin and it yields a greater surface area over the solvating diluents, demonstrating its use as a novelporogen. However, if one looks at the SP value of the solvents investigated, one observes a variation in the HSP values; heptane (15.3), cyclohexane (16.8), 1-chlorodecane (17.0), toluene (18.2), and dibutyl phthalate (23.3 MPa$^{1/2}$). The use of a one-component HSP criterion to explain the results, *i.e.*, if $|\Delta\delta| \sim 0$, the solvent is the solvating diluent and 1-chlorodecane should not have the greatest surface area. Cyclohexanol should have a surface area <25 m^{2}g^{-1} when compared to the results from [190].

Table 2. 10. Surface area (from nitrogen porosimetry), pore-volume, pore-size and average pore diameter of PCR synthesized in presence of different types of solvent porogens[195]

Polymer type	Porogen	Surface area, $m^2 g^{-1}$	Pore volume, mLg^{-1}	Porosity, %	Avarage pore diametre, nm
Poly(stirene-*co*-divinylbenzene)-1:3	Cycloxeanone	25	0.22	Non-measured (NM)	Non-detected (ND)
	2-ethylhexanol	242	1.13		20-45
	Toluene	599	0.44		<4
Glycidyl methacrylate-*co*-trimethylolpropane trimethacrylate - 1:1	Octan-2-one	174	1.31	NM	10-100
	n-butyl acetate	170	1.27		
	p-xylene	139	1.50		
	Toluene	145	1.02		
	Ethyl acetate	110	0.66		
	Benzonitrile	<1	0.07		
	Cyclohexanone	0.2	0.16		
	Dodecan-1-ol	ND	ND		
Poly(hydroxyethyl methacrylate-*co*-ethylene glycol dimethacrylate)- 1:20	Cycloxeanol	250	0.369	NM	6.3
	Dodecanol	28	0.06		5.6
Poly(divinyl benzene); Mixtures of isomers	Heptane	482	NM	45.3[a]	6.9[a]
				69.0[b]	86.8[b]
	Cycloxeane	640	NM	37.9[a]	3.8[a]
				47.7[b]	72.4[b]
	1-chlordecane	720	NM	56.3[a]	7.2[a]
				66.7[b]	53.4[b]
	Toluene	701	NM	35.6[a]	3.2[a]
				50.5[b]	68.1[b]
	Dibutyl phthalate	661	NM	37.1[a]	3.6[a]
				64.8[b]	60.2[b]
	Cycloxeanol	493	NM	29.1[a]	3.3[a]
				47.6[b]	77.8[b]

[a] Nitrogen porosimetry; [b]Mercury porosimetry

2.5 Cellulose

Nowadays, nanotechnology is recognized as one of the most promising areas for technological development. In line with the development of nanotechnology and recent concern about environmental issues, it has been paid more attention to utilizing biobased materials. In this regard, natural fibers have been gaining much more interest because of their promising characteristics such as biodegradable nature, renewability and lower price. Among these natural fibers, cellulose as the most plentiful biopolymer which exists in a wide variety of living species including plants, bacteria and some animal species like tunicates, has been the subject of extensive research in nanotechnology [201]. The impressive mechanical properties, reinforcing capabilities, abundance, low density, and biodegradability of these nanoparticles make them ideal candidates for the processing of polymer nanocomposites. With a Young's modulus in the range 100–130 GPa and a surface area of several hundred m^2 g^{-1}, new promising properties can be considered for cellulose [201].

However, the chemical structure of cellulose was described recently by the French chemist Payen [201]. Cellulose is a linear homopolymer formed by repeating β(1-4)-bound D-glucopyranose units with a degree of polymerisation of 10 000 to 15 000, depending on the source (Figure 2.10.). Intrachain hydrogen bonds between the hydroxyl groups and oxygen atoms of neighbouring ring molecules stabilise the cellulose chain and are responsible for the linear structure of the polymer chain.
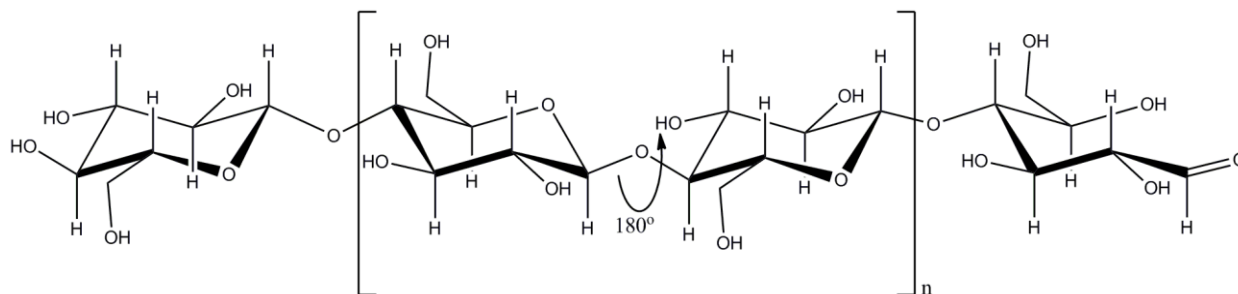
Figure 2.10. Chemical structure of cellulose[202]

71

Each *β*-D-glucopyranose units has three hydroxyl groups on C-2, C-3, and C-6 position making cellulose a hydrophilic polymer. Terminal groups on cellulose chains are chemically different. On one end the C-1 OH is an aldehyde and has reducing power and it is therefore called the reducing end. On the other end the C-4 OH is an alcohol and thus it is called the non-reducing end [201]. Cellulose presents a complex hierarchical structure: linear cellulose chains aggregate to form elementary fibrils and these aggregate into microfibrils which in turn form larger macroscopic cellulose fibres which, combined with hemicellulose and lignin, form the cell walls of wood and higher plants (Figure 2.11.). Extensive hydrogen-bond networks play an important role in the organisation of the hierarchical structure, and increase the stiffness of the cellulose fibrils [201].
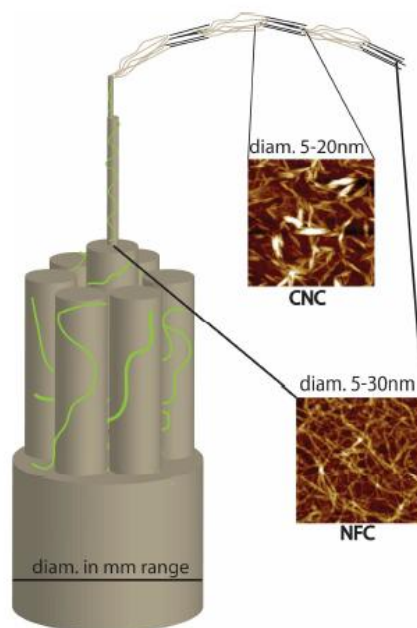
Figure 2. 11. A schematic illustration of the hierarchy in macroscopic cellulose fibers [202]

There are regions in the cellulose fibrils where the cellulose chains are arranged in a highly ordered structure (crystalline regions) and regions where the chains are disordered (amorphous regions). Cellulose can exist in six different polymorphs; I, II, III_I, III_{II}, IV_I, and IV_{II}. In nature cellulose is found in the cellulose I polymorph structure where the chains are packed parallel-up and edge-to-edge *via* extensive intra- and intermolecular hydrogen bonding to form sheet-like structures which form fibril structures. Cellulose I exists in two

crystalline forms, cellulose Iα and cellulose Iβ, which have different hydrogen bonding networks[202]. The two forms coexist in cellulosic materials but the ratio varies depending on the source. Cellulose Iβ is predominant in higher plants and cellulose Iα in bacteria and tunicate. In the fibrils the crystalline parts are accompanied with less structured amorphous-like regions. The ratio of crystalline-to-amorphous cellulose also varies depending on the source of cellulose. In wood, cellulose is found in the cell wall structures where it is hierarchically packed to form large fibers [202]. These fibers are formed by the stacking of cellulose chains to nanosized elemental fibrils with crystalline and less ordered amorphous parts. These in turn pack into larger nanofibrils that further pack into micron sized and microscopic fibers (Figure 2.11.). In wood cell wall hemicellulose, pectin, and lignin together with cellulose fibrils form a complex bio-composite that offers mechanical support to the tree and pro-tects the tree against environmental factors such as changing climate and pathogens[202].

2.5.1 Nanocellulose

Recently, methods combining chemical, mechanical and enzymatic treatments to disintegrate wood fibers to produce nanocellulose (NC) have been developed [203–211]. Depending on the treatment fibrils with a diameter of 5-30 nm and length in micrometers, or rod-like crystals with a diameter of 5-20 nm and length of tens to hundreds of nanometers to micrometers can be obtained. The fibril/crystal dimensions depend strongly on the treatment and the source. Cellulose fibrils or crystallites with at least one dimension on a nanoscale are termed nanocellulose [201]. Nanocellulose not only possesses the properties of cellulose, such as mechanical strength, good potential for chemical modification and biocompatibility, but it also has nanoscale characteristics like a high specific surface area, and mechanical, rheological and optical properties that can be tailored. With the development of nanotechnology and the increasing concerns about resource sustainability, nanocellulose has been attracting attention, and is emerging as a promising material for a wide range of applications, *e.g*. in tissue engineering [212], electronic devices [204], food packaging [213] and medical devices [214]. Nanocellulose materials can be broadly classified according to their source and dimensions: nanofibrillated cellulose (NFC), cellulose nanocrystals (CNC), bacterial cellulose (BC) and

algae cellulose (AC) but they are always nanosized in at least one dimensions. The name first adopted for the fibril material from wood source was microfibrillated cellulose (MFC), later the material has been referred to as nanofibrillated cellulose (NFC) or cellulose nanofibrils (CNF). The nanosized crystals have previously been called cellulose nanowhiskers or simply whiskers but later a more informative term, cellulose nanocrystals (CNC) has been adopted.

Table 2. 11. Comparison of material properties of cellulose [215]

Particle type	Particle size			Cross-Section	Crystallinity[a], %	Iβ
	Length, mm	Width, nm	Height, nm			
WF and PF	>2000	20–50 (mm)	20–50 (mm)	—	43–65	—
MCC	10–50	10–50 (mm)	10–50 (mm)	—	80–85	—
MFC	0.5–10's	10–100	10–100	—	51–69	10–66
NFC	0.5–2	4–20	4–20	—	—	—
CNC	0.05–0.5	3–5	3–5	Square	54–88	68–94
t-CNC	0.1–4	~20	~8	Parallelogram	85–100	76–90
AC					>80%	
(Valonia)	>1	~20	~20	Square	—	36–42
(Micrasterias)	>1	20–30	5	Rectangular	—	—
BC					65–79	12
(Acetobacter)	>1	30–50	6–10	Rectangular	63	3–27
(Acetobacter)[b]	>1	6–10	6–10	Square	—	53
Cellulose II	Filament	—	—	Cylindrical	27–43	—

[a] Degree of crystallinity relative to cellulose; [b] Chemical addition during culturing

Table 2. 12. Properties of cellulose based materials[215]

Material	E_A, GPa	E_T, GPa	σ_f, GPa	$\varepsilon_{f, \%}$
Wood	14–27	—	0.3–1.4	4–23
Plant	5–45	—	0.3–0.8	1.3–8
MCC	25 ± 4	—	—	—
MFC & NFC	N/A	—	—	—
CNC plant	57, 105	—	—	—
t-CNC	143	—	—	—
BC	78 ± 17	—	—	—

E_A= elastic modulus in axial direction; E_T= elastic modulus in transverse direction; σ_f= tensile strength (tensile testing); ε_f= strain to failure (tensile testing)

Nanofibrillated cellulose, NFC

Nanofibrillated cellulose (NFC) can be prepared from wood based pulp material by simultaneous enzymatic and mechanical treatment or just mechanical treatment [201]. NFC materials have extraordinary properties due to their nanoscale dimensions. The long and entangled fibrils have high aspect ratio and large surface area exhibiting vast amounts of reactive hydroxyls groups on their surface. They form an extensively percolating network with low weight percentages. In water NFC forms a gel, which strength is dependent on the fibril concentration. Upon drying NFC forms hierarchical nanoporous aerogels or strong films depending on the drying process. The mechanical properties of NFC paper films have been re-ported to be better than ordinary paper and the reinforcing ability in composite ma-terials has also been shown to be superior compared to pulp fibers. This is caused by the larger surface area of fibrils exhibiting extensive hydrogen bonding compared to macroscopic fibers. Moreover these films have good gas barrier properties which can be of benefit in many coating and barrier technologies. The aerogels have been shown to have very different properties compared to traditional aerogels due to the long and entangled fibrils forming a hierarchical nanoporous structure. They open up new application areas for the use of aerogels in general. Due to its biocompatibility NFC is also a promising material for biotechnological and pharmaceutical applications.

Cellulose nanocrystals, CNC

Cellulose nanocrystals (CNC) can be obtained from different sources by hydrolysis with a concentrated mineral acid [201]. The treatment hydrolyses the noncrystalline parts of cellulosic materials yielding a dispersion of rod-like crystalline cellulose sticks. These nanosized rods range in size depending on the source they are obtained from and by the reaction conditions but usually are 5 to 20 nm in width and 0.1 to ~1 μm in length. CNC has smaller aspect ratio than NFC and in solution does not form as strong gel as NFC due to the lack of extensive percolation of the network. Yet the rods are mechanically extremely strong. Experimentally, the Young's modulus of a single crystal of cellulose I is ~134 GPa and the strength in the GPa

range. Due to the crystalline rod-like structure, CNC display other interesting properties such as liquid crystallinity. The mineral acid used in the hydrolysis of cellulose material determines whether the resulting CNC will carry charge on their surface or not. By hydrochloric acid hydrolysis the surface of the crystals will be almost neutral and display almost solely hydroxyl groups. These CNC are usually referred to as HCl-CNC. In this form the CNC are poorly dispersed in water and other solvents due to their tendency to aggregate via strong hydrogen bonding. The colloidal stability of HCl-CNC is affected by their concentration and aggregation is more pronounced in higher concentrations. If the hydrolysis is performed with sulfuric acid the resulting CNC will hold sulfate groups on the surface and a net negative charge, referred to as sulfate-CNC. The sulfate-CNC are readily dispersed in water due to their charged surface. They form stable colloidal dispersions in water but can be aggregated with increasing ionic strength. CNC can also be dispersed in some organic polar solvents, such as DMSO.

2.5.2 Applications of nanocellulose materials[201]

There is a growing need for sustainable and more environmentally friendly materials and products in the market to replace plastics and other unsustainable materials. Cellulose as a material is well suited for that due to its large surface area and high aspect ratio leading to superior mechanical properties compared to macroscopic cellulose fibers and regenerated cellulose, NC could be used in applications where traditional cellulosic products would not be well suited, for example aerogels, composite reinforcement and flexible electronics. The research done in the field of nanocellulosic materials is growing and new application areas are being explored by the growing knowledge on these very interesting materials.

Rheology modifiers

Rheology studies the flow and flexure of materials. In many applications it is very useful if the flow of matter can be altered during processing. Altered flow properties can for example allow broader applicability for existing materials. Gels with percolating networks can be used to modify the rheological properties of other materials when mixed together. The need to modify how matter stands applied force is often useful in such cases as in paint and lacquer applications,

in cosmetic applications, in polymer processing, and in food technology. In many applications it is useful if the rheological properties of the material can be tuned to fit certain needs for example in processing; *e.g.* to ease the spreading of paint to wall or melt processing or extrusion of a polymer, or simply adding strength to the material in wet state in different environmental conditions. On the other hand, the rheological properties of a material determine how it can be used in specific applications, such as hydrogels, reinforcing phase in composites, thin film applications or emulsion and foam stabilization. NFC forms a strong gel in aqueous media in broad range of concentrations in contrast to CNC dispersions which form gels only in very high concentrations. Pääkkö et al. [216] have studied NFC (prepared from soft wood sulfate pulp by mechanical and enzymatic means) rheological properties. They showed that these materials display typical ideal gel behavior, *i.e.* elasticity, that is the storage modulus, G', is much greater than the loss modulus, G'', and G' is independent of frequency in low solid content dispersions (0.125 % w/w) as well as in high (5.9 % w/w). The strength of the gel or dispersion, i.e. G'-values, were dependent on the concentration. These investigations highlight the importance of the rheological properties of NFC and CNC in relation to many applications. The dependence of the viscosity and strength of the gel or dispersion on concentration and the shear thinning behavior can be especially interesting for many applications where ability to tune material properties and change behavior according to processing are desired, yet where it is important that gel properties and the entangled network structure are preserved. Also the fact that CNC undergo phase transitions during shearing process is relevant in many cases. Due to the different rheological behavior of CNC dispersions compared to NFC, *i.e.* lower viscosity, weaker dispersions/gels, and liquid crystallinity, the applications for them would be somewhat different.

2.5.3 Modification of nanocellulose surface [201]

The properties discussed above make NFC and CNC very promising materials for rheology modifiers, mechanical reinforcement, as templates for smart materials, in barrier technologies, flexible electronics, and many biotechnological and biomedical applications.

Common syntheses of CNs provide for distinctive surface chemistries: sulfuric acid treatment provides sulfate esters, hydrochloric acid treatment provides hydroxyl, acetic acid

provides acetyl, TEMPO mediated hypochlorite treatment provides carboxylic acid [215] (Figure 2.12.). CNC prepared by HCl-hydrolysis has a very poor colloidal stability [201]. This is due to lack of repulsive forces between the crystallites and thus the suspensions are very unstable. The use of H_2SO_4 in the hydrolysis adds enough negatively charged groups (sulfate) on the crystal surface to create repulsion between the individual rods and thus yields a more stable dispersions in aqueous media. If one wants to embed them in other materials such as hydrophobic polymers further surface modification is needed for sufficient interaction to take place between the two materials at the interface. The same need for surface modification applies for NFC yet it is more stable in aqueous media after preparation than unmodified CNC. In NFC materials derived from wood source this is most probably due to the hemicelluloses present in the material acting as a colloidal stabilizer and preventing aggregation. NFC is also less crystalline and contains substantial amount of unordered amorphous parts in the fibrils that do not aggregate as strongly as crystalline regions. Nevertheless NFC is very sensitive to processing and tends to flocculate or aggregate upon different treatments such as solvent exchange, application of mechanical force etc. Blending unmodified NFC or CNC together with other materials rarely works out due to the lack of interaction of the fibril surface with the other materials. In other words, the cellulose crystal and fibril surfaces are passive and do not readily interact with other materials.

To overcome these issues NFC and CNC surfaces need to be modified for their efficient use in most applications. The modification of NFC and CNC can be grouped to chemical and physical modifications as with any colloidal particles. Chemical modifications involve covalent bonding usually done in solvent media and that can involve chemicals that are hazardous, such as azides or metal catalyst, and the reaction conditions can be harsh, including extreme pH, high temperature, and inert gas environment. Physical modifications are generally done in less harsh conditions than chemical; they involve adsorption of molecules on to the surface via weaker chemical interactions than covalent bonding, *i.e.* electrostatic interactions, hydrophobic interactions, or van der Waals interactions.
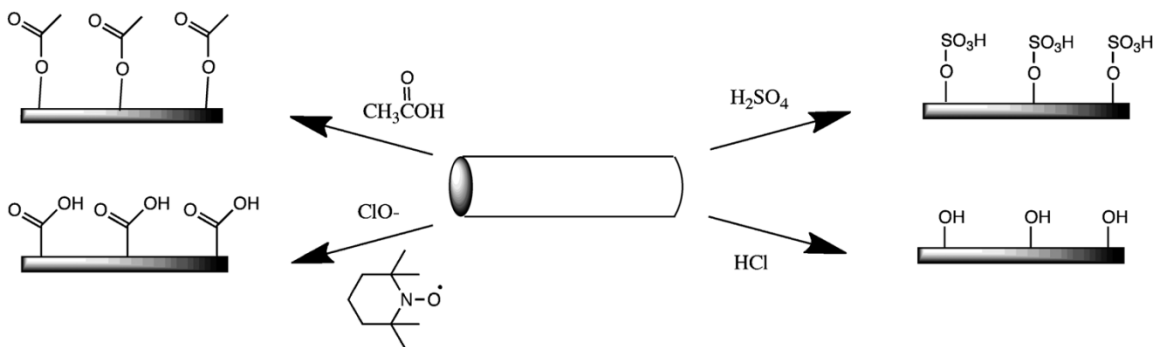
Figure 2. 12. Common syntheses of CNs [215]

Common syntheses of CNs provide for distinctive surface chemistries: sulfuric acid treatment provides sulfate esters, hydrochloric acid treatment provides hydroxyl, acetic acid provides acetyl, TEMPO mediated hypochlorite treatment provides carboxylic acid.

Chemical covalent modification of nanocellulose surface

The chemical functionality of CN surfaces dictates CN suspension properties, the composite fabrication processes and the resulting composite properties. Common modification chemistries of CN surfaces include sulfuric acid treatment providing sulfate esters, carboxylic acid halides creating ester linkages, acid anhydrides creating ester linkages, epoxides creating ether linkages, isocyanates creating urethane linkages, TEMPO mediated hypochlorite oxidation creates carboxylic acids, halogenated acetic acids create carboxymethyl surfaces, and chlorosilanes create an oligomeric silylated layer [215]. The different chemical modification of NFC and CNC can be divided roughly into three major groups; preparing negatively charged, positively charged, and hydrophobic NC. The degree of modification will affect the materials properties. In the case of CNC the amount of negative groups on the surface will determine how well the individual rods are dispersed and in what concentrations they will behave as gels or liquid crystals. In the case of NFC chemical modification can reduce the amount of hemicellulose and affect the colloidal stability (epoxy modified NFC) or it can alter the pH sensitivity of the material. The idea in NFC and CNC modification is to sustain the strong cellulose I crystal structure and to modify only the very surface of the fibril or crystal. Thus, the modification conditions need to be kept mild enough in order not to swell and subsequently

79

dissolve the cellulose. Also flocculation needs to be avoided and a good dispersion of fibrils and crystals during modification is important so that the product is evenly modified.
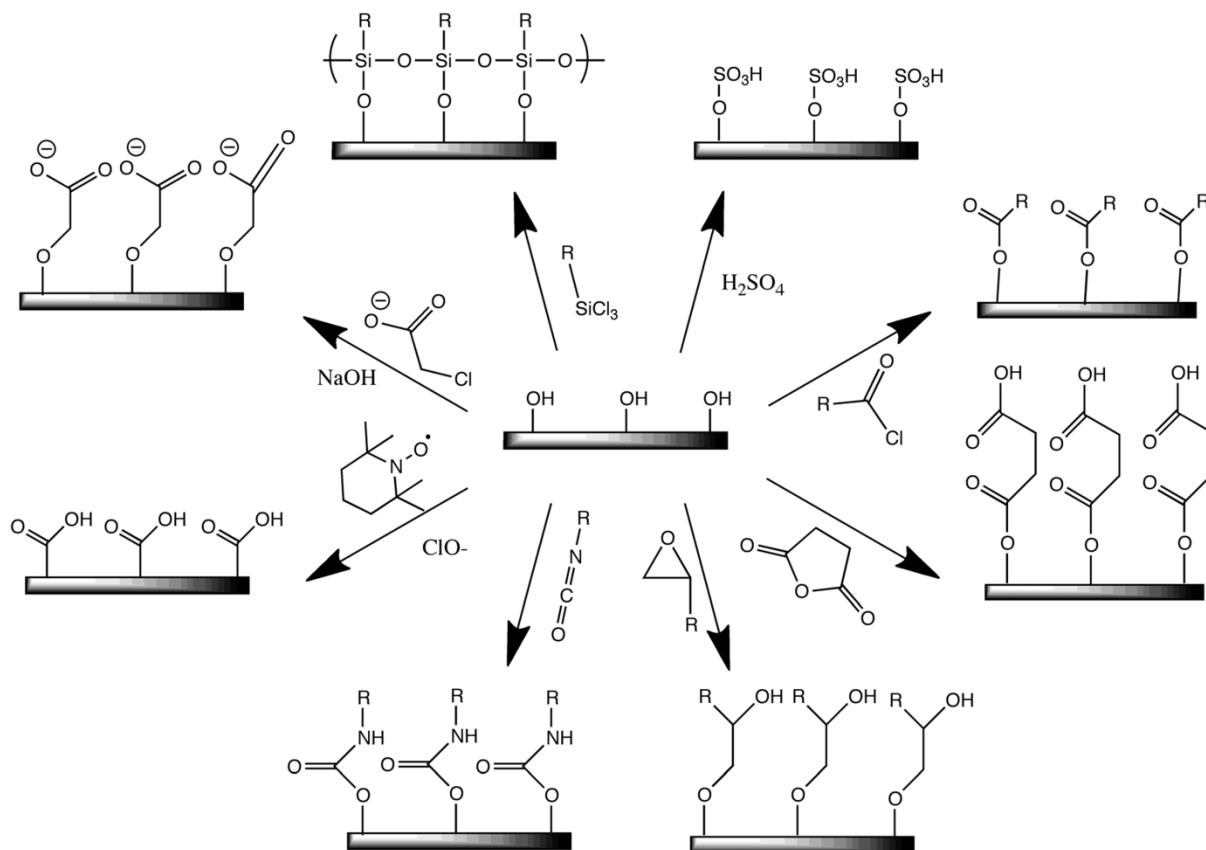
Figure 2.13. Common modification chemistries of CN surfaces [215]

Anionic functionalization [201]

As described earlier, CNC can be produced in such a way that the surface of the product will hold a net negative charge. This is simply done by choosing the acid for the hydrolysis reaction accordingly; sulfuric acid will derivate the resulting CNC surface with sulfate groups and hydrochloric acid will not derivate the CNC surface. The sulfate-CNCs can readily interact with positively charged molecules, can be dispersed in water and some polar solvents, and can be used for further modification or functionalization. The HCl-CNC can also be modified after

production either to contain sulfate groups (treated with sulfuric acid) or to contain carboxylic acid groups. The latter method is mostly applied to NFC materials and will be described in the following paragraph.

To produce negatively charged NFC with a very fine and even size distribution, a method called TEMPO (2,2,6,6,-tetramethylpiperidine-1-oxyl) catalyzed oxidation has been developed. TEMPO-oxidation of cellulosic material is solely specific to the C-6 hydroxyl (primary alcohols). The specificity and well controlled conditions of the reaction allow the reaction to take place only on the primary alcohols exposed on the fibril surface. The modification leads to fibrils where every second glucose unit on the fibril surface carries a modified C-6 hydroxyl. Due to the specific nature and well controlled reaction conditions TEMPO-oxidation produces cellulose fibrils with a very uniform diameter depending on the source they originate from. The properties of TEMPO-oxidized NFC (TEMPO-NFC) are very different from the original non-modified NFC first due to the high density of negative charge on the fibril surface and second due to the fibril dimensions being smaller and more homogeneous. The size of TEMPO-NFC fibrils and their fine dispersions in water allow fully transparent hydrogels with high viscosity in comparably small solid content and they form transparent films with high oxygen barrier properties upon drying. The wettability of TEMPO-NFC is very different from that of neat NFC. A dry TEMPO-NFC film adsorbs water almost immediately but this can be reduced by surface hydrophobization commonly used in papermaking. Also the thermal degradation of TEMPO-NFC is altered and it is lower than that of unmodified fibrils.

Cationic functionalization [201]

For interactions with negatively charge materials, such as kaolin clay and oxidized graphene, for further modifications with functional groups, such as proteins, or to add strength and antibacterial properties to materials, cationic groups have been introduced on NFC surface. Different routes to prepare cationic NFC have been reported in literature [201]. These reactions rarely alter the rheological properties of NFC dispersions or the fibril morphology too dramatically, as compared to for example TEMPO-mediated oxidation, but rather introduce reactive groups on the fibril surface with lower degree of substitution.

81

Hydrophobic functionalization [201]

Hydrophobicity of NFC and CNC materials is often desired for interactions with polymers that are hydrophobic. This is usually done by polymerization reactions either from or onto fibril and crystal surface. There are numerous examples of these reactions and they are well reviewed [201]. In some cases hydrophobicity in combination with nanoscale hierarchical structure of the material can lead to super hydrophobicity of the resulting material. Another reason for hydrophobizaton of NFC or CNC would be that some of these groups can easily reacted further. An example of such modification is the epoxy moiety. Epoxy groups are well known to react with amine groups and can be used to cross-link materials (epoxy glues) or covalently immobilize proteins onto solid supports.

Physical adsorption of molecules onto nanocellulose surface [201]

For NFC and CNC containing charged groups on their surface the adsorption of other molecules can be performed using charge interactions. This can be used to modify the fibrils or crystals with functional groups or to yield better interaction with another material in composites. CNC and NFC can also be readily modified by adsorption of other carbohydrate containing molecules such as hemicelluloses and branched polymers containing sugar moieties. In nature there are also proteins that specifically adsorb to cellulose surface. These are called cellulose binding modules (CBM, or cellulose binding domains, CBD), and they are produced by organisms that can degrade cellulose, for example some fungi and some bacteria.

Due to intensified ''green thinking'' in process industry as well as environmental protection, adsorption of arsenic using natural products has emerged as a viable option. Cellulose is most widely available and renewable biopolymer in nature. It is a very promising raw material vailable at low cost for the preparation of various functional materials. Due to the presence of hydroxyl groups, cellulose is considered to be an excellent material for surface modification. At the same time, a combination between bioadsorbents and iron oxide nanoparticles can pose an efficient biocomposite material, which could possibly show high adsorption capacity, intensified

stability, and easy recovery from treated effluents by applying a magnet. Introduction of terminal amino and carboxylic groups provides effective means for ferric (hydr)oxides precipitation. Functionalized nanosized [110,217–223], as well as microfibrillated cellulose was used for adsorption of As, F, Cr, Pb, Hg, Cu, Ag, U, and organic pollutants. There are some reports about the cellulose/ferric (hydr)oxide hybrid materials used for arsenic removal [110], whereas no influence of surface modification/type of functionalities of matrix on adsorption performances was studied.

3.EXPERIMENTAL PART

3.1 Materials and chemicals

All chemicals used in this study were p.a. quality, and used as received. Deionized water (DIW), resistivity 18 MΩ cm, was used as solvent and for dish washing. In the process of synthesis chemicals were purchased from different suppliers, *i.e*. Merck: glycidyl methacrylate (GMA), 2,2′-azobis(2-methylpropionitrile) (AIBN), cyclohexanol, hexadecanol, diethylene triamine (DETA), iron(II) chloride tetrahydrate ($FeCl_2x4H_20$) and xylene. The following chemicals were supplied from Sigma Algrich: tetrahydrofurane (THF), ethanol (EtOH), chloroform, sulfuric acid, glacial acetic acid (GAA), toluene, perchloric acid, maleic anhydride (MA), ethylenediamine (EDA), ethylenediaminetetraacetic acid (EDTA), *N,N*-dimethylformamide (DMF), iron(II) sulfate heptahydrate ($FeSO_4x7H_20$), potassium nitrate (KNO_3), potassium hydroxide (KOH), triethylamine (TEA), ethyl oxalyl chloride (EOC), *N,N*-dimethylacetamide (DMAc), *N*-methylpyrrolidone (NMP), coupling agent *N,N′*-diisopropyl carbodiimide, dicyclohexylcarbodiimide (DCC),sodium dihydrogen phosphate (NaH_2PO_4) (p.a.), sodium sulfate (Na_2SO_4), calcium nitrate ($Ca(NO_3)_2x4H_2O$), magnesium nitrate ($MgNO_3x6H_2O$), sodium metasilicate solution (Na_2SiO_3) and sodium chloride (NaCl) reagent. Ethylene glycol dimethacrylate (EGDMA) were purchased from Fluka. Poly(*N*-vinylpyrrolidone) (PVP) were purchased from BASF. Sodium hydrogencarbonate ($NaHCO_3$) were purchased from Zorka Pharma. PEG-6-arm amino polyethylene glycol (PEG-NH_2, Mr≈15000 g mol^{-1}) were purchased from Sunbio, South Korea. Cotton used for NC isolation was supplied from AD. Niva, Serbia (Turkish origin). Microfibrillated cellulose was supplied by Stora Enso Finland. These materials were used for synthesis nanocellulose and microfibrillated celullose modified with magnetite.

The As(V) and As(III) stock solutions were prepared with deionized water using sodium arsenate dibasic heptahydrate ($Na_2HAsO_4x7H_2O$)(Sigma-Aldrich) and sodium arsenite ($NaAsO_2$ p.a.)(J.T. Baker, reagent grade), respectively. Arsenic working solutions were freshly prepared by diluting arsenic stock solutions with DIW. The concentrations of arsenic species were always given as elemental arsenic concentration in this study.

Otherwise, the As(V), As(III), nickel, cadmium, lead and copper standard solutions (Sigma Aldrich), 1000 mg L^{-1}, were further diluted with DIW) to the required concentration. For pH adjustment, 1/0.1 mol L^{-1} solution of hydrochloric acid (HCl) (Sigma Aldrich) and 1/0.1 mol L^{-1} solution of sodium hydroxide (NaOH) (Sigma Aldrich) were used.

3.2 Adsorbents preparation: ER/DETA/FO/FD and ER/DETA/FO/VD

The optimal conditions were selected according to the adsorption maximum in relation to variable experimental parameters: amount of diethylene-triamine (DETA) and synthesis method in the second step, concentration of FeSO$_4$x7H$_2$O and drying technique in the third step, which was performed in the following way:

a)   Macroporous poly(glycidyl methacrylate-*co*-ethylene glycol dimethacrylate) cross-linked resin was prepared by a radical suspension copolymerization as described in the work of Vukoje *et al.*[224]. In brief, the monomer mixture (24.2 g GMA and 10.3 g EGDMA), initiator (0.800 g AIBN) and inert component (porogen agent) (36.5 g of cyclohexanol and 9.10 g of hexadecanol) were suspended in the aqueous phase (238 mL water and 2.40 g poly(*N*-vinyl pyrrolidone)). The copolymerization was carried out at 70 °C for 2 h and at 80 °C for next 6 h with a stirring rate of 200 rpm. The obtained copolymer was washed with water and ethanol, kept in ethanol for 12 h, vacuum dried at 40 °C and purified by Soxhlet extraction with chloroform. The fraction with average particle diameter in the range 0.20–0.50 mm was used in subsequent reactions and was named **ER.**

b)   The **ER** (10 g) was dispersed in tetrahydrofuran (THF) (100 mL) and sonicated for 30 min. The dispersion was transferred on magnetic stirrer and diethylene triamine (DETA) in 10; 20 or 30 mL in 50 mL of THF was added drop-wise for 30 min. Reaction took place at 25 °C for 1 hour, and after the increase of dispersion temperature to 60 °C the mixing continued for next 1, 2 and 4 hours. Analogous experiments were performed under ultrasound treatment. Product, **ER/DETA**, was filtered, washed twice with ethanol and deionized water (DIW), collected and dried in a vacuum oven at 40 °C for 6 hours. The **ER** modification with DETA provided amino functionalized **ER/DETA** support containing high affinity terminal group for iron coordination.

c)   The **ER/DETA** (10 g) was sonicated in DIW (30 mL) with simultaneous introduction of N_2 for 30 min. Reaction was continued, under magnetic stirring and inert atmosphere, by drop-wise addition of $FeSO_4 \cdot 7H_2O$ solutions: 33.3 mL, 0.5 M; 66.6 mL, 0.25 M; and 133.2 mL, 0.125 M; for 15 min. Ferri/ferro oxidation, in all experiments, was performed in air and by neutralizing of the reaction mixture with 1M $NaHCO_3$ buffer solution to cause precipitation of FO in goethite form [125]. The reaction took place for 48h while green-blue color of solution changed to an ocherous shade of product. The obtained product was filtered, washed with 200 mL DIW, divided in two portions and dried applying vacuum/drying (VD) and freeze/drying (FD) techniques. The product processed by VD at 40 °C for 10 h was named **ER/DETA/FO/VD**. The FD process was conducted by treating the obtained material at –30 °C for 24 h, followed by drying at –50 °C/0.05 mbar for 24 h, and last step was conducted at –70°C/0.01 mbar for 1h. The obtained material was named **ER/DETA/FO/FD**. Additionally, comparative experiment of **ER/DETA/FO/FD-3** synthesis was performed analogously to **ER/DETA/FO/FD** (3x22 mL, 0.25 M), except that after each precipitation step of FO (three-step process), the FD of intermediary material was applied. Analogously to **ER/DETA/FO**, nanoscale goethite was prepared [125].

3.2.1 Fabrication of aminated glycidyl methacrylate support media

Macroporous glycidyl methacrylate copolymer was fabricated by dissolving 3.9 g of PVP in 300 mL of deionized water (18MΩ cm), and then mixed with oil phase consisting of monomer precursors, porogen and initiator. The monomer precursor was composed of 30 mL glycidyl methacrylate and 13 mL ethylene glycol dimethacrylate, while 20 mL of 2-hexanone was used as a porogen agent, and 1 g of 2,2′-azobis(2-methyl propionitrile) as initiator. The two phases were vigorously stirred under inert atmosphere of nitrogen at 80 °C for a period of 2 h to facilitate a suspension polymerization process. The created copolymer was separated by filtration, washed firstly with ethanol followed by deionized water, aged in ethanol for a period of 12 h, and then dried in a vacuum oven at 40 °C for 4 h. The porogen agent was removed from the copolymer by a 48 h continuous Soxlet extraction with chloroform. The obtained material

was sieved and material consisted from the fraction in a range 150–600 μm was collected, and used in subsequent experiments.

Upon sieving, 10 g of glycidyl methacrylate copolymer was dispersed in 50 mL of dry tetrahydrofurane, and then 20 mL of diethylene triamine was added drop-wise to initiate the amination reaction, which was conducted at 60 °C for a period of 6 h. Introduction of terminal amino groups was conducted to demonstrate the possibility of functionalizing this base media and utilize the affinity of terminal amino groups to facilitate iron precursor diffusion. Modification of copolymer enriched by hydrophilic amino group helped surface wetting and more importantly the interaction of Lewis acid (ferric ions) with Lewis base site (surface amino groups) provides initial nucleation center for goethite precipitation. The aminated macroporous glycidyl methacrylate support media was then filtered, washed with ethanol and deionized water, collected, and dried in a vacuum oven at 40 °C for 6 hours.

3.2.1 Controllable impregnation of the support media with goethite

In order to increase the effectiveness of iron transport inside hydrophilic support media, mixture of hydrophilic (water)/hydrophobic (xylene) solvents was applied. A 10 g of the aminated glycidyl methacrylate copolymer was soaked with xylene and placed in a perforated column assembly as illustrated in Figure 3.1. Xylene was used as a copolymer suspension system, which was mixed by nitrogen bubbling thoughout the reactor in an upstream flow to provide a gentle movement/mixing of packed copolymer. Upon establishing a steady mixing and continuous flow of nitrogen (15 mL min^{-1}) through two phase system xylene/copolymer, 30 mL of $FeCl_2 x 4H_2O$ (0.5 mol L^{-1}) aqueous solution was added in the reactor over a 15 min period via a dropping funnel located at the top of reactor column. A glass frit assembly connected to the funnel was used to provide for homogeneous dispersion of $FeCl_2$/water droplets. Small droplets of the $FeCl_2$/water solution were attracted by hydrophilic copolymer, and nitrogen bubbling promotes formation of uniform film at surface and increase the effectiveness of iron transport inside the copolymer. After additional After additional bubbling of N_2 for 15 min, precipitation of goethite was performed in air at pH 7 ± 0.2 by neutralizing the generated acid with 1 mol L^{-1} $NaHCO_3$ (Zorka Pharma) buffer solution. Bubbling of air was continued for a period of 24 h to

complete the oxidation of the ferrous ions to ferric, and ensure complete formation of goethite. The change of the green–blue color to an ocherous shade of precipitated material was an indicator of completed oxidation/precipitation process. The first step of impregnation is completed by exhaustion of the column (removal of liquid phase), followed by careful vacuum drying. The entire media impregnation with iron was repeated. The newly fabricated goethite impregnated media was then washed with deionized water, filtrated and dried at 40 °C for 10 h, and further characterized.
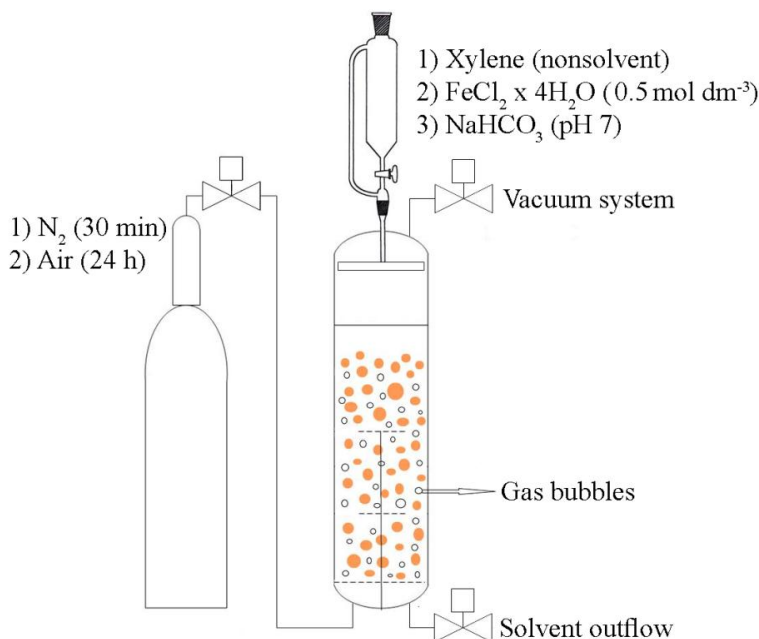
Figure 3. 1. Schematic presentaion of the resin impregnation assembly

3.2.2 Adsorbent preparation: NC-PEG/FO

Nanocellulose (NC) isolation

The **NC** was isolated from cotton microfiber (20 g) by treating with sulfuric acid (200 mL, 64 wt.%) at temperature <40 °C for 1 h [225]. Product was diluted with 800 mL of DIW, neutralized to pH 6, and three cycles of centrifugation/DIW water washing were applied. After dializing for 48 h, nanocellulose was filtered by using polytetrafluoroethylene (200 nm) filter membrane, and named **NC**.

The NC modification with maleic acid anhydride (NC-MA)

NC (10 g) was dispersed in the mixture of glacial acetic acid (100 mL), toluene (130 mL) and perchloric acid (0.5 mL) by the use of ultrasound. Solution of MA (5 g) in 45 mL of toluene was added drop-wise into reaction mixture for 15 minutes under sonication, and reaction was continued on magnetic stirrer for 1 h at room temperature. Raw product was washed thoroughly with toluene and ethanol, dried and designated as **NC-MA**[226].

NC-MA modification with PEG-NH$_2$

Dispersion of **NC-MA** (10 g) in the 50 mL dry DMF was added slowly into solution of 1 g of PEG-NH$_2$ in 50 ml dry DMF. After addition of 2 g of *N,N′*-diisopropylcarbodiimide in 20 mL DMF reaction was carried out by ultrasonic treatment for 30 min (5 min/5 min sonication/mixing cycles), and continued with magnetic stirring at 20-25 $^{\circ}$C for 3 h. The product was then diluted with 300 ml of methanol, vacuum-filtered with 0.05 μm pore size PTFE filter membrane, and washed extensively with excess methanol. The PEG-NH$_2$ functionalized **NC** (**NC-PEG**) was freeze/dried by keeping freshly obtained material at –30 $^{\circ}$C for 24 h, followed by freeze drying at –50 $^{\circ}$C maintaining 0.05 mbar for 24 h, and process was finished at –70 $^{\circ}$C and 0.01 mbar for 1 h material treatment. In that way obtained porous **NC-PEG** substrate was used for subsequent precipitation of iron oxide.

Precipitation of iron oxide (FO) on NC-PEG

NC-PEG (10 g) was sonicated in DIW (30 mL) with simultaneous introduction of N$_2$ for 30 min. Reaction was continued, under magnetic stirring and inert atmosphere, by drop-wise addition of FeSO$_4$x7H$_2$O solution: 83 mL (0.05, 0.1, 0.15, 0.2, 0.25, 0.3 and 0.35 mol L^{-1}) of FeSO$_4$x7H$_2$O solution, respectively, from dropping funnel for 15 min. Ferri/ferro oxidation was performed by changing nitrogen with air introduction, and neutralizing the reaction mixture with 75 cm^{-3} of different concentration: 0.1, 0.2, 0.3, 0.4 and 0.5 mol L^{-1} of sodium bicarbonate for 30 min to cause precipitation of iron oxide, in goethite form [125]. Reaction took place for 48 h while green-blue color of solution changed to ocher shade. Obtained product was filtered, washed with DIW, and freeze/dried was conducted by cooling and keeping freshly obtained

material at –30 °C for 24 h, followed by freeze drying at –50 °C maintaining 0.05 mbar for 24 h, and process was finished at –70 °C and 0.01 mbar for 1 h material treatment. The procedure for precipitation of **FO** was repeated in an analogous manner, and obtained adsorbent was named **NC-PEG/FO**.

Optimization of adsorbent preparation

Optimization of adsorbent synthesis **NC-PEG/FO**, by applying response surface methodology (RSM) [227,228], was based on three-level-two-factor central rotatable composite design (blocked single factor: temperature). The coded and operational values of the selected variables are shown in Table 3.1., together with the experimental plan, which comprised 16 experimental runs plus six replicates on the central point [74,229]. Each experiment (except the central point) was performed in duplicate. The output variable was the adsorption capacity. Data obtained in these experiments were fitted with a second-order polynomial equation and the coefficients of the response function and their statistical significance were evaluated by the least squares method using commercial software Design-Expert, Software Version 9 (Stat-Ease, Inc. 2021 E. Hennepin Ave. Suite 480 Minneapolis, USA). The Fisher test was used to determine the adequacy of the model and the Student distribution to evaluate the significance of the coefficients.

The coded and operational values of the selected variables are shown in Table 3.1., together with the experimental plan, which comprised 16 experimental runs plus six replicates on the central point.

Table 3. 1. Experimental plan for RSM and experiment results for adsorbent **NC-PEG/FO** (m/V = 100 mg L^{-1}, $C_{i[As(V)]}$ = 0.5 mg g^{-1}, T = 25 °C, pH = 6).

No.	$C_{[FeSO4]}$, X_1, mol L^{-1}	$C_{[NaHCO3]}$, X_2, mol L^{-1}	Obtained capacity As(V), mg g^{-1} mg g^{-1}
1.	0.35	0.32	2.039
2.	0.21	0.22	3.142
3.	0.21	0.22	3.142
4.	0.09	0.17	1.605
5.	0.35	0.05	2.440
6.	0.12	0.50	2.273
7.	0.12	0.50	2.273
8.	0.23	0.17	2.975
9.	0.21	0.22	3.209
10.	0.04	0.32	1.805
11.	0.35	0.05	1.471
12.	0.29	0.15	3.311
13.	0.35	0.50	2.106
14.	0.04	0.32	1.905
15.	0.18	0.05	2.340
16.	0.04	0.05	1.471

3.2.3 Adsorbent sznthesis: NC-L/FO

Nanocellulose (NC) isolation

NC isolation was performed according to procedure given in section 3.2.2.

The NC modification with maleic acid anhydride (NC-MA)

The NC modification with **MA** was performed according to method given in section 3.2.2.

NC-MA modification with ethylenediamine

Dispersion of **NC-MA** (10 g) in the 200 mL of tetrahydrofuran (THF) was added slowly into solution of EDA (10 mL) in THF (50 mL), previously charged in three necked flask (500 mL), under ultrasonic treatment. After addition of 2 g of *N,N'*-Diisopropylcarbodiimide in 20 mL

THF, reaction was carried out by ultrasonic treatment for 30 min (5 min/5 min sonication/mixing cycles), and continued with magnetic stirring at 20-25 $^{\circ}$C 3 h. Product was washed with THF, and denoted as **NC-MA-EDA**.

NC-MA-EDA modification with ethyl acrylate (EA)

EA (5 mL) was added slowly in the dispersion of 10 g of the **NC-MA-EDA** in 200 mL of absolute ethanol. Reaction took place for 12 h at room temperature and for 6 h at 60 $^{\circ}$C. Product was washed three times with ethanol, 50 mL, dried and denoted as **NC-MA-EDA-EA**.

NC-MA-EDA-EA modification with EDA

After 5 min of **NC-MA-EDA-EA** (10 g) sonication in dry *N*-methylpyrrolidone (NMP), EDA (10 mL) was added drop-wise for 10 min. After that heating at 50 $^{\circ}$C and mixing at magnetic stirrer was applied for 10 h. Obtained product was washed by using abundant quantity of NMP and DIW, dried at 60 $^{\circ}$C/12 h under vacuum, and denoted as **NC-MA-EDA-EA-EDA** (**NC-L**).

Precipitation of iron oxide (FO) on NC-L: synthesis of NC-L/FO adsorbent

NC-L(10 g) was sonicated in DIW (30 mL) with simultaneous introduction of nitrogen for 30 min. Reaction was continued, under magnetic stirring and inert atmosphere, by drop-wise addition of $FeSO_4$x$7H_2O$ solution: 33.3 mL, 0.5 mol L^{-1}, for 15 min. Ferri/ferro oxidation was performed by changing nitrogen with air introduction, and neutralizing the reaction mixture with 1 mol L^{-1} $NaHCO_3$ solution to cause precipitation of iron(oxy)hydroxide, in goethite form [114]. Reaction took place for 48 h while green-blue color of solution changed to ocher shade. Obtained product was filtered, washed with DIW, and freeze/dried was conducted by cooling and keeping freshly obtained material at -30 °C for 24 h, followed by freeze drying at -50 °C maintaining 0.05 mbar for 24 h, and process was finished at -70 °C and 0.01 mbar for 1 h material treatment. Adsorbent was named **NC-L/FO**.

Adsorbents preparation

The preparation of adsorbents was performed through five consecutive steps applying magnetic stirring (*Heidolph*) and ultrasonic treatment (*Bandello electronic, Berlin, Germany, power 120 W, frequency 35 kHz*) or combination of both method. Such methodology was applied in order to enhance reactant diffusivity/reactivity due to limited availability of surface functional group being positioned at the internal adsorbent surface. By the use of ultrasound, the liquid circulation and related turbulence generated the formation and collapse of bubbles known as cavitation, thus inducing and improving mass and energy transfer. In this work, ultrasound assisted synthesis proved increased frequency of collision and enhanced reaction efficiency of some reaction steps. In that way, it offers an acceptable alternative for the synthesis of the adsorbents *via* a simple, catalyst-free reaction conditions which help in overcoming rate limiting steps in the course of constructing branched/bridging organic structure at **NC** and **MC** surface [230,231].

3.2.4 Adsorbent synthesis: NC-MA/L-MG synthesis

Nanocellulose (NC) isolation

NC isolation was performed according to procedure given in section 3.2.2.

The NC modification with maleic acid anhydride (NC-MA)

The **NC** modification with MA was performed according to method given in section 3.2.2.

NC-MA modification with ethylenediamine (NC-MA/EDA)

The NC modification with MA was performed according to method given in section 3.2.3. except using *N,N'*-Diisopropylcarbodiimide as coupling agent.

NC-MA/EDA modification with tetraethyl ester of ethylenediaminetetra acetic acid

In the dispersion of 10 g of the **NC-MA/EDA** in 200 mL of absolute ethanol, ethanol solution of *N,N'*-1,2-ethanediylbis[*N*-(2-ethoxy-2-oxoethyl)]-1,1'-glycine diethyl ester (tetraethyl ester of EDTA) (27 g) was added slowly. Tetraethyl ester of EDTA was prepared according to literature procedure [232]. Reaction took place under ultrasonic treatment for 10 min, and followed with magnetic stirring at room temperature for 6 h. Product was washed with ethanol, dried and denoted as **NC-MA/EDA-EDTA**.

NC-MA/EDA-EDTA modification with EDA

NC-MA/EDA-EDTA (10 g) was subjected to ultrasound treatment in *N,N*-dimethylformamide (DMF) for 5 min, drop-wise addition of EDA (10 mL) for 10 min was followed by heating/mixing at magnetic stirrer for 2 h at 50 ^{o}C. Obtained product was washed by using abundant quantity of DMF and DIW, dried at 60 ^{o}C for 12 h under vacuum. Synthesized material was denoted as **NC-MA/EDA-EDTA-EDA** (**NC-MA/L'**).

Precipitation of magnetite (MG) on NC-MA/L': synthesis of NC-MA/L'-MG adsorbent

In order to achieve optimized method of **NC-MA/L'-MG** synthesis and shorten experimental procedure the Response Surface Methodology (RSM) was applied for designing of the optimization of MG precipitation on **NC-MA/L'** (Table 3.2; Section 3.2.7). The **NC-MA/L'** (10 g) was dispersed in 100 mL $FeSO_4x7H_2O$ solution of different concentration: 0.013, 0.04, 0.1, 0.13, 0.16, 0.19, 0.23, 0.27, 0.32, 0.35, 0.39 and 0.49 mol L^{-1} performed ultrasonic treatment under inert atmosphere (N_2) for 10 min. After sonication **NC** dispersion was transferred to oil bath, with constant gentle mixing, and temperature was adjusted at 90 °C using magnetic stirrer/heater. Afterwards, 45 mL of oxygen-free solution contained different quantity of reactants: from 0.03 g to 1.1 g KNO_3, and from 0.2 g to 7.6 g KOH, calculated according to literature method [125] with respect to starting $FeSO_4x7H_2O$, were added during 30 min providing continuous iron oxide precipitation. After precipitation, reaction was heated for additional 60 min at 90 °C, and left overnight. The adsorbent **NC-MA/L'-MG** was isolated in

the form of black precipitate, washed with DIW until getting free from ions in filtrate. For the comparative purpose a sample of **MG** was prepared according to literature method [125]. The results of the optimization procedure were applied for the controllable impregnation of **MG** on **NC-MA/L'** support.

3.2.5 Synthesis of MC-O/L'-MG hybrid adsorbent

MC (10 g) was soaked in a mixture of dry THF (250 mL) and triethylamine (TEA) (30 mL), and afterward it was followed by drop-wise addition of ethyl oxalyl chloride (EOC) (30 mL) in dry THF (50 mL). Reaction was sonicated for 1 h at room temperature. Isolated product ethyl oxalyl modified MC, **MC-O**, (10 g) was used as a media for linkage of EDA-EDTA-EDA structure in an analogous manner as it was performed for **NC-MA/L'**, in that way **MC-O/L'** modified microfibrilated MC material was obtained. **MC-O/L'** was subsequently modified with **MG** in the way analogous to preparation of **NC-MA/L'-MG** adsorbent recalculated according to determined total basic sites.

3.2.6 Solvent/nonsolvent (water/xylene) system applied for controllable impregnation of the NC-MA/L' and MC-O/L' with magnetite

The results of the optimization procedure were applied for the controllable impregnation of **MG** on **NC-MA/L'** supportin a solvent/nonsolvent system. **NC** (10 g) was soaked with xylene (non-solvent used to provide continual medium and wetting of the NC material; mixing of the medium was achieved by nitrogen/air bubbling in a upstream flow) in a perforated column with gas inlet/outlet valves, solvent exhaustion valve and system for vacuum drying of the **NC** at different modification step. After establishment of continuous flow of nitrogen through two phase systems xylene/**NC-MA/L'** and xylene/**MC-O/L',** slow addition (15 min) of the 40 mL (0.95 mol L^{-1}) and 20 mL (0.85 mol L^{-1}) of $FeSO_4x7H_2O$ solution, respectively, started from dropping funnel situated at the top of column. Fine distribution of the $FeSO_4x7H_2O$solution was achieved by the glass frit assembled at the funnel. Small droplets of water iron solution were attracted by hydrophilic **NC-MA/L'** and **MC-O/L'** surface (concomitantly forced by non-solvent), and nitrogen bubbling promoted formation of uniform film at suspended material

surface. Optimization of the water quantity was performed in a batch system in order to provide fulfillment of porous structure and formation water film at outer surface. Modification of NC surface with hydrophilic amino groups helps surface wetting and more importantly, the interaction of Lewis acid (iron ion) and Lewis base site (amino groups) provides initial nucleation center for magnetite precipitation. It was performed by continual bubbling of N_2 at 90 °C, and by drop-wise addition of an oxygen-free solution of 20 mL (0.86 g KNO_3 and 5.95 g KOH) or 10 mL (0.38 g KNO_3 and 2.65 g KOH) or for 20 min into dispersions of xylene/**NC-MA/L'** and xylene/**MC-O/L'** impregnated with appropriate quantity of $FeSO_4x7H_2O$, respectively. After precipitation, the reaction was heated for additional 60 min and cooled overnight. The adsorbent **NC-MA/L'-MG** and **MC-O/L'-MG** were isolated as black precipitate, washed with DIW until getting free from sulfate ion in filtrate and dried. No sieving was necessary to apply for material obtained by this method.

Optimization of adsorbent preparation

Response surface methodology (RSM) optimization of adsorbent syntheses was based on five-level-three-factor central rotatable composite design (blocked single factor: temperature). The coded and operational values of the selected variables are shown in Table 3.2., together with the experimental plan, which comprised 16 experimental runs plus six replicates on the central point [229]. Each experiment (except the central point) was performed in duplicate. The output variable was the adsorption capacity of the obtained adsorbent. Data obtained in these experiments were fitted with a second-order polynomial equation and the coefficients of the response function and their statistical significance were evaluated by the least squares method using commercial software Design-Expert, Software Version 9 (Stat-Ease, Inc. 2021 E. Hennepin Ave. Suite 480 Minneapolis, USA). The Fisher test was used to determine the adequacy of the model and the Student distribution to evaluate the significance of the coefficients.

Table 3. 2. Experimental plan for RSM and experiment results for **NC-MA/L'-MG** and **MC-O/L'-MG** adsorbents ($m/V = 100$ mg L^{-1}, $T = 25$ °C)

No.	NC-MA/L'-MG			MC-O/L'-MG		
	$C_{[FeSO4]}$, X_1	pH, X_2	Capacity As(V)	$C_{[FeSO4]}$, X_1	pH, X_2	Capacity As(V)
1.	0 (0.25)	0 (9)	0.92	0 (0.125)	0 (9)	0.82
2.	1 (0.5)	1 (12)	0.92	1 (0.25)	1 (12)	0.82
3.	0 (0.25)	0 (9)	0.96	0 (0.125)	0 (9)	0.83
4.	−1 (0.01)	0 (9)	0.57	−1 (0.01)	0 (9)	0.38
5.	−1 (0.01)	−1 (6)	0.47	−1 (0.01)	−1 (6)	0.32
6.	−1 (0.01)	1 (12)	0.45	−1 (0.01)	1 (12)	0.32
7.	1 (0.5)	−1 (6)	0.66	1 (0.25)	−1 (6)	0.45
8.	0 (0.25)	−1 (6)	0.95	0 (0.125)	−1 (6)	0.83
9.	0 (0.25)	1 (12)	0.96	0 (0.125)	1 (12)	0.83
10.	−1 (0.01)	−1 (6)	0.45	−1 (0.01)	−1 (6)	0.32
11.	1 (0.5)	0 (9)	0.96	1 (0.25)	0 (9)	0.83
12.	0 (0.25)	0 (9)	0.97	0 (0.125)	0 (9)	0.84
13.	−1 (0.01)	1 (12)	0.78	−1 (0.01)	1 (12)	0.63
14.	1 (0.5)	−1 (6)	0.87	1 (0.25)	−1 (6)	0.78
15.	1 (0.5)	1 (12)	0.97	1 (0.25)	1 (12)	0.83
16.	0 (0.25)	0 (9)	0.97	0 (0.125)	0 (9)	0.84

3.3 Methods used for adsorbent characterization and arsenic determination

The phase and structural analysis of obtained material was characterized using X-ray diffraction (XRD) (BRUKER D8 ADVANCE), with Vario 1 focusing primary monochromator), CuKα source in the range 10–90 °C, step of 0.01°, and room temperature. The textural parameters of the obtained adsorbents were examined using the BET (**B**runauer-**E**mmett-**T**eller) method for the determination of the specific surface area, the BJH (**B**arrett-**J**oyner-**H**alenda) method for the determination of the mesoporosity parameters and the Gurvich method for quantification of the total pore volume based on nitrogen adsorption and desorption data at liquid nitrogen temperature (ASAP 2020, Micromeritics-USA). Material morphology was analyzed as a result of scanning electron microscopy (FEG–SEM) (TESCAN MIRA3) and MIRA TESCAN in situ measurement software and JEOL JSM-6610LV, as well as transmission electron microscopy

(JEOL JEM 1400 - 120 kV). Fourier-transform infrared spectra (FTIR) were collected on BOMEM (Hartmann & Braun) spectrometer. Samples for FTIR determination were prepared as KBr pellets and measurements were made at room temperature in 500–4000 cm^{-1} range. Raman spectra were collected with a XploRA Raman spectrometer from Horiba Jobin Yvon. The system employed laser at 532 nm (maximum output power 20-25 mW).

The thermal stability of the samples was investigated by simultaneous non-isothermal thermo-gravimetric analysis (TGA) using a SETARAM SETSYS Evolution 1750 instrument. The measurements were conducted at a heating rate of 10 °C/min in argon atmosphere (flow rate was 20 mL/min) in the temperature range of 30-800 °C. Instrument Alpha 1-4 LSC plus, CHRIST was used for material freeze drying.

Determination of amino group was performed according to the literature volumetric method and degree of amination obtained by Kaiser test (DA_{Kaiser}) [233].

The acid value (*AV*) was determined according to ASTM D664 standard, and presented as mg KOH g^{-1} of the specimen.

The pH values at the point of zero charge (pH_{PZC}) of the samples, *i.e.* the pH above which the total surface of the samples is negatively charged, were measured using the pH drift method [234]. For this purpose, 50 mL of a 0.01 M NaCl solution was placed in a jacketed titration vessel, thermostated at 25 °C, and N_2 was bubbled through the solution to stabilize the pH by preventing the dissolution of CO_2. The pH was then adjusted to successive initial values between 2 and 12, by adding either HCl or NaOH and the adsorbent (0.03 g) to the solution. The final pH, reached after 48 h, was measured and plotted against the initial pH. The pH at which the curve crosses the line pH(final) = pH(initial) is taken as the pH_{PZC}[233].

Arsenic concentrations in solution after adsorption and kinetic experiments were analyzed by the use of inductively coupled plasma mass spectrometry (ICP-MS), according to the literature method, using an Agilent 7500ce ICP-MS system (Waldbronn, Germany) equipped with an octopole collision/reaction cell, Agilent7500 ICP-MS ChemStation software, a MicroMist nebulizer and a Peltier cooled (2.0 °C) quartz Scott-type double pass spray chamber. Standard optimization procedures and criteria specified in the manufacturer's manual were followed. ICP-MS detection limit was 0.030 µg L^{-1} and relative standard deviation (RSD) of all arsenic species investigated was between 1.3-5.1 %. The ICP-MS method is a highly

sophisticated technique providing very low limit of detection (*LoD*) of 1 μg L^{-1} for arsenic determination.

3.4 Adsorption experiments in batch study

Batch experiments were conducted in 10 mL polyethylene bottles in 100 mg L^{-1} suspension with 10 mL of arsenic solution of appopriate concentration, time period, temperature and pH value. Adsorption study was performed in a relation to:

- As(V) and As(III) ions by using **ER/DETA/FO/FD,**

- As(V), As(III), Ni^{2+} and Cd^{2+} by using **NC-PEG/FO,**

- Cd^{2+}, Pb^{2+} and Cu^2 and As(V)ions by using **NC-L/FO**, and

- As(V) and As(III) by using **NC-MA/L'-MG** and **MC-O/L'-MG** adsorbents.

Time dependent batch experiments were determined in 0.078 mg L^{-1} As(V) solution during 2, 3 , 5, 10, 15, 30, 45, 60 and 90 min (**ER/DETA/FO/FD**. This study revealed that 45 minutes for **ER/DETA/FO/FD.** The effect of pH value on As(V) removal was studied with an initial As(V) concentration of 0.078 mg L^{-1}varying the pH in the range 2-12. Adsorption isotherm and thermodynamic parameters were evaluated by varying As(V) concentration (0.078, 0.44, 1.8, 3.1, 4.3, 5.8, 7.1 and 8.1 mg L^{-1}) and temperature (25, 35, 45 °C) for (**ER/DETA/FO/FD**).

Time dependent batch experiments were determined in 1 mg dm^{-3} solution for cations and 0.5 mg dm^{-3} for As(V) solution during 5, 10, 15, 30, 45, 60 and 120 min (**NC-PEG/FO**). This study revealed that 60 minutes was sufficient for quantitative removal of pollutants. The effect of pH value on As(V) removal was studied with an initial As(V) concentration of 0.5 mg dm^{-3} varying the pH in the range 2-12. Adsorption isotherm and thermodynamic parameters were evaluated by varying initial concentration (C_i) of cation (1, 2, 3, 4, 5, 6 and 7 mg dm^{-3}) and oxyanions concentration (0.1, 0.2, 0.5, 1, 2, 5 and 10 mg dm^{-3}) and temperature (25, 35, 45 °C).

Time dependent batch experiments were determined in 1 mg L^{-1} solution for cations and 0.2 mg L^{-1}for As(V) solution during 5, 10, 15, 30, 45, 60 and 120 min. This study revealed that 60 minutes was sufficient for quantitative removal of Cd^{2+}, Pb^{2+} and Cu^{2+}and As(V)ions. The effect of pH value on As(V) removal was studied with an initial As(V) concentration of 0.2 mg

L^{-1} varying the pH in the range 2-12. Adsorption isotherm and thermodynamic parameters were evaluated by varying cations concentration (1, 2, 3, 4, 5, 6 and 7 mg L^{-1}) and As(V) concentration (0.1, 0.2, 0.5, 1, 2, 5 and 10 mg L^{-1}) and temperature (25, 35, 45 °C) for **NC-L/FO.**

Adsorption equilibrium and thermodynamic parameters were evaluated varying concentration: 0.10, 0.30, 0.60, 1.0, 2.0, 3.0, 5.0 and 7.0 mg L^{-1} (0.10, 0.30, 0.50, 0.60, 1.0, 2.0, 3.0, 5.0, 7.0, 10.0, 15.0 and 20.0 mg L^{-1}) at three temperatures (25, 35 and 45 °C). A laboratory pH meter, *Mettler Toledo FE20/FG2* (*Switzerland*), with an accuracy of ± 0.01 pH units, was used for the pH measurements. The effect of contact time was studied in the range from 2 to 90 min with an initial As(V) concentration of 0.1 mg L^{-1}. The systems were equilibrated at different rate of stirring, 100-150 rpm for **NC-MA/L'-MG** and **MC-O/L'-MG** adsorbents.

Batch experiments were performed in ultrasound bath (*Bandelin electronic, Berlin, Germany, power 120W, frequency 35 kHz*) under appropriate conditions or under classical mixing using magnetic stirrer *Heidolph MR 3001* with digital display and controlled number of rpm (the stirrer diameter was $d_{stirrer}$=0.055m). Supernatants were filtered with 0.22 μm membrane and analyzed. The adsorbent capacity was calculated according to the Eq. 3.1.:

$$q = \frac{C_i - C_f}{m} V \qquad (3.1.)$$

where q is adsorption capacity in mg g^{-1}, C_i and C_f are initial and final arsenic concentrations in mg L^{-1} (μg L^{-1}), respectively, V is volume of the solution in L, and m is mass of adsorbent in g. The results of arsenic and other ions adsorption on glass tube wall and filters showed negligible effect on the reliability of results.

Also, the degree of conversion (degree of adsorption) could be expressed by a dimensionless number defined by Equation (3.2.):

$$\alpha(t) = (C_i - C_t)/(C_i - C_f) \qquad (3.2.)$$

where C_t is the concentration of As at time t, and this expression is used for calculation of extent of adsorption.

3.4.1 Desorption study

To evaluate the regeneration capabilities, after adsorption experiments and washing with DIW, wet adsorbents (m/V=100 mg L^{-1}) were re-dispersed in 20 mL of regenerant. Different solution: NaOH (0.2 or 0.5 mol L^{-1}), NaCl (0.2 or 0.5mol L^{-1}) or citrate (0.01 mol L^{-1}) or their combination was used for arsenic elution. The amount of desorbed As(V) was measuredaftermagnetic mixing for 3 h in a batch system. Five consecutive adsorption/desorption cycles were performed in triplicate by using all adsorbents.

3.4.2 Adsorption data modeling ER/DETA/FO/FD

Commonly used isotherm models were applied for fitting of the experimental adsorption data [69] (Table 2.4). Calculations of equilibrium and thermodynamic parameters were obtained by using OriginPro 9.1$^{®}$ software with non-linear least-squares methods. Calculations of equilibrium and thermodynamic parameters were obtained by using OriginPro 9.1$^{®}$ software with non-linear least-squares methods. Unknown parameters of the isotherm models were determined using Levenberg-Marquardt (LM) algorithm and Orthogonal Distance Regression (ODR) algorithm (Theoretical part). Determination of thermodynamic parameters were calculated according to Equations (3.3.and 3.4.):

$$\ln(K_0) = \Delta S^{°}/R - \Delta H^{°}/RT \tag{3.3.}$$

$$\Delta G^{°} = -RT\ln(K_0) \tag{3.4.}$$

where R is the universal gas constant, T is temperature (K), and K_0 is the thermodynamic equilibrium constant; K_0 is Langmuir constant (K_L) or it is constant determined by using the method of Karthikeyan [235] by plotting $\ln(q_e/C_e)$ versus q_e and extrapolating $\ln(q_e/C_e)$ to zero.

3.4.3 Statistical criteria used for evaluation of the godness of fitting

In order to select the most appropriate isotherm and kinetic models comprehensive statistical analysis was applied. To assure the accuracy, reliability, and reproducibility of the collected data, all batch tests were performed in triplicate, and only mean values were reported.

Blank tests without sorbent addition showed that the losses resulting from sorption on container walls were negligible. All kinetic, isotherm and thermodynamic parameters and their standard errors were calculated, with non-linear least-squares methods, using commercial software (Microcal Origin 8.0). The non-linear isotherm modeling has numerous benefits over linearization models and one of them is the involvement of the minimization or maximization of error distribution between the experimental data and the modeled isotherm based on its convergence criteria. The quality of the fitting of experimental data was generally evaluated by the use of correlation coefficient (R^2). Herein, apart from the correlation coefficient (R^2), the quality of fitting experimental data was evaluated by other statistical criteria given in Table 2.6.

3.5 Kinetic modeling and activation parameters

Calculations of kinetic parameters were obtained by using OriginPro 9.1[®] software. Kinetic model used for fitting of experimental data: pseudo-firstorderorLagergrenmodel,pseudo-secondorderor Ho-McKay model, Roginsky-Zeldovich-Elovich equation and second-order rate equation, and adsorption diffusion models: homogeneous solid diffusion model, parabolic or Weber-Morris model, Dunwald-Wagner model and double exponential model [77]. The kinetic process was investigated by varying initial adsorbate concentration and mixing rate. Concentration ranges for kinetic study were selected based on adsorption experiments. The initial adsorbate concentrations were selected to produce the most significant system responses at appropriate period of time, *i.e.* at the beginning, middle and plateau parts of each isotherm. Mixing rate of 100, 250 and 400 rpm was used to study effect of agitation on mass transfer processes.

Rate constants and activation parameters were calculated from the results obtained in kinetic study at 25, 35, 45 °C using the following eqations(3.5.-3.8.) [236]:

$$\ln k = -(E_a/R)1/T + \ln A \qquad (3.5.)$$

$$\Delta S^{\neq}{}_{25} = (\ln[k_2 h/KT] + E_a/RT)R \qquad (3.6.)$$

$$\Delta H^{\neq}{}_{25} = E_a - RT \qquad (3.7.)$$

$$\Delta G^{\neq}{}_{25} = \Delta H^{\neq}{}_{25} - \Delta S^{\neq}{}_{25}T \qquad (3.8.)$$

where: h is Planck constant, K Boltzman constant and R gas constant (8.314 kJ mol^{-1} K^{-1}).

3.5.1 Model free kinetic: determination of activation parameters by iso-conversional method

The rate of the adsorption can be described as the amount of adsorbate adsorbed per unit of time, and could be described by following eq. (3.9).:

$$r_{ad} = d\alpha/dt \tag{3.9.}$$

where α isa dimensionless number which denotes the time-dependent fraction of bounded arsenic, defined by Eq. (3.2.).

The rate of chemical reaction/adsorption, for a particular isothermal process, could be given by the general formula in differential form:

$$d\alpha/dt = kf(\alpha), \text{ or in integral form of rate law, } g(\alpha) = kt \tag{3.10}$$

where k is the reaction constant/adsorption constant and $f(\alpha)$ the kinetic model, and $g(\alpha)$ is the integral form of reaction/adsorption model.

The temperature dependence of the reaction/adsorption rate constant k, given by Arrhenius eq. (3.5.), was substituted in eq. (3.10), and the following relation, presented by eq. 3.11., was obtained:

$$g(\alpha) = Ate^{-E_a/RT} \tag{3.11.}$$

Kinetic analysis of isothermal data can be conveniently performed by either using conventional model-fitting methods or model free isoconversional methods. In the first option, it was possible to calculate activation parameters, while in the second, activation energy, E_a, can only be calculated. The isoconversional method [12,13] is based on taking of the natural logarithm of eq. (3.11.) which gave eq. (3.12.):

$$-\ln t = \ln[A/g(\alpha)] - E_a/RT \tag{3.12}$$

3.5.2 Surface complexation modeling

Surface complexion models (SCMs), chemical models based on mechanistic and atomic scale approach, are developed to predict the adsorption of heavy metal ions by different forms of oxide adsorbents [101]. These models describe the development of surface charge and potential together with ion adsorption in a quantitative manner. MINTEQ is a SCMs computer program which was applied for modeling of the adsorption processes in this work. MINTEQ includes: mathematical structure from MINEQL [102] and thermodynamic data base, temperature correction of equilibrium constants using either the Van't Hoff relationship and ionic strength correction with the extended Debye-Hückel equation or the Davies equation from WATEQ3 [239]. Protonation/deprotonation constants ($\log K$) and arsenate intrinsic surface complexation constants and model parameters are given in Table 3.3. Adsorption model used in this study was HFO (Dzombak & Morel) for **ER/DETA/FO/FD**.

Table 3. 3. Intrinsic surface complexation constants for goethite and modeling parameters

Surface reaction	log K [102]
$=FeOH + H^+ \rightleftharpoons =FeOH_2^+$	7.29
$=FeOH \rightleftharpoons =FeO^- + H^+$	-8.93
$=FeOH + AsO_4^{3-} + 3H^+ \rightleftharpoons = FeH_2AsO_4 + H_2O$	30.98
$=FeOH + AsO_4^{3-} + 2H^+ \rightleftharpoons = FeHAsO_4^- + H_2O$	25.84
$=FeOH + AsO_4^{3-} + H^+ \rightleftharpoons = FeAsO_4^{2-} + H_2O$	19.50
$=FeOH + AsO_4^{3-} \rightleftharpoons =FeOHAsO_4^{3-}$	11.92
$=FeOH + Ca(OH)_2 \rightleftharpoons =FeOHCa^{2+} + 2OH^-$	4.97
$=FeOH + Ca(OH)_2 \rightleftharpoons =FeOCa^+ + H_2O + OH^-$	-5.85
$=FeOH + Mg(OH)_2 \rightleftharpoons =FeOMg^+ + H_2O + OH^-$	-4.6
$=FeOH + 3H^+ + PO_4^{3-} \rightleftharpoons =FeH_2PO_4 + H_2O$	32.08
$=FeOH + 2H^+ + PO_4^{3-} \rightleftharpoons =FeHPO_4^- + H_2O$	26.39
$=FeOH + H^+ + PO_4^{3-} \rightleftharpoons =FePO_4^{2-} + H_2O$	20.73
$=FeOH + 2H^+ + SO_4^{3-} \rightleftharpoons =FeSO_4^- + H_2O + H^+$	7.78
$=FeOH + SO_4^{3-} \rightleftharpoons =FeOHSO_4^{2-}$	0.79
$=FeOH + SiO_4^{4-} + 2H^+ \rightleftharpoons =FeOSiO_2OH^{2-} + H_2O$	-11.69
$=FeOH + SiO_4^{4-} + 3H^+ \rightleftharpoons =FeOSiO(OH)_2^- + H_2O$	-3.22
$=FeOH + SiO_4^{4-} + 4H^+ \rightleftharpoons =FeOSi(OH)_3 + H_2O$	4.28
Modeling parameters	
Surface site density	2.3 site nm^{-2}
Adsorbent surface area	143 m^2 g^{-1}
Goethite concentration	0.056 g L-1
Solid concentration	0.10 g L-1
As(V) concentration	0.078mg L-1
pH range	2-12

3.6 Modeling of adsorption processes in a fixed bed column study

Description of the dynamic behavior of solute in a fixed-bed is difficult to describe as the process does not occur at a steady state condition. Due to the difficulties related to appropriate mathematical modeling of adsorption processes in a fixed bed flow system, simplified modeling [240] of the experimental data was applied by using five mathematical models: The Bohart-Adams model [241], The Thomas model [242], The Yoon-Nelson model [243], and Modified dose-response model [244]. Assessment of the breakthrough performance of **ER/DETA/FO/FD** packed in a fixed bed-column was conducted at different As feed concentration and flow rates. The Bohart-Adams model [241] is given by eq. (3.13.):

$$\frac{C}{C_0} = \frac{1}{1+\exp\left[k_{BA}\left(N_0\frac{Z}{F}-C_0t\right)\right]}$$
(3.13.)

The Thomas model [242] is given by eq. (3.14):

$$\frac{C}{C_0} = \frac{1}{1+exp\left[k_{Th}\left(\frac{q_0m}{Q}-C_0t\right)\right]}$$
(3.14.)

The Yoon-Nelson model [243] is given by eq. 3.15.:

$$\frac{C}{C_0} = \frac{1}{1+exp[k_{YN}(\theta-t)]}$$
(3.15.)

The Modified dose-response model [244] is given by eq.3.16.:

$$\frac{C}{C_0} = 1 - \frac{1}{1+\left(\frac{Qt}{b}\right)^a}$$
(3.16.)

where, C_0 and C (mg L^{-1}) are the influent and effluent arsenic concentration; k_{BA} (L mg^{-1} min^{-1}) is the kinetic constant; F (cm min^{-1}) is the linear velocity calculated by dividing the flow rate by the column section area; Z (cm) is the bed depth of column; N_0 (mg L^{-1}) is the saturation concentration; k_{Th} is the Thomas rate constant (mL min^{-1} mg^{-1}); q_0 is the equilibrium uptake per g of the adsorbent (mg g^{-1}); m is the amount of the adsorbent in the column (g); Q is the flow rate of the solution passing through the column (mL min^{-1}); k_{YN} (min^{-1}) is the Yoon-Nelson rate constant, Θ (min) is the time required for 50 % adsorbate breakthrough; t (min) is the

breakthrough or sampling time and parameters *a* and *b* are from the modified dose-response model.

3.6.1 Fixed-bed column study

Fixed-bed column study was performed in order to examine the behavior of **ER/DETA/FO/FD** in a dynamic system. A glass tube of 0.8×12 cm (d×H) with sintered filter and PTFE valve packed with **ER/DETA/FO/FD** was used to conduct the flow-through column experiment with a down-flow design. Sand was added to the top of column bed after pre-treatment to prevent an even flow distribution. A column adapter was attached to the top of the column to allow PTFE tubing to be fitted into the column. Prior to the column being attached, the feeding solution (DIW) was pumped through the tubing to remove any impurities from the rig. After addition of DIW, a vacuum was applied to remove air bubbles trapped during inflow of feeding solution. The effluent samples were collected at predetermined period of time and the concentration of arsenic in the effluent was determined using ICP-MS technique.

The flow rate *Q*, empty bed volume (*EBV*), pH, and the mass of **ER/DETA/FO/FD**, were adjusted to obtain optimal empty bed contact time (*EBCT*). The flow rate of feed solution was varied at $Q = 0.5$, 1.0 and 2.0 mL min^{-1}. All experiments were performed at 25 °C. The feed water was allowed to pass through the hybrid adsorbent bed using peristaltic pump Ismatec. Residence time *EBCT* was calculated according to: $EBCT = H/\gamma$, where H is bed depth (cm) and γ is linear flow rate (mL cm^{-2} s^{-1}). Breakthrough point was designated as the feed volume supplied to a column up to $C/C_0 = 0.03$ ($C_0 = 0.33$ mg g^{-1}).

3.6.2 Modeling of adsorption in a flow system

A design modeling

Adsorbent media density and porosity were evaluated by pycnometer analysis according to procedure presented by the Sontheimer *et al*. (1988) [245]. Assuming cylindrical pores, the average pore diameter was calculated from the surface area–pore volume ratio as suggested by Crittenden et al. [245,246] (Eq. 3.17.):

$$\frac{2}{r_{pore}} = \frac{A_{ad}}{V_{ad}}$$ (3.17.)

where r_{pore} is the average pore radius (m); A_{ad} is the surface area of the adsorbent (m^2); and V_{ad} is the pore volume of the adsorbent (m^3).

Quantification of epoxy and amino groups were performed according to the literature volumetric methods [247,248]. The pH values at the point of zero charge (pH$_{PZC}$) of the samples, *i.e.* the pH above which the total surface of the samples is negatively charged, were measured using the pH drift method [249].

Equilibrium adsorption experiments

Arsenate removal in batch adsorption experiments with hybrid adsorbent were conducted in 10 mL model water with initial arsenate concentration $C_0 \approx 100$ µg L^{-1} with adsorbent dosages of 100-500 mg L^{-1} at pH values of 6.7±0.2. The sample solutions were agitated for 1 day and filtered through a Millipore 0.22 µm membrane filter (Bedford, MA, USA) before analysis. Adsorption equilibrium was analyzed using the Freundlich adsorption isotherm model (Eq. (3.18.)).

$$q = K \times C^{1/n}$$ (3.18.)

where q is adsorption capacity, K is the Freundlich adsorption capacity parameter, C_E is the equilibrium concentration of adsorbate in solution, and 1/n is the Freundlich adsorption intensity parameter.

Pore Surface Diffusion Model prediction of a Short Bed Adsorber column performance and its verification via a Short Bed Adsorber Test

Arsenic breakthrough curve of short bed column (SBC) was predicted by the Pore Surface Diffusion Model (PSDM) using the AdDesignS™ software developed by Michigan Technological University [35]. PSDM is a dynamic packed bed model that covers both pore and surface diffusion models and has been successfully applied in the prediction of the breakthrough

curve and the feasibility of adsorbent media [245,246,250,251]. Determination of the external mass transport coefficient were based on the Gnielinski correlation [245]:

$$k_f = \frac{[1+1.5(1-e)] \times D_l}{d_p} \times \left(2 + 0.644 \times Re^{1/2} \times Sc^{1/3}\right) \tag{3.19.}$$

$$Re = \frac{\rho_l \times \phi \times d_p \times v_l}{e \times \mu_l} \tag{3.20.}$$

$$Sc = \frac{\mu_l}{\rho_l \times D_l} \tag{3.21.}$$

Constraints: Re x $Sc > 500$; $0.6 \leq Sc \leq 10^4$; $1 \leq Re \leq 100$; $0.26 \leq e \leq 0.935$; k_f is the external mass transport coefficient (calculated $k_f \approx 6.5$ x 10^{-3} cm s^{-1}); Re is the Reynolds number (unitless); Sc is the Schmidt number (unitless); d_p is the adsorbent particle diameter ($d_p = 0.30$ x 10^{-3} m); $e_p \approx 0.7$; D_l is the free liquid diffusivity for arsenate ($D_l = 9.05$ x 10^{-10} m^2 s^{-1}); e is the bed void fraction ($e = 0.4$); μ_l is the dynamic viscosity of water at 20 °C ($\mu_l = 1.002$ x 10^{-3} N s m^{-2}); ρ_l is the density of water at 20 °C ($\rho_l = 998.2$ kg m^{-3}); Φ is the particle shape factor ($\Phi = 1$); v_l is the liquid superficial velocity ($v_l \approx 0.00265$ m s^{-1}).

Considering that the material was very porous (the particle porosity $e_p \approx 0.7$), the impact of surface diffusion was assumed negligible and the pore diffusion coefficient was estimated using eq. (3.22) [245,246,250–253]:

$$Dp = \frac{e_p \times D_l}{\tau} \tag{3.22.}$$

Applying the correlation for electrolyte solutions (eq. (3.23.)), the tortuosity was determined [32,246,251,252]:

$$\tau = \frac{(2-e_p)^2}{e_p} \tag{3.23.}$$

The estimated value for toruosity was $\tau \approx 2.4$ and $D_P \approx 2.6 \times 10^{-6}$ cm^2 s^{-1}.

The relative importance of internal and external mass transport resistance was evaluated by estimating the pore (BiP) Biot number using the relationship given by eq. (3.24.) [32,246,251,252]:

$$Bi_p = \frac{k_f \times d_p}{2 \times Dp} \tag{3.24.}$$

Although a number of studies have verified the validity of the PSDM to predict breakthrough curves of arsenic-only water matrices [32,246,251,252], the SBC tests were

conducted under the same pH and arsenic concentration conditions in order to validate PSDM prediction of arsenic removal by hybrid media. In the SBC test, 0.4 g of goethite impregnated media was packed at top a support of cotton and glass beads were placed above and below to provide evenly distributed flow. Wall effect on the mass transfer was neglected since used adsorbent media provided d_{column}/dp ratio of ~40 [254]. Arsenic-only water with initial arsenic concentration of ~150 μg L^{-1} was introduced through the column until complete breakthrough (Ce/Co >95%) at hydraulic loading rate of 2.65 L m^{-2} s^{-1} (4.2 gpm ft^{-2}), which is within the recommended loading rates for full scale operations. Although relatively high, this hydraulic loading rate was adequate in capturing the mass transfer zone and minimizing the film mass transport limitation.

Full-Scale System Modeling Using Validated Pore Surface Diffusion Model

The pore surface diffusion model was used to model the performance of full scale fix bed systems operating at the same loading rate as the SBA column tests. The length of the packed bed was changed to achieve the desired EBCTs of 2.5, 5, and 10 min. The modeling was conducted with a realistic value of C_0=30 μg L^{-1} while the water chemistry, pH, and bed porosity were assumed to be the same as those used in the SBA test [246,251].

4. RESULTS AND DISCUSSION

4.1 Efficient arsenic removal by cross-linked macroporous polymer impregnated with hydrous iron oxide

Specific topic of this study was aimed at the definition of optimal parameters for novel hybrid adsorbent synthesis to be applicable for effective arsenic removal. Few studies describe synthesis of the macroporous resin [255,256]. Growing interest in macroporus resin, based on glycidyl methacrylate, GMA, and ethylene glycol dimethacrylate, EGDMA, is due to innumerable possibilities for subsequent chemical transformation of pendant epoxy group. The resin synthesized in that way is used as a versatile support for subsequent modification/-impregnation with high affinity material for arsenic removal. In this work, the synthesis procedure was conducted in three successive steps.

Considering the above-mentioned guidelines, the research was focused on the development of new adsorbents and study of their performances in the processes of arsenic removal. In order to define optimal adsorbent synthesis, amination of the **ER** was conducted by either classical or ultrasonically assisted synthesis at different molar ratio of reactants. The optimal conditions for amination of the **ER** were: 20 mL of DETA in 50 mL of THF, under ultrasound treatment for 2 h at 30 °C. It was also found that ultrasonication was an efficient method usefully applied to the intensification of the nucleophilic attack by DETA. Controlled oxidative precipitation of porous and size-controlled aggregates of FO on the **ER/DETA**, and application of two post-processing methods: vacuum/drying and freeze/drying treatment of the wet **ER/DETA/FO** produce **ER/DETA/FO/VD** and **ER/DETA/FO/FD**, respectively. The best performances were obtained by using 66.6 mL, 0.25 mol L^{-1} of FeSO$_4$x7H$_2$O. Reaction between Lewis basic sites - primary and secondary amino group and Lewis acidic species - iron(III) ion, provide initial formation of nucleation center, which contribute to controlled FO nanocrystal growth on the **ER/DETA** surface. The usage of ultrasound, on the other hand, causes a detrimental effect on FO precipitation, *i.e.* significant amount of free non-bonded FO

nanomaterial was obtained. In other words, homogeneous precipitation in solution prevails over heterogeneous nanocrystal growth at the **ER/DETA** surface.

4.1.2 The results of adsorbents characterization

The structural analysis

The crystal structure of goethite was determined by XRD (X-ray diffraction), the most reliable technique for identifying a particular oxide based on the long range order of the atoms. The XRD patterns of the **ER**, **ER/DETA**, goethite and **ER/DETA/FO/FD** are shown in the Fig. 4.1. The analysis shows characteristic peaks corresponding to resins, amorphous goethite [257] and goethite impregnated **ER/DETA** observed at the 2θ value of 17.8, 21.2, 33.2, 36.6 and 53.2 ° (ICDD PDF2 No. 81-0464). The obtained XRD patterns show line broadening and significant scattering which may be the result of small crystallite size and amorphous properties of precipitated hydrous iron oxide mainly in goethite form.
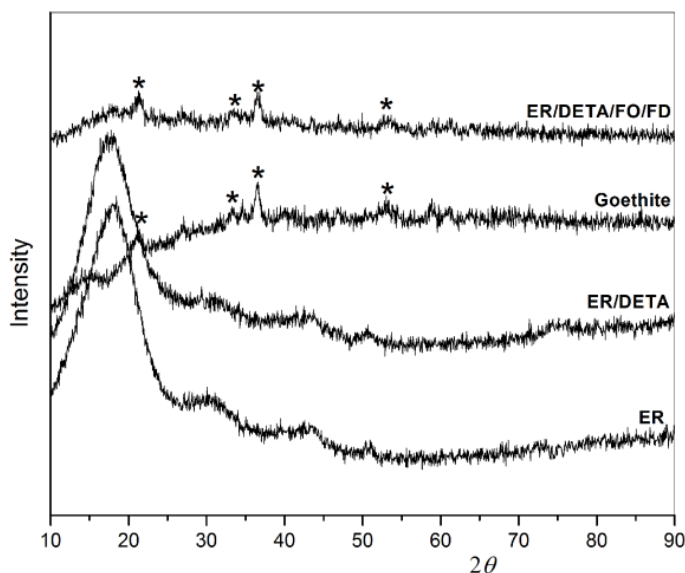
Figure 4. 1. XRD patterns of **ER**, **ER/DETA**, goethite and **ER/DETA/FO/FD**

The textural parameters and surface properties

The specific surface area and adsorbent porosity are important factors which govern the number of adsorbent active sites and thus affinity with respect to specific pollutants. Number of available functional sites per unit mass of material is directly related to nature of the material and its textural properties. The porosity contributes to the "internal" surface area of the material which has significant influence on the adsorption rate and capacity. In this study, to obtain optimal textural properties, beneficial for efficient arsenic removal, the design of pore structure and geometry was achieved by multi-step synthesis of adsorbents and post-processing of obtained material. The textural parameters of the synthesized adsorbents, given in Table 4.1, indicate higher surface area and moderate pore diameter for the **ER/DETA/FO/FD**, comparing to **ER/DETA/FO/VD**. Such findings show that the different drying processes cause formation of different packing properties of FO deposit. Classical drying methods cause shrinkage of FO yielding packed and dense structure. Otherwise, the ice-crystal nucleation and growth followed by water evaporation during freeze/drying process causes a larger porosity of FO in the **ER/DETA/FO/FD** sample. Negative effect of the FO precipitation on textural properties, *i.e.* clogging of mesopore in the **ER/DETA** occurred at some degree, is compensated by developed surface area and porosity of precipitated material. Similar results were found for calcite modified with FO in a previous work [121,230,231]. The results of both BET (Brunauer-Emmett-Teller) and BJH analysis (Table 4.1), and the adsorption studies indicate significant influence of the textural properties on the adsorbent performance. The magnitude of electrical charge density change (Table 4.1) shows that pH_{pzc} is shifted to lower value after adsorption which indicates specific arsenic adsorption.

Table 4. 1. The textural properties and pH_{PZC} of the examined adsorbents

Adsorbent	Specific surface area (m^2 g^{-1})	Total pore volume (mL g^{-1})	Pore diameter (nm)	pH_{PZC}[a]	pH_{PZC}[b]
ER	56	0.95	77	6	5.8
ER/DETA	75	1.45	98	7.5	6.2
ER/DETA/FO/VD	116	0.88	62	8.5	7.3
ER/DETA/FO/FD	143	0.99	68	8.8	7.5
ER/DETA/FO/FD-3	178	1.36	86	8.9	7.6

[a] before and [b] after adsorption

Morphology parameters

Considering small particle size of FO [121,230,231], the surfaces of such crystals were commonly examined by scanning electron microscopy (SEM). In this work, the morphologies of the macroporous resins, **ER**, **ER/DETA** and **ER/DETA/FO/FD**, were examined by FEG-SEM technique. The representative images are shown in Fig. 4.2.
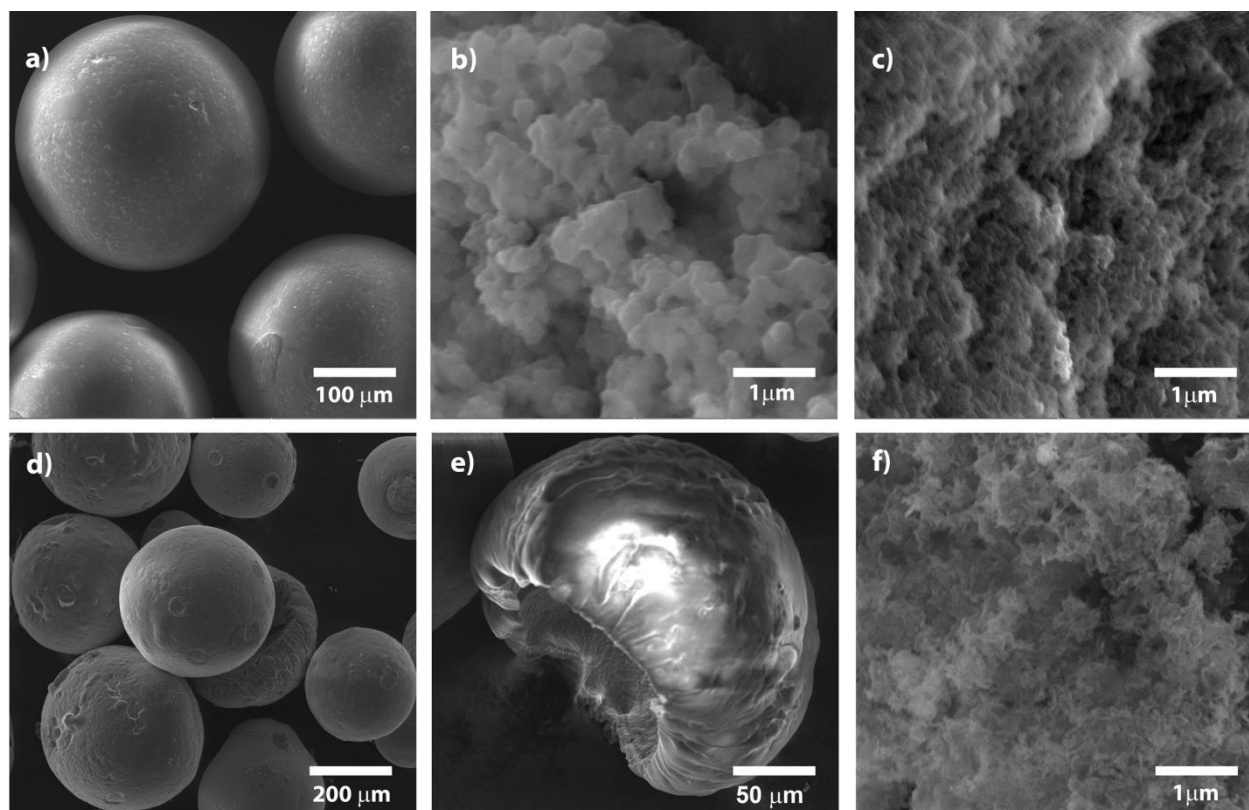
Figure 4. 2. FEG-SEM images of **ER** (a, b); **ER/DETA** (c); **ER/DETA/FO/FD** (d–f)

The **ER** has spherical structure with irregular shape, smooth surface and no sharp edges with the mean diameter of 200–500 nm (Fig. 4.2 a,b). The coarse surface of porous **ER** copolymer beads formed during the copolymerization process (Fig. 4.2 a,b) becomes more pronounced after modification of epoxy group with **DETA** (Fig. 4.2 c). The **ER/DETA** impregnation support with the FO does not affect significantly the shape and size of the basic structure. However, distinctive acicular morphology of FO appearedin the **ER/DETA/FO/FD** (Fig. 4.2 d-f) with occasional finding of irregular jellyfish like grain (Fig. 4.2 e).The obtained

needlelike FO with sharp-cut peak but with no preferential direction with the dimensions of adsorbent beads 286±72 μm, determined using MIRA TESCAN *in situ* measurement software, entirely covers surface of the **ER/DETA/FO/FD**.

FTIR spectra

FTIR analysis was applied for estimation of the presence of functional groups at adsorbent surface, the bond weakening or strengthening, and types of interactions between surface functional groups and adsorbed As(V) species. The qualitative differences in the FTIR spectra of examined materials were observed before and after As(V) adsorption is given on Fig. 4.3.
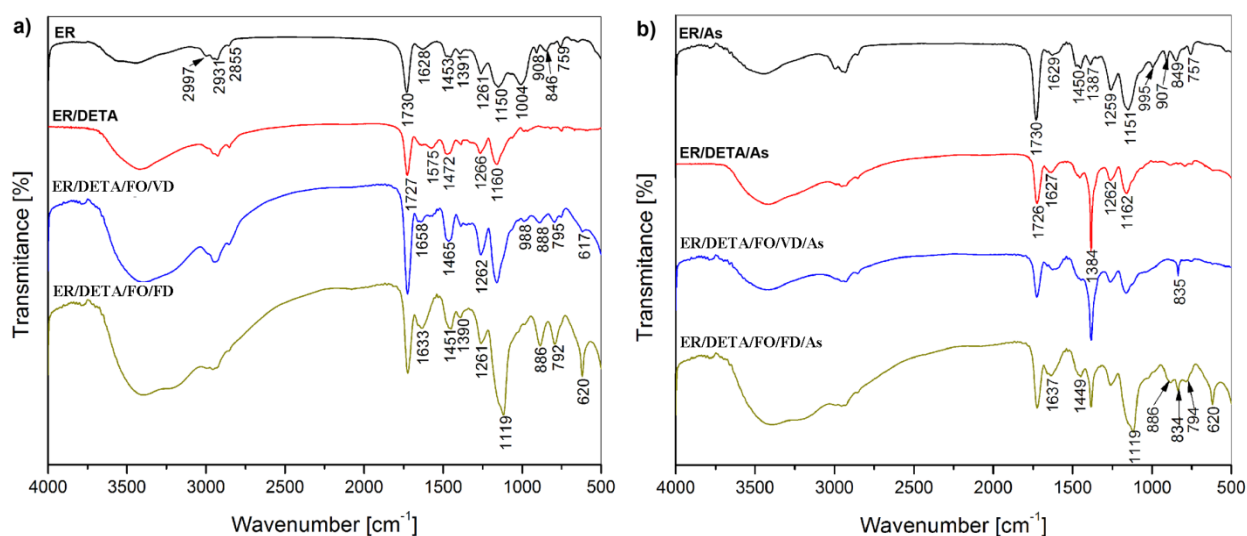
Figure 4. 3. FTIR spectra of **ER**, **ER/DETA**, **ER/DETA/FO/VD** and **ER/DETA/FO/FD** before (a) and after (b) As(V) adsorption

The chemical structure of the **ER** was confirmed with peaks characteristic for ester group at 1730 cm^{-1} and 1150 cm^{-1}, which was assigned to the stretching vibration of C=O and C−O bond, respectively. The asymmetric stretching vibration of epoxy group was observed at 908 cm^{-1}. In regards to the **ER**, distinct changes were displayed in the spectra of the amino modified **ER**/**DETA**, and the goethite modified materials. New bands in the range 3200-3400 cm^{-1}, at

1658/1633 and 1160/1119 cm^{-1} attributed to N-H and C-N vibrations and disappearance of epoxy group peak at 908 cm^{-1}, indicate successful modification of epoxy group with **DETA** in **ER/DETA**. The presence of epoxy and amino groups was determined volumetrically as well. The results of calculation show presence of 3.11 mmol g^{-1} of epoxy group in the **ER** and 6.1 mmol g^{-1} of amino in the **ER/DETA**. The characteristic peak of the goethite, as a result of vibration modes of hydroxyl groups, Fe–OH, was observedat 795 and 888 cm^{-1} for the **ER/DETA/FO/VD**, and 792 and 886 cm^{-1} for the **ER/DETA/FO/FD** [114]. Other characteristic goethite IR bands, usually found in the range 1100-1000 cm^{-1}, were not visible due to overlapping with strong broad peaks at 1160 and 1119 cm^{-1}. The significant difference in the peaks structure at position ≈795 and ≈888 cm^{-1} was noted after comparing spectra of the **ER/DETA/FO/VD** and the **ER/DETA/FO/FD**.

Differences between band structure in spectra of adsorbents, before and after adsorption, could be noticed from the results presented in Fig. 4.3. For all analyzed adsorbents, a gradual weakening of the bands which correspond to Fe–OH/FeO–OH group (peaks located at ≈790 and ≈880 cm^{-1}) was evident, due to As(V) complexation. In the spectra of **ER/DETA/FO/VD/As** and **ER/DETA/FO/FD/As** loaded adsorbents, a new band, corresponding to As–O stretching vibration of coordinated, uncomplexed/unprotonated As–O–Fe, arsenic species, appeared at ≈835 cm^{-1}, corresponds to the frequency of the As–O–Fe bond of complexed As(V) [258,259]. The significantly higher intensity of band ascribed to iron bonded As(V) is in accordance with published results [121,230,231], and was overlapped with the band from absorption of residual organic functionalities. At higher surface coverage bidentate binuclear complex was a preferential type of bonding [260], where two of four As–O bonds are bonded to an iron atom, and the remaining two are present as unprotonatedand/or protonated.

TGA analysis

The TG analysis of the **ER**, **ER/DETA** adsorbents show specific behavior (Fig. 4.4). The TG curve of the **ER** displayed a weight loss of 20 % in the temperature range 200-250 °C followed by rapid material transformation (degradation), the steep region showed 60 % of material loss until 350 °C, and final degradation of 20 % (probably highly carbonized and

condensed material) of residual above 450°C. The TG analysis of the **ER/DETA** showed 20 % weight loss at slow degradation rate (in the range 20-250 °C), followed by gradual degradation of the 50 % of starting material in the range of 250-425 °C. During the final temperature range 425-800 °C slow degradation rate of 30 % residual condensed organic material takes place. The differences in the stability of **ER** and **ER/DETA** arise from the presence of amino groups which participate in thermally supported/induced condensation reaction by creating heterocyclic structure of higher thermal stability, and thus low slope of the TGA curve in the final degradation step for the **ER/DETA** was observed.

The highest thermal stability was found for **ER/DETA/FO/FD**. The **ER/DETA/FO/FD** dehydration produces loss of 5 % of mass before 100 °C which is thermally stable up to 220 °C. The main weight loss phase (of 60 %) was determined in the temperature range 220-500 °C, at lower degradation rate than for the **ER/DETA**. Barely noticeably decrease in weight (around 3 %) was noticed in the range 500 to 600 °C, followed by 5 % material loss before 700 °C. At higher temperature a constant value of residual material shows 20 % of iron oxide (Fe_3O_4), which corresponds to 11.2 % of iron oxide deposit present in the **ER/DETA/FO/FD**.
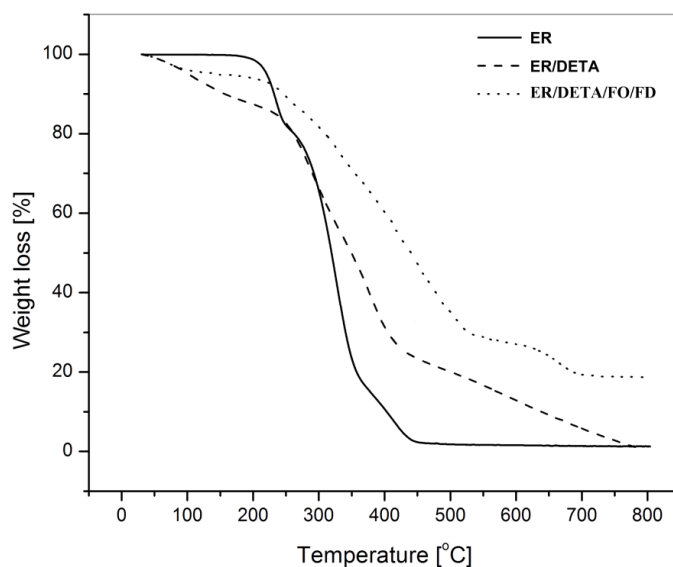
Figure 4. 4. TGA curves of **ER**, **ER/DETA** and **ER/DETA/FO/FD**

4.1. 3 Adsorbents performance in non-competitive conditions

Effect of pH on arsenic removal

      Considering pH influence on arsenic speciation and ionization state of adsorbent surface, in the first part of analysis, the influence of pH to arsenic adsorption was examined. Herein, two independent comparative experiments were conducted by applying classical stirring and ultrasound treatment and similar results of arsenic removal made the former method more preferable. Study of the arsenic removal efficiency with respect to mixing rate, from 100 to 400 rpm, revealed the optimal value to be 250 rpm, and it was used in subsequent experiments. The intensive mixing of the solution in contact with the adsorbent surface led to the suppression of the boundary layer and consequently increased adsorption rate. The percentages of arsenic removal *versus* equilibrium pH value for the **ER/DETA/FO/VD** and **ER/DETA/FO/FD** adsorbents are shown in Fig. 4.5.
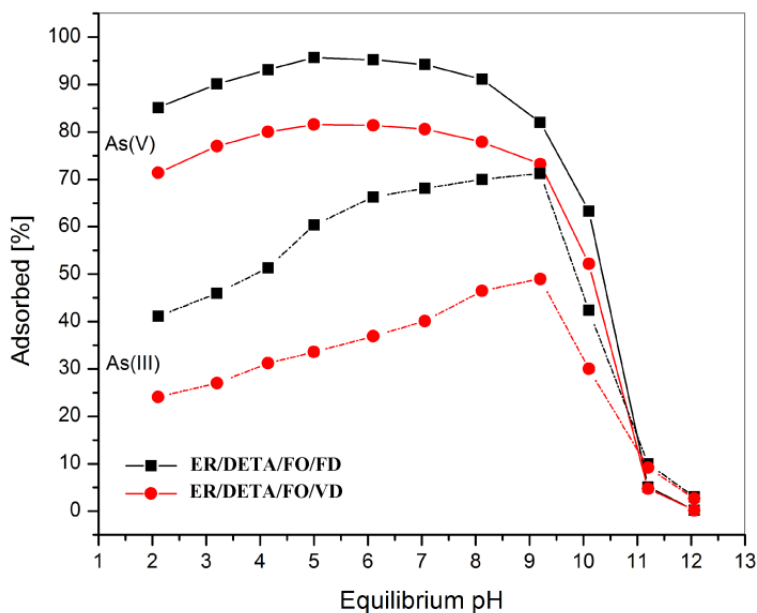
Figure 4. 5. Effect of pH on adsorption of As(V) and As(III) on **ER/DETA/FO/VD** and **ER/DETA/FO/FD** adsorbents

The arsenate is typically present in the mono and divalent anionic forms in natural water under oxidizing conditions. The presence of different arsenic species depending on the pH value of solution is described, from neutral to ionic and complex forms *vs* pH value [261,262]. The pK_a values of triprotic arsenic acid are 2.3, 7.0 and 11.5, which reveals that molecular form (H_3AsO_4) exists at pH<2.0, and anionic species, in the appropriate ratio of $H_2AsO_4^-$ or $HAsO_4^{2-}$ anion, at higher pH value. The most effective adsorption of weak acid is usually found at pH value in the vicinity of pKa [261,262]. It is in the accordance with maximum As(V) removal in pH value range 3.0-7.0. Also, low dependence of As(V) removal on the pH value change in this region was noticed. The As(V) removal decreased from 97 to 82 % when pH value increased from 5.0 to 9.0. From the fact that in the pH range 4.0-7.0 effective separation of As(V) could be accomplished, all further experiments were conducted at pH 5.0. At pH below 4.0 iron was remarkably dissolved, and due to **FO** erosion adsorbent performance significantly deteriorated.

The 60% of As(V) adsorbed on the **ER/DETA** at pH 5.0 imply that the **ER/DETA** is not suitable for arsenic removal at low pH value. However, 70% of the As(V) removal from the solution by the **ER/DETA** at pH 7.0 showed certain potential at higher pH. For the **ER** even lower removal efficiency was obtained. Due to the presence of amino groups surface basic properties were increased, and at the pH$_{PZC}$ value of the **ER/DETA** (7.5) preferable electrostatic interactions favored adsorption of mono- and divalent anionic species at pH<pH$_{PZC}$ value.

Equilibrium study

The interaction/bonding state between solutes and adsorbent surface at equilibrium can be described by fitting experimental data with adsorption isotherms. Chosen pH value of 5.0 was favorable for the selective binding of ionic forms of As(V) species. Moreover, this pH is usually found in natural waters, which means that most of the water samples are ready to use without additional pH adjustment. From the techno-economical aspect, this has beneficial impact on capital and operational costs of overall adsorption process.

Various isotherm models were used to evaluate the adsorption capacity and statistical criteria to evaluate quality of model fitting. The obtained experimental data gave satisfactory correlation (R^2>0.93) by applying non-linear regression method with commonly used isotherms:

119

Langmuir, Redlich-Peterson, Sips and Jovanovic. Appropriate statistical justification of the quality of experimental data fitting was obtained by using the Sips equation (Table 4.2; Fig. 4.6). The Sips isotherm combines Langmuir and Freundlich models, and reduces to Freundlich isotherm at low adsorbate concentration. Also, it predicts a monolayer adsorption, in accordance to the Langmuir isotherm, at higher concentrations. According to the Sips isotherm, mechanism of As(V) ion adsorption on the **ER/DETA/FO/FD** can be described as monolayer heterogeneous adsorption, where adsorbed ion/molecule possesses different enthalpies and adsorption activation energies.

The results of experimental data were fitted to the Langmuir isotherm model; high predicted adsorption capacities were obtained for the **ER/DETA/FO/FD**: 31.0 mg g^{-1} at 25 °C, 32.2 mg g^{-1} at 35 °C, and 34.0 mg g^{-1} at 45 °C (Table 4.2). Higher adsorption capacities, 38.4 mg g^{-1} at 45 °C, was due to preferable textural parameters of the **ER/DETA/FO/FD-3** adsorbent, which is of less significance in comparison to lower dimensional stability of this material. The collision of spherical adsorbent grains caused mechanical attrition and erosion of external **FO** deposit, and the appearance of turbidity, at low extent, was found in working medium with **ER/DETA/FO/FD-3**. Such behavior represents an operational problem at laboratory level, and due to this **ER/DETA/FO/FD-3** adsorbent is not used in subsequent research.

Table 4. 2. Results of fitting obtained by using different isotherm models and error analysis

Isotherm model	Adsorbent **ER/DETA/FO/FD**		
	25 °C	35 °C	45 °C
Langmuir			
Q_o (mg g^{-1})	31.0 ± 1.18	32.2 ± 1.12	34.0 ± 1.08
b (dm^3 mg^{-1})	2.13 ± 0.391	4.78 ± 1.03	5.81 ± 1.17
b (dm^3 mol^{-1})	283078	576596	718590
χ^2	1.66	2.69	2.68
R^2	0.986	0.982	0.984
Redlich-Peterson			
a_R (mg^{-1})	13.7 ± 8.37	66.8 ± 41.0	8.05 ± 4.12
g	0.802 ± 0.0391	0.831 ± 0.0255	0.952 ± 0.0612
K_R (dm^3 g^{-1})	232 ± 53	245 ± 57	256 ± 95
χ^2	1.27	1.82	2.99
R^2	0.995	0.995	0.998
Sips			
a_S (dm^3 mg^{-1})	1.10 ± 0.268	1.78 ± 0.425	2.80 ± 0.926
β_S	0.599 ± 0.0591	0.528 ± 0.0592	0.646 ± 0.103
K_S (dm^3 g^{-1})	42.7 ± 6.18	70.2 ± 11.6	106 ± 27.7
χ^2	**0.537**	**0.632**	**1.54**
R^2	**0.995**	**0.996**	**0.996**
Jovanovic			
q_m (mg g^{-1})	27.5 ± 0.993	29.7 ± 1.19	31.6 ± 1.23
K_J (dm^3 g^{-1})	1.55 ± 0.247	3.25 ± 0.714	3.76 ± 0.82
χ^2	3.14	5.76	6.10
R^2	0.974	0.962	0.965
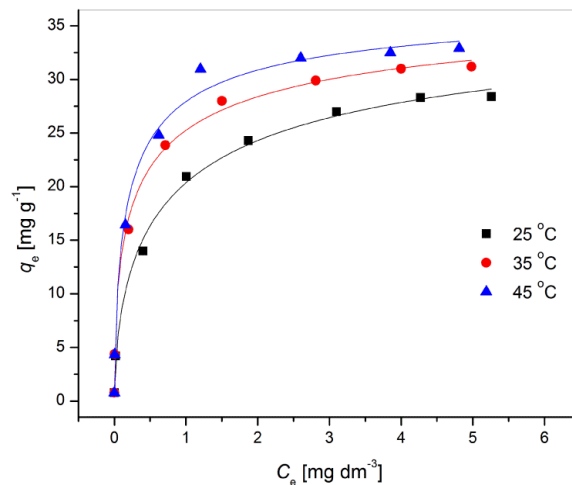
Figure 4. 6. The Sips adsorption isotherms of of As(V) ion adsorption on the **ER/DETA/FO/FD** ($m/V = 100$ mg L^{-1}, $C_{As(V)} = 0.078$, 0.44, 1.8, 3.1, 4.3, 5.8, 7.1 and 8.1 mg L^{-1}, pH $= 5.0 \pm 0.1$)

The time-dependent change of pH during adsorptionis shown in Fig. 4.7. These changes could be attributed to the release/retain of hydrogen ion by surface functional groups and the arsenic adsorption processes have certain contribution to pH value change. The pH_{fin}/pH_{in}value dependence is shown in Fig.4.7a). Hydroxide ion release in the pH_i range from 2 to 6 for the **ER/DETA/FO/FD** was found [263]. The $pH_{fin} \approx pH_{in}$at pH 6 is in accordance with plateau of highest As(V) removal (Fig.4.7). At higher pH almost constant ratio pH_{in}/pH_{fin} indicates low alteration of adsorption mechanism, *i.e.* hydroxide ion consumption is a dominant process. Similar trend was found for the **ER/DETA/FO/FD** with almost proportionally higher pH_{fin} for nearly 0.5 units at whole pH region.
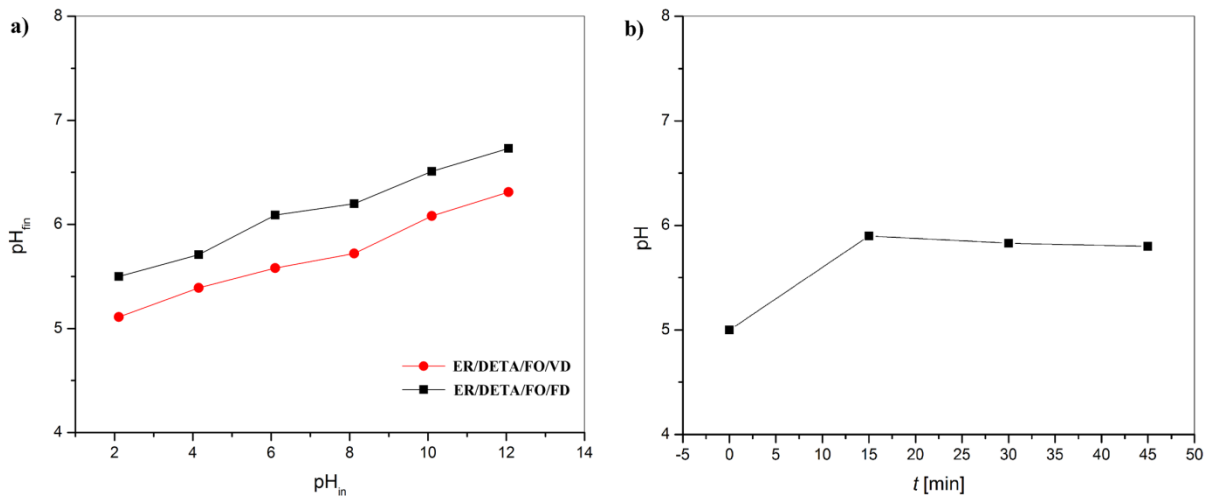
Figure 4.7. Dependence of $pH_{fin.}$ *vs* $pH_{in.}$ a) and time-dependent pH during arsenate removal b) ($m/V = 100$ mg L^{-1}, $C_{As(V)} = 0.44$ mg L^{-1}, pH $= 5.0 \pm 0.1$)

The point of zero charge (pH_{PZC}) is the pH value at which the net surface charge is zero. It means that at the pH_{pzc}, the number of $FeOH_2^+$ groups is equal to the number of FeO^- groups at FO surface. And after, with pH increasing, the number of FeO^- groups also increases. At $pH_{in}<pH_{PZC}$ the dominant $FeOH_2^+$ groups are responsible for the selective binding of molecular and ionic forms of arsenic species, indicating electrostatic nature of adsorption *i.e.* adsorbate removal by ionic exchange. For $pH_{in}>pH_{PZC}$, adsorbent surface groups are ionized and repulsion of negatively charged As(V) anion takes place at boundary layer of the solid interface. The results of pH_{fin} with pH_{in} change are in accordance with postulated mechanism of As(V)

adsorption on FO. Fendorf *et al.* [157] found, according to EXAFS analysis, that three different As(V) surface complexes could be present: monodentate, bidentate-binuclear and bidentate-mononuclear, and proved that their contribution is highly dependent on the coverage degree. In other researches [262], two-step adsorption mechanism has been proposed. The first fast step involved initial ligand exchange forming a monodentate complex, while the second slow step represented a ligand exchange resulting in the formation of an inner-sphere bidentate complex.

Removal of pollutant should not be accompanied by leaching of the iron into effluent water. Due to this, various water quality parameters, including iron concentration, were determined in the effluent water. It is found that water quality remains almost unaltered with slight change in pH value (Fig. 4.7), while total dissolved solid (TDS) increases. The assessment of the water quality before and after treatment with the **ER/DETA/FO/FD** also confirmed that there was low leaching of iron (less than 62 μg L^{-1}) which was below the EPA secondary maximum contaminant level (SMCL) of 0.3 mgL^{-1} [157].

Adsorption kinetics

The determination of adsorption rate and time after which system attains thermodynamic equilibrium offers deeper insight into As(V) adsorption mechanism, *i.e.* probable reaction pathways/steps. Due to complexity of adsorption process, *i.e.* contribution of mass transfer and chemical reaction processes to overall adsorption, different kinetic models were used to fit experimental data (*Exp. part*).

Time-dependent removal of As(V) (Fig. 4.8a)) was a fast process: 98 and 96 % of As(V) was removed by the **ER/DETA/FO/FD** and the **ER/DETA/FO/VD**, respectively, for 45 min, and then system gradually attained equilibration. The kinetic data were analyzed by linear and non-linear least-squares method in the form of pseudo-first, pseudo-second-order rate equations and intra-particle diffusion model (Weber-Morris model). Judging from the regression coefficients, kinetic data were satisfactorily fitted by using pseudo-second-order (PSO) equation [230,231].
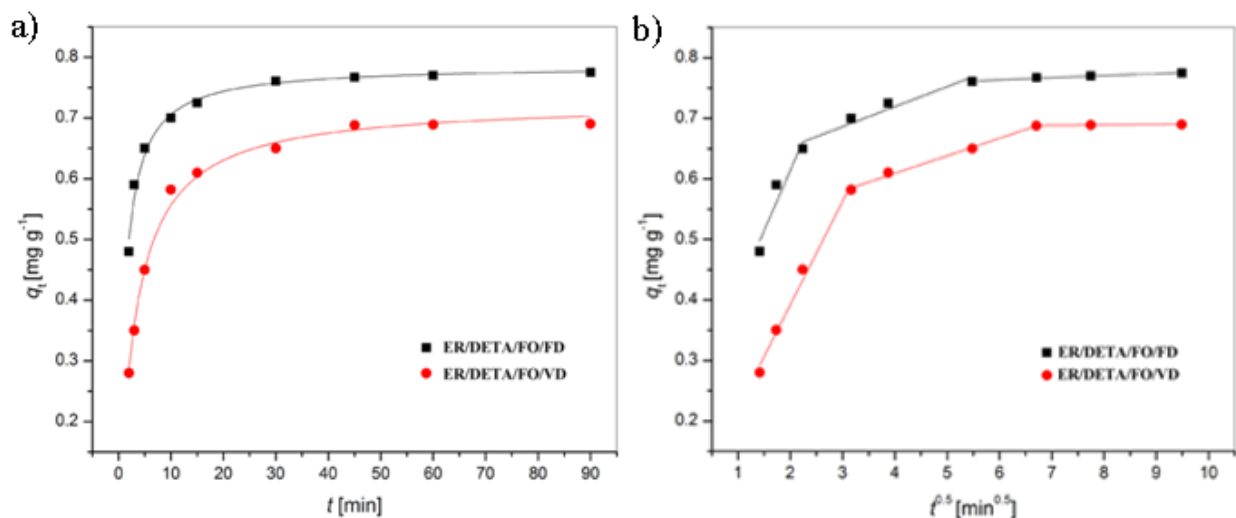
Figure 4. 8. The plot of a) PSO model and b) intra-particle diffusion plot for As(V) adsorption at 25 °C ($m/V = 100$ mg L^{-1}, $C_{As(V)} = 0.078$ mg L^{-1}, pH = 5.0 ± 0.10)

Table 4. 3. The kinetic parameters and activation parameters of As(V) adsorption obtained by the use of PSO equation at 25 °C

Constants	ER/DETA/FO/VD	ER/DETA/FO/FD
q_e (mg g^{-1})	0.727 ± 0.00772	0.786 ± 0.00611
K_2(g mg^{-1} min^{-1})	0.451 ± 0.0268	1.11 ± 0.0699
R^2	0.993	0.986
E_a (kJ mol^{-1})	20.60	18.63
$\Delta H_{25}^{\#}$ (kJ mol^{-1})	18.12	16.15
$\Delta G_{25}^{\#}$ (kJ mol^{-1})	-111.4	-113.6
$T\Delta S_{25}^{\#}$ (kJ mol^{-1})	129.4	129.7

The kinetic study of As(V) removal at 25, 35 and 45 °C afforded rate constants of 0.451, 0.528 and 0.781 g mg^{-1} min^{-1} for the **ER/DETA/FO/VD**, and 1.11, 1.31 and 1.79 g mg^{-1} min for the **ER/DETA/FO/FD**, respectively. The linear plot of the values of logarithms of rate constants *versus* $1/T$ (Arrhenius equation; eq. 3.5) were used for calculation of the activation parameters: the energy of activation E_a and frequency factor A. The obtained results were used for further calculations of the entropy of activation $\Delta S^{\#}$, Gibbs free energy of activation $\Delta G^{\#}$ and enthalpy of activation $\Delta H^{\#}$ of investigated elementary reaction (eqs. 3.5-3.8). The results are giveninTable 4.3.

The activation energy for the adsorption system of As(V) removal is 20.60 kJ mol^{-1} for the **ER/DETA/FO/VD** and 18.63 kJ mol^{-1} for the **ER/DETA/FO/FD**. The result obtained in a batch system is in agreement with study of As(V) adsorption on synthetic goethite presented in the work of Lakshmipathiraj *et al.*[238]. Adsorption kinetics is generally controlled by diffusive mass transfer, thus rates of approaching to equilibrium usually increase with increasing of temperature. The results show that the intra-particle diffusion is a rate-controlling step since the activation energy is low and with in the range of 8–22 kJ mol^{-1} characteristic for diffusion-controlled processes such as ion-exchange/complexation [264].

The results of PSO fitting simulate overall adsorption rate and could not help in assessing of the rate-limiting step. Therefore, the intra-particle diffusion model [265] was applied to analyze mass transfer phenomena of overall process. The adsorption is usually accomplished through a series of distinct consecutive steps: the external mass transfer (diffusion through the bulk liquid), the diffusion across boundary layer surrounding the particle (film diffusion), diffusional transport within the internal structure of adsorbent (intra-particle diffusion) and the adsorption on solid surface. Regarding the simplicity of the Weber-Morris model, it suffers from uncertainties caused by multi-linear nature, *i.e.* overall mass transport could be controlled by more than one step at different stage of the adsorption process. Generally, bulk diffusion and As(V) adsorption at **FO** surface is a fast process. The results of Weber-Morris fittings are given in Table 4.4.

Table 4.4. The kinetic parameters of the Weber-Morris (intra-particular) model for As(V) adsorption

Steps	Constants	**ER/DETA/FO/VD**	**ER/DETA/FO/FD**
Step 1	k_{p1}(mg g^{-1} min$^{-0.5}$)	0.171 ± 0.124	0.199 ± 0.0611
(Film/intra-particle diffusion)	C (mg g^{-1})	0.0505 ± 0.0278	0.217 ± 0.112
	R^2	0.984	0.827
Step 2	k_{p2}(mg g^{-1} min$^{-0.5}$)	0.0289 ± 0.00146	0.0331 ± 0.00552
(intra-particle diffusion)	C (mg g^{-1})	0.493 ± 0.00732	0.587 ± 0.0214
	R^2	0.992	0.921
Step 3	k_{p3}(mg g^{-1} min$^{-0.5}$)	0.00721[*]	0.00343[*]
(intra-particle diffusion)	C (mg g^{-1})	0.683[*]	0.743 ± 0.00318
	R^2	0.958	0.956

[*]Negligible statistical error

The results obtained following the Weber–Morris model show three successive linear steps (Fig. 4.8): fast kinetics in the first step followed by medium adsorption rate in the second and very slow attainment of equilibrium in the third step. A larger intercept found for the **ER/DETA/FO/FD** indicates higher resistance, *i.e.* slower ionic transport, due to intra-particle diffusion. The first linear part demonstrates external mass transfer from bulk solution to the most available adsorptive sites of outer adsorbent surface. The second and third part of Weber-Morris fit represent processes of high dependence on adsorbent porosity, *i.e.* pore geometry and network density. Due to the concentration gradient the ions diffuse through bulk solution and tree like system of macro-, meso- and micropores extending into adsorbent interior to reach all available surface active sites [230,231]. The intra-particle and film diffusion resistance slow down adsorbate transport, *i.e.* net transport in a direction of variable time-dependent concentration gradient. At the final stage of process, the adsorption takes place at low rate until saturation of all available surface sites is achieved. Additional analysis on the contribution of external mass transfer and diffusion inside the pores to overall diffusional adsorbate transport is also performed.

The evaluation of external mass transfer: analysis of kinetic data showed on Figs. 4.6 and 4.7 indicate that fast initial arsenic uptake, within 5-10 min, could be governed by significant contribution of external mass transport. Kinetic modeling of monovalent ion sorption onto organic zeolite, studied by Boyd *et al*. [82], was based on the assumptions which are best described with the eq. (4.1):

$$\ln\left(1 - {q_t}/{q_e}\right) = k_f a \times t \qquad (4.1)$$

where q_t (mmol g^{-1}) and q_e (mmol g^{-1}) are adsorbed amounts at time t and at equilibrium, while $k_f a$ (min^{-1}) is volumetric external mass transfer coefficient. The statistical validity of modeling was improved by inclusion of number kinetic data obtained by interpolation from Figs.4.8. The calculated parameters are given in Table 4.5. Low effect of the mixing rate change on $k_f a$ values points out to low resistance of the external surrounding film of fluid.

Mass transfer coefficient (k_f) was also obtained according to dimensional analysis, using calculation based on Sherwood (S_h), Schmidt (S_c) and Reynolds (R_e) numbers, which are valid for isolated sphere [266]:

$$Sh = 2 + 0.6 Re^{1/2} Se^{1/3} \qquad (4.2)$$

126

where $Sh = k_f d_p/D_m$; $Sc = v/D_m$; $Re = \frac{v}{d_p}/v$, and for agitated vessels peripheral velocity is given by: $v = d_{imp}N$; d_p (m) is particle diameter; v (m s^{-1}) is stirrer peripheral velocity; v (m^2 s^{-1}) is fluid kinematic viscosity (1.004×10^{-6} at 20 °C); d_{imp} (m) stirrer diameter; D_m (m^2 s^{-1}) is As(V) diffusivity (m^2 s^{-1}) in water and N (rpm) is stirrer speed.

With the increase of stirrer speed from 250 to 400 rpm, the k_f values also increased from 5.57 to 6.10×10^{-4} m min^{-1}. Small increases of k_f indicate that the resistance of diffusion through the pores of the particles is significant. Linear correlation ln k_f vs. ln(N) was found (Fig. 4.9), as it was obtained for hydroxyapatite [267], and it gives following empirical correlation:

$$k_f = 2.30 \times 10^{-4} \times N^{-0.49923} \ (R^2 = 0.995) \tag{4.3}$$

This equation may be used for the prediction of k_f for sorption processes onto investigated adsorbents in given ranges of agitation speeds.
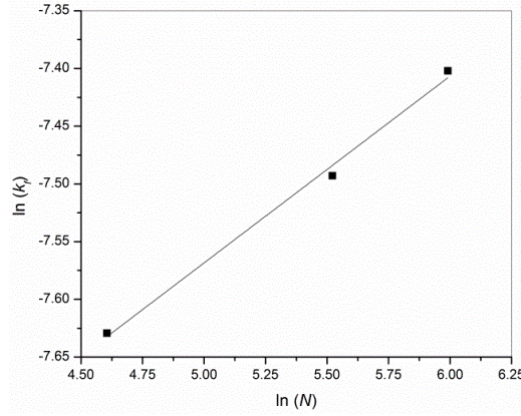
Figure 4. 9. The relation of ln (k_f) and agitation speed ln (N)

Diffusion inside the pores: Reichenberg [268] modified the pore diffusion model for the case of linear isotherm developed by Boyd, and the following approximation is obtained:

$$\ln\left(1 - \frac{q_t}{q_e}\right) = \ln\frac{6}{\pi^2} - \frac{4D_{eff}\pi^2}{d_p^{\ 2}}t \ \text{for} \quad \frac{q_t}{q_e} > 0.85 \tag{4.4}$$

where D_{eff} (m^2 min^{-1}) is an effective diffusion coefficient and d_p (m) is a particle diameter, assuming spherical particle. The following variables are adopted: $q_t/q_e = F$ fractional attainment and $B = 4D_{eff}\pi^2/d_p^{\ 2}$. It was concluded that all experimental data for sorption onto the **ER/DETA/FO/FD** for $t > 5$ min met the condition $q_t/q_e > 0.85$, enabling application of eq. (4.4).

Boundary film resistance is of low significance during the whole adsorption period, and the expressions given at the right side of eq. (4.4) are linear function of t, with intercept 0 and slope B given in Table 4.5. Parameter B is independent of the agitation speed (Table 4.4). Value of slope B decreases with the initial metal concentration increase, due to counter direction diffusion of surface released cations [267], which could be significant inside the pores. The calculated value B is somewhat lower than $k_f a$ (Table 4.5) which indicates that film diffusion could be of appropriate significance at the initial period of adsorption process, for $t < 10$ min, and the diffusion inside the pores also occurred at the beginning of the process and became prevailing rate-limiting step in the course of overall adsorption process. Calculated D_{eff} values (Table 4.5) are in the order of magnitude 10^{-11} m^2 min^{-1} for the **ER/DETA/FO/FD**. The enhanced diffusion of arsenic into the **ER/DETA/FO/FD** particles might be caused by a higher specific surface and diameter of mesopore (Table 4.1), and together with favorable As(V) adsorption on FO are prerequisites necessary for effective arsenic adsorption.

Table 4.5. The calculated mass transfer coefficients $k_f a$, D_{eff} and B for As(V) adsorption onto ER/DETA/FO/FD

N (rpm)	d_p (mm)	$k_f a$ (1/min)	R_e	S_h	k_f x 10^4 (m/min)	D_{eff}x 10^{11} (m^2/min)	B
100		0.0760	1.65	2.68	4.86	5.03	0.0478
250	0.300	0.0981	4.12	3.08	5.57	3.48	0.0696
400		0.103	6.59	3.37	6.10	3.61	0.0688

Due to beneficial textural properties, *i.e*. ratio of surface area/pore volume/pore diameter of the **ER/DETA/FO/FD** adsorbent, large number of the adsorption sites are situated at external adsorbent surface and interior pore network are favorable to provide effective As(V) bonding and lower resistivity to As(V) diffusional transport.

Comparison of equilibrium and kinetic data

Comparison of literature equilibrium and kinetic data, given in Table 4.6, with ones obtained in this work, given in Tables 4.2, 4.3 and 4.4. The discrepancies in the experimental conditions, *i.e*. diversity of initial arsenic concentration, render qualitative overview of the

literature on the adsorption and kinetic data related to As(V) adsorption in the presence of spherical polymer based material. The literature survey, shown in Table 4.6, is presented with respect to the adsorption kinetics (Tables 4.3 and 4.4) and maximum adsorption capacity (Table 4.2). Adsorbents with high surface area usually show higher adsorption capacity, but that is not always a rule. The q_{max} were found ina wide range between 0.0226 mg g^{-1}, reported for Fe/resin up to approximately 140.87 mg g^{-1} for glycidyltrimethylammonium chloride/resin (Table 4.6). The q_{max} obtained for the **ER/DETA/FO/FD**, and somewhat lower for the **ER/DETA/FO/VD** is comparable to the literature data. The q_{max} obtained from the Langmuir model for the **ER/DETA/FO/FD** was found to be 31.0 mg g^{-1} at 25 °C, 32.2 mg g^{-1} at 35 °C, with the highest value of 34.0 mg g^{-1} at 45 °C (Table 4.2). According to this it could be stated that high performance of the **ER/DETA/FO/FD** adsorbent together with beneficial techno-economical aspect, *i.e.* simple production and overall cost, offer an acceptable alternative to the adsorbents currently in use. This issue is discussed in more details in subsection 4.1.6.

Fast attainment of adsorption equilibrium, *i.e.* kinetic rate of arsenic adsorption in the presence of the **ER/DETA/FO/FD** mainly exceeds the values found in the literature (Table 4.6) which is also a faster process than it was found for nanometer size adsorbent. The relationship between textural data and adsorbent performance, *i.e.* kinetic and adsorption data related to specific adsorbent is well known. Most of the processes are of multiple natures controlled by boundary layer diffusion/intra-particle diffusion in the first step and the intra-particle diffusion in subsequent linear portions which correspond to mass transport in meso and micropore.

Table 4. 6. Adsorption capacity and kinetic properties of some reported adsorbents for As(V) removal

Adsorbent	Surface area $(m^2 \, g^{-1})$	Pore volume $(mL \, g^{-1})$	Pore diameter (nm)	k $(g \, mg^{-1} \, min^{-1})$	k $(mg \, g^{-1} \, min^{-0.5})$	q_{max} $(mg \, g^{-1})$	Ref.
ER/DETA/FO/VD	146	0.88	62	0.727	k_1 0.171; k_2 0.0289	22.5	**This work**
ER/DETA/FO/FD	173	0.99	68	0.786	k_1 0.199; k_2 0.0331	31.0	**This work**
Nanomaterials							
Cu(II) oxide nanoparticles	52.11	0.117	<40 nm	1.37	-	1.08	[269]
Fe(II)/Activated carbon	1231	0.125	0.589	-	-	4.663	[270]
Fe^{3+}/monoamine/SiO_2	379.8	0.6	5.825	0.00106	-	101.74	[271]
Fe^{3+}/diamine/SiO_2	272.0	0.379	3.943	0.00323	-	78.42	
Iron(III)-copper(II) binary oxide	282	0.31	4.3	0.00165	-	82.7	[272]
Ultrafine magnesium ferrite	438.2	0.648	3.89	0.079	-	83.2	[273]
Fe–Zr binary oxide	339	0.21	1.5-50	0.00215	-	46.1	[274]
Calcite/α-FeOOH	255.22	0.146	2.90	0.088	0.313	20.96	[231]
Calcite/α-FeOOH/α-MnO_2	264.32	0.532	21.42	0.141	0.466	42.29	
Eggshell/α-FeOOH	183	0.093	16.3	0.110	0.135	33.38	[230]
Eggshell/α-FeOOH /α-MnO_2	250	0.710	10.2	0.256	0.174	47.04	
e-MWCNT/Fe^{2+}	198.5	0.617	12.43	0.0439	0.1121	17.83	[121]
e-MWCNT/Fe^{3+}	240	1.028	17.08	0.0362	0.1081	10.43	
Irregular shape schwertmannite	199.43	1.09	-	0.001817	0.2894	36.56	
Cylindrical shape schwertmannite	189.27	0.82	-	0.00025	0.1274	27.614	[275]
Spherical shape schwertmannite	32.52	0.16	-	0.0042	0.0767	4.0672	

Table 4.6. Continued

Adsorbent	Surface area $(m^2\ g^{-1})$	Pore volume $(mL\ g^{-1})$	Pore diameter (nm)	k $(g\ mg^{-1}\ min^{-1})$	k $(mg\ g^{-1}\ min^{-0.5})$	q_{max} $(mg\ g^{-1})$	Ref.
Resins							
Amberlite IRA 458	2.03	-	6.46	0.100	0.049	53.34	[276]
Amberlite IRA 402	2.45	-	1.89	0.147	0.028	50.37	
Fe/resin	-	-	-	0.545	0.3049	0.0226	[259]
Iron(III)/resin	7.3	-	-	-	-	55.44	[277]
MnO$_2$/resin	-	-	-	-	-	22	[278]
Ce/resin	-	-	-	0.3159	-	2.384	[279]
Zr oxide/resin	7.44	0.0288	18.73	0.07	0.010	10.43	[280]
Zr(IV)/resin	7.3	-	-	-	-	88.73	[281]
Sn/Resin	-	-	-	0.00065	0.52	38.46	[282]
Fe/Amberlite 200CTNa	-	-	-	1.85	-	108.65	[283]
IRA-743 beads	20.84	-	-	-	-	14.7	
CRB-02 beads	27.91	-	-	-	-	14.9	
S-108 beads	20.58	-	-	-	-	14.8	[284]
GCP fibers	0.26	-	-	-	-	8.88	
GRY fibers	0.27	-	-	-	-	6.92	
GRY-L fibers	0.20	-	-	-	-	7.45	
Glycidyl trimethylammonium chloride/resin	-	-	-	0.077	8.57	140.87	[285]
Hydrochloric acid/resin	-	-	-	0.110	6.50	84.67	
Lewatit FO36	-	-	-	-	-	6.4	[286]

Thermodynamic study

The effect of temperature on As(V) adsorption onto the **ER/DETA/FO/FD** was deduced fromthe adsorption results performed at 25, 35 and 45 °C. The temperature dependence of arsenic adsorption was associated with changes in thermodynamic parameters such as ΔG^o (the standard Gibb's free energy change), ΔH^o (the enthalpy change), and ΔS^o (the entropy change); these parameters were calculated using the eqs. 3.3 and 3.4, according to the methodology presented by Karthikeyan [287]. The obtained results are given in Table 4.7.

Table 4. 7. Thermodynamic parameters of As(V) adsorption onto ER/DETA/FO/FD

T (°C)	K_o	$\Delta G°$ (kJ mol^{-1})	$\Delta H°$ (kJ mol^{-1})	ΔS^o (J mol^{-1} K^{-1})	R^2
25	6.30	−4.56			
35	7.21	−5.06	7.66	41.09	0.967
45	7.65	−5.38			

The negative values of $\Delta G°$ indicate spontaneity of adsorption, while positive $\Delta H°$ confirms that more effective adsorption is at higher temperatures (Table 4.7). Breakage of water hydration shells by arsenic anionic species and their transport through the bulk solution, within the pores and through the surface boundary layer is more intensive process at higher temperatures. The transport of exchangeable arsenic oxyanions to adsorption site, and on the otherside, a number of (exchangeable) water molecules was released into bulk solution contributing to increases of entropy change [230,231]. At steady-state condition randomness at adsorbent/solution interface is increased due to different intermolecular interactions which contribute to positive entropy change, *i.e.* adsorption is an entropy-driven process. All of these elementary processes, which take place in the course of equilibrium attainment, contribute to positive enthalpy change.

Regeneration and reusability

In accordance with the current trend of designing the environmentally friendly and economically viable concept of pollutant removal the following criteria play an important role:

life cycle of adsorbent, regeneration efficiency and safe disposal of adsorption/regeneration residue. In order to minimize the impact on material cost, development of high capacity adsorbent offers possibility for long-term use and together with development of successful regeneration technology provides high performance adsorbent for practical application. Regeneration efficiency, *i.e.* number of the cycles of adsorbent re-use contributes to the cost effectiveness of adsorption process. Also, the chemicals used for regeneration of spent adsorbent, used in the course of application of treatment technology, and disposal/storage and/or delivery (transportation) to waste processor (recycling/processing) are the factors which affect the material cost. The selection of an efficient reagent for the regeneration depends on the arsenic bonding type, nature of adsorbent and regulation concerning effluent water quality. The formation of surface complexes, monodentate, bidentate-mononuclear and bidentate-binuclear through formation of As–O–Fe bond [157], indicates a necessity of application of strong competitive anion capable to break off As-O-Fe bond, *i.e.* to displace As(V) anion. Sodium hydroxide and strong acids are most commonly used to elute As(V). Therefore, anion exchange of bonded As(V) should result in its release into solution leaving active surface sites free at the level as before the previous adsorption cycle. Subsequent rinsing with dilute acid, 2 % sulfuric acid, causes protonation of negatively charged surface functional groups regenerating their adsorption potential. Many systems for regeneration were used but NaOH, binary system NaOH/NaCl and ternary eluent NaOH/NaCl/citrate were selected as the best alternatives. The results of desorption study, performed in a batch system, are given in Table 4.8.

Table 4. 8. Results of As(V) desorption from **ER/DETA/FO/VD** and **ER/DETA/FO/FD**

Desorption agent	$C_{\text{desorption agent}}$ (mol L^{-1})	As(V) desorbed (%)	
		ER/DETA/FO/FD	**ER/DETA/FO/VD**
NaOH	0.2	69	68
	0.5	82	79
NaOH/NaCl	0.2/0.2	75	78
	0.5/0.2	88	86
	0.5/0.5	95	90
NaOH/NaCl/citrate	0.2/0.2/0.01	78	77
	0.5/0.2/0.01	89	85

The most efficient desorption system has proven to be NaOH/NaCl (0.5/0.5). With this binary system, in the first cycle, 95 and 90 % of As(V) was desorbed, and throughout five

consecutive cycles, desorption efficiency was decreased to 88 and 81% for adsorbents **ER/DETA/FO/FD** and **ER/DETA/FO/VD**, respectively. In summary, the **ER/DETA/FO/FD** is reusable in a multi-step processes and an efficient adsorbent for As(V) removal for over five adsorption/desorption cycles.

Regeneration versus safety

Waste management of hazardous residue after arsenate adsorption is an issue of high importance which must conform to regulations related to environmental protection. To avoid in appropriate disposal and consequent environmental pollution, adsorption wastes (arsenate loaded adsorbent – sludge, collected chemicals after regeneration and washing solution) need to be treated or disposed of properly. Treatment technology has to provide transformation of the generated wastes into non-hazardous material.

As it was presented in the section *Regeneration and reusability*, both processes produce appropriate amount of spent adsorbent and spent alkali concentrated arsenic solution which could be subjected to either safe disposal, development of appropriate purification technology or technology for processing hazardous solution into non-leaching non-hazardous solid waste. Disposal of waste is a short-term solution which is limited by storage space and by the regulations. The second method, development of technology for treatment of effluent medium was proved. The desorption and washing solution were mixed together, and pH value was adjusted to 7.0 by adding 15 % of hydrochloric acid, followed by addition of iron(II) sulfate. After 12 hours, heavy brown precipitate was filtered using combination of coarse (top) and fine (down) sand filter medium mixed with diatomaceous earth. The ferric (oxy)hydroxide colloids adsorb (bound) arsenic, decreasing the concentration of pollutants to acceptable level. It was very important to provide redox oxidizing environment in a precipitation chamber, *i.e.* proper agitation with impeller to provide enrichment of water by oxygen, in the course of waste treatment which was a favorable condition for forming heavy and stable precipitate resistant to leaching of arsenic species [288]. Afterward, sludge has to be stored at atmospheric conditions to disable iron and arsenate reduction. Third method is an optional method, and it could be performed by blending arsenic contaminated material using adequate technology which would produce stable waste or engineered materials such as glass, bricks, concrete or cement blocks

134

which incorporate arsenic into stable form. However, applying such technology could cause air pollution or water pollution downstream (gaseous products) from kilns burning bricks containing arsenic contaminated sludge due to volatilization at high temperature processing. The first and third method are not considered in the presented study.

According to EPA regulative [289] products obtained by implementation of the second technology must be subjected to testing according to toxicity characteristic leaching procedure (TCLP). TCLP was applied to evaluate hazardous characteristics of exhausted adsorbent and treated sludge in order to evaluate possibility for safe handling and disposal in landfills. The determined concentration of inorganic arsenic (iAs) is below established concentration by U.S. EPA standard of 0.1 mg L^{-1} [290], which indicates possible safe disposal of exhausted adsorbents and sludge from heavy precipitate containing arsenic.

Moreover, the decision on the treatment technology depends on many factors: complexicity/feasibility and material/maintenance cost of the adsorption and regeneration technology, as well as characteristics/properties of the treated material and technology applied. Detailed techno-economic (cost) analysis must be taken into account with all those factors which include capital and maintenance/operational (MO) cost of described processes. From the aspect of present study, the most important element of cost analysis is the effect of adsorption/regeneration performances of **ER/DETA/FO/FD**.

4.1.4 Adsorbent's performance in a competitive conditions

The adsorbent performances: capacities, selectivity and affinity depend on many factors such as mixing rate (for the batch system) or flow rate (for the fixed column study), textural properties (geometry, porosity), adsorption conditions (pH value, the initial concentration of solute), chemical properties of surface (functionality and density), and stability of the formed ligand exchange complexes, as well as on the presence of the interfering ions [288,289]. According to this, competitive study would be of decisive importance in determination of the possible use of appropriate adsorbent and the effect of interfering ions on successfulness of arsenic removal achieved in equilibrium and dynamic study.

Influences of competitive ions: experimental vs modeling

Commonly present interfering anions in natural water could have adverse effects on arsenic adsorption onto FO. The constituents of various types of natural waters are substantially different which make modeling of real water very challenging. Due to this, the simulation of natural water was prepared with the reference to the results of data on ion concentration in river and lake water from different regions of Serbia (Table 4.9). As an example, the concentration of ions of interest in the Sava river is given in Table 4.9. Both experimental and theoretical methodology was applied on studying the impact of interfering ions on the removal of arsenic with the **ER/DETA/FO/FD** and the **ER/DETA/FO/VD** (Figs. 4.10 and 4.11). The used surface complexation models help in analysis of adsorption mechanism, *i.e.* chemical reaction at adsorbent surface involved in the adsorption process (Table 4.10). Model was described by set of simultaneous equilibria, included in MINTEQ software, that can be solved by using the defined input parameters (Table 4.10). It was postulated that not only the specific surface areas, but also the numbers of hydroxyl groups influence the adsorption capacity of **FO** for selected pollutants [290]. Results of the competitive study in presence of different concentration of phosphate, sulphate and silica, as well as ionic strength are shown in Fig. 4.11.

Table 4. 9. Content of ions in model and real water samples

Ions	Concentration in model water	Concentration in real water (Sava river, Ostružnica)
PO_4^{3-} (mg L^{-1})	0.05; 2; 10	0.04
SO_4^{2-} (mg L^{-1})	10; 50; 100	14
Ca^{2+} (mg L^{-1})	1; 5	65
Mg^{2+} (mg L^{-1})	1; 10; 50	3
SiO_4^{4-} (mg L^{-1})	5; 15; 50	5
NaCl (mmol)	0.1; 1;10	0.5
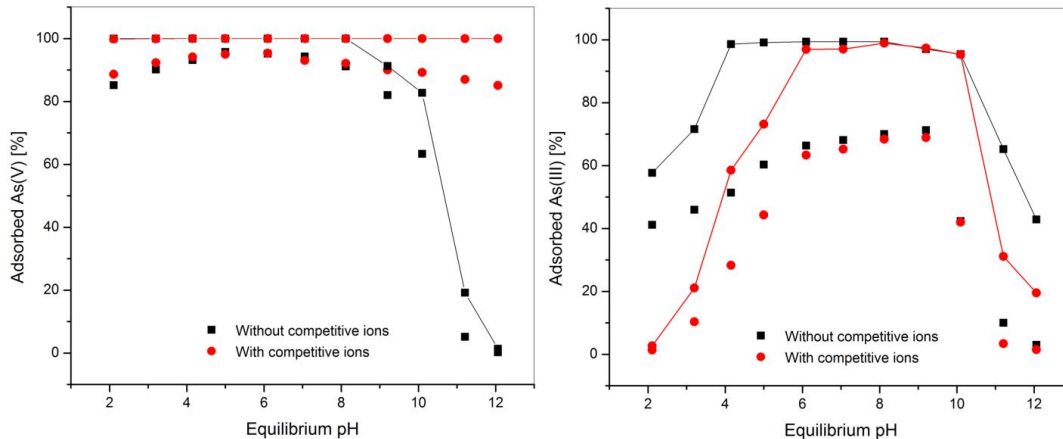
Figure 4. 10. The influence of pH *vs* modeling of overall effect of competitive ions on As(V) and As(III) adsorption by **ER/DETA/FO/FD**

The prepared model water with multiple co-existing ions promoted the adsorption of As(V) in the presence of appropriate ions which was beneficial to arsenate adsorption onto FO. Two- and three valence cations, Ca^{2+}, Mg^{2+} and Fe^{3+}, are preferably co-precipitated in the form of heavily soluble salts $CaHAsO_4$, $MgHAsO_4$ and $FeAsO_4x2H_2O$, thereby improving arsenate removal efficiency. Due to this, competitive adsorption study was performed using model water (Table 4.9) with the presence of Ca^{2+}, Mg^{2+} and Fe^{3+} ions (Fig. 4.11) and competing ion free water. The results of competitive arsenic adsorption study (Figs. 4.11 and 4.12) showed that phosphate had a profound effect on arsenic adsorption. This could be explained by the fact that PO_4^{3-} and AsO_4^{3-} have similar chemical structures; both molecules and ions are tetrahedral oxyanions with similar *p*Ka values. The low influence of commonly present interfering ions in natural water onto arsenate adsorption (Fig. 4.12), and pH_{PZC} change before/after adsorption (Table 4.1), are the features indicative of inner-sphere formation of arsenate complexes. Also, modeling and experimental results indicate slight increase of arsenate adsorption as ionic strength of solution increases. The adsorption capacity increases from 31.0 to 32.5 mg g^{-1} at 25 °C, most likely due to the compression of the electrostatic double charged layer potential, contributing to easier access of the arsenic species to the **FO** surface. Goldberg and Johnston [291] explained that higher ionic strength causes higher activity of the available counter ions and enables compensation of the surface charge generated by greater specific arsenate adsorption, *i.e*. formation of inner sphere complexes. Moreover, study of adsorption efficiency of the

137

ER/DETA/FO/FD in real water sample which contained 0.04 mg L^{-1} PO_4^{3-}; 14 mg L^{-1} SO_4^{2-}; 65 mg L^{-1} Ca^{2+}; 3 mg L^{-1} Mg^{2+}; 5 mg L^{-1} SiO_4^{4-}; 0.5 mM NaCl, showed slight increases of adsorption to 31.8 mg g^{-1}, a feature beneficial for consideration of possible application of synthesized adsorbent in a system for real water treatment. Similar results on competition of arsenic with common found interfering ions was published [292–294].
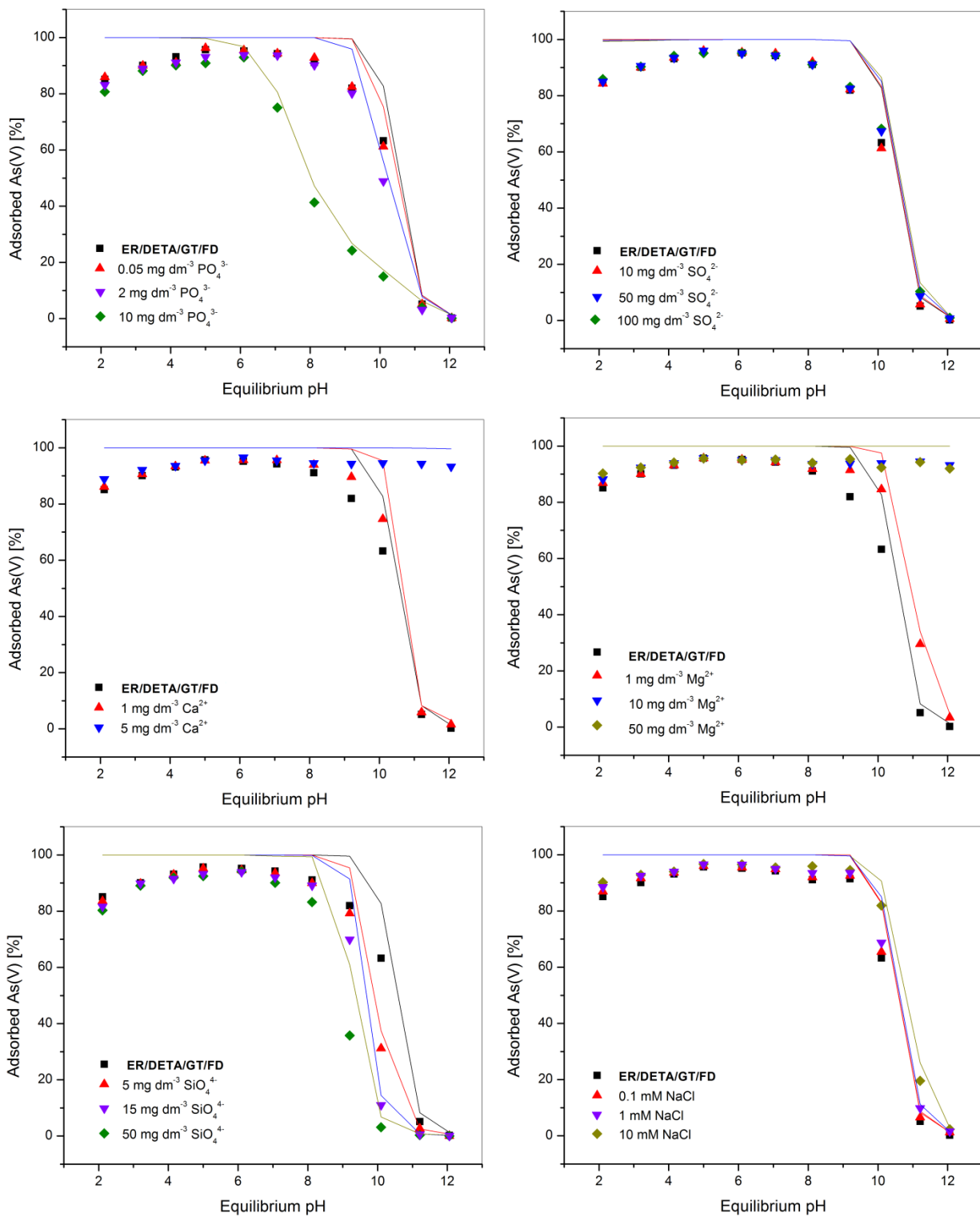
Figure 4. 11. Modeling the effect of competitive ions on As(V) adsorption by **ER/DETA/FO/FD** as a function of pH and concentration of interfering ions

Kinetic study performed under competitive conditions

The rate constant, K_2 and equilibrium sorption capacity, q_e, calculated from the values of the intercepts and slopes of corresponding plots following pseudo-first and pseudo-second-order equations, were calculated from the data obtained under competitive conditions (Table 4.10).The theoretical q_e estimated from the first-order kinetic model give significantly different values compared to experimental ones, and correlation coefficients were found to be low. The exception was a competitive arsenic adsorption from multi-component system with sulfate/silicate, for which the correlation coefficient is slightly lower and q_e value higher than experimental one for pseudo-second-order. This indicates that the first-order kinetic model is not applicable to the arsenic sorption on the **ER/DETA/FO/FD**. Therefore, PSO model was used and results of fitting are given in Table 4.10. As an illustration, plots $q_t - t$ and $t/q_t - t$ (pseudo-second order) for competitive sorption of As(V) and in the presence of one interfering ion: SiO_4^{4-}, CrO_4^{2-} and PO_4^{3-} ions by using **ER/DETA/FO/FD**are shown in Fig. 4.12.
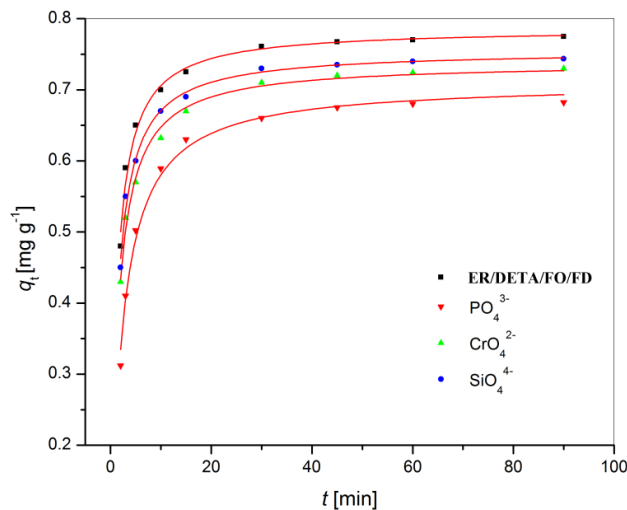
Figure 4. 12. The adsorption of As(V) under competitive condition in the presence of single interfering ions: 1 mg L^{-1} SiO$_4^{4-}$; 1 mg L^{-1} CrO$_4^{2-}$; 1 mg L^{-1} PO$_4^{3-}$

Table 4. 10. Results of the PSO fitting of As(V) removal in presence of single interfering ions

Correlation parameters	ER/DETA/FO/FD	SiO_4^{4-*}	CrO_4^{2-*}	PO_4^{3-*}
q_e (mg g^{-1})	0.786(±0.0061)	0.755(±0.0047)	0.738(±0.0051)	0.710(±0.0068)
K_2(g mg^{-1} min^{-1})	1.11(± 0.070)	1.05(± 0.050)	0.965(± 0.048)	0.627 (±0.037)
R^2	0.986	0.992	0.992	0.992

$^*C_i$=1 mg L^{-1}

On the other hand, theoretical q_e values show good agreement with the experimental data for second-order kinetics, with correlation coefficients higher than 0.98. This suggests that arsenic adsorption under competitive conditions on the **ER/DETA/FO/FD** follows PSO kinetics, meaning that sorption depends both on the arsenic and adsorbent properties. Single competitive As(V) adsorption showed the highest influence of phosphate (32 % lower K_2), followed by silicate (24 %) and chromate (18 %). Also, As(V) and As(III) sorption were considerably faster from multi-component system with Ca(II) and Mg(II) cations, than from the system with the presence of both selected anions and cations (data not presented). Co-precipitation of calcium and magnesium arsenate salt enhances adsorption kinetics as well as adsorption capacity. These results indicate that in the case of competitive sorption, pH and the presence of other ions have the most pronounced influence on the sorption kinetics and removal capacities.

4.1.5 Consideration of the ER/DETA/FO/FD performances in a column study

Application of nanomaterials is important from fundamental aspect and for better understanding of the adsorption processes. Low mechanical properties, poor durability and excessive pressure drop across the column make these materials inadequate for practical application in a fixed-bed column set-up. To overcome such problems large numbers of methodologies were developed [7]. Most of them are related to deposition/impregnation of the nano particles inside/outside functionalized spherical-likepolymers with favorable hydrodynamic properties. The use of **FO** as a modification agent is additionally stimulated by the low cost of raw-materials and the simplicity of their production. Preparation of hybrid material with improved properties (synergetic effect) with the possibility for usage in a dynamic system is

always a challenging task directed at developing an adsorbent for practical application. By preparation of cross-linked macroporous polymer impregnated with FO and adsorption study in a batch system, it was necessary to further perform preliminary study in a flow system. Capacity of the **ER/DETA/FO/FD** was determined according to breakthrough point, *i.e.* the number of bed volumes until effluent water contain more than 10 μg L^{-1}. Application of adsorbents in a fixed-bed column experiments demand further optimization of operational parameters. Model water was used, with the standard addition of As(V), 0.33 mg L^{-1}, adjusted at pH 5.0 and passed through the column at controlled flow rate: 0.5, 1.0 and 2.0 mL min^{-1}. The effluent was collected at regular intervals of time and used, after pH adjustment, for As concentration determination by ICP-MS. An example of dynamic flow experiment, used for calculation of adsorbent capacity for **ER/DETA/FO/FD**, is shown on Fig. 4.13.

The maximum capacity, q_{exp} (mg g^{-1}), obtained in a column system for a given feed concentration and flow rate could be calculated from the experimental data, *i.e.* area under breakthrough curve [295]. The complexity of mathematical calculation in the determination of adsorbent capacity by integrating total area below the breakthrough curve could be solved by different commercial software. An attractive alternative is a simplified modeling approach used for the prediction of dynamic behavior of the column. Multi-parameter fitting of the model to experimental points gives results (Table 4.11) which appropriately describe adsorbent performances by using Bohart-Adams, Yoon-Nelson, Thomas and Modified dose-response (Eqs. 3.13-3.16). These models consider that process limiting step is controlled by adsorption kinetics and can be applied only to one-component system, otherwise only results of experimental methodology are relevant.
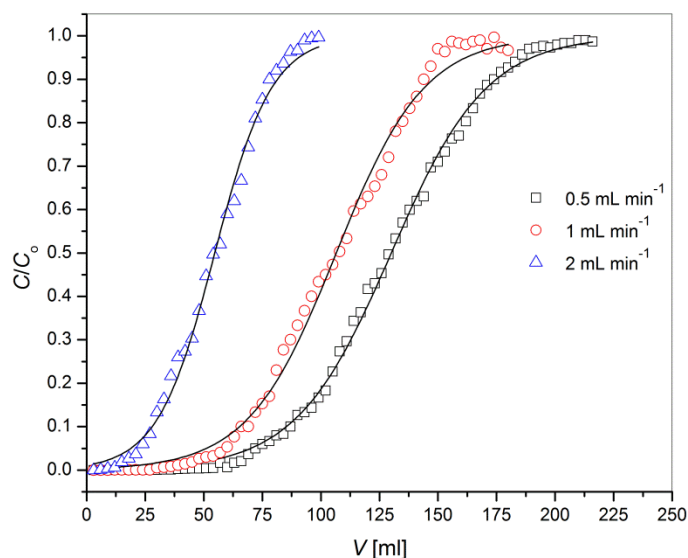
Figure 4. 13. The Bohart-Adams fitted breakthrough curves of As(V) adsorption by **ER/DETA/FO/FD** at different flow rate

Table 4. 11. Bohart-Adams, Thomas, Yoon-Nelson and Modified dose-response model fitting for As(V) adsorption by **ER/DETA/FO/FD** ($C_{As(V)}$=0.33 mg g^{-1}; t=25 °C; pH=5)

Q		mL min^{-1}	0.5	1	2
EBCT		min	7.94	3.94	1.96
Bohart-Adams model	k_{BA}	dm^3 mg^{-1} min^{-1}	0.0818	0.177	0.547
	q_o	mg g^{-1}	22.9	18.8	9.65
	R^2		0.99	0.99	0.99
Thomas model	k_{th}	dm^3 min^{-1} mg^{-1}	0.107	0.254	0.767
	q_e	mg g^{-1}	23.8	19.3	9.75
	R^2		0.99	0.99	0.99
Yoon-Nelson model	k_{YN}	min^{-1}	0.0321	0.0763	0.232
	θ	min	269	109	27.6
	R^2		0.99	0.99	0.99
Modified dose-response model	a		4.22	4.31	3.88
	q_o	mg g^{-1}	21.4	16.8	7.90
	R^2		0.89	0.90	0.93

143

On the basis of the results of experimental data fitted by the use of Bohart-Adams, Yoon-Nelson, Thomas and Modified dose-response model it could be deduced that the **ER/DETA/FO/FD** shows good column performances (Table 4.11). Increasing flow rate contributes to the decrease of the breakthrough time and adsorbent capacity. At higher flow rate, the rate of mass transfer increased, thus the amount of adsorbed arsenic onto the unit bed height (mass transfer zone) achieved fast saturation of easily available adsorption site before attainment of equilibrium. Insufficient retention time of the solute in the column, fast mass transport in a direction of column axis and slower diffusional processes through the pores limit equilibration and thus no saturation of the adsorbent occurred, *i.e*. lower adsorption capacity is a consequence. The decrease of flow rate leads to the opposite effect of adsorption capacity and significantly increases *EBCT* (>7 min). Following the fact that acceptable *EBCT* for industry practice is in the range of 5–15 min, using the **ER/DETA/FO/FD** and providing condition at *EBCT* ≈ 12 min revealed an increase of adsorption capacities to 24.2 mg g^{-1}. This result justifies increases of *EBCT* but this will be analyzed in more details at full scale modeling in a fixed-bed column system. Moreover, in this short analysis it could be observed those adsorption performances of hybrid nanocomposite ssuch as: effectiveness of the arsenic removal, the practical manipulation and effective regeneration, the avoidance/decrease of interference of other ions and natural organic matter are improved.

4.1.6 Preliminary techno-economic analysis of ER/DETA/FO/FD

A large number of publications were published dealing with the development of new adsorbents and technology: a) at laboratory level with potential quality to satisfy market demand as commercial products [286,296], b) applied at full scale [286,296–301]. In general, applied technologies are based on oxidation, coagulation, precipitation, adsorption, ion exchange and membrane techniques [7]. Among them, adsorptiono ffers some advantages: process simplicity, economic viability, technical feasibility, adsorbent reuse and possibility for easy transfer at full scale application. Although many of adsorption systems are examined and described, and applied in practice, there is still need for their improvement or development of new ones. Such conclusions are based on the state-of-the-art technology survey and assessments, consideration

on upgrading of existing technology and development of new ones with critical analysis of the progress toward technical goals, feasibility and compliance with the law.

The cost analysis of the production of newly synthesized adsorbent and developed technology are key criteria that must be considered at decisive point before continuation of the study at pilot and full-scale level of application. The techno-economic analysis is a complex procedure and generally includes two categories: capital and maintenance/operational (MO) cost. Design of technology provides data necessary for calculation of the values of capital investment (equipment, construction, installation, *etc.*). The differences in capital cost for the adsorbent of similar properties could be considered to be approximately negligible, and thus they are not considered in forthcoming analysis. MO cost elements such adsorbent preparation, chemicals, labor and energy cost are of different significance to techno-economic analysis. Due to this, selection of the most influential factors, without sacrificing validity of assessments, has been made. Adsorbent preparation, capacity (run length) and regeneration frequency have been selected as critical variables in calculating the preparation/replacement media cost.

The result of such analysis could provide satisfactory estimation of the applicability of the **ER/DETA/FO/FD**, withrespect to well-known Lanxess commercial adsorbent, Lewatit FO36 [286], for real water system treatment. Lewatit FO36 is weakly basic anion exchange resin doped with a nano-scaled film of hydrated iron oxides (HFO), and thus integrates the anion exchange function with adsorption. It is intended for selective oxyanions removal with regeneration capability, and for efficient and low cost operational treatment of the removal of arsenic species from water. Instead of cross-linked polystyrene matrix, in this work novel hybrid adsorbent materials, based on cross-linked macroporous resin, were developed in order to attain or to overcome adsorptive properties of Lewatit FO36. Adsorption capacity, at 25 °C, of 31.0 mg g^{-1} was found for the **ER/DETA/FO/FD** ,and 4.2 mg g^{-1} for As(III) and more than 3.5 mg g^{-1} of As(V) for Lewatit FO36 in a fixed bed column study [261]. Capacity of Lewatit FO36 in a batch experiment is 6.2 mg g^{-1}, which is significantly lower than one found for the **ER/DETA/FO/FD** of 31.0 mg g^{-1} for As(V). It was also confirmed, from comparison with other HFO based adsorbents (Table 4.6) and natural goethite [302], that the **ER/DETA/FO/FD** possesses beneficial adsorption performance.

The preliminary calculations showed that cost of the **ER/DETA/FO/FD** was approximately 2.6 \$/kg (2.24 €/kg). This price is higher than the other traditional adsorbents as activated carbons (≈0.08 \$/g) [303], in the range of synthetic resins 1-25 \$/kg (0.85-20.8 €/kg) [304], and higher than agricultural waste (100 \$/t) without consideration of production process cost [305]. The price of the Lewatit FO36 is around 1.5 \$/kg (1.36 €/kg), which is significantly lower than the **ER/DETA/FO/FD** cost. Assuming similar operational and regeneration costs, it was accepted that comparative analysis could be defined on the basis of the cost of adsorbent per gram of arsenic removal. By applying such calculation it is shown that 0.072 € and 0.218 € per gram of As(V) for the **ER/DETA/FO/FD** and Lewatit FO36 was obtained, respectively. Similar result was obtained in comparison to commercial adsorbent ArsenX^{np} developed by SolmeteX, Inc. and manufactured and distributed by Purolite Company [306].

Obtained results show outstanding opportunities for application of the **ER/DETA/FO/FD** in a water purification system. Production of highly porous spherical cross-linked resin (porosity higher than 0.5) is a promising route to reduce the cost of such material, and good basis for subsequent modification with HFO to obtain even better performances of new adsorbent. In that way a decrease of the price from around 2.6 \$/kg to 1.8-2.0\$/kg could be expected, and a new alternative for wide application of HFO impregnated cross-linked resin for removal of pollutants is proposed.

4.1.7. Removal of arsenic in a flow system

Removal of arsenic under pseudo-equilibrium batch conditions

The arsenic adsorption is characterized by a Freundlich adsorption capacity parameter of $K \approx 369$ $(\mu g\ g^{-1})(L\ \mu g^{-1})^{1/n}$ and Freundlich intensity parameter of $1/n \approx 0.54$. Obtained K value is in the range of reported values for nanostructured ZrO_2 spheres [246], however, in comparison to nano-iron(hydr)oxide modified support (Table 4.6), goethite impregnated media exhibits higher adsorption capacity. Since point of zero charge of the goethite impregnated media was estimated at $pH_{PZC} \approx 7.5$, the favorable adsorption process under the experimental thermodynamic conditions ($1/n < 1$) stems from the positively charged surface of the media and the negatively

charged arsenate species ($H_2AsO_4^-$ and $HAsO_4^{2-}$), which are dominant at pH range of the conducted sorption experiments .

Short bed adsorbent test and pore surface diffusion modeling

The PSDM prediction and experimental data from the SBC tests are presented in Fig. 4.14. For the initially estimated $k_f \approx 6.5 \times 10^{-3}$ cm s^{-1} and $D_P \approx 2.6 \times 10^{-6}$ cm^2 s^{-1}, the PSDM provided a good prediction ($R^2 = 0.93$). Considering high porosity of the material (the particle porosity ep ≈ 0.7) and strong inner-sphere complexes that arsenic forms with goethite *via* oxygen bridges, it is verified that surface diffusion can be ignored in comparison to several orders of magnitude higher pore diffusion, and estimated Biot number (Bi_P) of 43 confirmed that the intraparticle diffusion controls the overall mass transport [32,246,250]. As illustrated, breakthrough occurred rapidly for $C/C_0 \approx 0.5$ at 2500 BVT and for $C/C_0 \approx 0.95$ at 66 000 BVT.
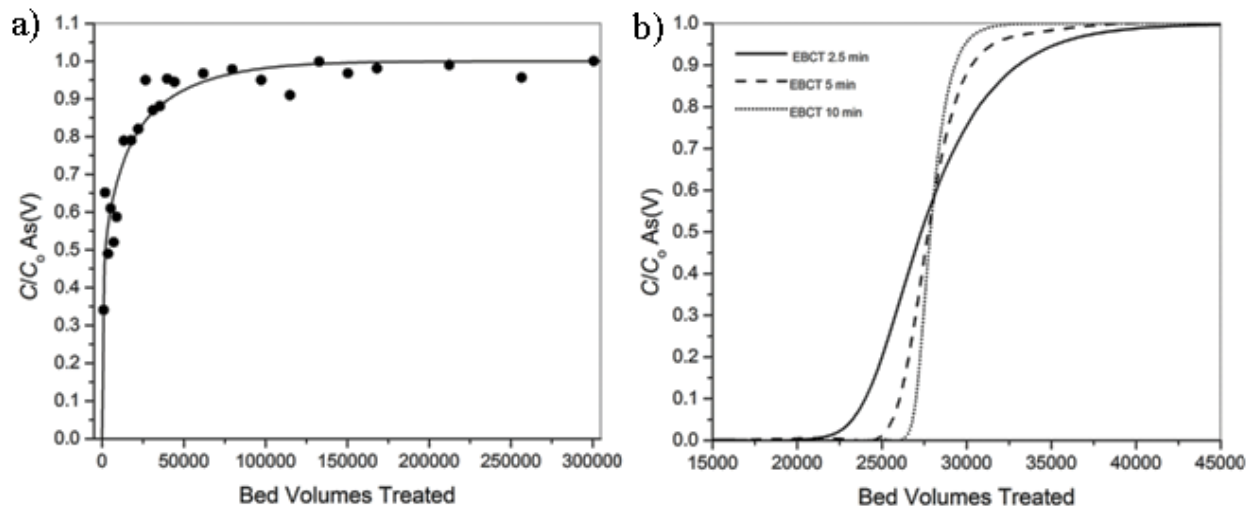
Figure 4.14. PSDM prediction and experimental data from the a) SBA tests for goethite impregnated media in arsenic-only water at 20 °C (C_o(As) $\approx$ 150 µg L^{-1}, pH 6.7 $\pm$ 0.2) and b) of a full-scale system packed with goethite impregnated media in arsenic-only water at 20 °C ($C_{o(As)}$ $\approx$30 µg L^{-1}, pH 6.7 $\pm$0.2)

Performance of full-scale packed bed systems

In order to evaluate the suitability of the developed goethite impregnated media for removing arsenic from water, the performance of a full scale system is predicted by the use of validated pore surface diffusion model at commonly used EBCTs. As illustrated in Fig. 4.14, the number of bed volumes that can be treated until the maximum contaminant level (MCL) of 10 μg L^{-1} is directly related to EBCT. The PSDM predicted that for $C/C_0 \approx 0.33$, 26 000 bed volumes can be treated at EBCT of 2.5 min. This number increases to 27 000 and 28 000 with increase of the EBCT to 5 and 10 min, respectively, implying that more bed volumes can be treated by extending the EBCT.

4.2 Efficient pollutants removal by nano/microcellulose based adsorbent

4.2.1. Efficient pollutants removal by PEG amino modified nanocellulose impregnated with iron oxide

Optimization of adsorbent preparation

The optimization goals were defined in relation to maximum adsorption capacity of **NC-PEG/FO**. In that sense, the optimization procedure, performed according to experimental plan, presented in Table 3.1, revealed that the optimal adsorbent performance was obtained following experimental conditions given on Fig. 4.15. Used materials was obtained according to optimal parameters and adjustment of the volume of reactant, defined by *exp. 3.2.2,* to precipitate thin film/porous **FO** deposit on **NC-PEG**. The maxima adsorption capacities with respect to As(V), was obtained at 12% iron loading on **NC-PEG** (Fig. 4.15 b)).
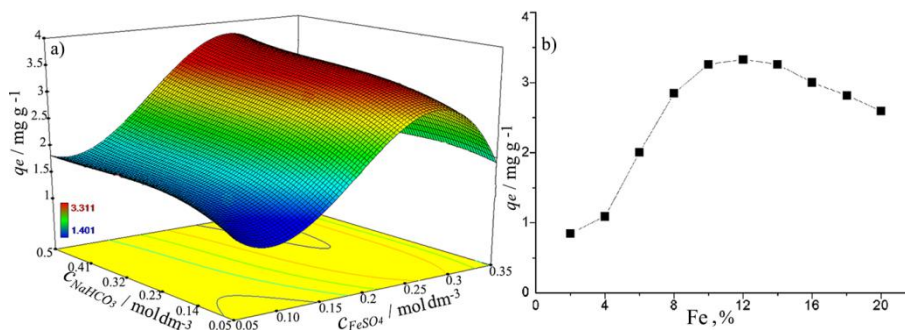
Figure 4. 15. Contour diagram representing **NC-PEG/FO**adsorbent capacity (q_e - mg g^{-1}) *vs*$C_{FeSO_4}$and C_{NaHCO_3}a), and capacity **NC-PEG/FO***vs* iron loading ($C_{i[As(V)]} = 0.5$ mg L^{-1}As(V), $m/V = 100$ mg L^{-1}, pH = 6, $T = 25$ °C) b).

The **NC-PEG** based adsorbent was obtained by modification of hydrophilic **NC** by performing two-step esterification/amidation reactions which provide introduction of branched PEG-6-arm structure. Modification of **NC,** with an acid value(*AV*) of 28, by MA to **NC-MA**, introduced ~1.50 mmol g^{-1} of carboxylic group (*AV* = 150). Lower efficiency of **NC-MA** modification with PEG-NH$_2$ resulted in 0.12 mmol g^{-1} of amino group in **NC-PEG**. This result indicates that extent of amidation, due to steric interference of the voluminous PEG-6-arm

149

structure, was significant. Experimental value of 0.12 mmol g^{-1} indicated that, regardless to lower extent of **NC** surface functionalization, the presented procedure provides large number of amino groups with high capabilities for iron binding/precipitation, as well as for the cations removal. Significance of the amino group involved in the cation complexation process was recently unequivocally presented [307]. Due to high coordination affinity of amino group and iron ion, and higher nucleophilicity of amino groups at $pH>pH_{PZC}$ provide condition for preferable complexation/chelation of iron at NC surface [233]. Also, the increased number of total basic sites contributed to uniform/high iron oxide loading.

The optimal deposition of **FO** onto **NC-PEG** was obtained by performing two step **FO** precipitation by using 82.5 mL (0.32 mol L^{-1}) of $FeSO_4 \times 7H_2O$ and 75 mL (0.38 mol L^{-1}) of $NaHCO_3$ solution for **NC-PEG/FO** production. The applied methodologies provided beneficial morphology/chemistry with a number available adsorptive sites at **NC-PEG/FO** surface for arsenate removal. It also provides means for controlled precipitation of hydrous iron oxide (HFO) in the goethite form to create nano-scaled deposit with improved textural properties.

The XRD analysis

The crystal structure of goethite was determined by using XRD technique. In a recent publication [226] was shown increase in crystallinity after modification of NC with maleic acid anhydride (Fig. 4.16). Both diffractograms display two well-defined peak doublets around $2\theta =$ 20º and 22.0º for (200) plane of cellulose which indicate the existence of cellulose I and cellulose II allomorphs. The signal at $2\theta = 35.0$ degree, having higher intensity in diffractogram of the sample NCMA corresponds to (004) atomic plane of cellulose I.

The XRD pattern of **NC-PEG/FO** is shown in the Fig. 4.17. The analysis shows characteristic peaks corresponding to amorphous goethite observed at the 2θ value of 21.2, 33.2, 36.6 and 53.2° (ICDD PDF2 No. 81-0464). XRD patterns showed large scattering which are the result of small crystallite size and amorphous properties of precipitated goethite.
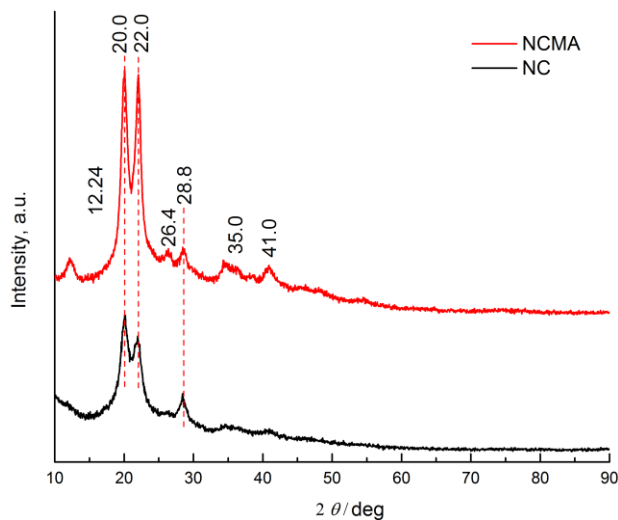
Figure 4.16. XRD diffractograms of **NC** and **NC-MA** [226]
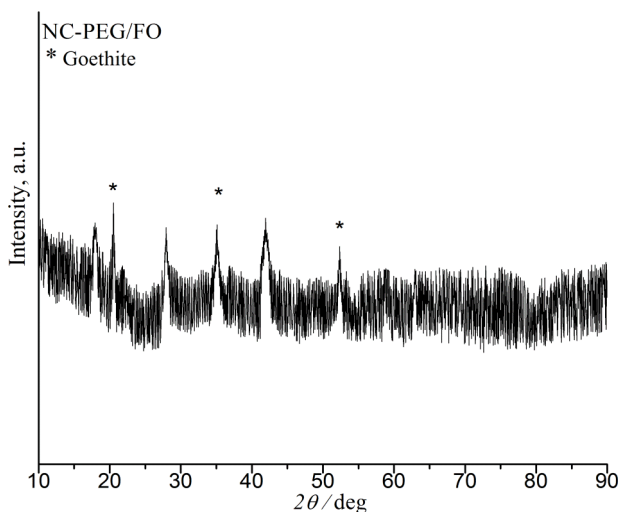
Figure 4. 17. XRD pattern of **NC-PEG/FO**

Textural properties and pH$_{PZC}$ of synthesized adsorbents

Multi-step adsorbents synthesis was performed in order to produce adsorbent material with an appropriate geometry, morphology and porosity. The determined values of a textural properties and zero point of charge (pH$_{PZC}$) are summarized in Table 4.12.

Table 4. 12. Textural properties and pH_{PZC} of studied adsorbents

Adsorbent	Specific surface area, $m^2 g^{-1}$	Pore volume, mLg^{-1}	Pore diameter, nm	pH_{PZC}[a]	pH_{PZC}[b]
NC-PEG	38.7	0.72	17.4	6.9	6.4
NC-PEG/FO	62.1	0.80	26.4	8.5	7.6

[a] before and [b] after adsorption; pH_{PZC} of **NC** was found to be <1, and pH_{PZC} of **NC-MA**<3

It was found that cations are strongly bonded to amino groups, by complexation/chelation interactions, and higher nucleophilicity of amino groups, at pH higher than pH_{PZC}, brings to stronger interaction with cadmium and nickel cations [230,233].

Due to different properties of **NC** (32.4 $m^2 g^{-1}$) and synthesized materials, the higher value of specific surface area are obtained for **NC-PEG** and **NC-PEG/FO**. Additionally, the shift of pH_{PZC} value indicates specific arsenate adsorption rather than electrostatic interaction [121,230,308], as well as formation of complexed/precipitated arsenic species at surface of goethite based adsorbent. Determination of iron content in acidic extract, by using 10% nitric acid and microwave digestion, showed that 11.7% of iron was precipitated in goethite form at **NC-PEG** surface.

Morphological characterization

Morphology of both materials indicated surface coverage by organic material, and the chemical treatment followed by **FO** deposition affects the morphological structure of the surface of **NC-PEG/FO** (Fig. 4.18). Evolution of the **NC-PEG/FO**morphology can be explained by heterogeneous reaction which takes place between **FO** and terminal amino branched structure at **NC-PEG** grains.
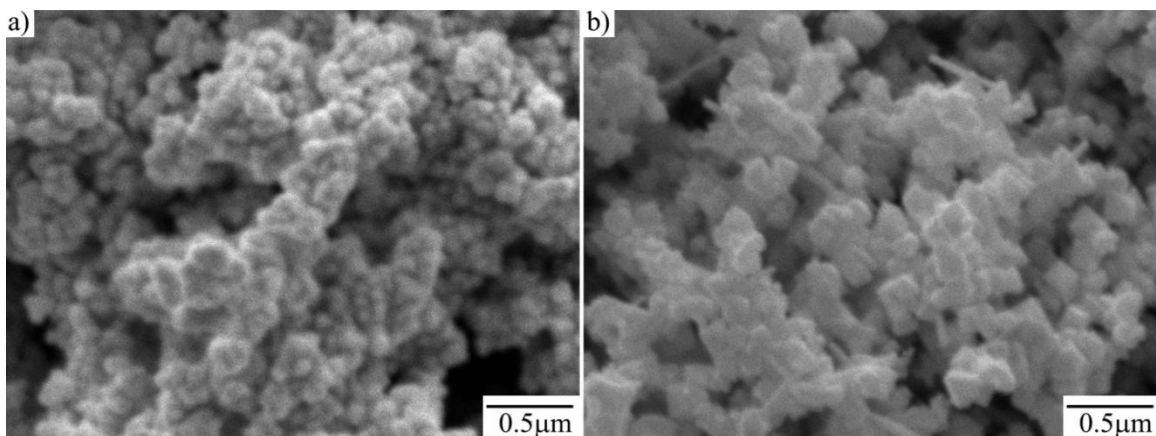
Figure 4. 18. SEM images of NC-PEG a), and NC-PEG/FO b).

FTIR analysis

Analysis of FTIR spectra provides information about bonding interaction of adsorbate and adsorbent's functional groups. Change in vibration frequency, caused by adsorbate/adsorbent group interaction is a result of bond strength change. Band shift to lower or higher frequencies indicates bond weakening or strengthening, respectively. In Fig. 4.19, presented FTIR spectra of both adsorbents recorded before and after arsenate adsorption at 3 mg L^{-1} concentration of Cd^{2+} and As(V). Lower concentration did not give significant change in absorption frequencies of the bands of interest. An analysis of FTIR spectra of **NC-PEG** showed presence of a weak band at $\approx$1640 cm^{-1} assigned to stretching of the amide carbonyl (C=O) overlapping with OH bending vibration. In addition, the bands at $\approx$1430 and 1150 cm^{-1}, correspond to N–H in-plane and C–N bond stretching vibration, respectively. The broad peaks at 3300–3600 cm^{-1} were due to the NH$_2$ stretch of the amine group overlapped with OH vibration.

Also, the broad band at $\approx$1680 and $\approx$1630 cm^{-1}, assigned to a carbonyl amide stretching vibration (amide I) and N-H in-plane vibration, respectively, is not significantly affected by interaction with increased cations concentration (Fig. 4.19). In addition, bands at $\approx$1158 and $\approx$860 cm^{-1}, corresponding to C-N stretching and out-of-plane NH$_2$ bending mode (twisting), respectively, almost completely disappeared. Role of the primary amino group to bonding of Cd^{2+} cation was observed in a significantly higher adsorption capacities. This indicates that positive charge bearing by cation has pronounced influence on electronic density at amino group, and this interaction of Cd^{2+} cation and amino lone pair restricts N-H out-of plane movement with

153

appropriate restriction N-H in-plane vibrations. Analogous analysis stands for FTIR spectra of **NC-PEG**/Ni^{2+} at different nickel cation loading.
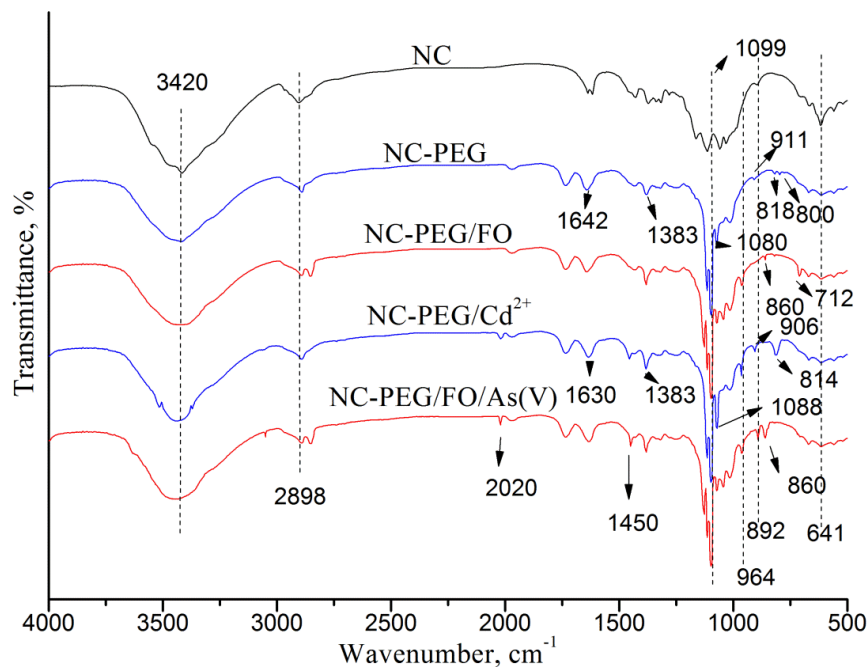
Figure 4.19. FTIR spectra of **NC**, **NC-PEG**, **NC-PEG/FO**, **NC-PEG**/Cd^{2+} and **NC-PEG/FO**/As(V)

The adsorption properties of **FO** in **NC-PEG/FO** adsorbent are mainly due to the existence of OH$_2^+$, OH, and O$^-$ functional groups at adsorbent surface. Iron oxide surface, exposed to water at different pH, develops surface charges and by adsorbing metal ions complete coordination shells with OH groups,which either bound to or released H$^+$. At neutral and acidic pH (less than 8), OH$_2^+$ and OH forms of goethite surface are dominant and responsible for the selective binding of molecular and ionic forms of arsenic species [121,233]. Differences in the spectra before and after As(V) adsorption could be noticed. Broad band at ≈3429 cm^{-1}, ascribed to OH and NH$_2$ stretching vibrations, asymmetric and symmetric, is not significantly affected by adsorbed pollutant. According to FTIR spectra of **NC-PEG/FO** and **NC-PEG/FO/**As(V) a low weakening of the Fe–OH bands (peaks at 1126, 1043 and 964 cm^{-1}) resulted in disappearance in spectra of **NC-PEG/FO**/As(V) by using As(V) concentration > 2 ppm. New band, corresponding

154

to As–O stretching vibration of coordinated arsenic species, appeared at 892 and 860 cm^{-1} [121,233]. It was explained that As–O–Fe bond strength increase with increasing coordination number, and consequently, the wavelength of the stretching vibration of the uncomplexed/unprotonated As–O–Fe is located at higher value (892 cm^{-1}), while one for complexed As–O–Fe band is located at lower frequency (860 cm^{-1}).

Effect of pH on adsorption efficiency

The pH influences equilibrium of ionic species and protonation/deprotonation of the sorbent functional groups. It is known that presence of hydrogen/hydroxide ion could modify the redox potential of both sorbate and sorbent, and provoke dissolution of the sorbent. The degree of As(V), As(III), Cd^{+2} and Ni^{2+} removal *vs* initial pH (pH$_i$) in presence of studied adsorbents are presented on Fig. 4.20.
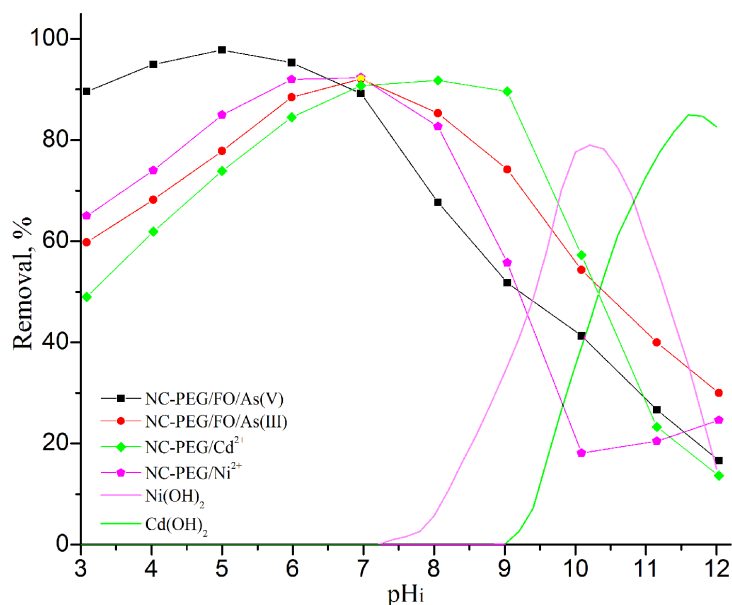
Figure 4.20. Influence of pH on As(V) and As(III) removal by **NC-PEG/FO**, and Cd^{+2} and Ni^{2+} removal by **NC-PEG** (C_i = 100 µg L^{-1}, m/V = 100 mg L^{-1}, T = 25 °C).

It could be noted from Fig. 4.20 that percentage of As(V) and As(III) adsorption on **NC-PEG/FO** was almost independent in the pH range 5-7 with >90% removal, and subsequently, gradual decrease starts at pH>7. According to pH-dependent ionization of triprotic arsenic and

155

arsenous acid, the highest adsorption shows the most effective removal at pH in the vicinity of pKa [121,309]. The charged As species participate in different electrostatic interactions (attraction/repulsion) with surface/ions charges influencing the intensity of As flux toward the specific adsorption sites. Positively charged surface of **NC-PEG/FO** adsorbent at pH < pH_{PZC}, attracts the negatively charged arsenate causing higher intensity of As flux toward the adsorbent surface. The opposite is true at higher pH. The selection of optimal pH 6 was dictated by three factors: adsorption capacity, adsorbent deposit stability (dissolution) and consideration of techno-economic indicator.

In order to eliminate the possible effect of precipitation of $Cd(OH)_2$ and $Ni(OH)_2$, quantitative determinations of precipitate was performed without addition of **NC-PEG** [121,309]. Results presented indicated that the precipitation of $Cd(OH)_2$ at pH>9 and $Ni(OH)_2$ at pH>7.5 takes place at significant extent (Fig. 4.20). According to this, at pH<8, it is certain that Cd^{+2} and Ni^{+2} removal is not affected by salt precipitation and obtained results could be considered without any misleading conclusions. Thus, the pH-dependent adsorption profiles (Fig. 4.20), for **NC-PEG**/Cd^{+2} and **NC-PEG**/Ni^{+2}, presents differences between the overall pollutant removal and precipitated salt. In that sense, optimal pH for all pollutant removal was chosen to be pH 6. The lower pH could have detrimental effect on organic functionalities or cause increased solubility of **FO** nanoscale deposit in **NC-PEG/FO** adsorbent. Moreover, the pH 5-6.5 is usually found in most natural waters which is beneficial for direct uses without prior pH adjustment of inlet water flow, and also it means that implementation of such technology could have positive techno-economic indicators.

Adsorption study: pollutants removal by NC-PEG and NC-PEG/FO

Considering significance of pH influence on pollutant speciation and ionization state of adsorbent surface, it was important to study influence of pH, in the range 3 - 10, on effectiveness of pollutant removal. The amino groups contribute to increased surface basic properties and, thus, according to the pH_{PZC} value of **NC-PEG** (6.9), preferable electrostatic interactions favor adsorption of cations at pH > pH_{PZC}. Due to this, optimal pH 6 was selected and applied during cations removal. It was shown in a previous work that optimal pH for As(V) removal in a

presence of goethite modified macroporous resin was 6 - 6.5, and this value was used throughout of the present work [121,308].

Various isotherm models are used to evaluate the adsorption capacity, and non-linear regression method with commonly used isotherms: Langmuir, Freundlich, Redlich-Peterson, Dubinin-Radushkevich (D-R), Sips and Jovanovic (Table 2.4). The highest correlation coefficients are obtained by the use of the D-R equation for **NC-PEG,** and Freundlich for **NC-PEG/FO** (Table 4.13 and Fig. 4.21). According to the Freundlich isotherm, mechanism of cations adsorption onto **NC-PEG** can be described by heterogenous adsorption, where adsorbed ion/molecule possesses different enthalpies and adsorption activation energies. The D–R isotherm model is mainly valid at low pollutant concentration, and usually was used for description of adsorption on both homogeneous and heterogeneous surfaces [230].
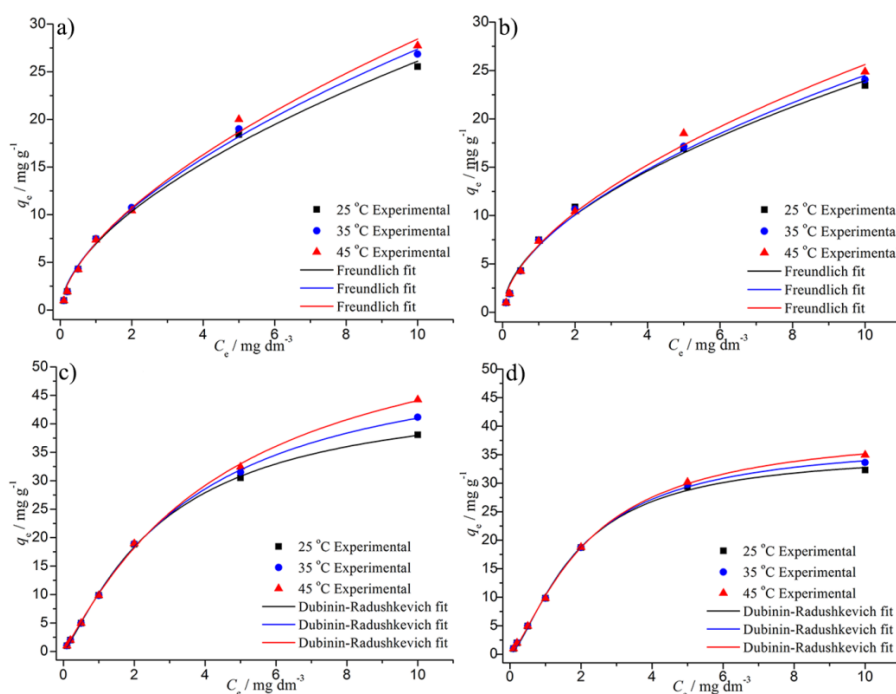
Figure 4. 21. Adsorption isotherms fitting for As(V) a) and As(III) b) (m/V = 100 mg dm^{-3}, C_i = 0.1, 0.2, 0.5, 1, 2, 5 and 10 mg dm^{-3}, pH = 6.0 ± 0.1) with **NC-PEG/FO** adsorbent, and Cd^{2+} c) and Ni^{2+} d) removal with **NC-PEG**, respectively, (m/V = 100 mg L^{-1}, C_i = 1, 2, 3, 4, 5, 6 and 7 mg L^{-1}, pH = 6.0 ± 0.1).

157

Table 4.13. The results of the fitting for NC-PEG/FO and NC-PEG obtained by using Freundlich and D-R models

Isotherm	NC-PEG/FO					
	As(V)			As(III)		
	25 °C	35 °C	45 °C	25 °C	35 °C	45 °C
Freundlich						
k_f / mg g^{-1}	11.756	12.134	12.202	11.349	11.375	11.579
$1/n$	0.3516	0.357	0.3631	0.3425	0.344	0.3518
R^2	0.996	0.995	0.992	0.998	0.997	0.996
	NC-PEG					
Isotherm	Ni^{2+}			Cd^{2+}		
	25 °C	35 °C	45 °C	25 °C	35 °C	45 °C
Dubinin-Radushkevich						
q_m / mg g^{-1}	27.49	27.99	28.48	29.54	30.71	31.88
β / mol^2 J^{-2} x10^9	7.67	7.65	7.64	7.67	7.63	7.6
E /kJ mol^{-1}	8.073	8.083	8.092	8.072	8.092	8.112
R^2	0.992	0.993	0.99	0.998	0.985	0.989

The maximum adsorption capacities for As(V) and As(III) by using **NC-PEG/FO** (m/V = 100 mg L^{-1}, C_i = 0.1, 0.2, 0.5, 1, 2, 5 and 10 mg L^{-1}, pH = 6.0 ± 0.1), as well as for Cd^{2+} and Ni^{2+} removal with **NC-PEG** (m/V = 100 mg L^{-1}, C_i = 1, 2, 3, 4, 5, 6 and 7 mg L^{-1}, pH = 6.0 ± 0.1), respectively, obtained by using Langmuir model, are given in Table 4.14.

Table 4.14. The maximum adsorption capacities for As(V), As(III), Cd^{2+} and Ni^{2+}, obtained by using Langmuir model

Adsorbent		q_e / mg g^{-1}		
		25 °C	35 °C	45 °C
NC-PEG/FO	As(V)	26.0	27.4	28.6
	As(III)	23.6	24.3	25.5
NC-PEG	Cd^{2+}	37.9	40.9	43.9
	Ni^{2+}	32.4	33.7	35.0

Results of fitting of experimental data by using Langmuir isotherm show high predicted adsorption capacity for As(V), and increases of adsorption capacity with temperature increase: from 26.0 mg g^{-1} at 25 °C, 27.4 mg g^{-1} at 35 °C, to 28.60 mg g^{-1} at 45 °C. The maximum

adsorption capacities of As(III), Cd^{2+} and Ni^{2+}, obtained by the use of Langmuir model, showed similar trend of increasing adsorption capacities (Table 4.14).

The *n* value from Freundlich isotherm is a measure of adsorption intensity or surface heterogeneity, becoming more heterogeneous as its value gets closer to zero. Whereas, a value *n*<1 implies chemisorptions process, while higher value is an indication of cooperative adsorption, *i.e.* physisorption and chemisorption, operative having different contribution at different steps of equilibration of the system. Values of *n*> 1 indicate that adsorption processes slightly decreased at lower sorbate concentration, and also indicate the presence of different active centers where the highest energies are of higher activity, *e.g.* participate in a initial adsorption step. Adsorption parameter, the separation factor values (K_R), describe whether a sorption system is favorable or unfavorable and can be expressed by eq. (4.5):

$$K_R = \frac{1}{1 + bC_0}$$ (4.5)

where K_R is a dimensionless separation factor, C_0 is initial concentration (mg L^{-1}) and *b* is Langmuir constant (L mg^{-1}). The K_R value implies the adsorption to be unfavorable (K_R> 1), linear ($K_R = 1$), favorable ($0 < K_R$<1) or irreversible (K_R =0) [310]. Obtained values of K_R, in the range from 0,0095 to 0,865, indicated favorable adsorption of investigated adsorbate on both **NC-PEG** and **NC-PEG/FO** adsorbents.

Adsorption kinetics

The determination of adsorption rate after which system attains equilibrium could help in better understanding of pollutant adsorption mechanism, *i.e.* probable reaction paths. Due to complexity of adsorption process, *e.g.*, complex adsorption process steps with contribution of mass transfer and chemical reaction processes, different kinetic models are used to fit experimental data. The kinetic data are analyzed by non-linear least-squares method in the form of pseudo-first, pseudo-second-order (PSO) rate equations and intra-particle diffusion model (Weber-Morris model; W-M). Judging from the regression coefficients, kinetic data are satisfactorily fitted by using pseudo-second-order (PSO) equation [230,233]. The fitting of the

159

kinetic data obtained for cations and arsenic removal at 25, 35 and 45 °C afforded rate constants given in Table 4.15.

Table 4.15. The kinetic parameters for investigated adsorbate removal obtained by the use of PSO equation

	Constants/adsorbent	**NC-PEG/FO**		**NC-PEG**	
		As(V)	As(III)	Cd^{2+}	Ni^{2+}
25°C	k_2 / g mg^{-1} min^{-1*}	0.054	0.063	0.037	0.050
	q_e / mg g^{-1}	4.419	4.384	8.488	4.391
	R^2	0.998	0.997	0.999	0.998

* $C_i = 1$ mg L^{-1} for As(V) and As(III) and 0.5 mg dm^{-3} for Cd^{2+} and Ni^{2+}

Activation energy for pollutants removal was calculated using Arrhenius eq. (4.6):

$$k_2 = k_0 \exp\left[\frac{-E_a}{RT}\right] \tag{4.6}$$

where $k^{'}$ (g mg^{-1} min^{-1}) is the pseudo-second order rate adsorption constant, k_0 (g mmol^{-1} min^{-1}) is the temperature independent factor, E_a (kJ mol^{-1}) is the activation energy, R (8.314 J mol^{-1} K^{-1}) is the gas constant and T (K) is the adsorption absolute temperature. A plot of ln $K^{'}$ versus 1/T gave straight line with slope $-E_a/R$ from which activation energy was calculated.

The calculated activation energies for As(V) and As(III) adsorption at **NC-PEG/FO** were found to be 9.58 and 15.46 kJ mol^{-1}, while 2.67 and 6.94 kJ mol^{-1} were obtained for Cd^{2+} and Ni^{2+} adsorption on **NC-PEG**, respectively. The results obtained are in agreement with study of As(V) adsorption on synthetic goethite presented in the work of Lakshmipathiraj *et al.*[238]. Adsorption kinetics is generally controlled by diffusive mass transfer, thusrates of approaching to equilibrium usually increase with increasing of temperature. The results show that the intra-particle diffusion is a rate-controlling step for arsenic removal since the activation energy is low and with in the range of 8–22 kJ mol^{-1}, characteristic for diffusion-controlled processes such as ion-exchange/complexation [311].

The results of PSO provide fitting of the kinetic related to overall adsorption rate, and could not help in assessing of the rate-limiting step. Therefore, the intra-particle diffusion model, [233], *i.e.* W-M model, was applied to analyze mass transfer phenomena of overall process, and

the results are given in Table 4.16. The adsorption is usually accomplished through a series of distinct consecutive steps: the external mass transfer (diffusion through the bulk liquid), the diffusion across boundary layer surrounding the particle (film diffusion), diffusional transport within the internal structure of adsorbent (intra-particle diffusion) and the adsorption on solid surface. Regardless on the simplicity of the W-M model, it suffers from uncertainties caused by multi-linear nature, *i.e.* overall mass transport could be controlled by more than one step at different stage of the adsorption process. Generally, bulk diffusion and As(V) adsorption at goethite surface are fast processes. The results of W-M fittings are given in Table 4.16.

Table 4.16. The kinetic parameters of the Weber-Morris (intra-particular) model for arsenate adsorption

Step	Constants	NC-PEG/FO		NC-PEG	
		As(V)	As(III)	Cd^{2+}	Ni^{2+}
Step 1	k_{p1} / mg g^{-1} min$^{-0.5}$	0.262	0.130	0.281	0.159
	C_1 / mg g^{-1}	2.467	3.099	4.891	2.387
	R^2	0.999	0.997	0.998	0.997
Step 2	k_{p2} / mg g^{-1} min$^{-0.5}$	0.118	0.078	0.0892	0.142
	C_2 / mg g^{-1}	3.099	3.340	7.317	2.891
	R^2	0.997	0.999	0.979	0.999
Step 3	k_{p3} / mg g^{-1} min$^{-0.5}$	0.033	0.0033	0.0577	0.020
	C_3 / mg g^{-1}	3.930	3.931	7.651	4.025
	R^2	0.969	0.971	0.985	0.997

The results obtained following the Weber–Morris model show three successive linear steps: fast kinetic in first step followed by medium to low adsorption rate in second step. The larger intercept found for **NC-PEG** indicates higher resistance, *i.e.* slower ionic transport, due to intra-particle diffusion. First linear part demonstrates external mass transfer from bulk solution to the most available outer adsorbent surface adsorptive sites. The second part of W-M fit represent processes of high dependence on adsorbent porosity, *i.e.* pore geometry and network density. Due to the concentration gradient the ions diffuse through bulk solution and tree like system of macro-, meso- and micropores extending into adsorbent interior to reach all available surface active sites [233]. The intra-particle and film diffusion resistance slow down adsorbate transport,

i.e. net transport in a direction of variable time-dependent concentration gradient. At the final stage of process, the adsorption takes place at low rate until saturation of all available surface sites is achieved. Additional analysis on the contribution of external mass transfer and diffusion inside the pores to overall diffusional adsorbate transport is also performed.

Thermodynamic study

The temperature effect on pollutants adsorption onto **NC-PEG** and **NC-PEG/FO**, respectively, is deduced from results of adsorption experiments performed at 25, 35 and 45 °C. The temperature dependence of arsenic adsorption is associated with changes in thermodynamic parameters such as ΔG^o (the standard Gibb's free energy change), ΔH^o (the enthalpy change), and ΔS^o (the entropy change); these parameters are calculated using the eqs. (3.3) and (3.4). The obtained results are given in Table 4.17.

Table 4.17. Thermodynamic parameters of adsorption processes of As(V), As(III), Cd^{2+} and Ni^{2+} removal

		t / °C	ΔG^o / kJ mol^{-1}	ΔH^o / kJ mol^{-1}	ΔS^o /J mol^{-1} K^{-1}	R^2
NC-PEG/FO	As(V)	25	-39.2	5.17	114.19	0.938
		35	-40.41			
		45	-41.48			
	As(III)	25	-39.58	5.25	115.13	0.999
		35	-40.72			
		45	-41.88			
NC-PEG	Cd^{2+}	25	-43.16	8.30	117.92	0.994
		35	-44.30			
		45	-45.50			
	Ni^{2+}	25	-44.21	9.39	116.77	0.998
		35	-45.36			
		45	-46.54			

The negative values of ΔG^o indicate spontaneity and more beneficial adsorption at higher temperature, while positive ΔH^o additionally confirms conclusion about more effective adsorption at higher temperature (Tabela 4.17). Somewhat higher enthalpy was obtained for Cd^{2+} and Ni^{2+} adsorption, which means more preferable adsorption for both adsorbate at higher

162

temperature. Lower value, 5.17 and 5.25 kJ mol^{-1}, was obtained for As(V) and As(III) removal with **NC-PEG/FO**, respectively. Breakage of water hydration shells by pollutant species and their transport through the bulk solution, within the pores and through the surface boundary layer is more intensive process at higher temperature. Transport of exchangeable pollutant ions to adsorption site, and, on the other side, a number of water (exchangeable) molecules was released into bulk solution contributing to increases of entropy change [230,233]. At steady-state condition increased randomness at adsorbent/solution is increased due to different intermolecular interactions which contribute to positive entropy change, *i.e.* adsorption is an entropy-driven process. All of these elementary processes, which take place in the course of equilibrium attainment, contribute to positive enthalpy change.

Regeneration and reusability

Design of environmentally friendly and economically acceptable technology for pollutant removal necessarily demands development of long term adsorbent application. Number of the re-use cycles of adsorbent contributes to the cost effectiveness of overall technology. The material cost of developed adsorption technology includes: the life-cycle of adsorbent, chemicals used for regeneration of spent adsorbent, residual materials handling, applied treatment technology and disposal/storage of waste to recycling company. In order to minimize material cost, development of high capacity adsorbent capable to be regenerated efficiently offers an alternative. The selection of an efficient reagent for the regeneration depends on the cations and arsenic bonding type, nature of sorbent, amino at **NC-PEG** and hydroxyl groups at **NC-PEG/FO**. The formation of surface complexes, monodentate, bidentate-mononuclear and bidentate-binuclear through formation of As–O–Fe bond, indicates necessity of the application of strong competitive anion capable to break off As-O-Fe bond, *i.e.* displace As(V) anion [121]. On the other hand, complexation of Lewis acid, Cd^{2+} and Ni^{2+} cations, and terminal amino groups present at **NC-PEG** surface could be easily desorbed by using stronger inorganic base [233]. Therefore, the objective of competitive cation and anion exchange from adsorbent surface should result by their release into solution leaving active surface sites at the level, as close as possible, to concentration before adsorption cycle. Subsequent rinsing of **NC-PEG/FO** with dilute acid, 2 % sulfuric acid,

163

causes protonation of negatively charged surface functional groups on that way providing their sorption potential. Many systems for regeneration were used, and the most efficient one was NaOH/NaCl, and the results of desorption study are presented in Table 4.18.

Table 4. 18. Results of arsenate desorption for sorbent **NC-PEG** and **NC-PEG/FO** in first cycle

		NC-PEG/FO		NC-PEG	
Desorption agent	C / mol L^{-1}	As(V)	As(III)	Cd^{2+}	Ni^{2+}
NaOH/NaCl	0.2/0.2	79	80	78	79
	0.5/0.2	87	88	83	85
	0.5/0.5	92	94	88	91

Low decreases of adsorption capacity were observed over five adsorption/regeneration cycles (in the range 10-25 %). The most efficient desorption system was found to be NaOH/NaCl (0.5/0.5) system. In a first cycle 92% of As(V) were desorbed, and throughout five consecutive cycles, desorption efficiencies was decreased to 80% in fifth desorption cycle for **NC-PEG/FO**. Similar situation stand for As(III): 94% in first and 82% in fifth desorption cycle. Desorption efficiency for Cd^{2+} and Ni^{2+} from **NC-PEG** adsorbent are: 91% and 88% in first and 79% and 77% in fifth desorption cycle, respectively. In summary, **NC-PEG** and **NC-PEG/FO** are reusable in a multi-step processes and efficient adsorbent for Cd^{2+} and Ni^{2+} cation, and As(V) and As(III) oxyanions removal for over five adsorption/desorption cycles.

4.2.2. Efficient pollutant removal by amino modified nanocellulose impregnated with hydrous iron oxide: material performance

The structural analysis

The crystal structure of goethite was determined by using XRD technique, and result of **NC-L/FO** is shown in the Fig. 4.22. The analysis show characteristic peaks corresponding to amorphous goethite observed at the 2θ value of 21.2, 33.2, 36.6 and 53.2° (ICDD PDF2 No. 81-0464). Observed XRD patterns show selective line broadening and large scattering which may be the result of small crystallite size and amorphous properties of precipitated goethite.
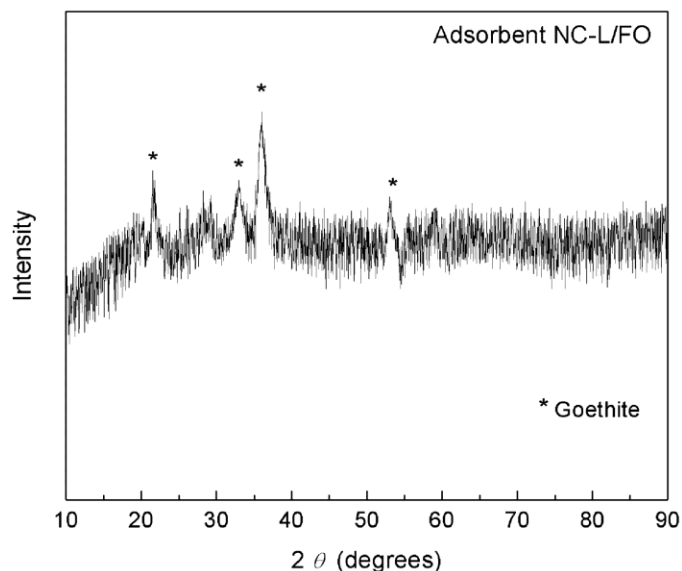
Figure 4. 22. XRD pattern of **NC-L/FO**

Textural properties and pH$_{PZC}$

Comprehensive experimental work through multi-step synthesis of adsorbents was applied in order to design the material with an appropriate geometry and pore structure. The determined values of a textural properties, zero point of charge (pH$_{PZC}$), elemental analysis, DA_{Kaiser} and CN values are summarized in Table 4.19.

Table 4. 19. Textural properties, pH$_{PZC}$, elemental analysis, DA_{Kaiser} and CN values of **NC-L** and **NC-L/FO**

Adsorbent	SSA $(m^2 g^{-1})$	V$_p$ (mLg^{-1})	d$_p$ (nm)	pH$_{PZC}$[a]	pH$_{PZC}$[b]	C (%)	H (%)	N (%)	O (%)	DA_{Kaiser} $(mmol\ g^{-1})$
NC-L	82.1	0.82	18.2	5.7	5.2	41.42	5.86	2.24	50.48	1.22
NC-L/FO[*]	112.5	1.12	30.4	8.7	7.4	35.13	5.66	2.01	43.44	-

[a] before; [b] after adsorption; pH$_{PZC}$ of **NC** was found to be <1, and pH$_{PZC}$ of NC-MA <3; [*] 13.76% of inorganic residue (mainly iron oxide)

It was described that cations are strongly bonded to amino groups, by complexation/-chelation interactions, and higher nucleophilicity of amino groups, at pH higher than pH$_{PZC}$, brings to stronger interaction with lead cation [233]. The increased number of total basic sites, 1.22 mmol g^{-1} for **NC-L**, contributed to uniform/high iron oxide loading. According to total

basic sites determination, and assuming that the most basic are primary amio groups, it was evaluated that ~20% for **NC-L** of amino terminal organic branched functionalities are present on **NC**, respectively. Stepwise modification of **NC,** $AV = 28$ mg g^{-1}, by MA to **NC-MA**, introduced ~1.50 mmol g^{-1} of carboxylic group ($AV = 150$ mg g^{-1}). Theoretical consideration of the number of amino groups in **NC-L** indicated that it could be expected 3 mmol g^{-1} of total basic sites in **NC-L**. Experimental value of 1.22 mmol g^{-1} indicates that lower efficiency of stepwise functionalization of **NC** surface, but regardless the presented procedure provides large number of amino groups with high capabilities for iron binding/precipitation.

Due to different properties of **NC** and synthesized materials, the higher value of specific surface area is obtained for **NC-L/FO**. Additionally, the shift of pH$_{PZC}$ value indicates specific arsenate adsorption rather than electrostatic interaction [230], as well as formation of complexed/precipitated arsenic species at surface of goethite based adsorbent. Additionally, determination of elemental content showed that 13.8% of inorganic material in the form of iron oxide. Determination of iron content in acidic extract, by using 10% nitric acid and microwave digestion, showed that 9.1% of iron was precipitated in a goethite form at **NC-L/FO** surface.

Morphological characterization

Morphology of both materials indicated surface coverage by organic material, and the chemical treatment followed by **FO** deposition affects the morphological structure of the surface of **NC-L/FO** (Fig. 4.23). Evolution of the **NC-L/FO** morphology can be explained by heterogeneous reaction which takes place between **FO** and terminal amino branched structure at NC grains.
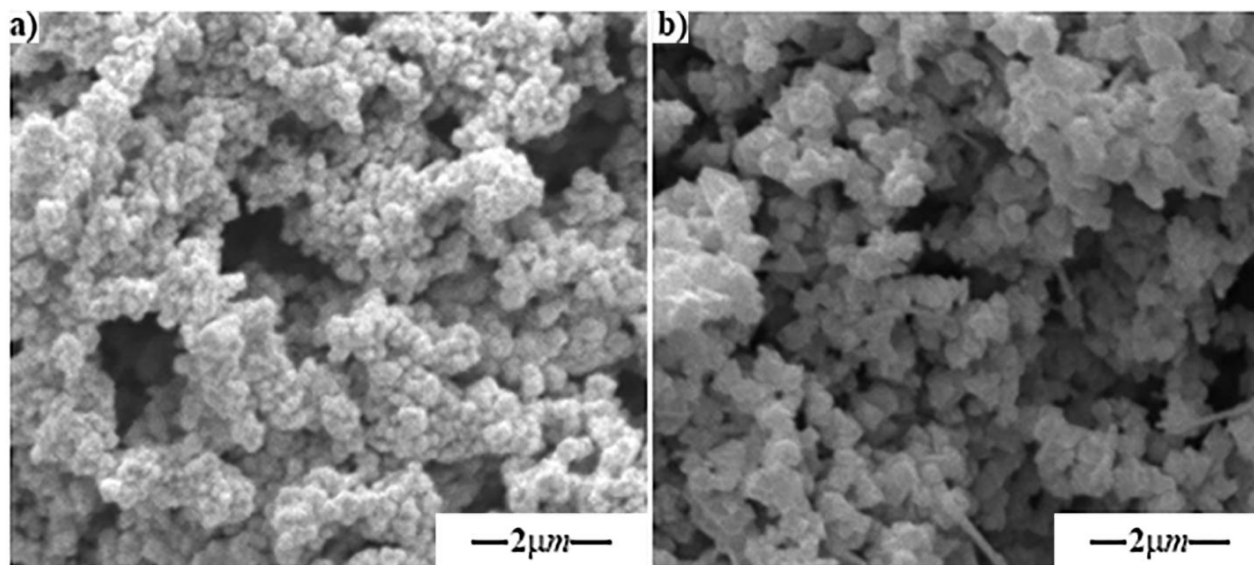
Figure 4.23. SEM images of **NC-L** a), and **NC-L/FO** b)

FTIR analysis

In Fig. 4.24, FTIR spectra of both adsorbents, **NC-L** and **NC-L/FO**, recorded before and after lead/arsenate adsorption are presented. An analysis of FTIR spectra of **NC-L** showed presence of a weak band at ≈ 1640 cm^{-1} assigned to stretching of the amide carbonyl (C=O) overlapping with OH bending vibration. In addition, the bands at ≈ 1430 and 1150 cm^{-1}, correspond to N–H in-plane and C–N bond stretching vibration, respectively. The broad peaks at 3300–3600 cm^{-1} were due to the NH$_2$ stretch of the amine group overlapped with OH vibration.
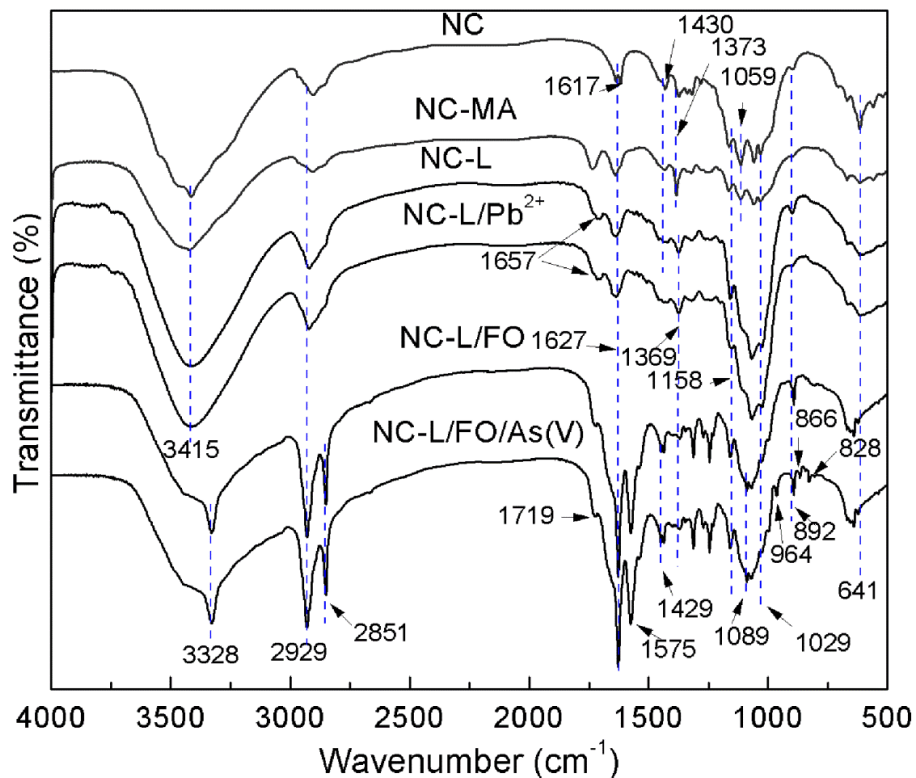
Figure 4.24. FTIR spectra of **NC, NC-MA, NC-L, NC-L/Pb^{2+}, NC-L/FO** and **NC-L/FO/As(V)**

Differences in the spectra before and after lead/arsenate adsorption could be noticed. Broad band at $\approx$3415 cm^{-1}, ascribed to OH and NH$_2$ stretching vibrations, asymmetric and symmetric, is not significantly affected by adsorbed pollutant. Also, the broad band at $\approx$1657 and $\approx$1627 cm^{-1}, assigned to a carbonyl amide stretching vibration (amide I) and N-H in-plane vibration, respectively, is not significantly affected by interaction with increases cations concentration (Fig. 4.24; **NC-L** and **NC-L/**Pb^{2+}). In addition, bands at $\approx$1158 and $\approx$860 cm^{-1}, correspond to C-N stretching and out-of-plane NH$_2$ bending mode (twisting), respectively, almost completely disappear. This indicates that positive charge bearing by lead cation has pronounced influences on electronic density at amino group. Also, this result indicates that appropriate interaction of Pb^{2+} cation and amino lone pair restricts N-H out-of plane movement with small restriction N-H in-plane vibrations, thus indicating that lead cation coordinate with nitrogen lone pair in such way to contribute to the motion of amino group [233].

168

According to FTIR spectra of **NC-L/FO** and **NC-L/FO/**As(V) a low weakening of the Fe–OH bands (peaks at 1126, 1043 and 964 cm^{-1}) resulted in disappearance in spectra of **NC-L/FO**/**As**(V) by using As(V) concentration >2 ppm. New band, corresponding to As–O stretching vibration of coordinated arsenic species, appeared at 828 and 866 cm^{-1} [230,233,308]. It was explained that As–O–Fe bond strength increase with increase of coordination number, and consequently, the wavelength of the stretching vibration of the uncomplexed/unprotonated As–O–Fe is located at higher value (866 cm^{-1}), while one for complexed As–O–Fe band is located at lower frequency (828 cm^{-1}).

Adsorption study: pollutants removal by NC-L and NC-L/FO

Considering significance of pH influences on pollutant speciation and ionization state of adsorbent surface, it was important to study influence of pH, in the range 3 - 10, on effectiveness of pollutant removal. The amino groups contribute to increased surface basic properties and, thus, according to the pH$_{PZC}$ value of **NC-L** (5.7), preferable electrostatic interactions favor adsorption of cations take place at pH>pH$_{PZC}$. Due to this, optimal pH 6 was selected and applied during for cations removal. It was shown in a previous work that optimal pH for As(V) removal in a presence goethite modified macroporous resin was 6-6.5, and it was used throughout of present work [308].

Various isotherm models are used to evaluate the adsorption capacity, and non-linear regression method with commonly used isotherms: Langmuir, Freundlich, Redlich-Peterson, Dubinin-Radushkevich (D-R), Sips and Jovanovic. The highest correlation coefficients are obtained by the use of the Freundlich and D-R equations for **NC-L** (Table 4.20 and Fig. 4.25), and Freundlich for **NC-L/FO**. According to the Freundlich isotherm, mechanism of cations adsorption onto **NC-L** can be described as heterogenous adsorption, where adsorbed ion/molecule possesses different enthalpies and adsorption activation energies. The D–R isotherm model is mainly valid at low pollutant concentration, and usually was used for description of adsorption on both homogeneous and heterogeneous surfaces [312].
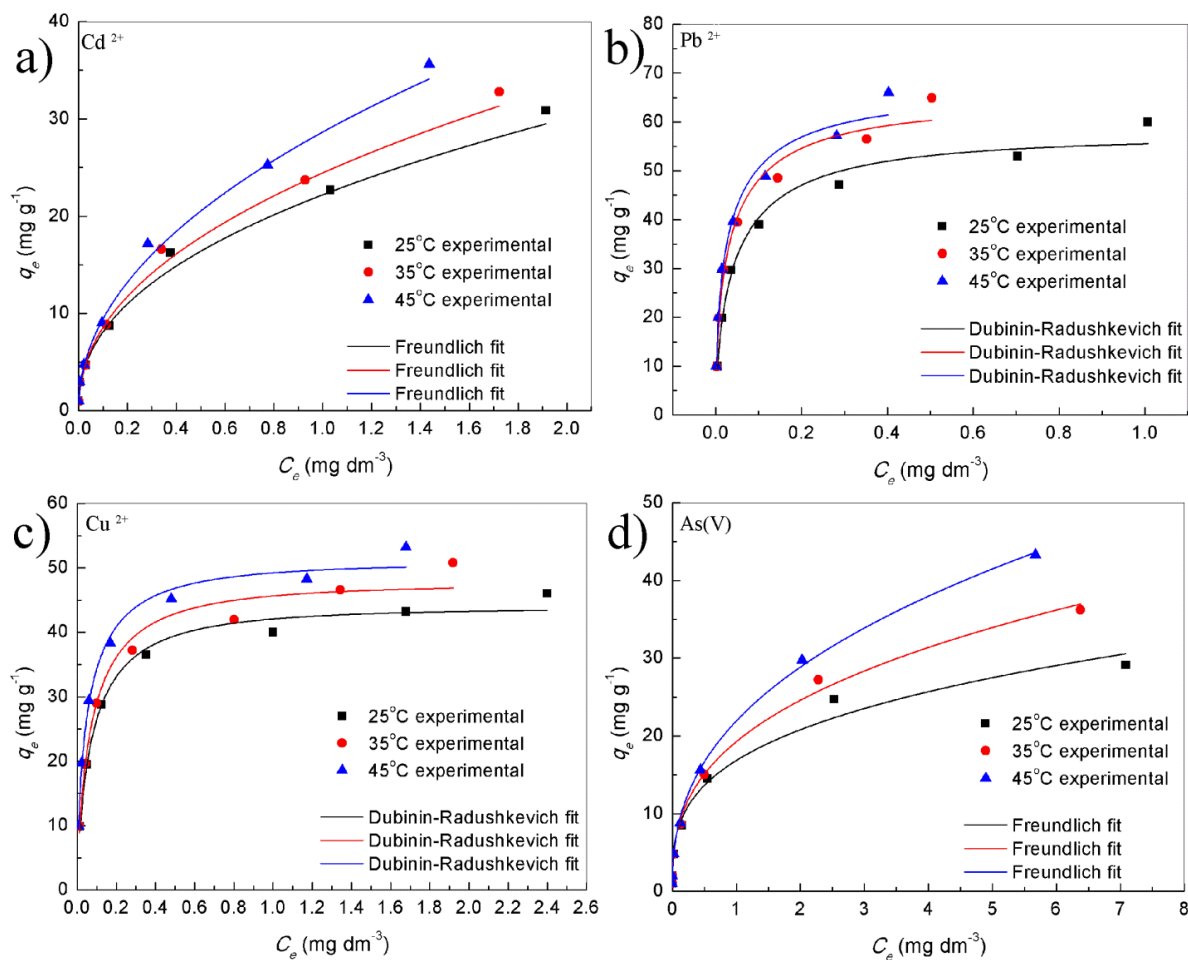
Figure 4. 25. Adsorption isotherms fitting for a) Cd^{2+}, b) Pb^{2+}, c) Cu^{2+} removal, respectively, ($m/V = 100$ mg L^{-1}, $C_i = 1, 2, 3, 4, 5, 6$ and 7 mg L^{-1}, pH $= 6.0 \pm 0.10$) with **NC-L**, and d) As(V) ($m/V = 100$ mg L^{-1}, $C_i = 0.1, 0.2, 0.5, 1, 2, 5$ and 10 mg L^{-1}, pH $= 6.0 \pm 0.10$) with **NC-L/FO**

Table 4. 20. The fitting results for **NC-L** and **NC-L/FO**obtained by using Freundlich and D-R models

Freundlich	Cd^{2+}			As(V)		
	25 °C	35 °C	45 °C	25 °C	35 °C	45 °C
k_f (mg g^{-1})	22.20	24.45	28.65	16.84	19.27	21.93
n	2.29	2.20	2.08	3.28	2.84	2.52
R^2	0.981	0.983	0.984	0.987	0.997	0.999
Dubinin-Radushkevich	Pb^{2+}			Cu^{2+}		
(D-R)	25 °C	35 °C	45 °C	25 °C	35 °C	45 °C
q_m (mg g^{-1})	57.15	64.06	66.01	43.89	47.57	50.88
β (mol^2 J^{-2}) x10^9	−9.85	−7.57	−6.66	−14.3	−13.0	−9.77
E (kJ mol^{-1})	−7.12	−8.13	−8.66	−5.91	−6.20	−7.15
R^2	0.983	0.983	0.984	0.988	0.978	0.990

Results of fitting of experimental data by using Langmuir isotherm show high predicted adsorption capacity fo As(V), and increases of adsorption capacity with temperature increase: from 33.4 mg g^{-1} at 25 °C, 35.2 mg g^{-1} at 35 °C, to 37.0 mg g^{-1} at 45 °C.. The maximum adsorption capacities of Cd^{2+}, Pb^{2+} and Cu^{2+},obtained by the use of Langmuir model, for initial pollutant concentration of 7 mg L^{-1}, were 30.5, 60.0 and 46.6 mg g^{-1} at 25 °C, respectively.

The best fitting of Pb^{2+} and Cu^{2+} adsorption on **NC-**L was obtained by using D-R model, which could be presented in the form:

$$q_e = q_{max} \exp(-\beta\varepsilon^2), \tag{4.7.}$$

or in linearized form:

$$ln\ q_e = ln\ q_{max} - \beta\varepsilon^2 \tag{4.8.}$$

where the saturation adsorption q_{max} represents the total specific micropore volume of the sorbent. Generally, the D–R model was used for description of the adsorption processes on both homogeneous and heterogeneous surfaces at low concentration ranges of sorbate. The value of β is related to the adsorption free energy, E (kJ mol^{-1}), which is defined as the free energy change required to transfer 1 mol of ions from solution to the solid surfaces, and ε is Polanyi potential:

$$\varepsilon = RTln(1 + \frac{1}{c_e}) \tag{4.9}$$

where R is the ideal gas constant (8.31 J mol^{-1} K^{-1}), and T is the temperature (K). The value of mean sorption energy, E (J mol^{-1}), can be calculated from D–R parameter β as follows:

$$E = -1/\sqrt{-2\beta} \tag{4.10}$$

and it gives information about the type of adsorption mechanism as chemical ion-exchange or physical adsorption. A value of E between 8 and 16 kJ mol^{-1} corresponds to chemical ion-exchange processes. In the case of $E < 8$ kJ mol^{-1}, adsorption mechanism is governed by physical sorption and it may be dominated by particle diffusion if $E > 16$ kJ mol^{-1}.

4.2.3 Adsorption kinetics

The determination of adsorption rate and time after which system attains equilibrium could help in better understanding of pollutant adsorption mechanism, *i.e.* probable reaction pathways/steps. Due to complexity of adsorption process, *e.g.*, complex adsorption process steps with contribution of mass transfer and chemical reaction processes, different kinetic models are used to fit experimental data. The kinetic data are analyzed by non-linear least-squares method in the form of pseudo-first, pseudo-second-order (PSO) rate equations and intra-particle diffusion model (Weber-Morrismodel,W-M model). Judging from the regression coefficients, kinetic data are satisfactorily fitted by using pseudo-second-order (PSO) equation [230]. The fitting of the kinetic data obtained for cations and As(V) removal at 25, 35 and 45 °C afforded rate constants given in Table 4.21.

Table 4.21. The kinetic parameters obtained by the use of PSO equation at 25 ^{o}C

	Constants	NC-L			NC-L/FO
		Cd^{2+}	Pb^{2+}	Cu^{2+}	As(V)
25°C	K_2 (g mg^{-1} min^{-1})	0.026±0.007	0.042±0.005	0.013±0.003	0.047±0.006
	q_e (mg g^{-1})	3.207±0.055	9.622±0.438	10.396±0.896	2.126±0.544
	R^2	0.994	0.999	0.998	0.997
35°C	K_2 (g mg^{-1} min^{-1})	0.031±0.009	0.052±0.011	0.019±0.008	0.052±0.011
45°C	K_2 (g mg^{-1} min^{-1})	0.037±0.012	0.065±0.020	0.026±0.012	0.076±0.018

The results of PSO provide fitting of the kinetic related to overall adsorption rate, and could not help in assessing of the rate-limiting step. Therefore, the intra-particle diffusion model [230,308], *i.e.* W-M model, was applied to analyze mass transfer phenomena of overall process, and the results are given in Table 4.22. The adsorption is usually accomplished through a series of distinct consecutive steps: the external mass transfer (diffusion through the bulk liquid), the diffusion across boundary layer surrounding the particle (film diffusion), diffusional transport

within the internal structure of adsorbent (intra-particle diffusion) and the adsorption on solid surface. Regardless on the simplicity of the W-M model, it suffers from uncertainties caused by multi-linear nature, *i.e.* overall mass transport could be controlled by more than one step at different stage of the adsorption process. Generally, bulk diffusion and As(V) adsorption at goethite surface are fast processes. The results of W-M fittings are given in Table 4.22.

Table 4. 22. The kinetic parameters of the W-M model for arsenate adsorption

Step	Constants	NC-L			NC-L/FO
		Cd^{2+}	Pb^{2+}	Cu^{2+}	As(V)
Step 1	k_{p1} (mg g^{-1} min$^{-0.5}$)	0.321±0.024	0.703±0.099	1.173±0.124	0.191±0.004
	C_1 (mg g^{-1})	0.537± 0.023	5.178±1.012	2.334±0.098	0.481±0.011
	R^2	0.999	0.999	0.981	0.992
Step 2	k_{p2} (mg g^{-1} min$^{-0.5}$)	0.152±0.006	0.082± 0.004	0.346± 0.007	0.071±0.006
	C_2 (mg g^{-1})	1.337±0.044	8.584±1.221	6.174±1.032	1.211±0.015
	R^2	0.985	0.996	0.965	0.996

The results obtained following the Weber–Morris model show two successive linear steps: fast kinetic in first step followed by medium to low adsorption rate in second step. The larger intercept found for **NC-L** indicates higher resistance, *i.e.* slower ionic transport, due to intra-particle diffusion. First linear part demonstrates external mass transfer from bulk solution to the most available outer adsorbent surface adsorptive sites. The second part of W-M fit represents processes of high dependence on adsorbent porosity, *i.e.* pore geometry and network density. Due to the concentration gradient the ions diffuse through bulk solution and tree like system of macro-, meso- and micropores extending into adsorbent interior to reach all available surface active sites [230,308]. The intra-particle and film diffusion resistance slow down adsorbate transport, *i.e.* net transport in a direction of variable time-dependent concentration gradient. At the final stage of process, the adsorption takes place at low rate until saturation of all available surface sites is achieved. Additional analysis on the contribution of external mass transfer and diffusion inside the pores to overall diffusional adsorbate transport is also performed.

Thermodynamic study

The temperature effect on cations and As(V) adsorption onto **NC-L** and **NC-L/FO**, respectively, is deduced from results of adsorption experiments performed at 25, 35 and 45 °C. The temperature dependence of arsenic adsorption is associated with changes in thermodynamic parameters such as ΔG^o (the standard Gibb's free energy change), ΔH^o (the enthalpy change), and ΔS^o (the entropy change); these parameters are calculated using the eqs. (3.3) and (3.4). The obtained results are given in Table 4.23.

Table 4. 23. Thermodynamic parameters of cations and As(V) adsorption onto **NC-L** and **NC-L/FO**

	T (°C)	$\Delta G°$ (kJ mol^{-1})	$\Delta H°$ (kJ mol^{-1})	ΔS^o (J mol^{-1} K^{-1})	R^2
Cd^{2+}	25	−42.70±2.56	5.38±0.56	161.18±8.59	0.942
	35	−44.24±3.11			
	45	−45.93±3.22			
Pb^{2+}	25	−47.97±4.11	28.71±1.22	257.61±11.26	0.947
	35	−50.94±2.98			
	45	−53.11±3.66			
Cu^{2+}	25	−44.82±4.02	24.66±1.32	232.61±13.88	0.916
	35	−46.74±3.85			
	45	−49.49±4.23			
As(V)	25	−52.43±4.65	12.90±1.04	219.03±14.12	0.992
	35	−54.56±4.71			
	45	−56.81±4.82			

The negative values of $\Delta G°$ indicate spontaneity and more beneficial adsorption at higher temperature, while positive $\Delta H°$ additionally confirm conclusion about more effective adsorption at higher temperature (Table 4.23). Somewhat higher enthalpy was obtained for Pb^{2+} adsorption, in comparison to Cu^{2+}, which means more preferable adsorption for both Pb^{2+} and Cu^{2+} at higher temperature. Lower value, 12.90 kJ mol^{-1}, was obtained for As(V) removal with **NC-L/FO,** and lowest one for Cd^{2+}. Breakage of water hydration shells by pollutant species and their transport through the bulk solution, within the pores and through the surface boundary layer is more intensive process at higher temperature. Transport of exchangeable pollutant ions to adsorption site, and, on the other side, a number of water (exchangeable) molecules was released into bulk

solution contributing to increases of entropy change [230,308]. At steady-state condition increased randomness at adsorbent/solution is increased due to different intermolecular interactions which contribute to positive entropy change, *i.e.* adsorption is an entropy-driven process. All of these elementary processes, which take place in the course of equilibrium attainment, contribute to positive enthalpy change.

Regeneration and reusability

Design of environmentally friendly and economically acceptable technology for pollutant removal demands development of long term adsorbent application. Number of the re-use cycles of adsorbent contributes to the cost effectiveness of overall technology. The material cost of developed adsorption technology includes: the life-cycle of adsorbent, chemicals used for regeneration of spent adsorbent, residual materials handling, applied treatment technology and disposal/storage of waste to recycling company. In order to minimize material cost, development of high capacity adsorbent capable to be regenerated efficiently offers an alternative. The selection of an efficient reagent for the regeneration depends on the cations and arsenic bonding type, nature of sorbent, amino at **NC-L** and hydroxyl groups at **NC-L/FO** and regulative concerning effluent water quality. The formation of surface complexes, monodentate, bidentate-mononuclear and bidentate-binuclear through formation of As–O–Fe bond, indicates necessity of the application of strong competitive anion capable to break off As-O-Fe bond, *i.e.* displace As(V) anion. Sodium hydroxide and strong acids are most commonly used to elute As(V). Therefore, objective of competitive anion exchange of bonded cations and As(V) should result by their release into solution leaving active surface sites at the level, as close as possible, to concentration before adsorption cycle. Subsequent rinsing of **NC-L/FO** with dilute acid, 2 % sulfuric acid, causes protonation of negatively charged surface functional groups bringing back their sorption potential. Many systems for regeneration were used but NaOH, binary system NaOH/NaCl and ternary eluent NaOH/NaCl/citrate was selected as the best alternative. The best results of desorption study are given in Table 4.24.

Table 4. 24. Results of arsenate desorption for sorbent **NC-L** and **NC-L/FO** in first cycle

Desorption agent	C (mol dm^{-3})	NC-L			NC-L/FO
		Cd^{2+}	Pb^{2+}	Cu^{2+}	As(V)
NaOH/NaCl	0.2/0.2	78	76	80	75
	0.5/0.2	86	80	88	83
	0.5/0.5	92	86	95	89

Subtle decreases in adsorption capacity were observed over five adsorption/regeneration cycles (around 10-25 %) in comparison to first cycle. The most efficient desorption system was NaOH/NaCl (0.5/0.5). In a first cycle 89% of As(V) were desorbed, and throughout five consecutive cycles, desorption efficiencies was decreased to 81% in fifth desorption cycle for **NC-L/FO**. Similar situation stand for **NC-L** adsorbent: 92%, 86% and 95% of Cd^{2+}, Pb^{2+} and Cu^{2+} were desorbed in a first cycle, and it were decreased to 82%, 72% and 86% in fifth desorption cycle. In summary, **NC-L** and **NC-L/FO** is reusable in a multi-step processes and efficient adsorbent for Cd^{2+}, Pb^{2+} and Cu^{2+} cations, and As(V) removal for over five adsorption/desorption cycles.

4.3. Adsorption performances of magnetite modified nano/micro cellulose for arsenate removal: effect of functionalization and media size

4.3.1. Optimization of the adsorbents synthesis

In order to design effective, reusable and selective hybrid adsorbents for As removal an optimization study was conducted. Optimization goals were directed to syntheses of adsorbent with high capacity/efficiency, improved chemical and mechanical stability of **MG** deposit, and fast adsorption of arsenic at operational time scale. The optimization procedure, performed according to *sections 3.2.5* and *3.2.6*, and according to experimental plan presented in Table 4.27, revealed that optimal performance was obtained by using:
- 100 mL of FeSO$_4$·7H$_2$O (0.38 mol L^{-1}) and 45 mL of pH adjustment solution (5.95 g KOH and 0.86 g KNO$_3$) for **NC-MA/L'-MG** adsorbent synthesis (Fig. 4.26 a)), and

- 100 mL of $FeSO_4 \cdot 7H_2O$ (0.17 mol L^{-1}) and 45 mL of pH adjustment solution (2.65 g KOH and 0.38 g KNO_3) used for **MC-O/L'-MG** adsorbent synthesis (Fig. 4.26 b)).

Results of the optimized procedure of adsorbent syntheses in a batch system (*sections 2.5 and 2.6*) were applied, with an adjustment of the volume of used solution to provide reaction in a water thin/hydrophylic precursor material, for syntheses of **NC-MA/L'-MG** and **MC-O/L'-MG** adsorbent according to methodology described in *section 3.2.6*.In that way, the highest adsorption capacities were obtained at ~29% loaded iron oxide in **NC-MA/L'-MG** and ~13% in **MC-O/L'-MG** (Fig. 4.26 c)). The most probable structure of designed intermediates and adsorbents are presented in Fig. 4.27.
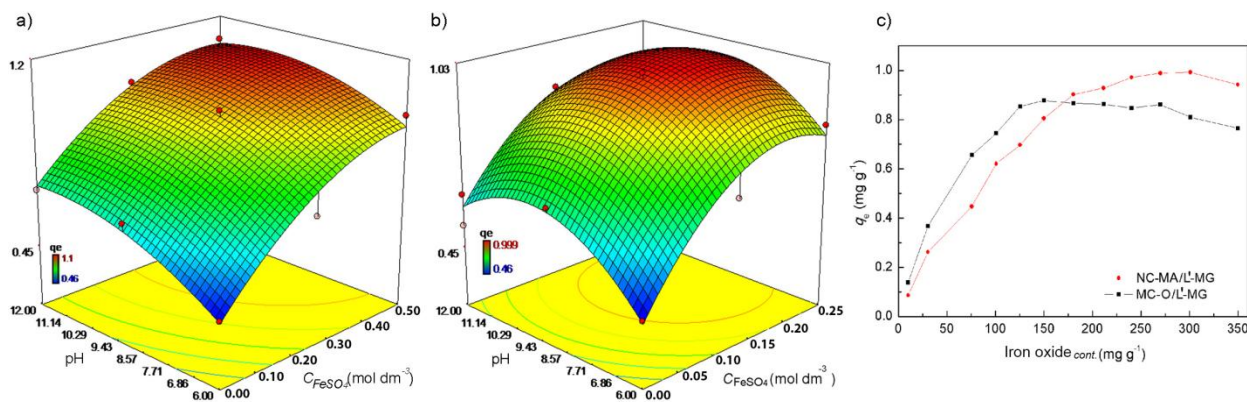
Figure 4. 26. Contour diagram representing adsorbent capacity *versus*C_{FeSO4} and pH in the synthesis **NC-MA/L'-MG** (a), **MC-O/L'-MG** (b), and capacity of both sorbents *vs* amount of iron oxide (c)
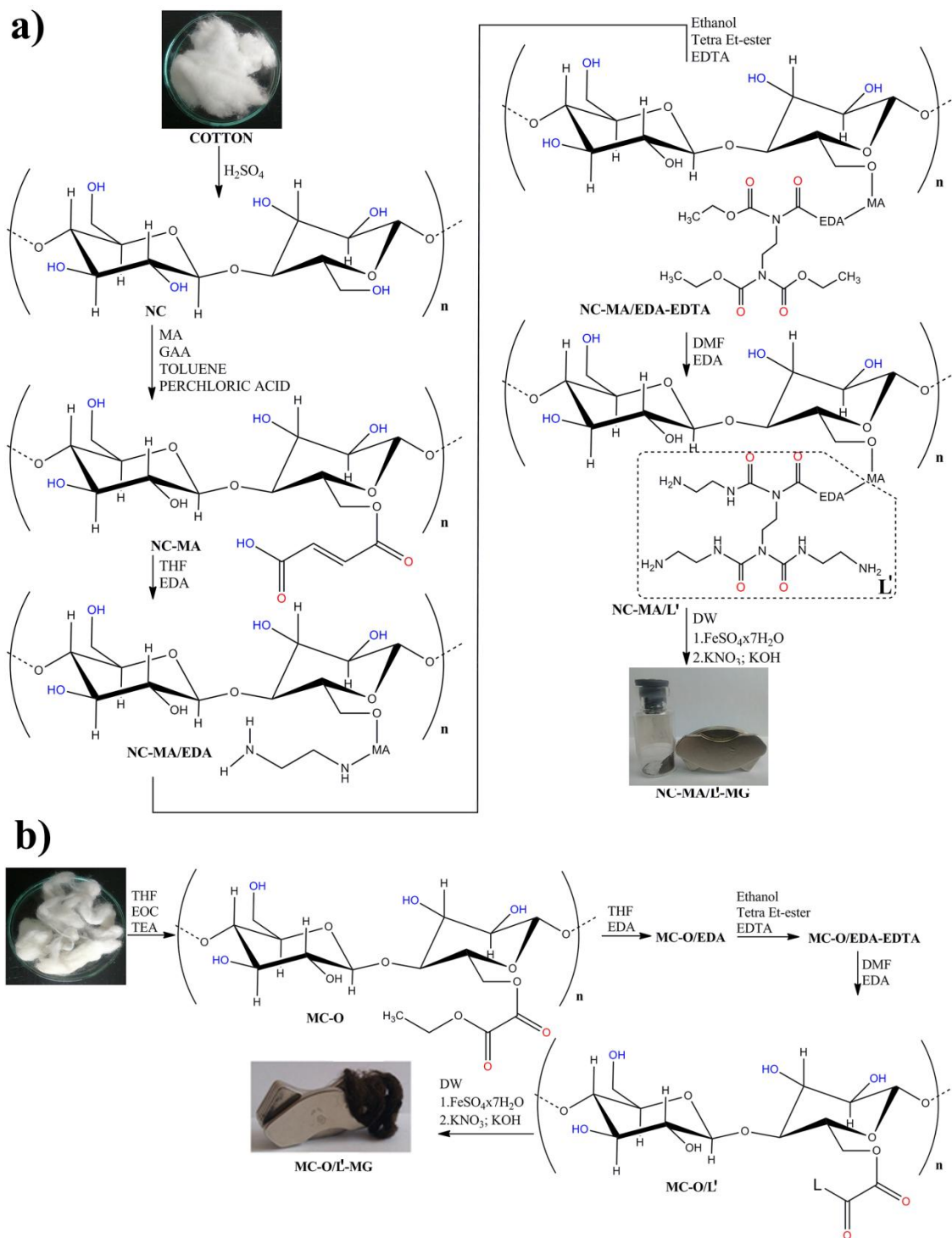
Figure 4. 27. Proposed reaction pathways applied for **NC-MA/L'-MG** and **MC-O/L'-MG** adsorbents synthesis

The most probable structure of designed intermediates and adsorbents are presented in Fig. 4.27. Significance of the amino groups involved in the complexation was recently unequivocally presented. Cations are strongly bonded to amino groups, by complexation/chelation interactions, and higher nucleophilicity of amino groups, at pH>pH$_{PZC}$, brings to stronger interaction with cation[233]. In that sense it was of utmost interest to introduce number of amino groups through hierarchical branching of organic structure covalently bonded to **NC** and **MC** surface (Fig. 4.27). The total basic sites, 0.60 and 1.02 mmol g^{-1} found for **MC-O/L'** and**NC-MA/L'**, respectively, contributed to uniform/high **MG** loading. According to total basic sites determination**,** it was evaluated that ~19 and ~11 wt.% of introduced organic functionalities are present in **NC-MA/L'** and **MC-O/L'**, respectively. Modification of **NC,** with an acid value (*AV*) of 28, by MA to **NC-MA**, introduced ~1.50 mmol g^{-1} of carboxylic group (*AV* = 150). Lower efficiency of **NC-MA** modification with EDA resulted in 0.92 mmol g^{-1} of amino group (~61% conversion) in **NC-MA/EDA**. According to stoichiometric ratio considered for subsequent modifications of **NC-MA/EDA** to **NC-L** (Fig. 4.27), it should be expected 2.76 mmol g^{-1} amino group. Experimental values of 1.02 mmol g^{-1} was found. This indicate lower efficiency of amino groups modification, present at **NC-MA/EDA** surface**,**due to steric hindrance of introduced voluminous tetraethyl ester of EDTA structure. Generally, optimal procedure for **MG** precipitation/complexation on **NC-MA/L'** and **MC-O/L'** was defined by using RSM methodology, were successful, according to *sections 3.2.4 - 3.2.6,* but controlled precipitation and uniform distribution was achieved according to *sec. 3.2.6*.

4.3.2. Characterization of the adsorbents

Textural properties and pH$_{PZC}$

Multi-step synthesis of adsorbents was applied in order to design the material with an appropriate geometry and pore structure. The textural properties and zero point of charge (pH$_{PZC}$) are summarized in Table 4.25.

Table 4.25. Textural properties, pH$_{PZC}$ of **MG**, **NC-MA/L-MG** and **MC-O/L-MG** adsorbent

Adsorbent	Specific surface area (m^2 g^{-1})	Pore volume (cm^3 g^{-1})	Pore diameter (nm)	pH$_{PZC}$[a]	pH$_{PZC}$[b]
MG	66.7	0.85	12.3	6.6	5.9
NC-MA/L'-MG	85.3	0.71	15.2	6.5	5.7
MC-O/L'-MG	35.5	0.45	18.4	6.1	5.8

[a] before and [b]after adsorption; pH$_{PZC}$ of **NC** was found to be <1, and pH$_{PZC}$ of **NC-MA**<3

Due to dimensional differences of parent materials, the higher value of specific surface area and pore volume was in favor of **NC-MA/L'-MG**, while higher pore diameter was found for **MC-O/L'-MG**. Literature data of unmodified nano- and microfibrillated cellulose [201], showed that differences in surface area and pore diameter is generally caused by the textural properties of substrate, applied modification method as well as post processing of obtained material. In contrast to mild thermal treatment applied for **NC-MA/L'-MG** and **MC-O/L'-MG** production, high temperature processing exerts significant change in textural properties of final material. The surface area and pore volume of thermally treated silica, after ligand immobilization, showed significant decrease of textural properties. Regardless to obtained results both methodologies could find application in production of adsorbents of different properties. Precipitation of **MG** on **NC-MA/L'** and **MC-O/L'** provided such conditions applicable for preservation of organic branched structures with controllable deposition of nanoscale materials. The shift of pH$_{PZC}$ value indicates specific arsenate adsorption rather than electrostatic interaction [231], as well as formation of complexed/precipitated arsenic species at surface of magnetite based adsorbent.

XRD analysis

XRD diffractograms of **NC** and **NC-MA,** presented on Fig. 4.28 a), provide insight in structural changes in the course of **NC** modification. An increase in crystallinity of **NC-MA** was observed. Both diffractograms display two well-defined peak doublets around $2\theta=20º$ and $22.0º$ which correspond to (200) plane of cellulose crystal structure. Those doublets indicate the existence of cellulose I and cellulose II allomorphs [313]. Modification with MA causes sharper signal, increases contribution of cellulose II crystallites, and overall degree of crystallinity. Also, in the sample of **NC-MA** signal at $12.24º$ correspond to (-110) crystal plane of cellulose I [205]. The signal at 35.0^{o} showed higher intensity for **NC-MA**, corresponds to (004) atomic plane of cellulose I [313]. Also, it was shown that appearance of new crystalline peaks at 2θ ~35° as well as at 41.0° indicates the increase of the crystallinity of **NC-MA**.

Phase and structural analysis of **NC-MA/L'-MG** and **MC-O/L'-MG** confirmed presence of **MG**, as it was indicated by peak at 30.16, 35.52, 37.16, 43.17, 57.10, 62.70° (JCPDS 19-629) (Fig. 4.28 b). Differences in peaks broadness and intensity indicate lower degree of crystalline phase of embedded **MG** in **MC-O/L'-MG**. The mean crystallite size, calculated by using Scherrer equation based on the half width of the most intense peaks in XRD patterns, indicate 22 and 19 nm of grain sizes of **MG** present on **NC-MA/L'-MG** and **MC-O/L'-MG** surface, respectively. These values are somewhat lower than ones observed by TEM (Fig. 4.32). A somewhat lower crystallite size, found for **MC-O/L'-MG,** is due to lower number of amino groups (crystallization centers) accessible for iron coordination. Obtained results indicated on high coverage of **NC-MA/L'** and **MC-O/L'** by **MG**. Due to the known fact that **MG** and maghemite (γ-Fe_2O_3) have similar XRD pattern it was necessary to apply Raman spectroscopy in order to clearly distinguish nanocrystalline form of deposited iron oxide.
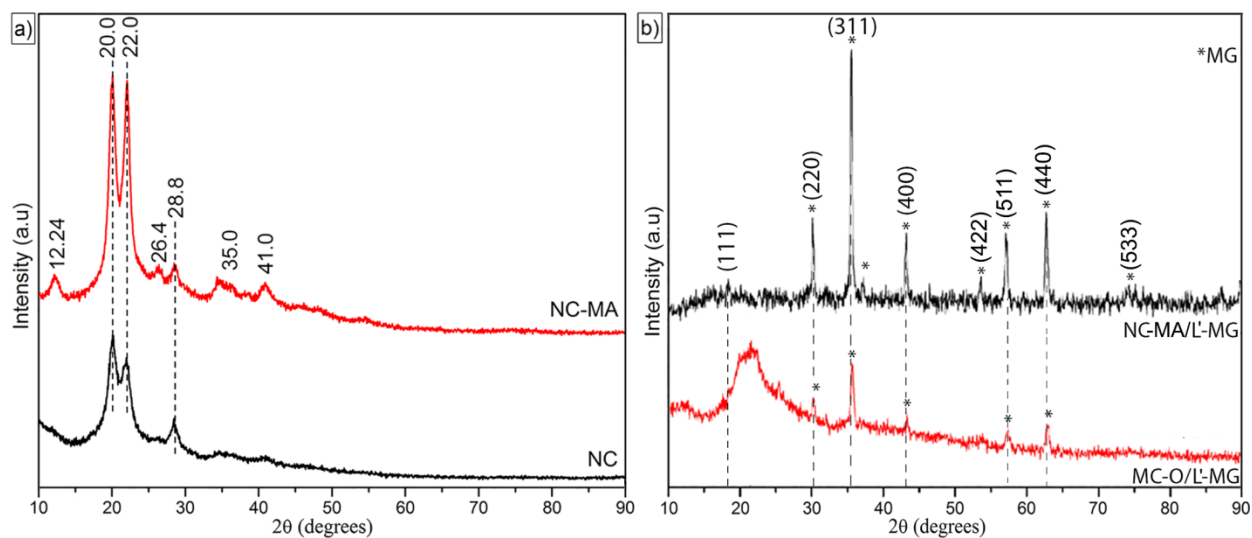
Figure 4.28. XRD patterns of a) **NC** and **NC-MA** and b) **MC-O/L'-MG** and **NC-MA/L'-MG**

Raman spectroscopy

Raman spectra of the **NC**, **NC-MA/L'** and **NC-MA/L'-MG**, and **MC** and **MC-O** are shown on Fig. 4.29. The region below 1750 cm^{-1}, observed at Raman spectra of **NC** and **NC-MA/L**, originates from the conformation of cellulose skeleton, while the region above 2888 cm^{-1} and higher than 3000 cm^{-1} originates from hydrogen bonding of OH group [314]. Comparing the Raman spectra of the **NC** and **NC-MA/L'**, the overlapped bands, observed in the region 3215–3405 cm^{-1}, are due to OH and NH$_2$ stretching vibration [315]. Also, the signals at 1456 cm^{-1} and 1473 cm^{-1}, a characteristic for methylene bending modes of two stereo-chemically nonequivalent CH$_2$OH groups of the crystalline NC skeletons, merge into one single signal at 1456 cm^{-1} in **NC-MA/L'.** This change explained the differences between the vibrational behavior of crystalline and amorphous domain in **NC** [316], and indicates transition from crystalline to amorphous form of these two CH$_2$ bending modes during surface modification [317,318]. Also, the intensity of the characteristic peak of highly crystalline **NC** (1473 cm^{-1}), and other signals decrease in comparison to amorphous **NC-MA/L'** domain.

Weak bands, observed in region from 964 cm^{-1} to 1113 cm^{-1}, originate from C6 atom bending vibrations (H-C-C and H-C-O), while the strong stretching vibration of unhydroglucose

182

skeleton are observed at 1145 cm^{-1} (C-C, C-O and C-O-C) [316,317]. The NC backbone deformation vibrations bands, δ(CH$_2$), δ(HCC), δ(HCO) and δ(COH), are observed at 1374 cm^{-1} [319]. Wide bands observed in the region between 1565 cm^{-1}–1992 cm^{-1} and 900 cm^{-1}–1500 cm^{-1} originate from the **MA** and EDTA moieties in **NC-MA/L'**, respectively.

The non-polarized spectrum of **NC-MA/L'-MG** shows magnetite predicted phonon bands as characteristic peak at 670 cm^{-1}[320]. Due to susceptibility of **MG** to transform into maghemite, under exposure to laser, two weak peaks appeared at 350 and 500 cm^{-1}. The absence of **NC** characteristic bands in **NC-MA/L'-MG** spectrum indicates homogenous distribution/entire surface coverage by deposited **MG** on amino functionalized **NC**.

The Raman spectra of the **MC** and **MC-O** showed similar peak structure and position, except that cellulosic structure of **MC** basis participates at higher extent in response to laser impulse. Regardless to adjustment of laser power the Raman spectrum of **MC-O/L'-MG** sample was not obtained.
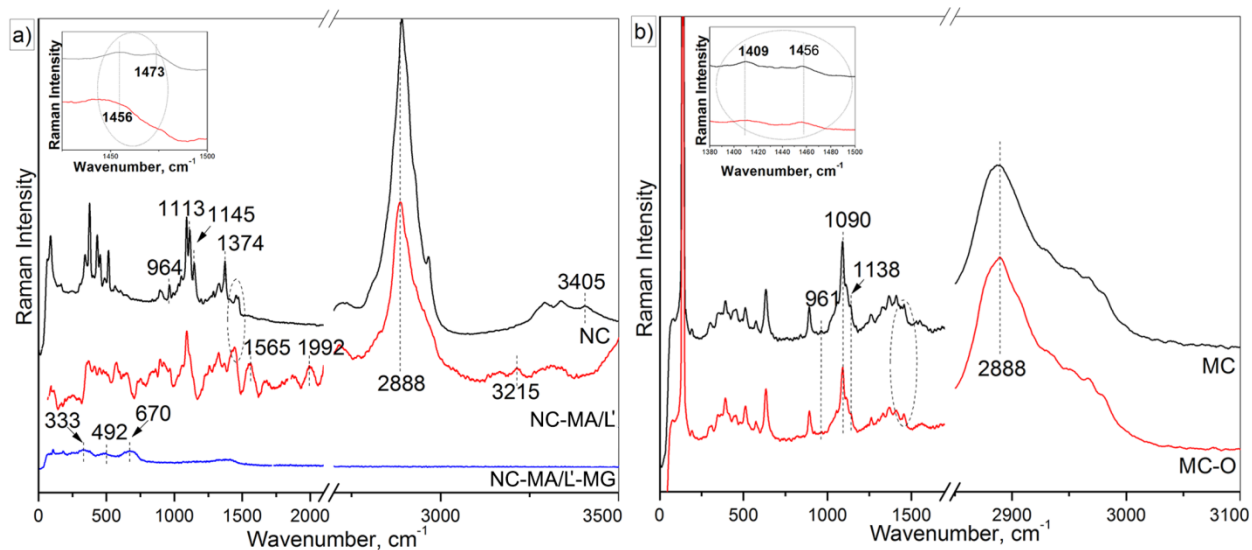
Figure 4.29. Raman spectra of a) **NC, NC-MA/L'** and **NC-MA/L'-MG** and b) **MC** and **MC-O**

FTIR spectroscopy

The FTIR spectra of intermediates and adsorbents, before and after arsenate adsorption, are presented in Fig. 4.30. From the FTIR spectra of all intermediatescan be observed a broad band about 3423 cm^{-1} ascribed to OH and NH stretching vibrations. Adsorption of arsenate

183

oxyanions cause shifting of the stretching vibration of OH band to 3451 cm^{-1}. Differences in the peak intensity, peak shifting and appearance of peak after adsorption indicate arsenate bonding by appropriate functional groups. Carbonyl group absorption at 1714 cm^{-1}, found in **NC-MA,** is missing in the spectrum after **MG** modification. Absorption peak, at 1635 cm^{-1}, originates from deformation vibrations of OH bond, is negligibly shifted to 1637 cm^{-1} after **MG** modification. A broad bands at ≈1714 and ≈1635 cm^{-1}, is shifted to ≈1637 cm^{-1}, in **NC-MA/EDA** and **NC-MA/L'**, a band corresponding to amide stretching vibration (amide I) coupled with in-plane N-H deformation vibration. The bands in the region 750–1000 cm^{-1}, and one at 1373 cm^{-1}, show presence of sulfonates and amino groups [321]. The strong bands at 582 cm^{-1}, assigned to Fe-OH vibrations present at **MG** surface, after arsenate adsorption appeared at 617 cm^{-1}. This region correspond to vibration of As–O–Fe complexed/precipitated arsenate species, and at different surface coverage, bidentate binuclear and mononuclear monodentate complex could be formed, where As–OH free bonds are present as unprotonated and/or protonated depending on pH.
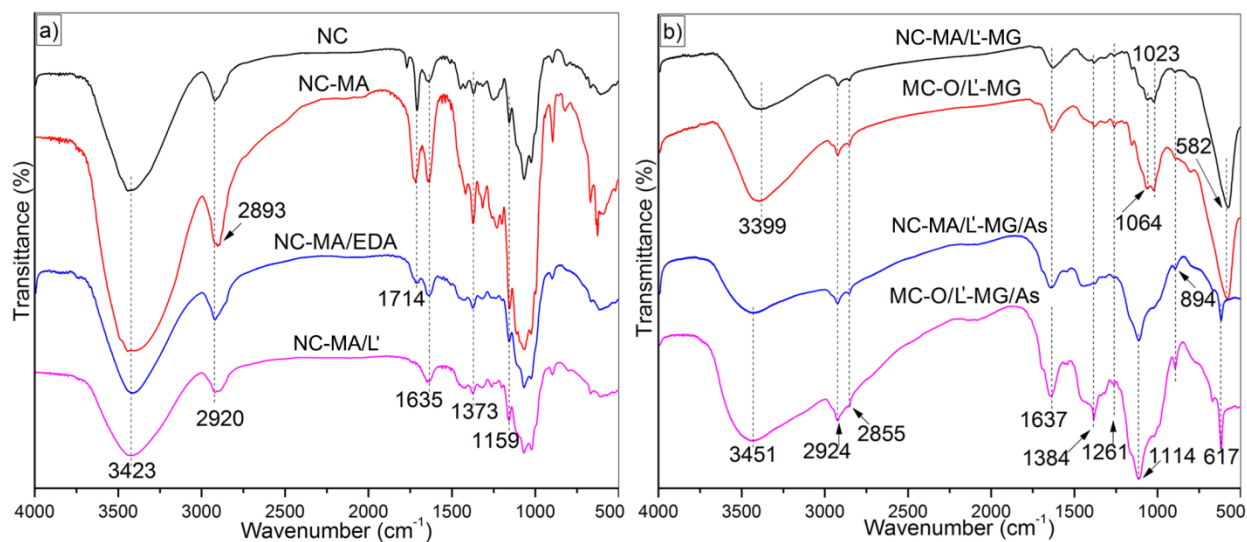
Figure 4. 30. FTIR spectra of a) **NC**, **NC-MA**, **NC-MA/EDA** and **NC-MA/L'** and b) **NC-MA/L'-MG**, **MC-O/L'-MG**, **NC-MA/L'-MG/As** and **MC-O/L'-MG/As**

Thermal analysis (TGA)

The success of nano/microcellulose modification and thermal stability of composites constituent was evaluated by the use of TGA. TGA and differential thermal analysis (DTG)

184

curves, recorded for **NC**, **MC**, **NC-MA/L'**, **NC-MA/L'-MG** and **MC-O/L'-MG,** are shown in Fig. 4.31. As it can be observed, the thermal decomposition of **NC** and **MC** occurred in three steps: (i) 30–225 °C, (ii) 225–325 °C, and (iii) 325–700 °C range. In the first stage, ~5% and ~11% weight loss was observed due to dehydration of **NC** and **MC**, respectively. In the second stage, almost 61% mass loss occurred due to the splitting/thermal decomposition of cellulose structure, *i.e*. chain scission which evolves gaseous products leaving condensation/carbonaceous residues. After 325 °C, 20% and 18% weight loss was observed due to the degradation of the **NC** and **MC** condensed carbonaceous material, respectively. The end of the first region is shifted to the lower temperature (145 °C) for the **NC-MA/L'** sample. Also, the weight loss difference, ~12%, between **NC** and **NC-MA/L'** issimilar to evaluated organic fraction, obtained according to amino gorups calculation ~18%.DTG peak for **NC-MA/L'** occured at 158 °C refers to dehydration and evaporation of residual solvents, while DTG peak at 273.4 °C refers to cellulose backbone decomposition.

The higher stability, comparing to **NC** and **MC**, and similar thermal behavior of **NC-MA/L'-MG** and **MC-O/L'-MG** was noticed (Fig. 4.31 a)). Higher thermal stability is due to contribution of **MG** protective layer which form, by sintering of **MG** nanocrystallite, a stable core shell like structure. The first stage of mass loss (<300 °C) is due to removal of physically adsorbed water and residual reactants. The weight loss in the range from 300 to 450 °C is ascribed to the rapture of weak head to head acetal linkage between celobioze units in an amorphous/lower crystallinity domain of cellulose. Corresponding DTG peaks could be observed at 306.8 °C, 324.6 °C and 379 °C for **MC-O/L'-MG** and 394.2 °C for **NC-L'-MG**, respectively. The third stage, at >400 °C, take place by random scission/gradual decomposition of main cellulose polymeric chain. A residual inorganic material of 42% and 28% in a inert atmosphere, and comparative experiments in air showed 33% and17% residuals in **NC-L'-MG** and**MC-O/L'-MG**, respectively. On the DTG curves of **NC-L'-MG** and **MC-O/L'-MG** peaks observed at temperatures >470 °C refer to thermal oxidation and dehydroxylation of precipitated magnetite.
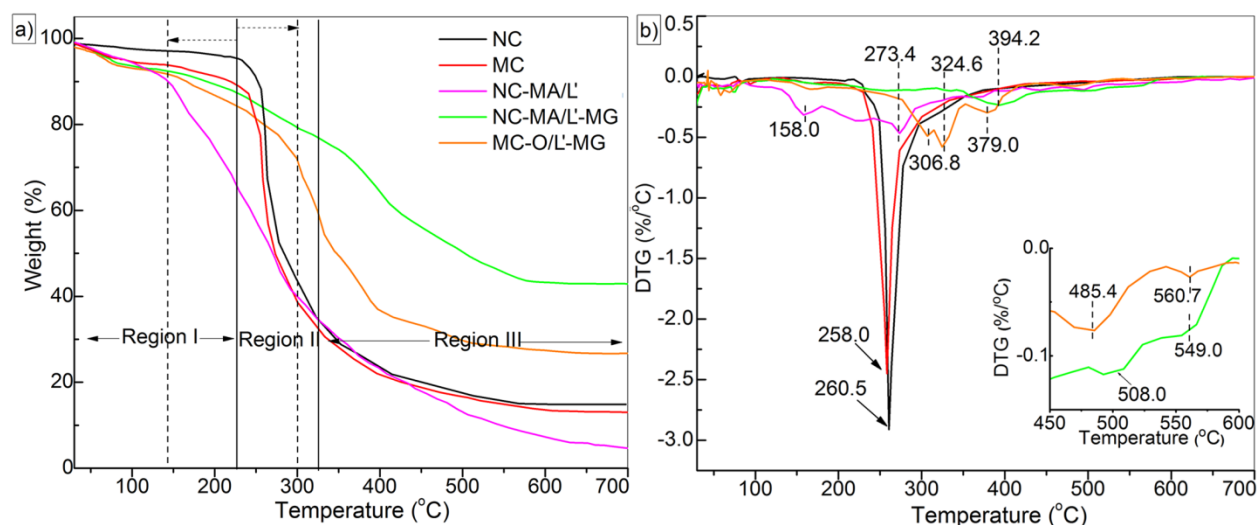
Figure 4. 31. TGA curves of **NC, MC, NC-MA/L', NC-MA/L'-MG** and **MC-O/L'-MG**

Morphological characterization

The morphology of the synthesized adsorbents were analyzed by using SEM/FEG–SEM techniques, results given in Fig. 4.32 a), b), d) and e), while TEM results are given on Fig. 4.32c) and f). Morphology of **NC-MA/L** (Fig. 4.32a)) indicated surface coverage by organic material due to chemical modification, and subsequent **MG** deposition affects the morphological structure of the surface of **NC-MA/L'-MG** (Fig. 4.34b)). SEM micrographs of **MC-O/L'-MG** adsorbent are given in Fig. 4.32 d) and e). The evaluated average diameter of **MC, MC-O** and **MC-O/L'-MG** were in the range 30±1.2 μm. The modified **MC** fibers showed small diameter changes of parent cylindrical strands due to organic modification and **MG** precipitation at **MC-O/L'** surface. Evolution of the **MC-O/L'-MG** morphology can be explained by heterogeneous reaction which takes place by **MG** precipitation on terminal amino branched structure with incorporated **NC** grains on the fiber surface. TEM analysis (Fig. 4.32 c) and f)) confirmed nanoscale dimension and irregular distribution of cubic **MG** nanoparticles onto irregular/porous morphology of **NC-MA/L'** and **MC-O/L'**. It can be concluded that morphology of both **NC-MA/L'-MG** and **MC-O/L'** are the result of both physical structure of nano/microscale material, and chemical structure/properties of functional groups present at intermediate surface.
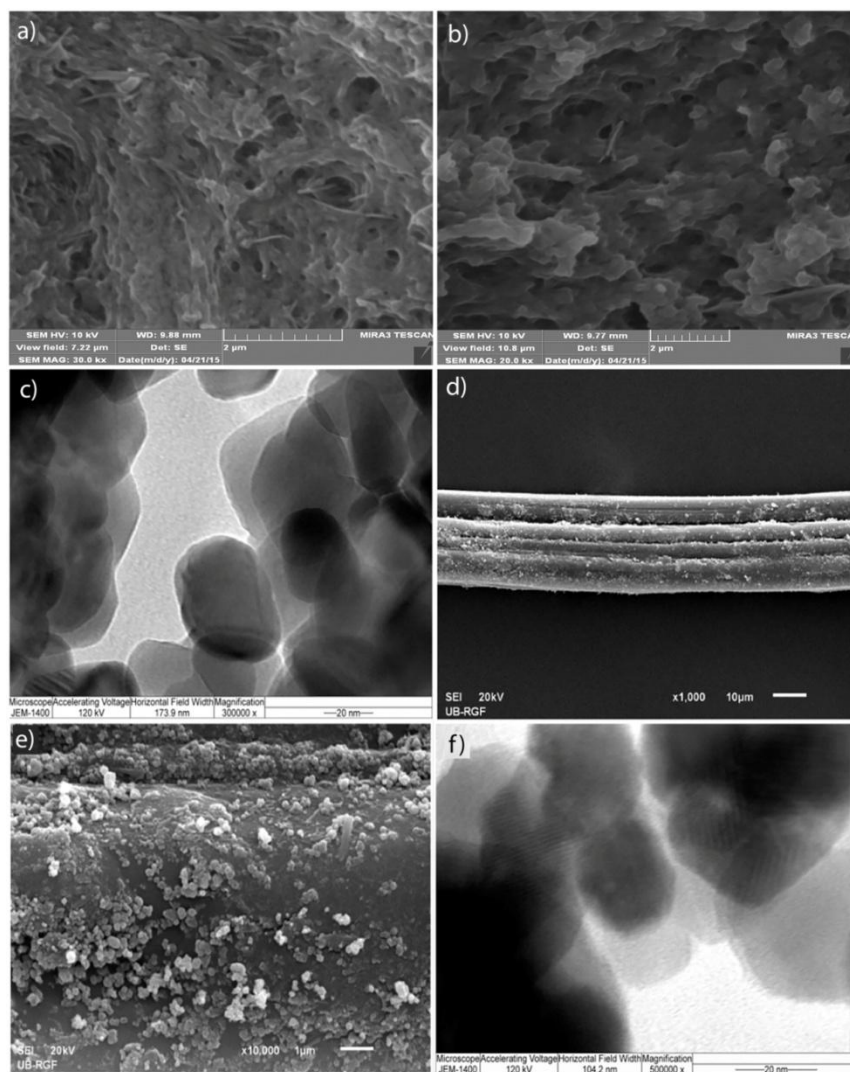
Figure 4.32. FEG SEM/SEM images of **NC-MA/L'** (a), **NC-MA/L'-MG** (b), **MC-O/L'-MG**(d) and (e); TEM images of **NC-MA/L'-MG** (c) and **MC-O/L'-MG** (f)

4.4 Adsorbents performance in a non-competitive conditions

4.4.1 pH-dependent, equilibrium, thermodynamic and competitive adsorption study

Considering significance of pH influences on arsenic speciation and ionization state of adsorbent surface, it was important to study influence of pH (in the range 3-10) on effectiveness of As removal. The results of the pH-dependent adsorption study, *i.e.* arsenate removal *versus*

initial pH (pH_i) for both **NC-MA/L'-MG** and **MC-O/L'-MG** adsorbents, and change of final pH (pH_f) in relation to initial pH (pH_i) are shown in Fig. 4.33. The extent of adsorption pH_f/pH_i relation is affected by both release/consumption of hydrogen ions, *i.e.* protonation/deprotonation of **MG** surface, and pH-dependent arsenic speciation. These factors determine that effective As(V) adsorption was obtained in pH range 3.0-7.0 (Fig. 4.33), while pH_f/pH_i relationship indicates similar arsenic adsorption mechanism with respect to both adsorbents.

The pKa values of arsenic acid: pKa_1 ~2.3, pKa_2 ~7.0 and pKa_3 ~11.5, indicate that molecular form mainly exists in a solution at pH<2.0, and pH-dependent equilibrium of anionic species, $H_2AsO_4^-$ or $HAsO_4^{2-}$, exists at pH in the range 2–10 [263]. At pH_i < pH_{PZC} (Table 4.25), the protonation of surface functional generate positive charge which contributes to favorable bonding of negatively charged arsenate ions. The both surface state and As speciation plays significant contribution to electrostatic interaction (attraction/repulsion) between surface/ions causing intensity of As flux toward the specific adsorption sites. Enhancement of electrostatic attraction is thus highly feasible for As(V) species, while it is of minor importance for the neutral form of arsenous acid. Simultaneous determination of arsenic and iron by ICP-MS showed that at pH<5 significant dissolution of **MG** precipitate was noticed. Good adsorption capacity and noticeable iron dissolution at pH < 5 dictated that selection of pH 6.0 was the best choice, and this pH was used in subsequent adsorption experiments.
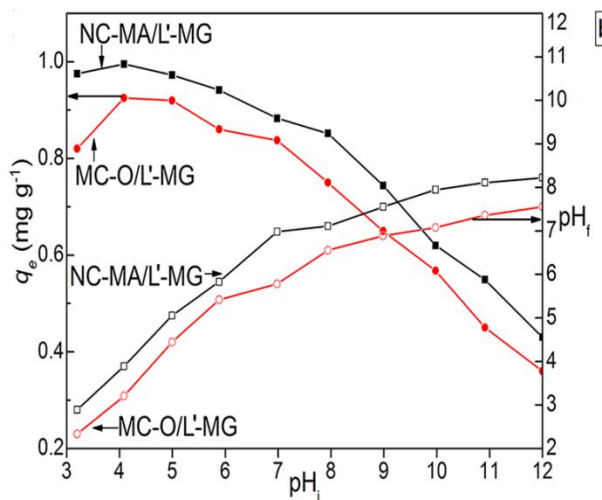
Figure 4.33. Effect of pH on adsorption of As(V) on **NC-MA/L'-MG** and **MC-O/L'-MG**, and pH_f *vs* pH_i relation

The state of adsorption equilibrium was analyzed by fitting experimental data with various isotherms model [69] by applying nonlinear least squares fitting to adsorption data. Statistical criteria were used to evaluate the model fitting of adsorption data. Results indicated that the good fitting were obtained by using Langmuir, eq. 1 from Table 2.4, and Freundlich, eq. 2 from Table 2.4, isotherm models.

Adsorption results presented in Fig. 34a) and b) and Table 4.26 showed that good fitting of the experimental data with Freundlich isotherm which indicates multilayer adsorption on heterogeneous surfaces. Significantly higher adsorption capacity for **NC-MA/L'-MG** (85.3 mg g^{-1})**,** in comparison to **MC-O/L'-MG** (18.5 mg g^{-1})**,** was obtained by using Langmuir model (Table 4.27). The favorable textural parameters of **NC-MA/L'-MG** contribute to higher arsenate uptake, *i.e*. larger number of available adsorptions sites at nanocomposite surface (Table 4.25). Somewhat lower capacity was obtained with **NC-MA/L'-MG** and **MC-O/L'-MG** in a processes of As(III) removal (Table 4.27), 68.2 and 17.8 mg g^{-1}, respectively. This result indicate on a wider applicability of synthesized adsorbents. Also, comparative adsorption study of arsenic removal by using **NC-MA/L'** showed that 15.4 mg g^{-1} and 4.8 mg g^{-1} were found for As(V) and As(III) at pH 6.0±0.1, respectively. Even lower capacities was obtained for **MC-O/L'** (<6 mg g^{-1} for As(V) removal). These results clearly indicate that validity of the modification of **NC-MA/L** and **MC-O/L'** with **MG** was justified by production of high performances **NC-MA/L'-MG** and **MC-O/L'-MG** adsorbents. Thermodynamic parameters are calculated, according to eqs. (3.3) and (3.4)[233], based on adsorption studies performed at different temperature and calculated K_L Langmuir constant (Table 4.27), and results are given in Table 4.27.

Table 4. 26. Adsorption isotherm (Freundlich) and thermodynamic parameters for As(V) removal at 298, 308 and 318 K

Freundlich parameters				
	T (K)	K_f ((mol/g)(L/mol)$^{1/n}$)	$1/n$	R^2
MG	298	0.0539±0.0016	0.396±0.012	0.997
	308	0.0473±0,0014	0.480±0.014	0.995
	318	0.0357±0.0012	0.349±0.011	0.993
NC-MA/L'-MG	298	0.2412±0.0961	0.562±0.024	0.995
	308	0.2005±0.0802	0.536±0.022	0.994
	318	0.1474±0.0598	0.503±0.020	0.993
MC-O/L'-MG	298	0.0032±0.00008	0.188±0.0047	0.995
	308	0.0025±0.00006	0.258±0.0065	0.997
	318	0.0020±0.00005	0.229±0.0057	0.994
Thermodynamic parameters				
	T (K)	ΔG^o (kJ mol^{-1})	ΔH^o (kJ mol^{-1})	ΔS^o (J mol^{-1} K^{-1})	R^2
MG	298	-40.56±0.81			
	308	-42.05±0.82	4.31±0.08	150.48±3.01	0.992
	318	-43.57±0.87			
NC-MA/L'-MG	298	-38.66±1.16			
	308	-40.23±1.21	10.77±0.32	165.69±4.97	0.978
	318	-41.98±1.26			
MC-O/L'-MG	298	-39.40±0.985			
	308	-40.90±1.022	10.99±0.27	168.80±4.22	0.954
	318	-42.78±1.069			
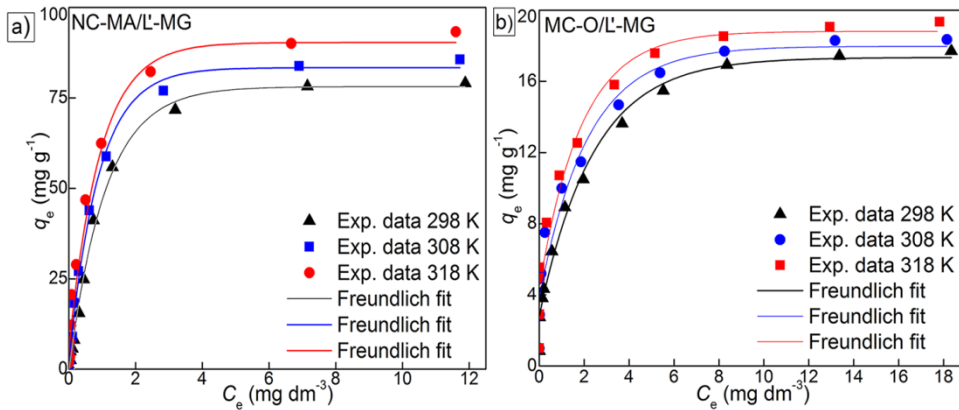
Figure 4. 34. Freundlich adsorption isotherm for **NC-MA/L'-MG** a), and **MC-O/L'-MG** b) (m/V = 100 mg L^{-1}, C_i = 0.10, 0.30, 0.60, 1.0, 2.0, 3.0, 5.0 and 7.0 mg L^{-1}, pH = 6.0)

Table 4. 27. Adsorption isotherm (Langmuir) parameters for for As(V) and As(III), removal at 298, 308 and 318 K

	T (K)	q_m (mg g^{-1})	K_L (L mol^{-1})	R^2
As(V)				
Langmuir parameters				
MG	298	91.23±1.83	230262±3453	0.991
	308	94.25±1.88	241635±3624	0.967
	318	97.19±1.96	256901±3853	0.977
NC-MA/L'-MG	298	85.33±2.56	106993±3207	0.965
	308	90.23±2.71	118963±3569	0.962
	318	90.63±2.72	140690±4218	0.963
MC-O/L'-MG	298	18.54±0.74	143892±5755	0.927
	308	18.78±0.75	154365±6174	0.937
	318	19.00±0.76	190458±7618	0.954
As(III)				
Langmuir parameters				
	T (K)	q_m (mg g^{-1})	K_L (L mol^{-1})	R^2
MG	298	87.35±1.83	116093±2436	0.990
	308	89.48±1.88	128109±2690	0.991
	318	91.51±1.92	143023±3003	0.993
NC-MA/L'-MG	298	68.26±2.46	278387±10021	0.998
	308	71.26±2.56	293938±10581	0.997
	318	74.21±2.67	311034±11197	0.995
MC-O/L'-MG	298	17.78±0.65	166626±4997	0.996
	308	18.95±0.69	190462±7730	0.996
	318	19.13±0.70	238289±11308	0.998

Thermodynamic parameters

	T (K)	ΔG^o (kJ mol^{-1})	ΔH^o (kJ mol^{-1})	ΔS^o (J mol^{-1} K^{-1})	R^2
MG	298	-38.86±0.82	8.22±0.17	157.89±3.31	0.997
	308	-40.42±0.85			
	318	-42.02±0.88			
NC-MA/L'-MG	298	-41.03±1.47	4.37±0.18	152.27±5.48	0.998
	308	-42.55±1.53			
	318	-44.08±1.58			
MC-O/L'-MG	298	-39.76±1.14	14.06±0.51	180.39±6.58	0.973
	308	-41.44±1.52			
	318	-43.37±1.61			

The negative value of Gibbs free energy together with positive enthalpy and entropy changes indicates spontaneity and endothermicity of adsorption processes (Table 4.26). The positive $\Delta H°$ confirms favorable adsorption at higher temperatures. It means that disruption of water hydration shells and transport of arsenic anionic species through the bulk solution, within the pores and through the surface boundary layer is more intensive process at higher temperatures. The transport of exchangeable arsenic oxyanions to adsorption site, and number of (exchangeable) water molecules was released into bulk solution contributing to the increase of entropy change [230,231]. At steady-state condition randomness at adsorbent/solution interface is increased due to different intermolecular interactions which contribute to positive entropy change, *i.e.* adsorption is an entropy-driven process. All of these elementary processes during equilibration contribute to positive enthalpy change. Thermodynamic parameters of both As(V) (Table 4.28) and As(III) (Table 4.29) were similar to ones given by Liu *et. al.* [322].

Preliminary evaluation of the potential of use of both adsorbents **NC-MA/L'-MG** and **MC-O/L'-MG** for arsenic removal from real water samples, contaminated natural water from the area of the city of Zrenjanin was used (located in Vojvodina, Serbia). Sample used in this work was collected at the point before any purification treatment. Total arsenic concentration, determined by ICP-MS, was found to be 106 μg L^{-1}. Other ionic species of interest presents in real water sample are PO_4^{3-} (5.6 mg L^{-1}), SO_4^{2-} (42.5 mg L^{-1}), Ca^{2+} (15.3 mg L^{-1}), Mg^{2+} (9.1 mg L^{-1}), SiO_4^{4-} (5 mg L^{-1}), Cl^-(1.2 mg L^{-1}), HCO_3^- (856 mg L^{-1}). pH of the sample was 7.4 and it was adjusted to pH 6±0.1.

The total arsenic concentration include following arsenic species: inorganic, As(III) and As(V), and methylated organic arsenic species (monomethylarsenic acid, MMAs(V), and dimethylarsenic acid, DMAs(V)). Due to this it was necessary to perform preliminary determination of present arsenic species. In a previous report we developed simple and efficient method for separation and determination of inorganic arsenic (iAs) and organic arsenic (oAs) in natural water[263]. Two types of resins were used for determination of arsenic species: a strong base anion exchange (SBAE) resin and HY−AgCl based on the activity of silver-chloride loaded on SBAE resin. The SBAE resin has been chosen as a selective resin for the separation of As(V) from As(III), and HY−AgCl for quantitative separation of molecular and ionic forms of iAs and oAs. Molecular form of As(III) that exists in the water at pH < 8.0 was not bonded with SBAE,

which was convenient for direct determination of As(III) concentration in the effluent. Experiments performed in a column system filled with HY−AgCl showed that oAs species are not presented in a sample water used. Additional experiment performed in a column system filled with SBAE resin showed that As(III) was present at the level less than 5 μg L^{-1}. In order to perform As(III) oxidation air bubbling for two hours was performed, and determined As(V) in oxidized solution was found to be 104 μg L^{-1}.

Preliminary adsorption study performed with real water sample, spiked with 10 mg L^{-1} of As(V), showed 19% decrease of adsorption capacity for **NC-MA/L'-MG** (69.1 mg g^{-1}), and 8% for **MC-O/L'-MG** (17.0 mg g^{-1}) with respect to experiments performed under non-competitive condition. These results showed possible application of synthesized adsorbents, even in the presence of significant concentration of interfering ions in natural water, in a processes of As(V) removal from groundwater.

Adsorption kinetics

Due to complexity of adsorption processes, i.e. contribution of mass transfer and chemical reaction, different kinetic models were used to fit experimental data: pseudo-first order, pseudo-second order (PSO), Roginsky-Zeldovich-Elovich and second-order rate equation. Also diffusion models: liquid film linear driving force rate equation, liquid film diffusion mass transfer rate equation, homogeneous solid diffusion model, Weber-Morris model (WM), Dunwald-Wagner model and double exponential model [230,323] was used. PSO and W−M models showed the best fitting (Fig. 4.35 and Table 4.28). Additionally, result of comparative kinetic experiments with As(III), and PSO fitting showed higher rate constant, 0.762±0.022 g mg^{-1} min^{-1} for **MC-O/L'-MG** at 25 °C, which is an additional evidence of high performances of obtained material.
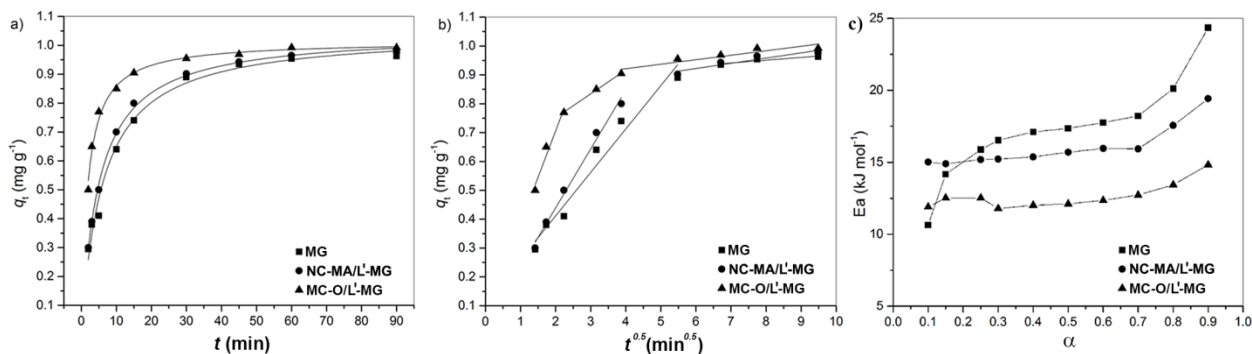
Figure 4.35. Plot of arsenate adsorption on **MG, NC-MA/L'-MG** and **MC-O/L'-MG** by using PSO a), and WM b) model at 25 °C (m/V= 100 mg dm^{-3}, C_i=0.1 mg dm^{-3}, pH=6.0), and diagram of activation energies E_a vs α (c)

The results obtained following the W–M model show three successive linear steps for **MC-O/L'-MG**, while two-line correlation lines was obtained for **NC-MA/L'-MG** (Fig. 4.35). Fast kinetic in the first step was followed by medium adsorption rate in the second, and very slow attainment of equilibrium in the third step was found for **MC-O/L'-MG**. Higher values of the rate constant, found for **MC-O/L'-MG** (Table 4.28), reflect better diffusibility/easier accessibility of surface active sites by sorbate due to shortening the path of ions inside the adsorbent body.

It is well known that multi-step nature of adsorption processes could be affected by bulk diffusion, boundary layer diffusion, intra-particle diffusion and surface adsorption. The first linear steep part demonstrates external mass transfer from bulk solution to the most available adsorptive sites at outer adsorbent surface. The second and the third parts of the adsorption process significantly depend on adsorbent porosity, *i.e.* pore structure, geometry and network density. Due to the concentration gradient, the ions diffuse through bulk solution and treelike pore system extending into adsorbent interior to reach all available surface active sites [222,223]. The intra-particle resistance slows down adsorbate transport, *i.e.* net transport in a direction of variable time-dependent concentration gradient. At the final stage of process, the adsorption takes place at low rate until the saturation of all available surface sites is achieved.

The activation parameters: entropy of activation $\Delta S^{\#}$, Gibbs free energy of activation $\Delta G^{\#}$ and enthalpy of activation $\Delta H^{\#}$ were calculated from kinetic data, obtained at 25, 35, 45 °C, by using eqs. 3.5–3.8. The results are presented in Table 4.28.

Table 4.28. Kinetic and activation parameters of As(V) removal by using **MG**, **NC-MA/L'-MG** and **MC-O/L'-MG** adsorbent

Adsorbent	Pseudo-second-order model			Weber–Morris model						
	q_e (mg g^{-1})	$K_2{}^{*}$	R^2	$k_{p1}{}^{**}$	C (mg g^{-1})	R^2	$k_{p2}{}^{**}$	R^2	$k_{p3}{}^{**}$	R^2
MG	1.047 ±0.024	0.156 ±0.017	0.985	0.151 ±0.014	0.110 ±0.047	0.957	0.0096 ±0.0035	0.807	-	-
NC-MA/L'-MG	1.0463 ±0.0084	0.189 ±0.008	0.997	0.204 ±0.011	0.031 ±0.030	0.987	0.0181 ±0.0047	0.829	-	-
MC-O/L'-MG	1.0155 ±0.0095	0.541 ±0.033	0.989	0.320 ±0.063	0.065 ±0.115	0.926	0.0827 ±0.0025	0.998	0.016 ±0.004	0.813
Activation parameters										
	E_a (kJ mol^{-1})		$\Delta H_{25}{}^{\#}$ (kJ mol^{-1})		$\Delta G_{25}{}^{\#}$ (kJ mol^{-1})		$\Delta S_{25}{}^{\#}$ (J mol^{-1}K^{-1})			
MG	20.10±0.96		17.63±0.86		77.23±3.8		-200.8±9.36			
NC-MA/L'-MG	13.28±0.65		10.8±0.54		76.96±3.7		-222.5±10.6			
MC-O/L'-MG	10.87±0.53		8.39±0.42		74.55±3.5		-221.9±10.3			

* g mg^{-1} min^{-1}; ** mg g^{-1} min$^{-0.5}$

The activation energies of 13.28 and 10.87 kJ mol^{-1} for As(V) removal with **NC-MA/L'-MG** and **MC-O/L'-MG**, respectively**,** were obtained. These results arein agreement with similar result obtained for synthetic goethite [238]. Adsorbate transport is generally controlled by diffusive mass transfer, thus rates of approaching to equilibrium usually increase with increasing of temperature. The results show that the intra-particle diffusion is a rate-controlling step since the activation energy is low and within the range of 8–22 kJ mol^{-1}, characteristic value for diffusion-controlled processes such as ion-exchange/complexation [264].

Improvement of the analysis of kinetic data for whole period of adsorption was performed by applying model free kinetic of adsorption, *i.e.* determination of activation parameters by iso-conversional method. Model free kinetic was selected in order to get the most reliable system responses at appropriate period of time, *i.e.* at the beginning, middle and plateau (approaching to steady state condition) parts of the process. The adsorption rate can be described as the amount of adsorbed pollutant per unit of time by using dimensionless number α. It denotes

time-dependent fraction of bounded arsenic, and could be described by eqs. 3.9–3.12. A plot $-\ln t$ versus $1/T$ at appropriates α yield E_a from the slope regardless of the kinetic/adsorption model used. The reason for choosing the 'model free' method of kinetic analysis is based on the fact that any misidentification of the kinetic model has got a profound effect on the values obtained for the Arrhenius parameters. Sewry and Brown [324], and Galwey [325] have critically reviewed the use of various kinetic models and asserted that caution has to be exercised in choosing the right kinetic model. By applying the fitting of conversion-time data, using predetermined point for calculation of α value, obtained results are presented on Fig. 4.35c).

From the slope of correlations eq. 3.11, at appropriate T and α, a series of activation energy data (E_a) was calculated, and results are presented on Fig. 4.35c). The plots show that overall adsorption mechanism progressively changed from the initial point of the process to attainment of equilibrium. In general, E_a varies from 15 to 18 kJ mol^{-1} for **NC-MA/L'-MG,**and from 12 to 14 kJ mol^{-1} for **MC-O/L'-MG**. In the first part of adsorption ($0<\alpha<0.3$), favorable process was noticed for **MG** due to synergetic effect of geometry/surface group density. Afterward, a steady region ($0.3<\alpha<0.7$) was attained, and followed by steep increases in the course of equilibration. Similar trend of low change of E_a, for both **NC-MA/L'-MG** and **MC-O/L'-MG**, was found for $\alpha<0.7$, and at $\alpha>0.7$ somewhat higher slope was found for **NC-MA/L'-MG**. Generally, the change of Ea values (Fig. 4.35) indicate that adsorption is diffusion controlled process, and it is in accordance with the concept of variation of E_a in a real system due to multi-step nature of most processes encountered in practice. The time-dependent change in kinetics is attributed to textural properties, material structure/defects at exposed plane, steric hindrances and electrostatic attraction/repulsion between adsorbed/released molecules/ionic species. Significance of external/internal mass transport and diffusion inside the pores was indicated [230,323]. The obtained activation energy for the As(V) removal with vacuum and freeze dried goethite modified macroporous resin were 18.63 and 20.60 kJ mol^{-1}[308], which indicate that similar phenomena dictate diffusional transport inside morphologically/chemically similar porous system.

Additionally, performance of synthesized adsorbents was evaluated from comparison with other magnetite based adsorbents (Table 4.29). Among the large numbers of cellulose based adsorbents synthesized up to date, most of them are claimed and considered to be the best

196

candidates to feasible and applicable for effective arsenic removal. The agreement of the adequate response of cellulose based adsorbents with respect to established criteria in the areas of environmental protection mainly arises from their low cost and well-known properties. The extensive literature survey, shown in Table 4.29, is presented with respect to the adsorption kinetics and maximum adsorption capacity of actual material.

Table 4. 29. Adsorption capacity and kinetic data of magnetite based adsorbents

Adsorbent	K_2 (g mg^{-1} min^{-1})	Adsorption capacity (mg g^{-1})	References
Magnetite	0.156	**91.2**	This paper
Magnetite	11.33 mg/min	88.4	[326]
Magnetite/Activated carbon fiber	0.0081	4.16	[115]
Magnetite/Starch	-	248	[327]
NC-MA/L'-MG	0.189	**85.3**	This paper
Cellulose Cu	0.0187	98.9	[223]
Amino/G3MA/TiO$_2$/Cellulose	0.010	108.7	[217]
Amino/Dianhydride/Cellulose	0.64	12.06	[221]
Amino/Cellulose	0.029	187	[219]
MC-O/NC-L'-MG	0.540	**18.5**	This paper
Magnetite/Cellulose fiber	0.00005	2.46	[328]
PDMAEMA/Cellulose fiber	-	27.9	[329]
Amino/Cellulose fiber	0.0011	75.1	[330]

The diversity of experimental condition makes impossible convenient overview/comparison of the literature and presented adsorption data. General consideration of the relation adsorbent performances/textural properties indicates positive dependence of increased surface area with respect to obtained adsorption capacity. According to the results presented (Table 4.29), the q_{max} were found in a wide range between 2.46 mg g^{-1} for Magnetite/Cellulose fiber and 108.7 mg g^{-1} for Amino/GMA/TiO$_2$/Cellulose. The q_{max} obtained from the Langmuir model for the **NC-MA/L'-MG** was found to be 85.3 mg g^{-1} at 25 °C, and lower for the **MC-O/L'-MG**, 18.5mg g^{-1} was found, which iscomparable to the literature data. It means that synthesized high performance adsorbents offer an acceptable alternative to those published in literature or eventually used in a real processes, and production of adsorbents based on presented material offer many benefits to existing ones. Fast attainment of adsorption

equilibrium, *i.e.*, kinetic rate of arsenic adsorption in the presence of the **MC-O/L'-MG** mainly exceeds the values found in the literature (Table 4.29), and capacity of **NC-MA/L'-MG** is similar to those found in literature. Obtained results are in accordance with general experienced rules on relationship between textural data and adsorbent performance, *i.e.* kinetic and adsorption data. The developed fibers integrated mechanical integrity (stability), hydraulic properties and arsenic selectivity. Despite lower adsorption capacity, another factor contributes to substantial improvement of its performance, namely the results of adsorption kinetic open an alternative for the use of **MC-O/L'-MG** exchange fibers relative to **NC-MA/L'-MG** counterparts. The results presented point out to the advantage of application of micro-sized adsorbent which contributes to adsorption performances of chemically identical but physically different materials **NC-MA/L'-MG** and **MC-O/L-MG**.

Obtained rate constant for arsenic adsorption in the presence of the **MC-O/L'-MG** mainly exceeds the values found in literature, and capacity of **NC-MA/L'-MG** is similar/higher to literature data which confirm high applicability of both adsorbents.

Competitive kinetic study

Except of high capacity and fast adsorption rate of arsenic removal, the synthesized adsorbents should possess high affinity/selectivity with respect to selected pollutant. Similarly to non-competitive kinetic study, the data obtained in competitive study, in the presence of one interfering ion: SiO_4^{4-}, CrO_4^{2-} and PO_4^{3-} ions, were processed by using PSO equation. The other kinetic models were of limited validity to be applied for description of the arsenic sorption. Therefore, PSO model was used and results of fitting, obtained from plots q_t–t and t/q_t–t, are given in Table 4.30.

Table 4. 30. Results of the PSO fitting of As(V) removal in presence of single interfering ions

		non-competitive	competitive condition		
			SiO_4^{4-*}	CrO_4^{2-*}	PO_4^{3-*}
MG	q_e^{**}	1.047(±0.024)	0.998(±0.014)	0.938(±0.014)	0.926(±0.016)
	K_2^{***}	0.156(±0.017)	0.144(±0.045)	0.141(±0.040)	0.138(±0.037)
	R^2	0.985	0.989	0.990	0.992
NC-MA/L'-MG	q_e	1.046(±0.084)	0.999(±0.013)	0.936(±0.019)	0.918(±0.028)
	K_2	0.189(±0.008)	0.181(± 0.022)	0.179(±0.020)	0.140(±0.027)
	R^2	0.997	0.987	0.989	0.991
MC-O/L'-MG	q_e	1.016(±0.010)	0.968(±0.015)	0.932(±0.032)	0.886(±0.029)
	K_2	0.541(±0.033)	0.536(±0.029)	0.519(±0.022)	0.489(±0.0)
	R^2	0.989	0.990	0.982	0.992

[*] C_i = 0.1 mg L^{-1}, m/V = 100 mg L^{-1}, t = 90 min; [**] mg g^{-1}; [***] g mg^{-1} min^{-1}

On the other hand, theoretical values show good agreement with the experimental data for PSO kinetic which means that sorption depends on the both concentration of arsenic and adsorbent surface functionalities. Single competitive As(V) adsorption showed the highest influence of phosphate (11.5 % decrease of K_2) for **MG**, 23.0% for **NC-MA/L'-MG** and 9.6% for **MC-O/L'-MG**. Similar trend but of lower extent was found for chromate and the lowest influence of silicate was noticed. Co-precipitation of calcium and magnesium arsenate salt enhances adsorption kinetics as well as adsorption capacity. The low influence of interfering ions (Table 4.30) and pH$_{PZC}$ decreases after adsorption are the properties indicative for the formation of inner-sphere surface complexes. Except of this, experiments performed with **NC-MA/L'-MG** in different concentration of KNO$_3$ showed that increased ionic strength caused increased arsenate uptake. This result also indicate formation of inner-sphere complexes [230,323]. Due to bonding of arsenic species H$_2$AsO$_4^-$/HAsO$_4^{2}$, concentration of negative charge is increased in a electrical double layer [260], and at higher ionic strength of solution, increased concentration of counter cations are available tocompensate the surface negative charges.

Regeneration and reusability

Design of the environmentally friendly and economically viable concept of pollutant removal by adsorption, beside the achievement of high adsorption capacity and fast pollutant uptake, needs optimization of other process parameters: life cycle of adsorbent, regeneration efficiency and safe disposal of adsorption/regeneration residue. Minimization of the contribution of material cost could be solved by development of high capacity adsorbent, and together with possibility of the effective adsorbent regeneration, provides high performance adsorbent for practical application. Regeneration efficiency, *i.e.* number of the cycles of adsorbent reuse contributes to the cost effectiveness of adsorption process. Due to magnetic properties of presented materials, separation is successfully achieved regardless of whether the processes was carried out in a batch of flow system, and high desorption rate is reached. Both developed composites can be considered as eco-friendly, however, structural and morphological properties of designed adsorbents caused the differences in terms of adsorption efficiency after the multistage desorption. The selection of an efficient regenerant depends on the arsenic bonding type, nature of adsorbent and regulation concerning effluent water quality. The formation of surface complexes [308] demands application of strong competitive anion capable to break off As-O-Fe surface bond. Sodium hydroxide and strong acids are most commonly used to elute As(V). Therefore, anion exchange of bonded As(V) would leave active surface sites at the level before the previous adsorption cycle. Subsequent rinsing with dilute acid, *e.g*. 2% sulfuric acid, causes protonation of negatively charged surface preserving adsorptive potential to some extent which depends on regeneration cycle. It is well known that NaOH, binary system NaOH/NaCl and ternary eluent NaOH/NaCl/oxalate have been shown to be the best alternatives [308]. The results of desorption study, performed in a batch system, are given in Fig. 4.36.
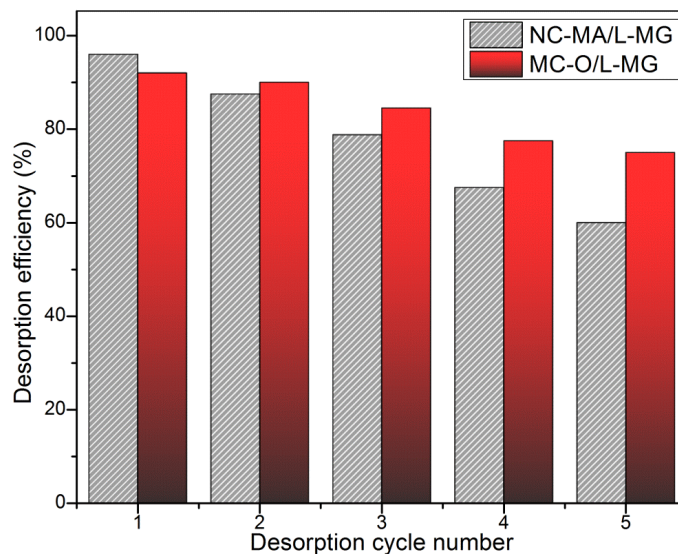
Figure 4. 36. Adsorption/desorption efficiency of **NC-MA/L'-MG** and **MC-O/L'-MG** in the course of five cycles

The most efficient desorption system has proven to be NaOH/NaCl (0.5/0.5). With this binary system, in the first cycle, 96 and 92 % of As(V) was desorbed, and throughout five consecutive cycles, desorption efficiency was decreased to 60 and 72 % for **NC-MA/L'-MG** and **MC-O/L'-MG**, respectively. In summary, both adsorbents are is reusable in a multi-step processes and an efficient adsorbent for As(V) removal for over five adsorption/desorption cycles.

Regeneration versus safety

The major factors limiting the use of adsorbents is related to high cost of the media, the complexity of regeneration, spent regenerant and spent media disposal. Waste management of hazardous residues is an important issue which must be actively monitored/implemented to conform the actual law/regulation. Generated adsorption wastes: arsenate loaded adsorbent – sludge, waste chemicals and washing solution need to be treated or disposed in proper way. Designed treatment technology has to provide transformation of the generated wastes by

different processes to produce non-hazardous material that can be safely landfilled. In that sense, as a results of desorption study, an appropriate amount of spent waste alkali concentrated arsenic solution is generated. These materials could be safely disposed, subjected to processing of hazardous solution into non-leaching non-hazardous solid waste. Waste disposal is a short-term solution which is limited by storage space and long term material stability (leaching of hazardous material). The design of the technology for treatment of effluent medium is the justified solution. Similar methodology was applied as in recent publication[308]: the desorption and washing solutions were mixed, pH was adjusted to 6.5 by adding 15 % of hydrochloric acid, and followed by addition of 30 % excess of iron(II) sulfate solution (5 %) with respect to determined As concentration. All operations are performed in a oxic and anoxic conditions. Coagulation/-precipitation process last for 12 hours, and processing of heavy dark brownish precipitate was continued by filtration. The formed colloids adsorb (bound) arsenic, and by exerting proper agitation enriched oxygenated solution provided favorable condition for formation of heavy precipitate resistant to leaching of arsenic. Additionally, more stable material for safe landfilling could be obtained by blending/lining iron/arsenic complexed precipitate processed with inorganic/organic material. Thus production of engineered core-shell structured materials would be of main concern of the future study. Recently it was shown, according to X-ray photoelectron spectroscopy (XPS) and X-ray absorption near edge structure (XANES) analyses, that complex redox reactions take place at outer surface of As-adsorbed MNPs (magnetic nanoparticles) in an oxic condition. Simultaneous As(III)/As(V) oxidation and reduction with concomitant magnetite/maghemite oxidation take place in comparison to anoxic condition. The As(III)/As(V) oxidation was exerted by participation of oxygen and facilitated by other highly oxidizing species[322]. Due to this finding careful consideration regarding to safe landfilling to keep arsenic leaching at lowest level another experiment of coagulation/precipitation of spent regenerant was performed in an inert (anoxic) atmosphere. According to EPA regulative (USEPA, Test methods for evaluating solid waste, physical/ chemical methods, 1992) all solidified products was subjected to testing according to toxicity characteristic leaching procedure (TCLP). TCLP was applied to evaluate hazardous characteristics of exhausted adsorbent and treated sludge in order to evaluate possibility for safe handling and disposal in landfills. The determined concentration of inorganic arsenic (iAs) is below established

concentration by U.S. EPA standard of 0.1 mg L^{-1} (USEPA, National Primary Drinking Water Regulations, 2001), which indicates possibility for safe disposal of final solidified inert material.

Future challenges

The adsorption performances, comparable/higher than that of the most common referenced material, observed for well-dispersed/manipulative **NC-MA/L'-MG** and **MC-O/L'-MG** adsorbentsresult from the contribution of two factors: (i) design of surface modification with branched organic structure with number of amino terminal groups, and (ii) development of controllable method for magnetite precipitation. The main goal of presented study was devoted to understanding of scientific principles related to influences of the parent media size, **NC** *versus* **MC**, on the adsorption properties of produced adsorbents. Also, investigation on the influences of chemical structure/properties of the modified precursor surface on the optimization of the method for magnetite precipitation was an additional goal of this study. Obviously, crystal structure of precipitated magnetite, exposed surface and crystal faces, had pronounced influence on adsorbent properties and strongly depends on experimental condition and **NC/MC** surface properties. It was shown that in a moderately acidic/neutral condition arsenic species are strongly bonded to iron oxide surface. EXAFS analysis suggested predominant formation of bidentate binuclear corner-sharing complexes (^2C) for As(V), with dominant complexes formed between AsO_4^{3-} tetrahedron and two FeO_6 octahedra on {100} surfaces of magnetite [322]. Also, calculation using density functional theory (DFT) predicted the relative energies and geometries of surface complexes using density functional theory showed higher stability of ^2C complex for 55 kJ mol^{-1} in relation to ^2E edge-sharing bidentate complex. According to this, good adsorption performances of the novel adsorbents was related to proper **NC** and **MC** modification, and controllable **MG** precipitation which cause beneficial facet evolution at MG surface. As a result, high affinity and efficient arsenate removal from water, as well as acceptable kinetics with possibility for adsorbent use in the processes of natural water remediation even in the presence of competing ions were obtained. Also, exceptional adsorption performances and magnetic properties of **MG** nanoparticles, precipitated on modified **NC** and **MC** surfaces, provide an opportunity for practical application and easy separation from aqueous solution by applying

external magnetic field. In that way, three main goals were realized by understanding/explaining of scientific principles related to the influences of parent media size, **NC** *versus* **MC**, chemical structure/properties of organic functionalities bonded on **NC** and **MC** surface, and **MG** precipitation method on adsorption performances of novel synthesized adsorbents. Additionally, a number of idea/strategy was designed based on presented results/conclusions, and future work will be focused on development/production of woven nano/micro cellulose **MG** modified hybrid textile materials.

5. CONCLUSIONS

In the first part of the work, an efficient and moderate cost adsorbent for arsenic removal was obtained by impregnation of **FO** on amino modified cross linked macroporous polymer. Amination of pendant epoxy groups of macroporous glycidyl methacrylate support facilitated fabrication of hybrid media. High specific surface area, mesopore volume and diameter, as well as contribution of hybrid nature resulted in the best adsorption performances of the **ER/DETA/FO/FD**. The changes in pH value revealed that adsorbent show high adsorption affinity with respect to As in a broad pH value range. Adsorption equilibrium was described by the Sips isotherm. The best fitting of kinetic data was obtained by the use of pseudo-second-order and Weber-Morris kinetic model and indicated on intra-particle diffusional transport as a limiting step. Thermodynamic parameters revealed that adsorption processes are favorable and more spontaneous at higher temperatures, 34.0 mg g^{-1} at 45 *vs.* 31.0 mg g^{-1} at 25 °C. The **ER/DETA/FO/FD** was successfully applied to the removal of arsenic from model water in the presence of the interfering ions. The results of theoretical modeling, obtained by the use of HFO model, incorporated in MINTEQ, were in good agreement with experimental data, and both results illustrated negligible influence of most coexisting ions present in natural water. Calcium and magnesium ions showed positive effect on adsorption and kinetics, while in the presence of phosphate ions the adsorption of arsenate decreased.

Experimental results showed that **ER/DETA/FO/FD** is efficient and reusable for arsenic removal from natural water in the batch and fixed-bed column mode. Good agreement of q_{exp} and q_{cal} indicated advantageous use of the Bohart-Adams, Yoon-Nelson and Thomas model: simplicity of application and consistency in predicting the breakthrough curve and adsorption capacity. Also, it was shown that glycidyl methacrylate copolymer exhibits high macroporosity which enables fast intraparticle mass transport at high hydraulic loading rates and creates short mass transfer zones in fixed bed reactor configuration. By selecting the appropriate solvent mixture, goethite impregnation on the surface and inside the pores of aminated glycidyl methacrylate support media has been achieved uniformly while pore clogging during in-situ nanomaterial synthesis was minimized. Designed goethite impregnated media showed to be effective in a simple water matrix without competition ions and applied methodology of PSDM

full-scale packed bed simulation operated under realistic conditions showed to be reliable and significantly simpler than time-consuming and expensive pilot tests. In this part of the work a couple of important points were emphasized: efficient arsenate removal from water, good affinity, acceptable kinetics and possibility for use in the processes of natural water remediation even in the presence of competing ions in high concentration, positive economic regarding possible application analysis in a real water purification system.

In the second part of the work, a highly efficient and moderate costly adsorbents for As(V), As(III), Cd^{2+}, Ni^{2+}, Pb^{2+} and Cu^{2+} removal was obtained by impregnation of goethite on amino modified **NC**. The best adsorption performance of **NC-PEG** and **NC-L,** and subsequent modififcation with goethite produced **NC-PEG/FO** and **NC-L/FO** adsorbetns, respectively, were discussed to be the consequence of adsorbent specific surface area, mesopore volume and diameter, as well as contribution of their hybrid nature. By the use of adequate statistical analysis and proper selection of the isotherm model, *i.e.* Freundlich and D-R models showed the best correlation of the adsorption data. The best fitting of kinetic data was obtained by the use of pseudo-second-order and W-M kinetic model which showed that intra-particle diffusional transport is a limiting step. Thermodynamic parameters revealed that adsorption processes were favorable and more spontaneous at higher temperature, example presented for As(V): 37.0 mg g^{-1} at 45 °C *versus* 33.4 mg g^{-1} at 25 °C for **NC-L/FO**. Experimental results showed that the used adsorbents are efficient and reusable for cations and As(V) removal from natural water in the batch mode. In summary, presented results addressed the role of amino modification of adsorbent to obtain novel environmentally friendly adsorbent materials **NC-L** and **NC-PEG** which could be used in small (laboratory) scale as high performance adsorbent for cations removal. Also, additional modification of both **NC-PEG** and **NC-L** with goethite precipitation produced **NC-PEG/FO** and **NC-L/FO** adsorbents applicable for As(V) and As(III) removal.

In the last part of the work, the presented results demonstrated that parent media size microfibrillated cellulose (**MC**) *versus* nanocellulose (**NC**) support, functionalities/architecture of organic modifying structure and nanohybrid material have significant influence on adsorption properties of physically different materials. Compared to unsupported **MG**, two novel designed nano and micro cellulose supported adsorbents with organic support (amino functionalized) and inorganic nanohydrid precipitated adsorptive material (magnetite) exhibited favorable adsorption

properties toward arsenate. Different geometry (aspect/ratio) and morphological/textural properties caused better adsorptive properties of **NC-MA/L'-MG,** *i.e*. nearly five times higher adsorption capacity (85.3 *vs* 18.5 mg g^{-1}) in comparison to **MC-O/L'-MG** counterpart. Such results reflect the significance of increased number of amino surface bonding sites, present at **NC-L** surface, which are susceptible for effective **MG** precipitation. The results of kinetic study, for both adsorbents, were well fitted with the PSO and WM kinetic model. However, **MC-O/L'-MG** demonstrated significantly faster kinetic, around three times higher value of K_2, 0.541 *vs* 0.189 g mg^{-1} min^{-1}, indicates better availability of surface active sites in **MC-O/L'-MG**. Iso-conversional method applied on kinetic data of both adsorbents showed that **MC-O/L'-MG** was preferable material due tolower dependence of E_a on the extent of adsorption. Additionally, both adsorbents showed applicability in a competitive condition, reusability (regeneration capability) and possibility for separation of saturated adsorbent by magnetic field.

6. References

[1]   A. Tubić, J. Agbaba, B. Dalmacija, I. Ivančev-Tumbas, M. Dalmacija, Removal of arsenic and natural organic matter from groundwater using ferric and alum salts: A case study of central Banat region (Serbia), J. Environ. Sci. Heal. Part A. 45 (2010) 363–369. doi:10.1080/10934520903467931.

[2]   A. Tubić, J. Agbaba, B. Dalmacija, S. Rončević, M. Klašnja, I. Ivančev-Tumbas, Effects of O_3 , O_3/H_2O_2 and coagulation on natural organic matter and arsenic removal from typical northern serbia source water, Sep. Sci. Technol. 45 (2010) 2453–2464. doi:10.1080/01496395.2010.492376.

[3]   B. Mandal, Arsenic round the world: A review, Talanta. 58 (2002) 201–235. doi:10.1016/S0039-9140(02)00268-0.

[4]   S. Murcott, Arsenic contamination in the corld: An international sourcebook 2012, Water Intell. Online. 11 (2012). doi:10.2166/9781780400396.

[5]   J.T. Hindmarsh, R.F. McCurdy, J. Savory, Clinical and environmental aspects of arsenic toxicity, CRC Crit. Rev. Clin. Lab. Sci. 23 (1986) 315–347. doi:10.3109/10408368609167122.

[6]   J. Liu, Focal adhesion kinase as a potential target in arsenic toxicity, Toxicol. Sci. 84 (2005) 212–213. doi:10.1093/toxsci/kfi111.

[7]   D. Mohan, C.U. Pittman, Arsenic removal from water/wastewater using adsorbents-A critical review, J. Hazard. Mater. 142 (2007) 1–53. doi:10.1016/j.jhazmat.2007.01.006.

[8]   T. Viraraghavan, K. Subramanian, J. Aruldoss, Arsenic in drinking water ? Problems and solutions, Water Sci. Technol. 40 (1999) 69–76. doi:10.1016/S0273-1223(99)00432-1.

[9]   G.T. Yan, T. Viraraghavan, Heavy-metal removal from aqueous solution by fungus Mucor rouxii, Water Res. 37 (2003) 4486–4496. doi:10.1016/S0043-1354 (03)00409-3.

[10]   B.D. Kocar, W.P. Inskeep, Photochemical oxidation of As(III) in ferrioxalate solutions, Environ. Sci. Technol. 37 (2003) 1581–1588. doi:10.1021/es020939f.

[11]   W. Inskeep, T. McDermott, S. Fendorf, Arsenic (V)/(III) cycling in soils and natural waters: chemical and microbiological processes, in: W. Frankenberger (Ed.), Environ. Chem. Arsen., Marcel Dekker, New York, 2002: pp. 183–215.

[12]   M. Sumner, ed., Handbook of soil science, CRC Press Taylor & Francis Group, New York, n.d.

[13]   R. Singh, S. Singh, P. Parihar, V.P. Singh, S.M. Prasad, Arsenic contamination, consequences and remediation techniques: A review, Ecotoxicol. Environ. Saf. 112 (2015) 247–270. doi:10.1016/j.ecoenv.2014.10.009.

[14]   R. Johnston, H. Heijnen, Safe water technology for arsenic removal, Report, Bangladesh University of Engineering and Technology, Dhaka, Bangladesh 2001.

[15]   N. Pous, B. Casentini, S. Rossetti, S. Fazi, S. Puig, F. Aulenta, Anaerobic arsenite oxidation with an electrode serving as the sole electron acceptor: A novel approach to the bioremediation of arsenic-polluted groundwater, J. Hazard. Mater. 283 (2015) 617–622. doi:10.1016/j.jhazmat.2014.10.014.

[16]   N.R. Nicomel, K. Leus, K. Folens, P. Van Der Voort, G. Du Laing, Technologies for arsenic removal from water: Current status and future perspectives, Int. J. Environ. Res. Public Health. 13 (2015) 1–24. doi:10.3390/ijerph13010062.

[17]   X. Guan, J. Du, X. Meng, Y. Sun, B. Sun, Q. Hu, Application of titanium dioxide in arsenic removal from water: A review, J. Hazard. Mater. 215-216 (2012) 1–16. doi:10.1016/j.jhazmat.2012.02.069.

[18]   T.S.Y. Choong, T.G. Chuah, Y. Robiah, F.L. Gregory Koay, I. Azni, Arsenic toxicity, health hazards and removal techniques from water: an overview, Desalination. 217 (2007) 139–166. doi:10.1016/j.desal.2007.01.015.

[19]   P. Mondal, S. Bhowmick, D. Chatterjee, A. Figoli, B. Van der Bruggen, Remediation of inorganic arsenic in groundwater for safe water supply: A critical assessment of technological solutions, Chemosphere. 92 (2013) 157–170. doi:10.1016/j.chemosphere.2013.01.097.

[20]   H. Garelick, A. Dybowska, E. Valsami-Jones, N. Priest, Remediation technologies for arsenic contaminated drinking waters (9 pp), J. Soils Sediments. 5 (2005) 182–190. doi:10.1065/jss2005.06.140.

[21]   J. Hering, P.-Y. Chen, J. Wilkie, E. Menachem, Arsenic removal from drinking water during coagulation, J. Environ. Eng. 123 (1996) 800–807.

[22]   M.C. Shih, An overview of arsenic removal by pressure-driven membrane processes, Desalination. 172 (2005) 85–97. doi:10.1016/j.desal.2004.07.031.

[23]   B. Van Der Bruggen, C. Vandecasteele, T. Van Gestel, W. Doyen, R. Leysen, A review of pressure-driven membrane processes in wastewater treatment and drinking water production, Environ. Prog. 22 (2003) 46–56. doi:10.1002/ep.670220116.

[24]   T.S. Singh, K.K. Pant, Equilibrium, kinetics and thermodynamic studies for adsorption of As(III) on activated alumina, Sep. Purif. Technol. 36 (2004) 139–147. doi:10.1016/S1383-5866(03)00209-0.

[25]   M. Jang, W. Chen, F.S. Cannon, Preloading hydrous ferric oxide into granular activated carbon for arsenic removal, Environ. Sci. Technol. 42 (2008) 3369–3374. doi:10.1021/es7025399.

[26]   A. Anjum, Removal of As(III) from aqueous solutions using montmorillonite, J. Anal. Sci. Methods Instrum. 01 (2011) 25–30. doi:10.4236/jasmi.2011.12004.

[27]   V. Lenoble, O. Bouras, V. Deluchat, B. Serpaud, J.-C. Bollinger, Arsenic adsorption onto pillared clays and iron oxides., J. Colloid Interface Sci. 255 (2002) 52–58. doi:10.1006/jcis.2002.8646.

[28]   D.E. Giles, M. Mohapatra, T.B. Issa, S. Anand, P. Singh, Iron and aluminium based adsorption strategies for removing arsenic from water, J. Environ. Manage. 92 (2011) 3011–3022. doi:10.1016/j.jenvman.2011.07.018.

[29]   B. Samiey, C.H. Cheng, J. Wu, Organic-inorganic hybrid polymers as adsorbents for removal of heavy metal ions from solutions: A review, Materials (Basel). 7 (2014) 673–726. doi:10.3390/ma7020673.

[30]   M. Habuda-Stanic, M. Nujic, Arsenic removal by nanoparticles: A review, Environ. Sci. Pollut. Res. 22 (2015) 8094–8123. doi:10.1007/s11356-015-4307-z.

[31]   G. Jegadeesan, K. Mondal, S.B. Lalvani, Arsenate remediation using nanosized modified zerovalent iron particles, Environ. Prog. 24 (2005) 289–296. doi:10.1002/ep.10072.

[32]   K. Hristovski, A. Baumgardner, P. Westerhoff, Selecting metal oxide nanomaterials for arsenic removal in fixed bed columns: From nanopowders to aggregated nanoparticle media, J. Hazard. Mater. 147 (2007) 265–274. doi:10.1016/j.jhazmat.2007.01.017.

[33]   Y.H. Li, S. Wang, Z. Luan, J. Ding, C. Xu, D. Wu, Adsorption of cadmium(II) from

aqueous solution by surface oxidized carbon nanotubes, Carbon N. Y. 41 (2003) 1057–1062. doi:10.1016/S0008-6223(02)00440-2.

[34] C. Lu, C. Liu, Removal of nickel(II) from aqueous solution by carbon nanotubes, J. Chem. Technol. Biotechnol. 81 (2006) 1932–1940. doi:10.1002/jctb.1626.

[35] S.C.N. Tang, I.M.C. Lo, Magnetic nanoparticles: Essential factors for sustainable environmental applications, Water Res. 47 (2013) 2613–2632. doi:10.1016/j.watres.2013.02.039.

[36] J. Zhang, Q. Liu, Y. Ding, Y. Bei, 3-aminopropyltriethoxysilane functionalized nanoscale zero-valent iron for the removal of dyes from aqueous solution, Polish J. Chem. Technol. 13 (2011). doi:10.2478/v10026-011-0021-x.

[37] S.R. Kanel, B. Manning, L. Charlet, H. Choi, Removal of arsenic (III) from groundwater by nanoscale zero-valent iron, Environ. Sci. Technol. 39 (2005) 1291–1298. doi:10.1021/es048991u.

[38] M. Ramos, W. Yan, X. Li, B.E. Koel, W. Zhang, Simultaneous oxidation and reduction of arsenic by zero-valent iron nanoparticles: Understanding the significance of the core−shell structure, J. Phys. Chem. C. 113 (2009) 14591–14594. doi:10.1021/jp9051837.

[39] G. Limousin, J.P. Gaudet, L. Charlet, S. Szenknect, V. Barthes, M. Krimissa, Sorption isotherms: A review on physical bases, modeling and measurement, Appl. Geochemistry. 22 (2007) 249–275. doi:10.1016/j.apgeochem.2006.09.010.

[40] S.J. Allen, G. Mckay, J.F. Porter, Adsorption isotherm models for basic dye adsorption by peat in single and binary component systems, J. Colloid Interface Sci. 280 (2004) 322–333. doi:10.1016/j.jcis.2004.08.078.

[41] M. Ghiaci, A. Abbaspur, R. Kia, F. Seyedeyn-Azad, Equilibrium isotherm studies for the sorption of benzene, toluene, and phenol onto organo-zeolites and as-synthesized MCM-41, Sep. Purif. Technol. 40 (2004) 217–229. doi:10.1016/j.seppur.2004.03.001.

[42] M.C. Ncibi, Applicability of some statistical tools to predict optimum adsorption isotherm after linear and non-linear regression analysis, J. Hazard. Mater. 153 (2008) 207–212. doi:10.1016/j.jhazmat.2007.08.038.

[43] E. Bulut, M. Özacar, I.A. Şengil, Adsorption of malachite green onto bentonite: Equilibrium and kinetic studies and process design, Microporous Mesoporous Mater. 115 (2008) 234–246. doi:10.1016/j.micromeso.2008.01.039.

[44] A. Malek, S. Farooq, Comparison of isotherm models for hydrocarbon adsorption on activated carbon, AIChE J. 42 (1996) 3191–3201. doi:10.1002/aic.690421120.

[45] I. Langmuir, the Constitution and Fundamental Properties of Solids and Liquids. Part I. Solids., J. Am. Chem. Soc. 252 (1916) 2221–2295. doi:10.1021/ja02268a002.

[46] A.L. Myers, J.M. Prausnitz, Thermodynamics of mixed-gas adsorption, AIChE J. 11 (1965) 121–127. doi:10.1002/aic.690110125.

[47] M.M. Dubinin, The potential theory of adsorption of gases and vapors for adsorbents with energetically nonuniform surfaces., Chem. Rev. 60 (1960) 235–241. doi:10.1021/cr60204a006.

[48] R. Douglas M., Principles of adsorption and adsorption processes, Wiley, New York, 1984.

[49] K. Vijayaraghavan, T.V.N. Padmesh, K. Palanivelu, M. Velan, Biosorption of nickel(II) ions onto Sargassum wightii: Application of two-parameter and three-parameter isotherm models, J. Hazard. Mater. 133 (2006) 304–308. doi:10.1016/j.jhazmat.2005.10.016.

[50] S. Kundu, A.K. Gupta, Arsenic adsorption onto iron oxide-coated cement (IOCC): Regression analysis of equilibrium data with several isotherm models and their optimization, Chem. Eng. J. 122 (2006) 93–106. doi:10.1016/j.cej.2006.06.002.

[51] A.B. Perez-Marin, V.M. Zapata, J.F. Ortuno, M. Aguilar, J. Saez, M. Llorens, Removal of cadmium from aqueous solutions by adsorption onto orange waste, J. Hazard. Mater. 139 (2007) 122–131. doi:10.1016/j.jhazmat.2006.06.008.

[52] T.W. Weber, R.K. Chakravorti, Pore and solid diffusion models for fixed-bed adsorbers, AIChE J. 20 (1974) 228–238. doi:10.1002/aic.690200204.

[53] H.M. Freundlich, Over the adsorption in solution, J. Phys. Chem. 57A (1906) 385470.

[54] A. Adamson, A. Gast, Physical chemistry of surfaces, 6th ed., 1997.

[55] J. Zeldowitsch, Adsorption site energy distribution, Acta Phys. Chim. URSS 1 (1934) 961–973.

[56] F. Haghseresht, G.Q. Lu, Adsorption characteristics of phenolic compounds onto coal-reject-derived adsorbents, Energy & Fuels. 12 (1998) 1100–1107. doi:10.1021/ef9801165.

[57] M. Dubinin, L. Radushkevich, Equation of the characteristic curve of activated charcoal, Proc. Acad. Sci. Phys. Chem. Sec. 55 (1947) 875–890.

[58] J.P. Hobson, Physical adsorption isotherms extending from ultrahigh vacuum to vapor pressure, J. Phys. Chem. 73 (1969) 2720–2727. doi:10.1021/j100842a045.

[59] C. Aharoni, M. Ungarish, Kinetics of activated chemisorption. Part 2.—Theoretical models, J. Chem. Soc. Faraday Trans. 1 Phys. Chem. Condens. Phases. 73 (1977) 456. doi:10.1039/f19777300456.

[60] M. Horsfall Jnr, A.I. Spiff, Equilibrium sorption study of Al^{3+}, Co^{2+} and Ag^+ in aqueous solutions by fluted pumpkin (telfairia sccidentalis HOOK f) waste biomass, Acta Chim. Slov. 52 (2005) 174–181.

[61] A.V. Hill, The possible effects of the aggregation of the molecules of haemoglobin on its dissociation curves, J. Physiol. 40 (1910) 4–7.

[62] O. Redlich, D.L. Peterson, A useful adsorption isotherm, J. Phys. Chem. 63 (1959) 1024–1024. doi:10.1021/j150576a611.

[63] R. Sips, Combined form of Langmuir and Freundlich equations, J. Chem. Phys. 16 (1948) 490–495.

[64] A. Günay, E. Arslankaya, I. Tosun, Lead removal from aqueous solution by natural and pretreated clinoptilolite: Adsorption equilibrium and kinetics, J. Hazard. Mater. 146 (2007) 362–371. doi:10.1016/j.jhazmat.2006.12.034.

[65] J. Toth, State equations of the solid gas interface layer, Acta Chim. Acad. Sci. Hungaricae. 69 (n.d.) 311–317.

[66] R.A. Koble, T.E. Corrigan, Adsorption isotherms for pure hydrocarbons, Ind. Eng. Chem. 44 (1952) 383–387. doi:10.1021/ie50506a049.

[67] A. Khan, R. Ataullah, A. Al-Haddad, Equilibrium adsorption studies of some aromatic pollutants from dilute aqueous solutions on activated carbon at different temperatures, J. Colloid Interface Sci. 194 (1997) 154–65. doi:10.1006/jcis.1997.5041.

[68] S. Brunauer, P.H. Emmett, E. Teller, Gases in multimolecular layers, J. Am. Chem. Soc. 60 (1938) 309–319. doi:citeulike-article-id:4074706.

[69] K.Y. Foo, B.H. Hameed, Insights into the modeling of adsorption isotherm systems, Chem. Eng. J. 156 (2010) 2–10. doi:10.1016/j.cej.2009.09.013.

[70] A. Dada, A. Olalekan, A. Olatunya, O. Dada, Langmuir, Freundlich, Temkin and Dubinin

– Radushkevich isotherms studies of equilibrium sorption of Zn^{2+} unto phosphoric acid modified rice husk, IOSR J. Appl. Chem. 3 (2012) 38–45. doi:10.9790/5736-0313845.

[71] E. Demirbas, M. Kobya, A.E.S. Konukman, Error analysis of equilibrium studies for the almond shell activated carbon adsorption of Cr(VI) from aqueous solutions, J. Hazard. Mater. 154 (2008) 787–794. doi:10.1016/j.jhazmat.2007.10.094.

[72] T.L. Hill, Theory of physical adsorption, Adv. Catal. 4 (1952) 211–258.

[73] W.G. McMillan, E. Teller, The assumptions of the B.E.T. theory, J. Phys. Colloid Chem. 55 (1951) 17–20.

[74] J.W. Zwolak, P.T. Boggs, L.T. Watson, Algorithm 869, ACM Trans. Math. Softw. 33 (2007) 27–es. doi:10.1145/1268776.1268782.

[75] D.D. Marković, B.M. Lekić, V.N. Rajaković-Ognjanović, A.E. Onjia, L. V. Rajaković, A New approach in regression analysis for modeling adsorption isotherms, Sci. World J. 2014 (2014) 1–17. doi:10.1155/2014/930879.

[76] L. Largitte, R. Pasquier, A review of the kinetics adsorption models and their application to the adsorption of lead by an activated carbon, Chem. Eng. Res. Des. 109 (2016) 495–504. doi:10.1016/j.cherd.2016.02.006.

[77] H. Qiu, L. Lv, B. Pan, Q.Q. Zhang, W. Zhang, Q.Q. Zhang, Critical review in adsorption kinetic models, J. Zhejiang Univ. Sci. A. 10 (2009) 716–724. doi:10.1631/jzus.A0820524.

[78] S. Lagergren, About the theory of so-called adsorption of soluble substances, K. Sven. Vetenskapsakademiens. 24 (1898) 1–39.

[79] Y.S. Ho, G. McKay, Sorption of dye from aqueous solution by peat, Chem. Eng. J. 70 (1998) 115–124. doi:10.1016/S0923-0467(98)00076-1.

[80] Y.S. Ho, Review of second-order models for adsorption systems, J. Hazard. Mater. 136 (2006) 103–111. doi:10.1016 /j.jhazmat.2005.12.043.

[81] J.A. Heimberg, K.J. Wahl, I.L. Singer, A. Erdemir, Superlow friction behavior of diamond-like carbon coatings: Time and speed effects, Appl. Phys. Lett. 78 (2001) 2449. doi:10.1063/1.1366649.

[82] G.E. Boyd, A.W. Adamson, L.S. Myers, The exchange adsorption of ions from aqueous solutions by organic zeolites. II. kinetics 1, J. Am. Chem. Soc. 69 (1947) 2836–2848. doi:10.1021/ja01203a066.

[83] J. Crank, Mathematics of diffusion, Oxford at the Clarendon Press, England, London, 1956.

[84] H.L. Wang, J.L. Chen, Z.C. Zhai, Study on thermodynamics and kinetics of adsorption of p-toluidine from aqueous solution by hypercrosslinked polymeric adsorbents, Environ. Chem. 23 (2004) 188–192.

[85] A. Wilczak, T.M. Keinath, Kinetics of sorption and desorption of copper(II) and lead(II) on activated Carbon, Water Environ. Res. 65 (1993) 238–244.

[86] N. Chiron, R. Guilet, E. Deydier, Adsorption of Cu(II) and Pb(II) onto a grafted silica: isotherms and kinetic models, Water Res. 37 (2003) 3079–3086. doi:10. 1016/S0043-1354(03)00156-8.

[87] K.V. Kumar, Comparative analysis of linear and non-linear method of estimating the sorption isotherm parameters for malachite green onto activated carbon, J. Hazard. Mater. 136 (2006) 197–202. doi:10.1016/j.jhazmat.2005.09.018.

[88] D.H. Lataye, I.M. Mishra, I.D. Mall, Adsorption of 2-picoline onto bagasse fly ash from aqueous solution, Chem. Eng. J. 138 (2008) 35–46. doi:10.1016/j.cej.2007.05.043.

[89] B. Boulinguiez, P. Le Cloirec, D. Wolbert, Revisiting the determination of Langmuir parameters-Application to tetrahydrothiophene adsorption onto activated carbon, Langmuir. 24 (2008) 6420–6424. doi:10.1021/la800725s.

[90] J.C. Ng, W. Cheung, G. McKay, Equilibrium studies of the sorption of Cu(II) ions onto chitosan, J. Colloid Interface Sci. 255 (2002) 64–74. doi:10.1006/jcis.2002.8664.

[91] A. Kapoor, R.T. Yang, Correlation of equilibrium adsorption data of condensible vapours on porous adsorbents, Gas Sep. Purif. 3 (1989) 187–192. doi:10.1016/0950-4214(89)80004-0.

[92] J.C.Y. Ng, W.H. Cheung, G. McKay, Equilibrium studies for the sorption of lead from effluents using chitosan., Chemosphere. 52 (2003) 1021–1030. doi:10.1016/S0045-6535(03)00223-6.

[93] D.W. Marquardt, An algorithm for least-squares estimation of nonlinear parameters, J. Soc. Ind. Appl. Math. 11 (1963) 431–441. doi:10.1137/0111030.

[94] A. Seidel, D. Gelbin, On applying the ideal adsorbed solution theory to multicomponent adsorption equilibria of dissolved organic components on activated carbon, Chem. Eng. Sci. 43 (1988) 79–88. doi:10.1016/0009-2509(88)87128-8.

[95] K.V. Kumar, K. Porkodi, F. Rocha, Isotherms and thermodynamics by linear and non-linear regression analysis for the sorption of methylene blue onto activated carbon: Comparison of various error functions, J. Hazard. Mater. 151 (2008) 794–804. doi:10.1016/j.jhazmat.2007.06.056.

[96] K.V. Kumar, S. Sivanesan, Pseudo second order kinetics and pseudo isotherms for malachite green onto activated carbon: Comparison of linear and non-linear regression methods, J. Hazard. Mater. 136 (2006) 721–726. doi:10.1016/j.jhazmat.2006.01.003.

[97] S. Goldberg, Surface Complexation modeling, Ref. Modul. Earth Syst. Environ. Sci. (2013). doi:10.1016/B978-0-12-409548-9.05311-2.

[98] C. Koretsky, The significance of surface complexation reactions in hydrologic systems: A geochemist's perspective, J. Hydrol. 230 (2000) 127–171. doi:10.1016/S0022-1694(00)00215-8.

[99] S. Goldberg, Adsorption models incorporated into chemical equilibrium models, Chem. Equilib. React. Model. (1995) 75–95. doi:10.2136/sssaspecpub42.c5.

[100] D.A. Dzombak, Toward a uniform model for the sorption, Signat. Redacted. (1986).

[101] D. Dzombak, F. Morel, Surface complexation modeling: Hydrous ferric oxide, John Wiley & Sons Inc., New York, 1990.

[102] W. Schecher, D. McAvoy, MINEQL+: User's manual, environmental research software, Edgewater, Hallowell, Maine, USA, 2001.

[103] T. Tuutijarvi, J. Lu, M. Sillanpaa, G. Chen, As(V) adsorption on maghemite nanoparticles, J. Hazard. Mater. 166 (2009) 1415–1420. doi:10.1016/j.jhazmat.2008.12.069.

[104] L. Lorenzen, J.S.J. van Deventer, W.M. Landi, Factors affecting the mechanism of the adsorption of arsenic species on activated carbon, Miner. Eng. 8 (1995) 557–569. doi:10.1016/0892-6875(95)00017-K.

[105] I. Rau, A. Gonzalo, M. Valiente, Arsenic(V) removal from aqueous solutions by iron(III) loaded chelating resin, J. Radioanal. Nucl. Chem. 246 (2000) 597–600. doi:10.1023/A:1006713618799.

[106] S. Chakravarty, V. Dureja, G. Bhattacharyya, S. Maity, S. Bhattacharjee, Removal of arsenic from groundwater using low cost ferruginous manganese ore, Water Res. 36

(2002) 625–632. doi:10.1016/S0043-1354(01)00234-2.

[107] Z. Gu, J. Fang, B. Deng, Preparation and evaluation of adsorbents for arsenic removal, Environ. Sci. Technol. 39 (2005) 3833–3843. doi:10.1021/es048179r.

[108] Q. Liu, H. Guo, Y. Li, H. Xiang, Acclimation of arsenic-resistant Fe(II)-oxidizing bacteria in aqueous environment, Int. Biodeterior. Biodegrad. 76 (2013) 86–91. doi:10.1016/j.ibiod.2012.06.018.

[109] K. Wu, R. Liu, T. Li, H. Liu, J. Peng, J. Qu, Removal of arsenic(III) from aqueous solution using a low-cost by-product in Fe-removal plants-Fe-based backwashing sludge, Chem. Eng. J. 226 (2013) 393–401. doi:10.1016/j.cej.2013.04.076.

[110] Y. Zhao, M. Huang, W. Wu, W. Jin, Synthesis of the cotton cellulose based Fe(III)-loaded adsorbent for arsenic(V) removal from drinking water, Desalination. 249 (2009) 1006–1011. doi:10.1016/j.desal.2009.09.015.

[111] S.K. Maji, Y.H. Kao, C.J. Wang, G.S. Lu, J.J. Wu, C.W. Liu, Fixed bed adsorption of As(III) on iron-oxide-coated natural rock (IOCNR) and application to real arsenic-bearing groundwater, Chem. Eng. J. 203 (2012) 285–293. doi:10.1016/j.cej.2012.07.033.

[112] I. Ali, New generation adsorbents for water treatment, Chem. Rev. 112 (2012) 5073–5091. doi:10.1021/cr300133d.

[113] S.R. Kanel, J.M. Greneche, H. Choi, Arsenic(V) removal from groundwater using nano scale zero-valent iron as a colloidal reactive barrier material, Environ. Sci. Technol. 40 (2006) 2045–2050. doi:10.1021/es0520924.

[114] J.F.W. Bowles, Iron Oxides in the Laboratory, 1992. doi:10.1180/minmag.1992.056.383.20.

[115] S. Zhang, X. yan Li, J.P. Chen, Preparation and evaluation of a magnetite-doped activated carbon fiber for enhanced arsenic removal, Carbon N. Y. 48 (2010) 60–67. doi:10.1016/j.carbon.2009.08.030.

[116] A.K. Mishra, S. Ramaprabhu, Magnetite decorated multiwalled carbon nanotube based supercapacitor for arsenic removal and desalination of seawater, J. Phys. Chem. C. 114 (2010) 2583–2590. doi:10.1021/jp911631w.

[117] R.C. Vaishya, S.K. Gupta, Modelling arsenic(III) adsorption from water by sulfate-modified iron oxide-coated sand (SMIOCS), J. Chem. Technol. Biotechnol. 78 (2003) 73–80. doi:10.1002/jctb.745.

[118] M.A. López-Leal, R. Cortés-Martínez, R. Alfaro-Cuevas-Villanueva, H.E. Martínez-Flores, C.D.J. Cortés-Penagos, Arsenate biosorption by iron-modified pine sawdust in batch system: kinetics and equilibrium studies, BioResources. 7 (2012). doi:10.15376/biores.7.2.1389-1404.

[119] Z. Li, J.S. Jean, W.T. Jiang, P.H. Chang, C.J. Chen, L. Liao, Removal of arsenic from water using Fe-exchanged natural zeolite, J. Hazard. Mater. 187 (2011) 318–323. doi:10.1016/j.jhazmat.2011.01.030.

[120] S. Addo Ntim, S. Mitra, Removal of trace arsenic to meet drinking water standards using iron oxide coated multiwall carbon nanotubes, J. Chem. Eng. Data. 56 (2011) 2077–2083. doi:10.1021/je1010664.

[121] Z. Veličković, G.D. Vuković, A.D. Marinković, M.S. Moldovan, A.A. Perić-Grujić, P.S. Uskoković, M.D. Ristić, Adsorption of arsenate on iron(III) oxide coated ethylenediamine functionalized multiwall carbon nanotubes, Chem. Eng. J. 181-182 (2012) 174–181. doi:10.1016/j.cej.2011.11.052.

214

[122] B.M. Jovanović, V.L. Vukašinović-Pešić, Lj. Rajaković, Enhanced arsenic sorption by hydrated iron(III) oxide-coated materials—mechanism and performances, Water Environ. Res. 83 (2011) 498–506. doi:http://dx.doi.org/10.2175/106143010X12851009156484.

[123] R. Cornell, U. Schwertmann, The iron oxides: Structure, properties, reactions, occurrences and uses, Wiley-VCH Verlag GmbH, 2003.

[124] H. Liu, T. Chen, R.L. Frost, An overview of the role of goethite surfaces in the environment, Chemosphere. 103 (2014) 1–11. doi:10.1016/j.chemosphere.2013.11.065.

[125] U. Schwertmann, R. Cornell, Iron Oxides in the Laboratory, Preparation and Characterization, 2nd ed., WILEY-VCH Verlag GmbH, 2000.

[126] R.J. Atkinson, A.M. Posner, J.P. Quirk, Adsorption of potential-determining ions at the ferric oxide-aqueous electrolyte interface, J. Phys. Chem. 71 (1967) 550–558. doi:10.1021/j100862a014.

[127] R. Strauss, G.W. Brümmer, N.J. Barrow, Effects of crystallinity of goethite: II. Rates of sorption and desorption of phosphate, Eur. J. Soil Sci. 48 (1997) 101–114. doi:10.1111/j.1365-2389.1997.tb00189.x.

[128] F.J. Hingston, R.J. Atkinson, A.M. Posner, J.P. Quirk, Specific adsorption of anions, Nature. 215 (1967) 1459–1461. doi:10.1038/2151459a0.

[129] F.J. Hingston, A.M. Pposner, J.P. Quirk, Adsorption of selenite by goethite, in: 1968: pp. 82–90. doi:10.1021/ba-1968-0079.ch008.

[130] K. Saeki, S. Matsumoto, Mechanisms of ligand exchange reactions involving selenite sorption on goethite labeled with oxygen-stable isotope, Commun. Soil Sci. Plant Anal. 29 (1998) 3061–3072. doi:10.1080/00103629809370176.

[131] R.P.J.J. Rietra, T. Hiemstra, W.H. van Riemsdijk, Comparison of selenate and sulfate adsorption on goethite, J. Colloid Interface Sci. 240 (2001) 384–390. doi:10.1006/jcis.2001.7650.

[132] S. Das, M. Jim Hendry, J. Essilfie-Dughan, Adsorption of selenate onto ferrihydrite, goethite, and lepidocrocite under neutral pH conditions, Appl. Geochemistry. 28 (2013) 185–193. doi:10.1016/j.apgeochem.2012.10.026.

[133] N.J. Barrow, A simple equation to describe sorption of anions by goethite, Eur. J. Soil Sci. 50 (1999) 151–155. doi:10.1046/j.1365-2389.1999.00203.x.

[134] B. Nowack, A.T. Stone, The influence of metal ions on the adsorption of phosphonates onto goethite, Environ. Sci. Technol. 33 (1999) 3627–3633. doi:10.1021/es9900860.

[135] B. Nowack, A.T. Stone, Competitive adsorption of phosphate and phosphonates onto goethite, Water Res. 40 (2006) 2201–2209. doi:10.1016/j.watres.2006.03.018.

[136] L. Li, R. Stanforth, Distinguishing adsorption and surface precipitation of phosphate on goethite (alpha-FeOOH)., J. Colloid Interface Sci. 230 (2000) 12–21. doi:10.1006/jcis.2000.7072.

[137] Y. Gao, A. Mucci, Individual and competitive adsorption of phosphate and arsenate on goethite in artificial seawater, Chem. Geol. 199 (2003) 91–109. doi:10.1016/S0009-2541(03)00119-0.

[138] Y. Gao, A. Mucci, Acid base reactions, phosphate and arsenate complexation, and their competitive adsorption at the surface of goethite in 0.7 M NaCl solution, Geochim. Cosmochim. Acta. 65 (2001) 2361–2378. doi:10.1016/S0016-7037(01)00589-0.

[139] K. Dideriksen, S.L.S. Stipp, The adsorption of glyphosate and phosphate to goethite: A molecular-scale atomic force microscopy study, Geochim. Cosmochim. Acta. 67 (2003)

3313–3327. doi:10.1016/S0016-7037(02)01369-8.

[140] A. Ler, R. Stanforth, Evidence for surface precipitation of phosphate on Gg, Environ. Sci. Technol. 37 (2003) 2694–2700. doi:10.1021/es020773i.

[141] A.L. Gimsing, O.K. Borggaard, P. Sestoft, Modeling the kinetics of the competitive adsorption and desorption of glyphosate and phosphate on goethite and gibbsite and in soils, Environ. Sci. Technol. 38 (2004) 1718–1722. doi:10.1021/es030572u.

[142] S.H. Lin, H.C. Kao, C.H. Cheng, R.S. Juang, An EXFAS study of the structures of copper and phosphate sorbed onto goethite, Colloids Surfaces A Physicochem. Eng. Asp. 234 (2004) 71–75. doi:10.1016/j.colsurfa.2003.12.005.

[143] K. Wang, B. Xing, Mutual effects of cadmium and phosphate on their adsorption and desorption by goethite, Environ. Pollut. 127 (2004) 13–20. doi:10.1016/S0269-7491(03)00262-8.

[144] J. Antelo, M. Avena, S. Fiol, R. López, F. Arce, Effects of pH and ionic strength on the adsorption of phosphate and arsenate at the goethite-water interface, J. Colloid Interface Sci. 285 (2005) 476–486. doi:10.1016/j.jcis.2004.12.032.

[145] R. Chitrakar, S. Tezuka, A. Sonoda, K. Sakane, K. Ooi, T. Hirotsu, Phosphate adsorption on synthetic goethite and akaganeite, J. Colloid Interface Sci. 298 (2006) 602–608. doi:10.1016/j.jcis.2005.12.054.

[146] T. Cheng, M.O. Barnett, E.E. Roden, J. Zhuang, Reactive transport of uranium(VI) and phosphate in a goethite-coated sand column: An experimental study, Chemosphere. 68 (2007) 1218–1223. doi:10.1016/j.chemosphere.2007.01.063.

[147] C. Luengo, M. Brigante, M. Avena, Adsorption kinetics of phosphate and arsenate on goethite. A comparative study, J. Colloid Interface Sci. 311 (2007) 354–360. doi:10.1016/j.jcis.2007.03.027.

[148] R. Rahnemaie, T. Hiemstra, W.H. van Riemsdijk, Carbonate adsorption on goethite in competition with phosphate, J. Colloid Interface Sci. 315 (2007) 415–425. doi:10.1016/j.jcis.2007.07.017.

[149] J. Kim, W. Li, B.L. Philips, C.P. Grey, Phosphate adsorption on the iron oxyhydroxides goethite (α-FeOOH), akaganeite (β-FeOOH), and lepidocrocite (γ-FeOOH): a 31P NMR Study, Energy Environ. Sci. 4 (2011) 4298. doi:10.1039/c1ee02093e.

[150] T. Hiemstra, Van Riemsdijk WH, Fluoride adsorption on goethite in relation to different types of surface sites., J. Colloid Interface Sci. 225 (2000) 94–104. doi:10.1006/jcis.1999.6697.

[151] F.J. Hingston, A.M. Posner, J.P. Quirk, Anion adsorption by goethite and gibbsite, J. Soil Sci. 23 (1972) 177–192. doi:10.1111/j.1365-2389.1972.tb01652.x.

[152] L. Sigg, W. Stumm, The interaction of anions and weak acids with the hydrous goethite (??-FeOOH) surface, Colloids and Surfaces. 2 (1981) 101–117. doi:10.1016/0166-6622(81)80001-7.

[153] J.S. Geelhoed, W.H. Van Riemsdijk, G.R. Findenegg, Effects of sulphate and ph on the plant-availability of phosphate adsorbed on goethite, Plant Soil. 197 (1997) 241–249. doi:10.1023/A:1004228715984.

[154] M. Kersten, N. Vlasova, Silicate adsorption by goethite at elevated temperatures, Chem. Geol. 262 (2009) 372–379. doi:10.1016/j.chemgeo.2009.02.002.

[155] P.R. Grossl, D.L. Sparks, Evaluation of contaminant ion adsorption/desorption on goethite using pressure jump relaxation kinetics, Geoderma. 67 (1995) 87–101. doi:10.1016/0016-

7061(95)00023-H.

[156] H. Abdel-Samad, P.R. Watson, An XPS study of the adsorption of chromate on goethite (α-FeOOH), Appl. Surf. Sci. 108 (1997) 371–377. doi:10.1016/S0169-4332(96)00609-5.

[157] S.A.-E. Fendorf M.J. AU3 - Grossl, P. AU4 - Sparks, D.L., Arsenate and chromate retention mechanisms on goethite. 1. Surface structure: RN - Environ. Sci. Technol., v. 31, p. 315-320., 31 (1997) 315–320.

[158] T. Hiemstra, R. Rahnemaie, W.H. Van Riemsdijk, Surface complexation of carbonate on goethite: IR spectroscopy, structure and charge distribution, J. Colloid Interface Sci. 278 (2004) 282–290. doi:10.1016/j.jcis.2004.06.014.

[159] H. Guo, Y. Ren, Q. Liu, K. Zhao, Y. Li, Enhancement of arsenic adsorption during mineral transformation from siderite to goethite: Mechanism and application, Environ. Sci. Technol. 47 (2013) 1009–1016. doi:10.1021/es303503m.

[160] J.T. Mayo, C. Yavuz, S. Yean, L. Cong, H. Shipley, W. Yu, J. Falkner, A. Kan, M. Tomson, V.L. Colvin, The effect of nanocrystalline magnetite size on arsenic removal, Sci. Technol. Adv. Mater. 8 (2007) 71–75. doi:10.1016/j.stam.2006.10.005.

[161] S. Yean, L. Cong, C.T. Yavuz, J.T. Mayo, W.W. Yu, A.T. Kan, V.L. Colvin, M.B. Tomson, Effect of magnetite particle size on adsorption and desorption of arsenite and arsenate, J. Mater. Res. 20 (2005) 3255–3264. doi:10.1557/jmr.2005.0403.

[162] J. Jönsson, D.M. Sherman, Sorption of As(III) and As(V) to siderite, green rust (fougerite) and magnetite: Implications for arsenic release in anoxic groundwaters, Chem. Geol. 255 (2008) 173–181. doi:10.1016/j.chemgeo.2008.06.036.

[163] W.H.R. H. G. Yuan, G. Kalfas, Journal of Macromolecular Science, 1991.

[164] E. Vivaldo-lima, P.E. Wood, A.E. Hamielec, A. Penlidis, An updated review on suspension polymerization, Ind. Eng. Chem. 36 (1997) 939–965. doi:S0888-5885(96)00361-2.

[165] R. Ashady, Colloid Polym. Sci., Colloid Polym. Sci. 270 (1992) 717.

[166] P.H.H. Arajo, C. Sayer, R. Giudici, J.G.R. Poo, Techniques for reducing residual monomer content in polymers: A review, Polym. Eng. Sci. 42 (2002) 1442–1468. doi:10.1002/pen.11043.

[167] P.F.O. C. H. Bamford, W. G. Barb, A. D. Jenkins, The Kinetics of vinyl polymerisation by radical mechanisms, Butterworth, London, 1957.

[168] B.W. Brooks, Basic aspects and recent developments in suspension polymerisation, Makromol. Chemie. Macromol. Symp. 35-36 (1990) 121–140. doi:10.1002/masy.19900350110.

[169] J.S.T. Bogunjoko, B.W. Brooks, Kinetics of free-radical polymerisation at high viscosities, Die Makromol. Chemie. 184 (1983) 1603–1621. doi:10.1002/macp.1983.021840808.

[170] N. Tefera, G. Weickert, R. Bloodworth, J. Schweer, Free radical suspension polymerization kinetics of styrene up to high conversion, Macromol. Chem. Phys. 195 (1994) 3067–3085. doi:10.1002/macp.1994.021950906.

[171] J.H. Duerksen, A.E. Hamielec, J.W. Hodgins, Polymer reactors and molecular weight distribution: Part I. Free radical polymerization in a continuous stirred-tank reactor, AIChE J. 13 (1967) 1081–1086. doi:10.1002/aic.690130609.

[172] L.I. Atanase, G. Riess, Poly(vinyl alcohol-co-vinyl acetate) complex formation with anionic surfactants particle size of nanogels and their disaggregation with sodium dodecyl

[173] S.U. Pickering, CXCVI.—Emulsions, J. Chem. Soc., Trans. 91 (1907) 2001–2021. doi:10.1039/CT9079102001.

[174] M.A. Malik, R. Mukhtar, S.A.R. Zaidi, S. Ahmed, M.A. Awan, Ion-exchange properties of 4-vinylpyridine-divinylbenzene-based anion exchangers for ferric chloride complex anions, React. Funct. Polym. 51 (2002) 117–120. doi:10.1016/S1381-5148(02)00036-6.

[175] R. Arshady, G.W. Kenner, A. Ledwith, Phenolic resins for solid-phase peptide synthesis: Copolymerization of styrene and p-acetoxystyrene, J. Polym. Sci. Polym. Chem. Ed. 12 (1974) 2017–2025. doi:10.1002/pol.1974.170120915.

[176] B. Brooks, Suspension polymerization processes, Chem. Eng. Technol. 33 (2010) 1737–1744. doi:10.1002/ceat.201000210.

[177] E.T. M. Munzer, Polymerization Processes, in: Wiley (Ed.), Polym. Process., Chapter 5, New York, 1977.

[178] M. Zerfa, B.W. Brooks, Vinylchloride dispersion with relation to suspension polymerisation, 51 (1996).

[179] F.S. Macintyre, D.C. Sherrington, Control of porous morphology in suspension polymerized poly(divinylbenzene) resins using oligomeric porogens, Macromolecules. 37 (2004) 7628–7636. doi:10.1021/ma0491053.

[180] D.E.Witenhafer. J. A. Davidson, Particle structure of suspension poly(vinyl chloride) and its origin in the polymerization process , J. Polym. Sci., Polym. Phys.Ed. 18 (1980) 51.

[181] M. Zerfa, B.W. Brooks, Drop coalescence processes in suspension polymerization of vinyl chloride, J. Appl. Polym. Sci. 60 (1996) 2077–2086. doi:10.1002/(SICI)1097-4628(19960620)60:12<2077::AID-APP5>3.0.CO;2-J.

[182] X. Ni, J.C. Johnstone, K.C. Symes, B.D. Grey, D.C. Bennett, Suspension polymerization of acrylamide in an oscillatory baffled reactor: From drops to particles, AIChE J. 47 (2001) 1746–1757. doi:10.1002/aic.690470807.

[183] S.C. qing MI Jing-yu, Advances of application of macroporous resin in study of traditional chinese herbs, Chinese Tradit. Pat. Med. 23. (2001) 914–917.

[184] Q.Z. and H.H.P.F. Zhaoyi Xu1, Applications of porous resin sorbents in industrial wastewater treatment and resource recovery, J. Chem. Inf. Model. (2002) 1–37. doi:10.1017/CBO9781107415324.004.

[185] J.C. and Z.H. Tu Pengfei, Application of macroporous adsorption resins to study and production of TCM new drugs, World Sci. Technol. Tradit. Chinese Med. 6 (2004) 22–28.

[186] C.B. Lin, The study of mscroporoud adsorption resin (MAR) on preparative, separation and purification of saikosaponius from the crude herbal extract, The Hong Kong Polytechnic University, 2006. www.lib.polyu.edu.nk.

[187] D.C. Sherrington, Preparation, structure and morphology of polymer supports, Chem. Commun. (1998) 2275–2286. doi:10.1039/a803757d.

[188] S.J. Drake, R.; Dunn, R.; Sherrington, D.C.; Thomson, Optimisation of polystyrene resin-supported pt catalysts in room temperature, solvent-less, oct-l-ene hydrosilylation using methyldichlorosilane, Comb. Chem. High Throughput Scr. 5 (2002) 201–209.

[189] P.D. Verweij, D.C. Sherrington, High-surface-area resins derived from 2,3-epoxypropyl methacrylate cross-linked with trimethylolpropane trimethacrylate, J. Mater. Chem. 1 (1991) 371. doi:10.1039/jm9910100371.

[190] O.M.J. Ortiz-Palacios, J. Cardoso, Production of macroporous resins for heavy-metal removal. I. Nonfunctionalized polymers, J. Appl. Polym. Sci. 107 (2008) 2203–2210. doi:10.1002/app.

[191] J.S. Park, C. Han, J.Y. Lee, S.D. Kim, J.S. Kim, J.H. Wee, Synthesis of extraction resin containing 2-ethylhexyl phosphonic acid mono-2-ethylhexyl ester and its performance for separation of rare earths (Gd, Tb), Sep. Purif. Technol. 43 (2005) 111–116. doi:10.1016/j.seppur.2004.10.007.

[192] Z.H. Lin, C.J. Guan, X.L. Feng, C.X. Zhao, Synthesis of macroreticular p-(ω-sulfonic-perfluoroalkylated)polystyrene ion-exchange resin and its application as solid acid catalyst, J. Mol. Catal. A Chem. 247 (2006) 19–26. doi:10.1016/j.molcata.2005.11.008.

[193] A.K. Hebb, K. Senoo, R. Bhat, A.I. Cooper, Structural control in porous cross-linked poly(methacrylate) monoliths using supercritical carbon dioxide as a "pressure-adjustable" porogenic solvent, Chem. Mater. 15 (2003) 2061–2069. doi:10.1021/cm020979i.

[194] C. Viklund, F. Svec, J.M.J. Fréchet, K. Irgum, Monolithic, "molded", porous materials with high flow characteristics for separations, catalysis, or solid-phase chemistry: control of porous properties during polymerization, Chem. Mater. 8 (1996) 744–750. doi:10.1021/cm950437j.

[195] M.H. Mohamed, L.D. Wilson, Porous copolymer resins: tuning pore structure and surface area with non reactive porogens, Nanomaterials. 2 (2012) 163–186. doi:10.3390/nano2020163.

[196] A.K. Nyhus, S. Hagen, A. Berge, Formation of the Porous Structure During the Polymerization of meta-Divinylbenzene and para- Divinylbenzene with Toluene and 2-Ethylhexanoic Acid (2-EHA) as Porogens, (2001) 7–9.

[197] M. Terada, R.H. Marchessault, Determination of solubility parameters for poly (3-hydroxyalkanoates), Int. J. Biol. Macromol. 25 (1999) 207–215.

[198] H. Deleuzel, X. Schultze, D.C. Sherrington, Porosity analysis of some poly(styrene/divinylbenzene)beads by nitrogen sorption and mercury intrusion porosimetry, Polym. Bull. 44 (2000) 179–186. doi:10.1007/s002890050590.

[199] D. Blondeau, M. Bigan, a. Ferreira, Experimental-design study of the influence of the polymerization conditions on the characteristics of copolymers used for liquid chromatography, Chromatographia. 51 (2000) 713–721. doi:10.1007/BF02505410.

[200] Q. Liu, L. Wang, A. Xiao, H. Yu, Q. Tan, J. Ding, G. Ren, Unexpected behavior of 1-chlorodecane as a novel porogen in the preparation of high-porosity poly(divinylbenzene) microspheres, J. Phys. Chem. C. 112 (2008) 13171–13174. doi:10.1021/jp8037329.

[201] A. Dufresne, Nanocellulose: From Nature to High Performance Tailored Materials, De Gruyter, Berlin, 2012.

[202] S. Arola, Biochemical modification and functionalization of nanocellulose surface, Aalto University School of Science, 2015.

[203] S.J. Eichhorn, A. Dufresne, M. Aranguren, N.E. Marcovich, J.R. Capadona, S.J. Rowan, C. Weder, W. Thielemans, M. Roman, S. Renneckar, W. Gindl, S. Veigel, J. Keckes, H. Yano, K. Abe, M. Nogi, A.N. Nakagaito, A. Mangalam, J. Simonsen, A.S. Benight, A. Bismarck, L.A. Berglund, T. Peijs, Review: Current international research into cellulose nanofibres and nanocomposites, 2010. doi:10.1007/s10853-009-3874-0.

[204] J.H. Kim, B.S. Shim, H.S. Kim, Y.J. Lee, S.K. Min, D. Jang, Z. Abas, J. Kim, Review of nanocellulose for sustainable future materials, Int. J. Precis. Eng. Manuf. - Green Technol.

219

2 (2015) 197–213. doi:10.1007/s40684-015-0024-9.

[205] D. Klemm, F. Kramer, S. Moritz, T. Lindström, M. Ankerfors, D. Gray, A. Dorris, Nanocelluloses: A new family of nature-based materials, Angew. Chemie - Int. Ed. 50 (2011) 5438–5466. doi:10.1002/anie.201001273.

[206] H.P.S. Abdul Khalil, A. H. Bhat, a. F. Ireana Yusra, Green composites from sustainable cellulose nanofibrils: A review, Carbohydr. Polym. 87 (2012) 963–979. doi:10.1016/j.carbpol.2011.08.078.

[207] N. Lin, J. Huang, A. Dufresne, Preparation, properties and applications of polysaccharide nanocrystals in advanced functional nanomaterials: a review., Nanoscale. 4 (2012) 3274–94. doi:10.1039/c2nr30260h.

[208] A. Dufresne, Cellulose-based composites and nanocomposites, Elsevier, 2008. doi:10.1016/B978-0-08-045316-3.00019-3.

[209] A. Dufresne, Nanocellulose: A new ageless bionanomaterial, Mater. Today. 16 (2013) 220–227. doi:10.1016/j.mattod.2013.06.004.

[210] Y. Habibi, L.A. Lucia, O.J. Rojas, Cellulose nanocrystals: Chemistry, self-assembly, and applications, Chem. Rev. 110 (2010) 3479–3500. doi:10.1021/cr900339w.

[211] Y. Habibi, Key advances in the chemical modification of nanocelluloses., Chem. Soc. Rev. 43 (2014) 1519–42. doi:10.1039/c3cs60204d.

[212] M.M. Reddy, S. Vivekanandhan, M. Misra, S.K. Bhatia, A.K. Mohanty, Biobased plastics and bionanocomposites: Current status and future opportunities, Prog. Polym. Sci. 38 (2013) 1653–1689. doi:10.1016/j.progpolymsci.2013.05.006.

[213] J.A. Sirviö, A. Kolehmainen, H. Liimatainen, J. Niinimäki, O.E.O. Hormi, Biocomposite cellulose-alginate films: promising packaging materials., Food Chem. 151 (2014) 343–51. doi:10.1016/j.foodchem.2013.11.037.

[214] V. Ojijo, S. Sinha Ray, Processing strategies in bionanocomposites, Prog. Polym. Sci. 38 (2013) 1543–1589. doi:10.1016/j.progpolymsci.2013.05.011.

[215] R.J. Moon, A. Martini, J. Nairn, J. Simonsen, J. Youngblood, Cellulose nanomaterials review: structure, properties and nanocomposites, 2011. doi:10.1039/c0cs00108b.

[216] M. Pääkkö, M. Ankerfors, H. Kosonen, A. Nykänen, S. Ahola, M. Österberg, J. Ruokolainen, J. Laine, P.T. Larsson, O. Ikkala, T. Lindström, Enzymatic hydrolysis combined with mechanical shearing and high-pressure homogenization for nanoscale cellulose fibrils and strong gels, Biomacromolecules. 8 (2007) 1934–1941. doi:10.1021/bm061215p.

[217] T.S. Anirudhan, J. Nima, S. Sandeep, V.R.N. Ratheesh, Development of an amino functionalized glycidylmethacrylate-grafted-titanium dioxide densified cellulose for the adsorptive removal of arsenic(V) from aqueous solutions, Chem. Eng. J. 209 (2012) 362–371. doi:10.1016/j.cej.2012.07.129.

[218] T.S. Anirudhan, J.R. Deepa, Binusreejayan, Synthesis and characterization of multi-carboxyl-functionalized nanocellulose/nanobentonite composite for the adsorption of uranium(VI) from aqueous solutions: Kinetic and equilibrium profiles, Chem. Eng. J. 273 (2015) 390–400. doi:10.1016/j.cej.2015.03.007.

[219] T.S. Anirudhan, S. Jalajamony, Cellulose-based anion exchanger with tertiary amine functionality for the extraction of arsenic(V) from aqueous media, J. Environ. Manage. 91 (2010) 2201–2207. doi:10.1016/j.jenvman.2010.05.019.

[220] A.M. Donia, A.A. Atia, F.I. Abouzayed, Preparation and characterization of nano-

magnetic cellulose with fast kinetic properties towards the adsorption of some metal ions, Chem. Eng. J. 191 (2012) 22–30. doi:10.1016/j.cej.2011.08.034.

[221] K. Singh, T.J.M. Sinha, S. Srivastava, Functionalized nanocrystalline cellulose: Smart biosorbent for decontamination of arsenic, Int. J. Miner. Process. 139 (2015) 51–63. doi:10.1016/j.minpro.2015.04.014.

[222] X. Sun, L. Yang, Q. Li, J. Zhao, X. Li, X. Wang, H. Liu, Amino-functionalized magnetic cellulose nanocomposite as adsorbent for removal of Cr(VI): Synthesis and adsorption studies, Chem. Eng. J. 241 (2014) 175–183. doi:10.1016/j.cej.2013.12.051.

[223] A.M. Yousif, O.F. Zaid, I.A. Ibrahim, Fast and selective adsorption of As(V) on prepared modified cellulose containing Cu(II) moieties, Arab. J. Chem. (2014) 2–10. doi:10.1016/j.arabjc.2015.02.004.

[224] I.D. Vukoje, E.S. Džunuzović, V. V. Vodnik, S. Dimitrijević, S.P. Ahrenkiel, J.M. Nedeljković, Synthesis, characterization, and antimicrobial activity of poly(GMA-co-EGDMA) polymer decorated with silver nanoparticles, J. Mater. Sci. 49 (2014) 6838–6844. doi:10.1007/s10853-014-8386-x.

[225] P. Lu, Y.-L. Hsieh, Preparation and properties of cellulose nanocrystals: Rods, spheres, and network, Carbohydr. Polym. 82 (2010) 329–336. doi:10.1016/j.carbpol.2010.04.073.

[226] N. Djordjević, A. Marinković, J. Nikolić, S. Drmanić, M. Rančić, D. Brković, P. Uskoković, A study of the barrier properties of polyethylene coated with nanocellulose/magnetite composite film, J. Serbian Chem. Soc. (2016) 19–19. doi:10.2298/JSC151217019D.

[227] M. Iqbal, N. Iqbal, I.A. Bhatti, N. Ahmad, M. Zahid, Response surface methodology application in optimization of cadmium adsorption by shoe waste: A good option of waste mitigation by waste, Ecol. Eng. 88 (2016) 265–275. doi:10.1016/j.ecoleng.2015.12.041.

[228] A. Witek-Krowiak, K. Chojnacka, D. Podstawczyk, A. Dawiec, K. Pokomeda, Application of response surface methodology and artificial neural network methods in modelling and optimization of biosorption process, Bioresour. Technol. 160 (2014) 150–160. doi:10.1016/j.biortech.2014.01.021.

[229] S.A. Jafari, S. Cheraghi, M. Mirbakhsh, R. Mirza, A. Maryamabadi, Employing response surface methodology for optimization of mercury bioremediation by vibrio parahaemolyticus PG02 in coastal sediments of bushehr, Iran, CLEAN − Soil, Air, Water. 43 (2014) n/a–n/a. doi:10.1002/clen.201300616.

[230] J.S. Markovski, D.D. Marković, V.R. Dokić, M. Mitrić, M.D. Ristić, A.E. Onjia, A.D. Marinković, Arsenate adsorption on waste eggshell modified by goethite, α-MnO$_2$ and goethite/α-MnO$_2$, Chem. Eng. J. 237 (2014) 430–442. doi:10.1016/j.cej.2013.10.031.

[231] J.S. Markovski, V. Crossed D Signokić, M. Milosavljević, M. Mitrić, A.A. Perić-Grujić, A.E. Onjia, A.D. Marinković, Ultrasonic assisted arsenate adsorption on solvothermally synthesized calcite modified by goethite, α-MnO$_2$ and goethite/α- MnO$_2$, Ultrason. Sonochem. 21 (2014) 790–801. doi:10.1016/j.ultsonch.2013.10.006.

[232] A. Badinand, A. Boucherle, C. Charbonnier, Bulletin de la Societe Chimique de France, 1958.

[233] G.D. Vuković, A.D. Marinković, S.D. Škapin, M.T. Ristić, R. Aleksić, A.A. Perić-Grujić, P.S. Uskoković, Removal of lead from water by amino modified multi-walled carbon nanotubes, Chem. Eng. J. 173 (2011) 855–865. doi:10.1016/j.cej.2011.08.036.

[234] E. Erdem, N. Karapinar, R. Donat, The removal of heavy metal cations by natural zeolites,

J. Colloid Interface Sci. 280 (2004) 309–314. doi:10.1016/j.jcis.2004.08.028.

[235] T. Karthikeyan, S. Rajgopal, L.R. Miranda, Chromium(VI) adsorption from aqueous solution by Hevea Brasilinesis sawdust activated carbon, J. Hazard. Mater. 124 (2005) 192–199. doi:10.1016/j.jhazmat.2005.05.003.

[236] J. March, Advanced organic chemistry: Reaction, mechanisms and structure, John Wiley & Sons Inc., New York, 1985.

[237] S. Vyazovkin, Computational aspects of kinetic analysis. Part C. The ICTAC Kinetics Project - The light at the end of the tunnel?, Thermochim. Acta. 355 (2000). doi:10.1016/S0040-6031(00)00445-7.

[238] P. Lakshmipathiraj, B.R. V Narasimhan, S. Prabhakar, G. Bhaskar Raju, Adsorption of arsenate on synthetic goethite from aqueous solutions., J. Hazard. Mater. 136 (2006) 281–7. doi:10.1016/j.jhazmat.2005.12.015.

[239] J. Gustafsson, Visual MINTEQ, Department of Land and Water Resource Engineering, Stockholm, 2006.

[240] G. Alberti, V. Amendola, M. Pesavento, R. Biesuz, Beyond the synthesis of novel solid phases: Review on modelling of sorption phenomena, Coord. Chem. Rev. 256 (2012) 28–45. doi:10.1016/j.ccr.2011.08.022.

[241] G.S. Bohart, E.Q. Adams, Some aspects of the behavior of charcoal with respect to chlorine, J. Am. Chem. Soc. 42 (1920) 523–544. doi:10.1021/ja01448a018.

[242] H.C. Thomas, Heterogeneous Ion Exchange in a Flowing System, J. Am. Chem. Soc. 66 (1944) 1664–1666. doi:10.1021/ja01238a017.

[243] Y.H. Yoon, J.H. Nelson, Application of gas adsorption kinetics I. A theoretical model for respirator cartridge service life, Am. Ind. Hyg. Assoc. J. 45 (1984) 509–516. doi:10.1080/15298668491400197.

[244] G. Yan, T. Viraraghavan, Heavy metal removal in a biosorption column by immobilized M. rouxii biomass, Bioresour. Technol. 78 (2001) 243–249. doi:10.1016/S0960-8524(01)00020-7.

[245] H. Sontheimer, J. Crittenden, S. Summers, Activated Carbon for Water Treatment, DVGW-Forschungsstelle, Engler-Bunte Institut, Karlsruhe, 1988.

[246] K.D. Hristovski, P.K. Westerhoff, J.C. Crittenden, L.W. Olson, Arsenate removal by nanostructured ZrO_2 spheres, Environ. Sci. Technol. 42 (2008) 3786–3790. doi:10.1021/es702952p.

[247] H.-S. Jung, D.-S. Moon, J.-K. Lee, Quantitative analysis and efficient surface modification of silica nanoparticles, J. Nanomater. 2012 (2012) 1–8. doi:10.1155/2012/593471.

[248] A. Durbetaki, Direct titration of oxirane oxygen with hydrogen bromide in acetic acid, Anal. Chem. 28 (1956) 5–6. doi:10.1021/ac60120a055.

[249] S.K. Milonjić, L.S. Čerović, D.M. Čokeša, S. Zec, The influence of cationic impurities in silica on its crystallization and point of zero charge, J. Colloid Interface Sci. 309 (2007) 155–159. doi:10.1016/j.jcis.2006.12.033.

[250] G. Athanasaki, L. Sherrill, K.D. Hristovski, The pore surface diffusion model as a tool for rapid screening of novel nanomaterial-enhanced hybrid ion-exchange media, Environ. Sci. Water Res. Technol. 1 (2015) 448–456. doi:10.1039/C5EW00108K.

[251] K. Hristovski, P. Westerhoff, T. Möller, P. Sylvester, W. Condit, H. Mash, Simultaneous removal of perchlorate and arsenate by ion-exchange media modified with nanostructured

iron (hydr)oxide, J. Hazard. Mater. 152 (2008) 397–406. doi:10.1016/j.jhazmat.2007.07.016.

[252] A.M. Cooper, K.D. Hristovski, T. Möller, P. Westerhoff, P. Sylvester, The effect of carbon type on arsenic and trichloroethylene removal capabilities of iron (hydr)oxide nanoparticle-impregnated granulated activated carbons, J. Hazard. Mater. 183 (2010) 381–388. doi:10.1016/j.jhazmat.2010.07.036.

[253] D. Yan, D.D. Gang, N. Zhang, L. Lin, Adsorptive selenite removal using iron-coated gac: modeling selenite breakthrough with the pore surface diffusion model, J. Environ. Eng. 139 (2013) 213–219. doi:10.1061/(ASCE)EE.1943-7870.0000633.

[254] E. Smith, Modeling activated carbon adsorption of target organic compounds from leachate-contaminated groundwaters, Environ. Sci. & Technol. 22 (1988) 313–321.

[255] W. Yuan, Y. Cai, Y. Chen, X. Hong, Z. Liu, Porous microsphere and its applications, Int. J. Nanomedicine. (2013) 1111. doi:10.2147/IJN.S41271.

[256] J. Park, Y.-H. Kim, H.-J. Yoon, B.-H. Jun, Y.-S. Lee, Preparation of pore size controllable macroporous polymer beads, J. Ind. Eng. Chem. 17 (2011) 794–798. doi:10.1016/j.jiec.2011.05.023.

[257] U.S. Rochelle M. Cornell, The iron oxides: Structure, properties, reactions, occurrences and uses, 2nd, Completely Revised and Extended Edition, 2006.

[258] G. Zhang, H. Liu, R. Liu, J. Qu, Adsorption behavior and mechanism of arsenate at Fe-Mn binary oxide/water interface, J. Hazard. Mater. 168 (2009) 820–825. doi:10.1016/j.jhazmat.2009.02.137.

[259] M. Ciopec, A. Negrea, L. Lupa, C.M. Davidescu, P. Negrea, Studies regarding As(V) adsorption from underground water by Fe-XAD8-DEHPA impregnated resin. Equilibrium sorption and fixed-bed column tests, Molecules. 19 (2014) 16082–16101. doi:10.3390/molecules191016082.

[260] P.R. Grossl, M. Eick, D.L. Sparks, S. Goldberg, C.C. Ainsworth, Kinetic evaluation using a pressure-jump relaxation technique, Environ. Sci. Technol. 31 (1997) 321–326. doi:10.1021/es950654l.

[261] N. Ben Issa, V.N. Rajaković-Ognjanović, B.M. Jovanović, L. V. Rajaković, Determination of inorganic arsenic species in natural waters-Benefits of separation and preconcentration on ion exchange and hybrid resins, Anal. Chim. Acta. 673 (2010) 185–193. doi:10.1016/j.aca.2010.05.027.

[262] G.-S. Zhang, J.-H. Qu, H.-J. Liu, R.-P. Liu, G.-T. Li, Removal mechanism of As(III) by a novel fe−mn binary oxide adsorbent: Oxidation and sorption, environ. Sci. Technol. 41 (2007) 4613–4619. doi:10.1021/es063010u.

[263] N. Ben Issa, V.N. Rajaković-Ognjanović, A.D. Marinković, L. V. Rajaković, Separation and determination of arsenic species in water by selective exchange and hybrid resins, Anal. Chim. Acta. 706 (2011) 191–198. doi:10.1016/j.aca.2011.08.015.

[264] M.M. Haring, The Theory of Rate Processes (Glasstone, Samuel; Laidler, Keith J.; Eyring, Henry), J. Chem. Educ. 19 (1942) 249. doi:10.1021/ed019p249.1.

[265] J.C.M. W.J. Weber Jr., Kinetics of adsorption on carbon from solution, J. Sanit. Eng. Div. 89 (1963) 31–59.

[266] Y. Jia, R. Wang, A.G. Fane, Atrazine adsorption from aqueous solution using powdered activated carbon - Improved mass transfer by air bubbling agitation, Chem. Eng. J. 116 (2006) 53–59. doi:10.1016/j.cej.2005.10.014.

[267] M. Šljivić Ivanović, I. Smičiklas, S. Pejanović, Analysis and comparison of mass transfer phenomena related to Cu^{2+} sorption by hydroxyapatite and zeolite, Chem. Eng. J. 223 (2013) 833–843. doi:10.1016/j.cej.2013.03.034.

[268] D. Reichenberg, Properties of ion-exchange resins in relation to their structure. III. Kinetics of exchange, J. Am. Chem. Soc. 75 (1953) 589–597. doi:10.1021/ja01099a022.

[269] A. Goswami, P.K. Raul, M.K. Purkait, Arsenic adsorption using copper (II) oxide nanoparticles, Chem. Eng. Res. Des. 90 (2012) 1387–1396. doi:10.1016/j.cherd.2011.12.006.

[270] U.B. A.Ö.A. Tuna, E. Özdemir, E.B. ŞimŞek, Removal of As(V) from aqueous solution by activated carbon-based hybrid adsorbents: Impact of experimental conditions, Chem. Eng. J. 223 (2013) 116–128. doi:10.1016/j.cej.2013.02.096.

[271] J.C. Zuo, S.R. Tong, X.L. Yu, L.Y. Wu, C.Y. Cao, M.F. Ge, W.G. Song, Fe^{3+} and amino functioned mesoporous silica: Preparation, structural analysis and arsenic adsorption, J. Hazard. Mater. 235-236 (2012) 336–342. doi:10.1016/j.jhazmat.2012.08.009.

[272] G. Zhang, Z. Ren, X. Zhang, J. Chen, Nanostructured iron(III)-copper(II) binary oxide: A novel adsorbent for enhanced arsenic removal from aqueous solutions, Water Res. 47 (2013) 4022–4031. doi:10.1016/j.watres.2012.11.059.

[273] W. Tang, Y. Su, Q. Li, S. Gao, J.K. Shang, Superparamagnetic magnesium ferrite nanoadsorbent for effective arsenic (III,V) removal and easy magnetic separation, Water Res. 47 (2013) 3624–3634. doi:10.1016/j.watres.2013.04.023.

[274] Z. Ren, G. Zhang, J. Paul Chen, Adsorptive removal of arsenic from water by an iron-zirconium binary oxide adsorbent, J. Colloid Interface Sci. 358 (2011) 230–237. doi:10.1016/j.jcis.2011.01.013.

[275] X. Dou, D. Mohan, C.U. Pittman, Arsenate adsorption on three types of granular schwertmannite, Water Res. 47 (2013) 2938–2948. doi:10.1016/j.watres.2013.01.035.

[276] J. Jachuła, Z. Hubicki, Removal of Cr(VI) and As(V) ions from aqueous solutions by polyacrylate and polystyrene anion exchange resins, Appl. Water Sci. 3 (2013) 653–664. doi:10.1007/s13201-013-0110-5.

[277] H. Matsunaga, T. Yokoyama, R.J. Eldridge, B.A. Bolto, Adsorption characteristics of arsenic(III) and arsenic(V) on iron(III)-loaded chelating resin having lysine-Nα,Nα-diacetic acid moiety, React. Funct. Polym. 29 (1996) 167–174. doi:10.1016/1381-5148(96)00041-7.

[278] V. Lenoble, C. Chabroullet, R. al Shukry, B. Serpaud, V. Deluchat, J.-C. Bollinger, Dynamic arsenic removal on a MnO_2-loaded resin., J. Colloid Interface Sci. 280 (2004) 62–7. doi:10.1016/j.jcis.2004.07.034.

[279] Z. He, S. Tian, P. Ning, Adsorption of arsenate and arsenite from aqueous solutions by cerium-loaded cation exchange resin, J. Rare Earths. 30 (2012) 563–572. doi:10.1016/S1002-0721(12)60092-1.

[280] C. Li, W. Xu, D. Jia, X. Liu, Removal of Arsenic from Drinking Water by Using the Zr-Loaded Resin, J. Chem. Eng. Data. 58 (2013) 427–435. doi:10.1021/je301148t.

[281] T. Balaji, T. Yokoyama, H. Matsunaga, Adsorption and removal of As(V) and As(III) using Zr-loaded lysine diacetic acid chelating resin, Chemosphere. 59 (2005) 1169–1174. doi:10.1016/j.chemosphere.2004.12.007.

[282] J. Haron, W. Zin, W. Yunus, W.C. Tan, A. Kassim, Sorption removal of arsenic (V) by sn-loaded chelating resin poly (hydroxamic) acid, J. Ion Exch. 18 (2007) 240–245.

[283] W. Shao, X. Li, Q. Cao, F. Luo, J. Li, Y. Du, Adsorption of arsenate and arsenite anions from aqueous medium by using metal(III)-loaded amberlite resins, Hydrometallurgy. 91 (2008) 138–143. doi:10.1016/j.hydromet.2008.01.005.

[284] L. Dambies, R. Salinaro, S.D. Alexandratos, Immobilized *N*-Methyl- d -glucamine as an arsenate-selective resin, Environ. Sci. Technol. 38 (2004) 6139–6146. doi:10.1021/es040312s.

[285] A.M. Donia, A.A. Atia, D.H. Mabrouk, Fast kinetic and efficient removal of As(V) from aqueous solution using anion exchange resins, J. Hazard. Mater. 191 (2011) 1–7. doi:10.1016/j.jhazmat.2011.01.056.

[286] Lanxess, Product information, http://www.lenntech.com/-Data-sheets/Lewatit-FO-36-L.pdf, Arsenic separation from ground water using Lewatit FO 36 Ion Exchange/Iron Oxide Hybrid System, 2011., (2011) 1–5.

[287] G. Karthikeyan, K. Anbalagan, N.M. Andal, Adsorption dynamics and equilibrium studies of Zn (II) onto chitosan, J. Chem. Sci. 116 (2004) 119–127. doi:10.1007/BF02708205.

[288] A. Maiti, J.K. Basu, S. De, Experimental and kinetic modeling of As(V) and As(III) adsorption on treated laterite using synthetic and contaminated groundwater: Effects of phosphate, silicate and carbonate ions, Chem. Eng. J. 191 (2012) 1–12. doi:10.1016/j.cej.2010.01.031.

[289] M. Stachowicz, T. Hiemstra, W.H. van Riemsdijk, Multi-competitive interaction of As(III) and As(V) oxyanions with Ca^{2+}, Mg^{2+}, PO_3^{-4}, and CO_2^{-3} ions on goethite, J. Colloid Interface Sci. 320 (2008) 400–414. doi:10.1016/j.jcis.2008.01.007.

[290] H. Liu, T. Chen, J. Chang, X. Zou, R.L. Frost, The effect of hydroxyl groups and surface area of hematite derived from annealing goethite for phosphate removal, J. Colloid Interface Sci. 398 (2013) 88–94. doi:10.1016/j.jcis.2013.02.016.

[291] S. Goldberg, C.T. Johnston, Mechanisms of arsenic adsorption on amorphous oxides evaluated using macroscopic measurements, Vibrational Spectroscopy, and Surface Complexation Modeling, J. Colloid Interface Sci. 234 (2001) 204–216. doi:http://dx.doi.org/10.1006/jcis.2000.7295.

[292] M.R. Awual, A. Jyo, S.A. El-Safty, M. Tamada, N. Seko, A weak-base fibrous anion exchanger effective for rapid phosphate removal from water, J. Hazard. Mater. 188 (2011) 164–171. doi:10.1016/j.jhazmat.2011.01.092.

[293] M.R. Awual, A. Jyo, T. Ihara, N. Seko, M. Tamada, K.T. Lim, Enhanced trace phosphate removal from water by zirconium(IV) loaded fibrous adsorbent, Water Res. 45 (2011) 4592–4600. doi:10.1016/j.watres.2011.06.009.

[294] M.R. Awual, A. Jyo, Assessing of phosphorus removal by polymeric anion exchangers, Desalination. 281 (2011) 111–117. doi:10.1016/j.desal.2011.07.047.

[295] A. Ghosh, S. Chakrabarti, U.C. Ghosh, Fixed-bed column performance of Mn-incorporated iron(III) oxide nanoparticle agglomerates on As(III) removal from the spiked groundwater in lab bench scale, Chem. Eng. J. 248 (2014) 18–26. doi:10.1016/j.cej.2014.03.010.

[296] P. Rietkerk, Master Thesis, University of California, Davis, 2007, http://small-watersystems.ucdavis.edu/researchprojects/documents/arsenic_review_11-07.pdf,.

[297] J.A. Baig, T.G. Kazi, A.Q. Shah, G.A. Kandhro, H.I. Afridi, S. Khan, N.F. Kolachi, Biosorption studies on powder of stem of Acacia nilotica: Removal of arsenic from surface water, J. Hazard. Mater. 178 (2010) 941–948. doi:10.1016/j.jhazmat.2010.02.028.

[298] S. Wang, X. Zhao, On the potential of biological treatment for arsenic contaminated soils and groundwater, J. Environ. Manage. 90 (2009) 2367–2376. doi:10.1016/j.jenvman.2009.02.001.

[299] D. Sud, G. Mahajan, M.P. Kaur, Agricultural waste material as potential adsorbent for sequestering heavy metal ions from aqueous solutions - A review, Bioresour. Technol. 99 (2008) 6017–6027. doi:10.1016/j.biortech.2007.11.064.

[300] A. Demirbas, Heavy metal adsorption onto agro-based waste materials: A review, J. Hazard. Mater. 157 (2008) 220–229. doi:10.1016/j.jhazmat.2008.01.024.

[301] T.A. Kurniawan, G.Y.S. Chan, W. hung Lo, S. Babel, Comparisons of low-cost adsorbents for treating wastewaters laden with heavy metals, Sci. Total Environ. 366 (2006) 409–426. doi:10.1016/j.scitotenv.2005.10.001.

[302] L.D. J. Giménes, M Martinés, J. de Pablo, M. Rovira, Arsenic sorption onto natural hematite, magnetite, and goethite, J. Hazard. Mater. 141 (2007) 575–580. doi:10.1016/j.jhazmat.2006.07.020.

[303] H.-H. Cho, B.A. Smith, J.D. Wnuk, D.H. Fairbrother, W.P. Ball, Influence of surface oxides on the adsorption of naphthalene onto multiwalled carbon nanotubes, Environ. Sci. Technol. 42 (2008) 2899–2905. doi:10.1021/es702363e.

[304] T. Vaughan, C.W. Seo, W.E. Marshall, Removal of selected metal ions from aqueous solution using modi ® ed corncobs, J.Bioresource Technol. 78 (2001) 133–139. doi:Doi: 10.1016/s0960-8524(01)00007-4.

[305] Z. Reddad, C. Gerente, Y. Andres, P. Le Cloirec, Adsorption of several metal ions onto a low-cost biosorbent: Kinetic and equilibrium studies, Environ. Sci. Technol. 36 (2002) 2067–2073. doi:10.1021/es0102989.

[306] Engineering Bulletin, PUROLITE® ArsenXnp, Available from: http://50.244.15.10/techlib/Purolite/ArsenXnp.pdf., (n.d.).

[307] S.E. Cabaniss, Forward modeling of metal complexation by NOM: II. Prediction of binding site properties, Environ. Sci. Technol. 45 (2011) 3202–3209. doi:10.1021/es102408w.

[308] K. Taleb, J. Markovski, M. Milosavljević, M. Marinović-Cincović, J. Rusmirović, M. Ristić, A. Marinković, Efficient arsenic removal by cross-linked macroporous polymer impregnated with hydrous iron oxide: Material performance, Chem. Eng. J. 279 (2015) 66–78. doi:10.1016/j.cej.2015.04.147.

[309] G.D. Vuković, A.D. Marinković, M. Čolić, M.D. Ristić, R. Aleksić, A.A. Perić-Grujić, P.S. Uskoković, Removal of cadmium from aqueous solutions by oxidized and ethylenediamine-functionalized multi-walled carbon nanotubes, Chem. Eng. J. 157 (2010) 238–248. doi:10.1016/j.cej.2009.11.026.

[310] M.A. Karimi, M. Kafi, Removal, preconcentration and determination of Ni(II) from different environmental samples using modified magnetite nanoparticles prior to flame atomic absorption spectrometry, Arab. J. Chem. 8 (2015) 812–820. doi:10.1016/j.arabjc.2013.05.018.

[311] H.E. S. Glasston, K.J. Laidler, The Theory of Rate Processes, McGraw-Hill, New York, 1941.

[312] S. Lin, Heavy metal removal from water by sorption using surfactant-modified montmorillonite, J. Hazard. Mater. 92 (2002) 315–326. doi:10.1016/S0304-3894(02)00026-2.

[313] Y. Peng, D.J. Gardner, Y. Han, A. Kiziltas, Z. Cai, M.A. Tshabalala, Influence of drying method on the material properties of nanocellulose I: Thermostability and crystallinity, Cellulose. 20 (2013) 2379–2392. doi:10.1007/s10570-013-0019-z.

[314] M. Szymańska-Chargot, J. Cybulska, A. Zdunek, Sensing the structural differences in cellulose from apple and bacterial cell wall materials by Raman and FT-IR Spectroscopy, Sensors. 11 (2011) 5543–5560. doi:10.3390/s110605543.

[315] Ž. Gabelica, Vibrational studies of metal-ethylenediamine thiosulfates-I. Infrared and Raman spectra of the tris-ethylenediamine thiosulfates $M^{II}(en)_3S_2O_3(M^{II}$=Zn, Cd, Fe,Ni, Co, Mn) and some of their N-deuterated analogues, Spectrochica Acta. 32 (1976) 327–336.

[316] K. Schenzel, S. Fischer, E. Brendler, New method for determining the degree of cellulose I crystallinity by means of FT Raman spectroscopy, Cellulose. 12 (2005) 223–231. doi:10.1007/s10570-004-3885-6.

[317] J.H. Wiley, R.H. Atalla, Band assignments in the raman spectra of celluloses, Carbohydr. Res. 160 (1987) 113–129. doi:10.1016/0008-6215(87)80306-3.

[318] K. Schenzel, S. Fischer, NIR FT Raman spectroscopy - A rapid analytical tool for detecting the transformation of cellulose polymorphs, Cellulose. 8 (2001) 49–57. doi:10.1023/A:1016616920539.

[319] K. Zhang, A. Feldner, S. Fischer, FT Raman spectroscopic investigation of cellulose acetate, Cellulose. 18 (2011) 995–1003. doi:10.1007/s10570-011-9545-8.

[320] O.N. Shebanova, P. Lazor, Raman spectroscopic study of magnetite ($FeFe_2O_4$): A new assignment for the vibrational spectrum, J. Solid State Chem. 174 (2003) 424–430. doi:10.1016/S0022-4596(03)00294-9.

[321] G. Socrates, Infrared and Raman characteristic group frequencies: Tables and Charts, John Wiley & Sons, 2004.

[322] C.-H. Liu, Y.-H. Chuang, T.-Y. Chen, Y. Tian, H. Li, M.-K. Wang, W. Zhang, Mechanism of arsenic adsorption on magnetite nanoparticles from water: thermodynamic and spectroscopic studies, Environ. Sci. Technol. 49 (2015) 7726–7734. doi:10.1021/acs.est.5b00381.

[323] S. Dale, J. Markovski, K. Hristovski, Modeling packed bed sorbent systems with the Pore Surface Diffusion Model: Evidence of facilitated surface diffusion of arsenate in nano-metal (hydr)oxide hybrid ion exchange media, Sci. Tot. Enviro. 1 (2016) 965–970. doi 10.1016/j.scitotenv.2015.11.176.

[324] J.D. Sewry, M.E. Brown, "' Model-free '" kinetic analysis ?, 390 (2002) 217–225.

[325] A.K. Galwey, Eradicating erroneous Arrhenius arithmetic, Thermochim. Acta. 399 (2003) 1–29. doi:10.1016/S0040-6031(02)00465-3.

[326] S. Lin, D. Lu, Z. Liu, Removal of arsenic contaminants with magnetic γ-Fe_2O_3 nanoparticles, Chem. Eng. J. 211-212 (2012) 46–52. doi:10.1016/j.cej.2012.09.018.

[327] B. An, Q. Liang, D. Zhao, Removal of arsenic(V) from spent ion exchange brine using a new class of starch-bridged magnetite nanoparticles, Water Res. 45 (2011) 1961–1972. doi:10.1016/j.watres.2011.01.004.

[328] S. Hokkanen, E. Repo, S. Lou, M. Sillanpää, Removal of arsenic(V) by magnetic nanoparticle activated microfibrillated cellulose, Chem. Eng. J. 260 (2015) 886–894. doi:10.1016/j.cej.2014.08.093.

[329] Y. Tian, M. Wu, R. Liu, D. Wang, X. Lin, W. Liu, L. Ma, Y. Li, Y. Huang, Modified

native cellulose fibers-A novel efficient adsorbent for both fluoride and arsenic, J. Hazard. Mater. 185 (2011) 93–100. doi:10.1016/j.jhazmat.2010.09.001.

[330] X. Yu, S. Tong, M. Ge, L. Wu, J. Zuo, C. Cao, W. Song, Synthesis and characterization of multi-amino-functionalized cellulose for arsenic adsorption, Carbohydr. Polym. 92 (2013) 380–387. doi:10.1016/j.carbpol.2012.09.050.

BIOGRAPHY

Khaled Ahmed Taleb je rođen 7.10.1970. godine u Tripoliju, Libija, gde je završio osnovno obrazovanje. Osnovne studije na Fakultetu tehničkih nauka, Univerziteta Tripoli, upisao je 1994/1995. Diplomski rad pod nazivom "*Cementation factor*" odbranio je 2004/2005 godine na katedri za Hemiju, Fakultet za inženjerstvo, Univerzitet u Tripoliju. Magistarske studije je upisao 2004/2005 godine na Tehnološko-metalurškom fakultetu Univerziteta u Beogradu. Magistarsku tezu pod naslovom „Copper(II)-*N*-(n-alkyl)salycilaldimine chelates as additives for composite materials" odbranio je 2005. godine na Tehnološko-metalurškom fakultetu Univerziteta u Beogradu. Školske 2013/14 započeo je izradu doktorske disertacije na Tehnološko-metalurškom fakultetu Univerziteta u Beogradu, studijski program Hemija i hemijska tehnologija. Oblast naučno-istraživačkog rada Khaled Taleba obuhvata sintezu, karakterizaciju i ispitivanje svojstava novih adsorbenata za uklanjanje arsena iz vode. Khaled Taleb je do sada objavio dva rada sa SCI liste. Osim toga, Khaled Taleb govori engleski jezik, poznaje rad na računaru, kao i na instrumentima koji se koriste za karakterizaciju sintetisanih adosrbenata (FTIR, Raman, XRD, SEM, TEM, BET i određivanja površinskih svojstava materijala).

Lične informacije:
Ime i prezime: Khaled Ahmed Ali Taleb
Nacionalnost: Libija
Pasoš broj: LCKG7PNJ
Mesto i datum rodjenja: Tripoli, 07.11.1970
Mesto stanovanja: Tripoli – Libya
Mesto stanovanja u Srbiji:
Mobilni: 0612502663
E-mail: khaled_taleb1970@yahoo.com

Personal Information:
Full Name: Khaled Ahmed Ali Taleb
The Nationality: Libyan
Passport Number: LCKG7PNJ
Place & date of birth: Tripoli, 07.11.1970
Residence Place: Tripoli – Libya
Residence Place in Serbia:
Mobile: 0612502663
E-mail : khaled_taleb1970@yahoo.com

Stečeno naučno-istraživačko iskustvo

Khaled Taleb je koautor 3 rada objavljena u časopisima međunarodnog značaja (M21 – 1 rad, M23 – 1 rad i jedan rad u međunarodnom časopisu koji nije na SCI listi). Iz oblasti istraživanja kojoj pripada predložena tema doktorske disertacije, kandidat je autor 2 rada M20 kategorije.

Spisak objavljenih radova i saopštenja

__Radovi objavljeni u časopisima međunarodnog značaja – M20__

Rad objavljen u vrhunskom međunarodnom časopisu - M21

1.**TalebK**., Markovski J., Milosavljević M., Marinović-Cincović M., Rusmirović J., Ristić M., Marinković A.: Efficient arsenic removal by cross-linked macroporous polymer impregnated with hydrous iron oxide: Material performance, *Chemical Engineering Journal*, vol. 279, 2015, pp. 66–78; ISSN: 1385-8947 (IF=4.321); doi:10.1016/j.cej.2015.04.147

Rad objavljen u međunarodnom časopisu - M23

1. **Taleb K. A**., Rusmirović J. D., Rančić M.P., Nikolić J.B., Drmanić S.Ž., Veličković Z.S., Marinković A.D., Efficient pollutants removal by amino modified nanocellulose impregnated with iron oxide, *Journal of the Serbian Chemical Society*, (2016), doi: 10.2298/JSC160529063T

Predavanje po pozivu na međunarodnom skupu štampano u izvodu - M32

1. Markovski J., **Taleb K.**, Rančić M., Marinković A.: *Ultrasonically enhanced synthesis and adsorption/desorption properties of novel micro-nano structured cellulose based material for arsenate removal*, Ultrasonics 2014,Caparica,Portugal, 2014, pp.122,ISBN 978-989-98793-1-7.

2. **Taleb, K.**, Markovski, J., Hristovski K.D., Rajaković-Ognjanović, V.N., Marinković, A.: *Goethite nanoparticles impregnated cross-linked macroporous polymer for arsenic removal: full-scale system modeling*,250AmericanChemicalSociety National Meeting, Boston, August 17, 2015.

Radovi objavljeni u časopisisma međunarodnog značaja (nije na SCI listi)

1. **Taleb K.**, Markovski J., Hristovski K.D., Rajaković-Ognjanović V.N., Onjia A., Marinković A., Aminated glycidyl methacrylates as a support media for goethite nanoparticle enabled hybrid sorbents for arsenic removal: From copolymer synthesis to full-scale system modeling, *Resource-Efficient Technologies* (2016), http://dx.doi.org/10.1016/j.reffit.2016.04.002

Прилог 1.

Изјава о ауторству

Потписани Khaled Ahmed Ali Taleb

Број индекса

Изјављујем

да је докторска дисертација под насловом

Primena makroporoznih smola i materijala na bazi celuloze modifikovanih oksidima gvožđa za uklanjanje arsena

Application of macroporous resin and cellulose based materials modified with iron oxides for arsenic removal

- резултат сопственог истраживачког рада,

- да предложена дисертација у целини ни у деловима није била предложена за добијање било које дипломе према студијским програмима других високошколских установа,

- да су резултати коректно наведени и

- да нисам кршио/ла ауторска права и користио интелектуалну својину других лица.

Потпис докторанда

У Београду, 13.06.2016. године

_____

Прилог 2.

Изјава о истоветности штампане и електронске верзије докторског рада

Име и презиме аутора Khaled Ahmed Ali Taleb

Број индекса

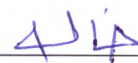Студијски програм   Хемија и хемијска технологија

Наслов рада   Primena makroporoznih smola i materijala na bazi celuloze modifikovanih oksidima gvožđa za uklanjanje arsena

Application of macroporous resin and cellulose based materials modified with iron oxides for arsenic removal

Ментор др АлександарМаринковић, доцент

Потписани Khaled Ahmed Ali Taleb

Изјављујем да је штампана верзија мог докторског рада истоветна електронској верзији коју сам предао/ла за објављивање на порталу **Дигиталног репозиторијума Универзитета у Београду.**

Дозвољавам да се објаве моји лични подаци везани за добијање академског звања доктора наука, као што су име и презиме, година и место рођења и датум одбране рада.

Ови лични подаци могу се објавити на мрежним страницама дигиталне библиотеке, у електронском каталогу и у публикацијама Универзитета у Београду.

<div align="right">

Потпис докторанда

</div>

У Београду, 13.06.2016. године

Прилог 3.

Изјава о коришћењу

Овлашћујем Универзитетску библиотеку „Светозар Марковић" да у Дигитални репозиторијум Универзитета у Београду унесе моју докторску дисертацију под насловом:

Primena makroporoznih smola i materijala na bazi celuloze modifikovanih oksidima gvožđa za uklanjanje arsena

Application of macroporous resin and cellulose based materials modified with iron oxides for arsenic removal

која је моје ауторско дело.

Дисертацију са свим прилозима предао/ла сам у електронском формату погодном за трајно архивирање.

Моју докторску дисертацију похрањену у Дигитални репозиторијум Универзитета у Београду могу да користе сви који поштују одредбе садржане у одабраном типу лиценце Креативне заједнице (CreativeCommons) за коју сам се одлучио/ла.

1. Ауторство

2. Ауторство - некомерцијално

3. Ауторство – некомерцијално – без прераде

4. Ауторство – некомерцијално – делити под истим условима

5. Ауторство – без прераде

6. Ауторство – делити под истим условима

(Молимо да заокружите само једну од шест понуђених лиценци, кратак опис лиценци дат је на полеђини листа).

<div align="right">

Потпис докторанда

</div>

У Београду, 13.06.2016. године

1. Ауторство - Дозвољавате умножавање, дистрибуцију и јавно саопштавање дела, и прераде, ако се наведе име аутора на начин одређен од стране аутора или даваоца лиценце, чак и у комерцијалне сврхе. Ово је најслободнија од свих лиценци.

2. Ауторство – некомерцијално. Дозвољавате умножавање, дистрибуцију и јавно саопштавање дела, и прераде, ако се наведе име аутора на начин одређен од стране аутора или даваоца лиценце. Ова лиценца не дозвољава комерцијалну употребу дела.

3. Ауторство - некомерцијално – без прераде. Дозвољавате умножавање, дистрибуцију и јавно саопштавање дела, без промена, преобликовања или употребе дела у свом делу, ако се наведе име аутора на начин одређен од стране аутора или даваоца лиценце. Ова лиценца не дозвољава комерцијалну употребу дела. У односу на све остале лиценце, овом лиценцом се ограничава највећи обим права коришћења дела.

4. Ауторство - некомерцијално – делити под истим условима. Дозвољавате умножавање, дистрибуцију и јавно саопштавање дела, и прераде, ако се наведе име аутора на начин одређен од стране аутора или даваоца лиценце и ако се прерада дистрибуира под истим или сличном лиценцом. Ова лиценца не дозвољава комерцијалну употребу дела и прерада.

5. Ауторство – без прераде. Дозвољавате умножавање, дистрибуцију и јавно саопштавање дела, без промена, преобликовања или употребе дела у свом делу, ако се наведе име аутора на начин одређен од стране аутора или даваоца лиценце. Ова лиценца дозвољава комерцијалну употребу дела.

6. Ауторство - делити под истим условима. Дозвољавате умножавање, дистрибуцију и јавно саопштавање дела, и прераде, ако се наведе име аутора на начин одређен од стране аутора или даваоца лиценце и ако се прерада дистрибуира под истим или сличном лиценцом. Ова лиценца дозвољава комерцијалну употребу дела и прерада. Слична је софтверским лиценцама, односно лиценцама отвореног кода.